Spin injection from epitaxial Heusler alloy thin films into InGaAs/GaAs quantum wells

Damsgaard, Christian Danvad; Hansen, Jørn Bindslev; Jacobsen, Claus Schelde; Lindelof, Poul Erik

Publication date:
2006

Document Version
Publisher's PDF, also known as Version of record

DTU

Nano•DTU
Center for Nanotechnology at DTU

Spin injection from epitaxial Heusler alloy thin films into InGaAs/GaAs quantum wells

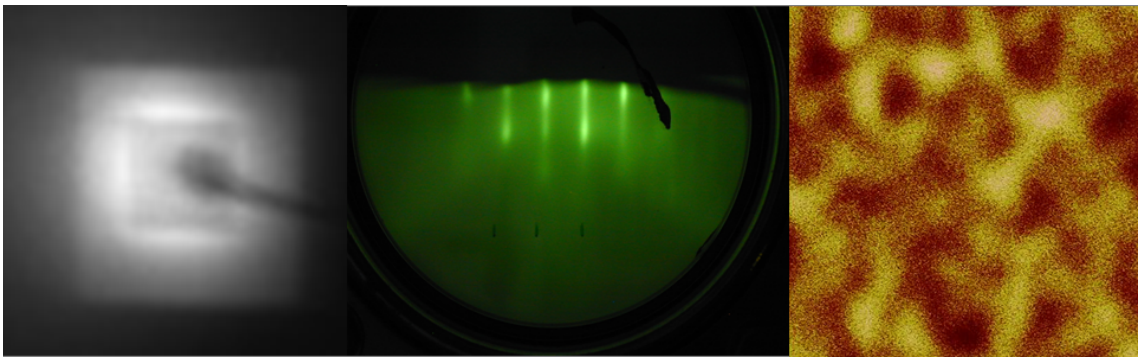

Christian Danvad Damsgaard

March 2006

Ph.D. Thesis
Department of Physics
Technical University of Denmark

Abstract

Spin injection from epitaxial Heusler alloy thin films into InGaAs/GaAs quantum wells

A study has been carried out on the suitability of using the Heusler alloy, Co_2MnGa as spin injector into GaAs. A range of appropriate theoretical and experimental tools has been employed.

Our calculations predict Co_2MnGa to have a spin polarization $P = 63$ %. Calculations have been made on off-stoichiometric crystals and crystals with site swapping defects. Significant decrease in the spin polarization has been predicted for disorder defects involving especially Co on Mn or Ga sites. From an estimate based on the calculated defect formation energies it is found that Mn on Co-sites are likely to exist with a concentration of 2 %, while Ga on Mn-sites are likely to exist with a concentration of 21 %.

Epitaxial magnetic Co_2MnGa thin films have been grown by molecular beam epitaxy. The reproducibility is approximately within 2 % of the correct stoichiometry. Furthermore epitaxial growth of hetero-structures of Co_2MnGa and Al and Al_xO_y layers has been performed succesfully. In the growth optimization process, inductively coupled plasma optical emission spectroscopy has been found to be a reliable and efficient way of determining the stoichiometry of thin films.

The thin films have been characterized structurally, magnetically, and electrically.

The crystal structure has been studied by X-ray diffraction techniques. The expected Heusler structure $L2_1$ has been observed.

Anisotropy of in-plane magnetization in near stoichiometric thin films grown on a 2×4 Ga-rich reconstructed GaAs surface has been observed while no anisotropy is seen for near stoichiometry thin films on an ordinary GaAs surface. Typically thin films grown on GaAs show lower saturation magnetization than expected from bulk properties.

The electrical characterizations have revealed resistivities around $\rho = 350\mu\Omega$cm at $300\,K$. Generally, the near stoichiometric films have a very weak temperature dependence, with resistivity dropping slightly when cooled. A small room temperature anisotropic magneto resistance has been measured to 0.062 %. From transmission line measurements at low current, interface resistance in δ-doped GaAs-ferromagnet is found to typically 0.02-0.1 Ωmm^2 for Fe and Co contacts but two orders of magnitude higher for the Co_2MnGa contacts. Point contact Andreev reflection measurements on an off-stoichiometric thin film ($Co_{2.4}Mn_{1.6}Ga$) show a spin polarization of $P \approx 50$ %.

Furthermore spin injection into a InGaAs/GaAs quantum well have been characterized optically in the oblique Hanle geometry. The highest steady state spin polarization in the quantum well has been found to $P \approx 6$ % at $T = 5$ K. The spin polarization decreases with increasing temperature and is unmeasurably small above 20 K, contrary to Fe reference samples exhibiting a room temperature steady state spin polarization of $P = 2.3$ %.

Resumé

Spininjektion fra epitaksielle tyndfilm af Heuslerlegering ind i InGaAs/GaAs kvantebrønde

Et studie af egnetheden af Heuslerlegeringen Co_2MnGa til spininjektion ind i GaAs er blevet gennemført. En række udvalgte teoretiske og eksperimentielle værktøjer er blevet benyttet.

Vores beregninger forudsiger at Co_2MnGa har en spinpolarisering på $P = 63$ %. Beregninger er blevet lavet på ikke-støkiometriske krystaller og på krystaller med uorden i atomplaceringen. Specielt defekter der involverer Co på Mn eller Ga pladser er blevet forudsagt at medføre en signifikant formindskelse af spinpolariseringsgraden. Et estimat baseret på defektformationsenergier forudsiger, at Mn på Co pladser forefindes med en koncentration på 2 %, og Ga på Mn pladser forefindes med en koncentration på 21 %.

Epitaksielle magnetiske tyndfilm er dyrket ved hjælp af molekylær stråleepitaksi. Reproducerbarheden skønnes at være indenfor 2 % af den korrekte støkiometri. Ydermere er der med succes blevet dyrket epitaksielle heterostrukturer af Co_2MnGa, Al og Al_xO_y-lag. I optimeringen af dyrkningen har vi fundet, at induktivt koblet plasma optisk emission spektroskopi er en troværdig og effektiv metode til at bestemme støkiometrien af tyndfilm.

Tyndfilmene er blevet karakteriseret strukturelt, magnetisk og elektrisk.

Krystal strukturen er blevet undersøgt ved brug af røngtendiffraktionsmetoder. Den forventede Heuslerstruktur $L2_1$ blev observeret.

Anisotropi af magnetiseringen i filmplanet blev observeret pånær støkiometriske tyndfilm dyrket på en Ga-rig 2×4 rekonstrueret GaAs overflade. Nær-støkiometriske tyndfilm dyrket på en ordinær GaAs overflade viste ikke anisotropi. Typisk viste tyndfilm dyrket på GaAs en mindre mætningsmagnetisering end den forventede fra krystalegenskaber.

Elektriske karakteriseringer har vist resistiviteter på omkring $\rho = 350\mu\Omega$cm ved 300 K. Generelt har nær-støkiometriske film en svag temperaturafhængighed med en resistivitet, som daler ved køling. En lille stuetemperatur magnetisk anisotropimodstand er blevet målt til 0.062 %. Transmissionslinjemålinger ved lav strøm har typisk vist "interface"-modstande for en δ-doteret GaAs-ferromagnet kontakt på 0.02-0.1 Ωmm^2 for Fe og Co, men 2 ordner større for Co_2MnGa kontakter. Punktkontakt Andreev reflektionsmålinger på en ikke-støkiometrisk film ($Co_{2.4}Mn_{1.6}Ga$) viser spinpolarisering på $P \approx 50$ %.

Ydermere er der optisk, ved brug af "oblique Hanle" geometri, vist spininjektion ind i en InGaAs/GaAs kvantebrønd. Den stationære spinpolarisering i kvantebrønden er målt til $P \approx 6$ % ved $T = 5$ K. Spin polariseringen falder med stigende temperatur og er ikke målbar over 20 K, modsat Fe-referenceprøver, der udviser en stuetemperatur stationær spin polarisering på $P = 2.3$ %

Preface

This thesis is submitted in candidacy for the PhD degree from the Technical University of Denmark (DTU). It is based on work carried out in the Nano Structured Materials Group at the Department of Physics, from February 2003 till March 2006 under the supervision of Associated Professor Jørn Bindslev Hansen (main supervisor), Associated Professor Claus Schelde Jacobsen, and Professor Poul Erik Lindelof. Part of the work was done during a stay abroad in the spring of 2004 in the group of Dr. Stuart N. Holmes and Dr. Anke Husmann at Cambridge Research Laboratory (CRL), Toshiba Research Europe Ltd. (TREL), UK.

Our goal with this project was to achieve high efficient spin injection into a semiconductor at room temperature. This would get us one step closer to a functional room temperature spin field effect transistor as proposed by Datta and Das in 1990 [1]. In February 2003, when this project started, Heusler alloys seemed to be a promising approach to achieve high spin polarization, due to their candidacy of being half metals [2]. Our collaborators Dr. Stuart N. Holmes and Dr. Anke Husmann at CRL, TREL, UK already had obtained some promising results on Co_2MnGa [3, 4], which is a full Heusler alloy almost lattice matched with InP(1.7 %) or GaAs(2%) [5]. Theoretical predictions showed a bulk spin polarization $P < 100$ % [6, 7] (our own predictions show $P = 63$ %), implying that Co_2MnGa is not a half metal. We did, however, initiate the synthesis, even though Co_2MnGa does not theoretically show half metallic properties. Our choice of this particular Heusler was made for the following reasons:

- The structure is lattice matched with GaAs, indicating that the formation of high quality interfaces should be possible.
- The material is ferromagnetic at room temperature ($T_C = 694$ C$^\circ$).
- The spin polarization is predicted higher than other conventional injector materials, such as Fe, FeNi, Co etc.
- By varying strain or stoichiometry we hoped to increase the spin polarization.

This study should also be considered to be methodological. We have selected methods and techniques both theoretical and experimentally to investigate half metallic candidates.

This thesis presents structural, electrical, and magnetic properties of Co_2MnGa thin films. Furthermore electrical spin injection into a GaAs/InGaAs Quantum Well (QW) has been investigated optically.

Acknowledgements

A lot of people have been involved and very helpful throughout this project. At first I would like thank my supervisors Associate Professor Jørn Bindslev Hansen, Associate Professor Claus Schelde Jacobsen, from the Department of Physics, Technical University of Denmark, and Professor Poul Erik Lindelof, at the Niels Bohr Institute (NBI), Copenhagen University, Denmark, for their invaluable guidance and support. I also thank the Danish Research Council for Technology and Production (STVF/FTP) and the Danish Natural Science Research Council (SNF/FNU) for funding.

In the following I would like to express my further appreciation to:

Niels Bohr Institute, Copenhagen University, Copenhagen, DK:

Prof. Robert Feidenhans'l for structural guidance and characterization, and for inviting me to Hasylab in October 2005.
Simon Oddsson Mariager for structural measurements.
Nader Payami for helping with SEM-lithography.
Dr. Ane Jensen for helping with processing and measurements of Tedrow-Merservey samples.
Dr. Søren Erfurt Andresen (Now Center for Quantum Computer Technology, University of New South Wales, Sydney, Australia) for designing spinLED structures, for developing the Faraday setup at the NBI and for theoretical discussions on "optical orientation".
Dr. Brian Skov Sørensen for letting us use his design for Tedrow-Merservey samples.
Dr. Claus B. Sørensen for his expertise and growth of III-V semiconductor structures.
Magda Utko for theoretical discussions on "optical orientations" and for developing the Faraday setup at NBI.
Niels Vestergaard Jensen for making Faraday geometry measurements on some of our samples. **Jonas Ralf Hauptmann** for making AMF/MFM measurement.
Martin Aagesen for making AMF/MFM measurement.
Janusz Sadowski (formerly NBI) for discussions on MBE growth.

Risø National Laboratory, Roskilde, DK:

Lars Frøsig stertgaard for making stoichiometry analyses by use of Inductively Coupled Plasma - Optical Emission Spectroscopy.

Cavendish Laboratory, Cambridge University, Cambridge, UK:

Dr. Ian Farrer for guidance and growth of spinLED structures.
Prof. Dave Ritchie for collaborating on Co_2MnGa growth on Cavendish Laboratory semiconductor structures.
Dr. Mark C. Hickey for all the hours in the laboratory, for designing spinLED structures,

for developing and testing the setup, and for making Hanle-measurements at Toshiba Research Europe Ldt. Cambridge Research Laboratory.
Dr. Geb Jones for letting me be a part of his group at Cavendish Laboratory during my stays in Cambridge.
Ken Cooper for helping out with processing during my stays in Cambridge.

Toshiba Research Europe Ldt., Cambridge, UK:

Dr. Anke Husmann for guidance in setting up a system to measure point contact Andreev reflection, and for her discussions on structural matter on heusler alloys, and for her always competent help on low temperature electrical measurements.
Dr. Stuart N. Holmes for guidance and discussions, and for making high field, low temperature Hall measurements. To him as well his lovely family for letting me stay at their house during my visits in Cambridge.
Dr. Martin Ward for his expertise in optical measurements.
Dr. David Gevaux for making Time-resolved measurements on some of the spinLED structures.
Michael D. Godfrey for all the hours in the transport lab.

York University

Dr. Jill .S. Claydon, Y.B. Xu, and S. Hassan for making XMCD-measurements, and providing their interpretation of the results.

The Daresbury Synchrotron Radiation Source (SRS), Warrington, UK

N.J. Farley, N.D. Telling and G. van der Laan for making XMCD-measurements.

Technical University of Denmark, Lyngby, DK:

Department of Physics:

Dr. Jesper Mygind for good guidance and support.
Werner Qualmann for his competent technical assistance.
Inge Rasmussen for her expertise in sample processing.
Dr. Leif Gervard for help and guidance on structural characterization.
Prof. Hans L. Skriver for guiding me in using his DFT-program, for theoretical investigation of stoichiometry and swapping defects in ordered Co_2MnGa crystals.
John Larsen for performing Auger Emission Spectroscopy measurements.
Sam Shallcros for proof reading and guidance of chapter two.

Department of Micro- and Nanotechnology:

Prof. Mikkel F. Hansen for his expertise in magnetic thin films, and for letting me use his vibrating sample magnetometer.

Dr. Mads J. Jensen for proofreading and for helping me out with the numerical routine for fitting PCAR data.
Thomas A. Anhøj for general discussions and proofreading.

Department of Production and Management:

Prof. Andy Horsewell for discussions on Stoichiometry determination by use of the energy dispersive X-ray spectroscopy feature on their scanning electron microscope.
Inger Søndergaard for making stoichiometry analyses by use of the energy dispersive X-ray spectroscopy feature on their scanning electron microscope.

Personal:

On a personal level I would like to express my deepest gratitude to my family and especially to my wife Stinna, for her love, help and endless support, and to Maja and Jakob for being my wonderful children.

Christian Danvad Damsgaard
Department of Physics, Technical University of Denmark, Lyngby, Denmark
March 15, 2006.

Contents

Chapter 1

Introduction

This chapter includes introductions to the essential topics of the thesis. At First some spintronic devices will be described. Secondly a selection of the relevant spin processes in semiconductors will be given, followed up by the theory involved in injection of electron spins into different materials. Finally different approaches to establish a high spin injection efficiency will be discussed.

1.1 Spintronics

The main idea in spintronics is to use the intrinsic angular momentum **S** of an electron, as an extra degree of freedom in electronic devices. **S** is also called the electron spin. An electron is often said to have either a spin up or a spin down. The reason for this is the two anti-aligned possible projections of **S** onto the axis of observation (for example z) $S_z = \pm 1/2$ (in units of $\hbar$). As a result from the electron spin the electron carries a magnetic moment of $\mu_z = \pm \mu_B g/2$, where $\mu_B = 9.27 \cdot 10^{-24}$ J/T is the Bohr magneton, and $g = 2.002$ is the electron g-factor. Ferromagnets possess a natural approach for introducing the electron spin in electronic devices, due to the intrinsic imbalance in the electron spin. The reason for this is the quantum mechanical exchange interaction between electron spins contributing from valence and conduction bands. The spin-imbalance in the conduction electron system of ferromagnetic metals such as Fe, Ni, and Co are generally specified by the spin polarization coefficient

$$P = n_\uparrow(E_F) - n_\downarrow(E_F)/(n_\uparrow(E_F) + n_\downarrow(E_F)) \tag{1.1}$$

where $n(E_F)$ is the density of states at the Fermi energy, and varies typically from 20 % to 45 %. By using ferromagnetic materials combined with other materials such as normal metals and insulators the spin imbalance can be injected into other materials and may be electrically utilized due to longer spin lifetimes. A very promising spintronic device was proposed by Datta and Das in 1990 [1]. They described a ballistic device which could control spin transport through the system. The device was named a spin Field Effect Transistor (spinFET) and was the first of its kind which involved semiconductors in spintronics. A sketch of the device can be seen in Figure 1.1.

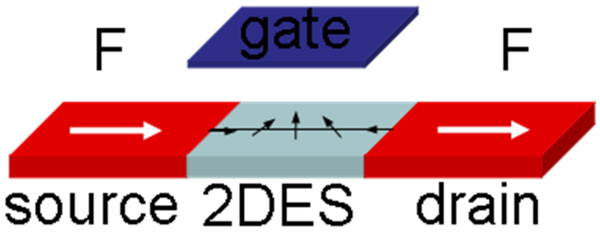

Figure 1.1: *A sketch of a spinFET. Concept adapted from [1]*

Due to the spin-orbit interaction a gate voltage rotates the spin of an injected electron in a two Dimensional Electron Gas (2DEG). If the electron moves in the x-direction, the conductance of the device is controlled by the charge current as a usual Field Effect Transistor (FET), but also by the spin current. The spin current is controlled by the direction of the injected electron spin at the interface to the drain-contact compared to the spin direction in the source-contact. As an example the conductance of the device shown in Figure 1.1 is zero. The direction of the electron spin in the 2DEG has been rotated (precessed) to be anti-aligned, compared with the spin direction in the drain-contact. By either increasing or decreasing the gate voltage the conductance will increase. The precession process has been experimentally investigated by many groups and in various 2DEG systems. Promising results have been obtained in InAs QW systems by Nitta *et al.* [8] and Grundler *et al.* [9] and in InGaAs QW systems by Yamada *et al.* [10], all showing tunable spin-orbit coupling. Further review of the obtained results in the various systems can be found in [11].

The SpinFET has not yet been realized due to problems with injection and detection of electron spin in a semiconductor. The main problem is caused by the conduction mismatch between the ferromagnetic metal and the semiconductor together with poor spin polarization in the ferromagnetic metal. This is described in further details in section 1.3.2.

To give an impression on how close the realization of a spinFET is, we will in the following describe some of the spintronic devices already realized.

GMR Giant Magneto Resistance devices

MTJ Magnetic Tunnel Junctions

SpinLED Spin Light Emitting Diodes

1.1.1 Giant Magneto Resistance devices

Giant Magneto Resistance (GMR) is observed in a hetero junction consisting of ferromagnetic contacts connected through a Normal metal (F/N/F) [12, 13]. A schematic representation of spin polarized transport from an ideal 100 % spin polarized ferromagnetic contact into a normal metal and further into a second 100 % polarized ferromagnetic contact is seen in Figure 1.2.

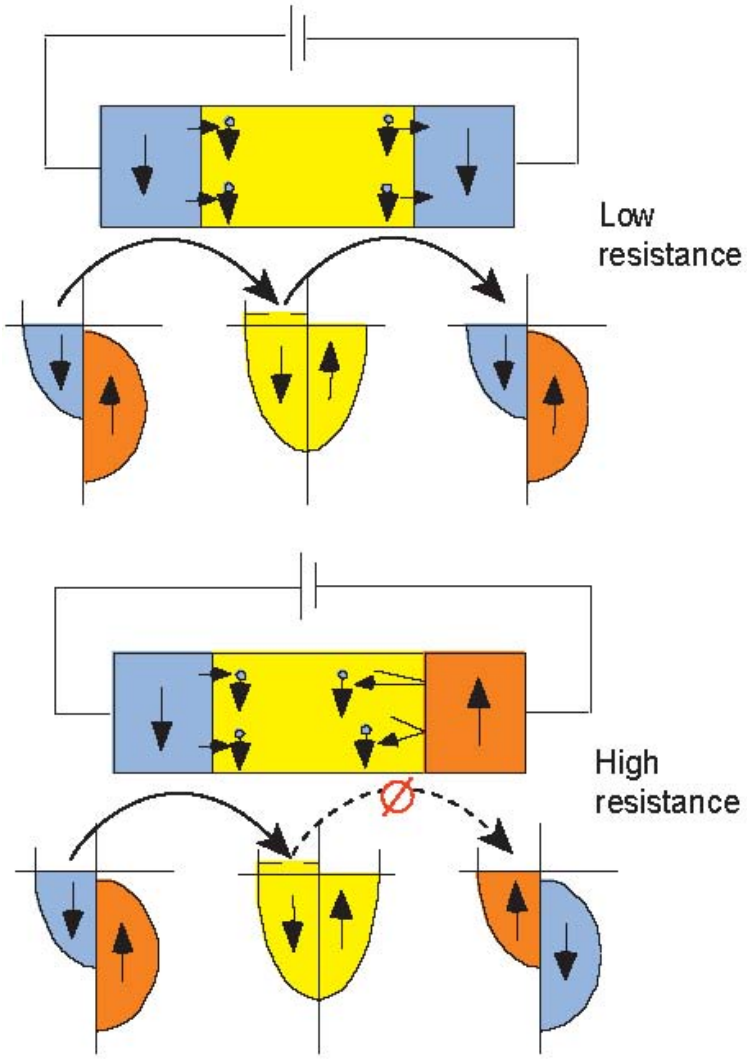

Figure 1.2: *A schematic representation of spin polarized transport from an ideal 100 % spin polarized ferromagnetic contact into a normal metal and further into a second 100 % polarized ferromagnetic contact. Adapted from [14].*

When the contacts are magnetized in parallel configuration (↓↓) the injected spin ↓ electron in the normal metal can easily travel further into the free spin ↓ states. This results in a low resistance, whereas the antiparallel configuration (↓↑) results in a high resistance due to the scattering of the spin-states at the interface. The GMR-effect is the relative difference between the resistance with aligned and anti-aligned spin-states $\Delta R/R = (R_{\downarrow\uparrow} - R_{\downarrow\downarrow})/R_{\downarrow\downarrow}$. The GMR-effect of a device with ferromagnetic metals as contact material is typically from 5 % to 10 % [15]. The best room temperature GMR effect reported is 110 % obtained by several alternating Co/Cu layers [16].

By pinning [1] one of the contacts to a given magnetization direction, the junction will be able to detect and distinguish between parallel and antiparallel magnetization directions. Such a device is often refereed to as a spin-valve. This makes it possible to detect the magnetization direction of very small magnetic bits on a hard disk [17].

1.1.2 Magnetic Tunnel Junctions (MTJs)

The MTJ differs from the GMR device by having an insulator in between the ferromagnetic contacts (F/I/F). Again parallel configuration ($\downarrow\downarrow$) of the ferromagnetic contacts result in a low resistance whereas the antiparallel configuration ($\downarrow\uparrow$) results in a high resistance. The size of the Tunneling Magneto Resistance (TMR) effect $\Delta R/R = (R_{\downarrow\uparrow} - R_{\downarrow\downarrow})/R_{\downarrow\downarrow}$ in a MTJ is typically 20 % to 40 % [15] with ferromagnetic metals as contacts. The best room temperature MTJ effect reported (Djayaprawira *et al.*) is 230 % obtained by a MgO barrier layer sandwiched between amorphous CoFe ferromagnetic electrodes [18]. Another remarkable device showing TMR effect, is an all-semiconductor device reported by Ruster *et al.*. The ferromagnetic contacts are, in this device, made of Dilute Magnetic Semiconductor (DMS) GaMnAs-layers, while the intermediate tunnel barrier is made of a GaAs. Figure 1.3 shows a sketch of the device and some of the results.

[1] An antiferromagnetic layer in direct contact with one of the contacts "fixes" or "pins" the magnetization direction. [15]

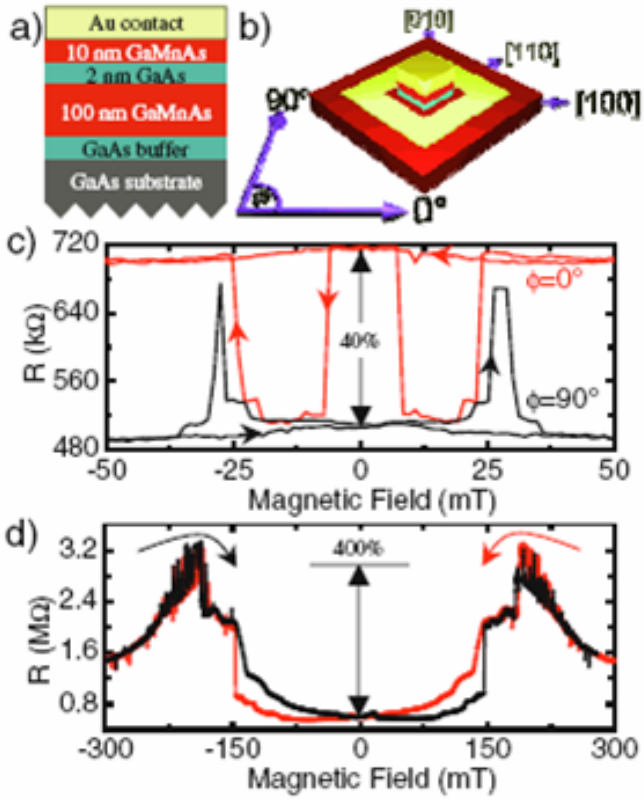

Figure 1.3: *(a) Layer stack and (b) sample layout. (c) 4 K magneto resistance near each in-plane easy axis showing both positive and negative 40 % effects. (d) 4 K magneto resistance in perpendicular field showing a 400 % signal. Adapted from [19].*

At 1.7 K the effect was measured to 150000 %. At temperatures above the GaMnAs Curie temperature $T_c \approx 120$ K the effect disappears.

The TMR effect was recently exploited in a device called Magnetic Random Access Memory (MRAM). This type of RAM is promising due to the fact that it does not need a battery to remember bits.

1.1.3 Spin Light Emitting Diodes (spinLEDs)

In the search of an all electrical spin-dependent component (e.g spinFET) optical methods have been used to determining the efficiency of spin injection into a semiconductor. By use of a PN-junction with a ferromagnetic metal as injector, spin polarized carriers are injected into the semiconductor and through recombination the device emits light. The emitted light is circularly polarized with the polarization degree determined by a set of selection rules (see section 1.2.3). The highest reported spin injection efficiency in a semiconductor was obtained by a DMS GaMnAs-injector and a Zenor diode GaAs/AlGaAs

heterostructure giving a spin injection efficiency of 82 ± 10 % at $T = 4$ K. The spin injection was analyzed in the oblique Hanle geometry (see section 1.2.3) and vanishes at $T = 120$ K corresponding to the Curie temperature of GaMnAs (Van Dorpe *et al.* [20]).

The highest spin injection efficiency from a ferromagnetic metal into a semiconductor measured by electroluminescence is obtained by a CoFe contact through a MgO tunneling barrier into a GaAs/AlGaAs quantum well (QW). The steady state spin polarization in the QW was analyzed in the Faraday geometry (see section 1.2.3) and shows 57 % at $T = 100$ K and 47 % at $T = 290$ K placing the device at the top of the list for room temperature spinLEDs (Wang *et al.* [21, 22]).

Studies of a spinLED with InAs/GaAs self-assembled Quantum Dots (QDs) as spin detector, have recently been reported with a spin injection efficiency on 20 % at $T = 15$ K . The spin injection was done by a Fe contact through a AlGaAs Schottky barrier and was analyzed in the oblique Hanle geometry (Itskos *et al.* [23]).

The highest spin injection efficiency from a Heusler alloy into a semiconductor measured by electroluminescence is obtained by a Co_2MnGe contact through a highly doped AlGaAs Schottky barrier into a GaAs/AlGaAs QW. The spin injection in the QW was analyzed in the Hanle geometry and shows 27 % at $T = 2$ K (Dong *et al.* [24])

1.2 Spin processes in semiconductors

Spin equilibrium in a system is reached by the process of spin relaxation and spin dephasing [25, 11]. The processes are described by characteristic two times called the spin relaxation time T_1 (longitudinal or spin-lattice time) and the spin dephasing time T_2 (transverse or decoherence time). Traditionally the processes are defined within the framework of the Bloch-Torrey equations for magnetization dynamics of a spin ensemble [25, 26, 27]. For mobile electrons, the characteristic times are defined through precessing, decay, and diffusion of the electronic magnetization $\mathbf{M} = (M_x, M_y, M_z)$ in an applied magnetic field $\mathbf{B}(t) = B_0\hat{\mathbf{z}} + \mathbf{B}_1(t)$, with a static longitudinal component B_0 and a transverse oscillating part $\mathbf{B}_1$:

$$\frac{\partial M_x}{\partial t} = \gamma(\mathbf{M} \times \mathbf{B})_x - \frac{M_x}{T_2} + D\nabla^2 M_x \tag{1.2}$$

$$\frac{\partial M_y}{\partial t} = \gamma(\mathbf{M} \times \mathbf{B})_y - \frac{M_y}{T_2} + D\nabla^2 M_y \tag{1.3}$$

$$\frac{\partial M_z}{\partial t} = \gamma(\mathbf{M} \times \mathbf{B})_z - \frac{M_z - M_z^0}{T_1} + D\nabla^2 M_z \tag{1.4}$$

$\gamma = \mu_B g^*/\hbar$ is the electron gyromagnetic ratio (μ_B is the Bohr magneton and g^* is the effective electronic g-factor), D is the diffusion constant, and $M_z^0 = \chi B_0$ is the magnetization in thermal equilibrium where χ is the static susceptibility.

T_1 is the time it takes for the longitudinal magnetization to reach equilibrium or equivalently the time of thermal equilibrium of the spin population with the lattice. During T_1 energy must be taken from the spin ensemble and given to the lattice. T_2 is the

time it takes a spin ensemble initially precessing in phase around the longitudinal field, to loose the phase due to, for example, spatial fluctuations.

In isotropic and cubic solids $T_1 = T_2$ if $\gamma B_0 \ll 1/\tau_c$ where τ_c is the correlation (also called interaction) time. The correlation time is the time over which phase losses occur and it is usually smaller than a picosecond, which corresponds to several tesla. In electronic systems τ_c is given by the momentum scattering time τ_p or by the time of the interaction of electrons with phonons and holes. The fact that $T_1 = T_2$ can be explained classically by observing precession of a spin ensemble that is oriented along the direction of an applied magnetic field B_0. For low magnetic fields spins precess a full period about the perpendicular fluctuating field, feeling the same dephasing or relaxing fields as a transverse component, which imply the same physical mechanism for relaxation and dephasing. The equality is very convenient when comparing experiments with theory, since measurements often yields T_2 and theory often predicts T_1

When working with conduction electrons in metals and semiconductors four mechanisms for spin relaxation or dephasing are relevant: Elliot-Yafet (EY), D'yakonov-Perel' (DP), Bir-Aronov-Pikus (BAP), and hyperfine-interactions (HFI). The mechanisms are schematically drawn in Figure 1.4

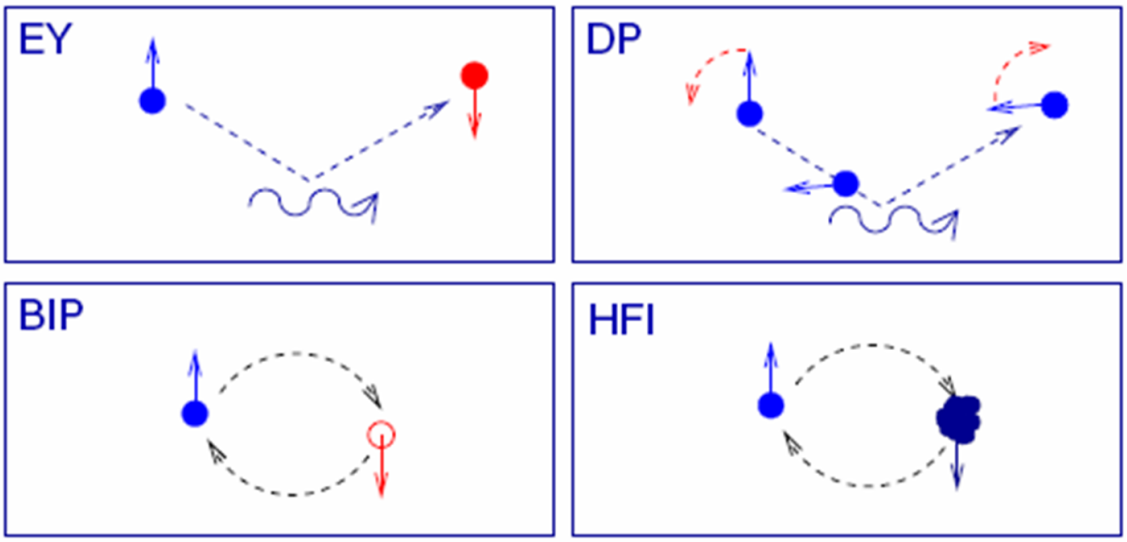

Figure 1.4: *Spin relaxation mechanisms: In the ElliottYafet (EY) mechanism electrons have a small probability of being scattered (here illustrated on a phonon) with a spin flip. In the DyakonovPerel (DP) mechanism the electron spins precess in between scatterings. Scattering events change the precession direction. The BirAronovPikus (BIP) mechanism applies for p-doped semiconductors. Here electron spin is exchanged with the spin of holes (preserving the total spin), while the hole spin then soon relaxes. Finally, the mechanism based on the hyperfine interaction (HFI) is dominant for confined electrons on donors or in quantum dots. The electron spin is exchanged with that of nuclei. Adapted from [28, 29].*

In GaAs and InGaAs/GaAs QWs, which are the semiconductors used in this projet,

at moderate magnetic fields and impurity densities DP dominates the relaxation process [25].

1.2.1 D'yakonov-Perel' mechanism

D'yakonov-Perel' mechanism is a dephasing effect through spin orbit interaction in solids which form a crystal lattice without a center of symmetry. Examples of materials without inversion symmetry are III-V and II-VI semiconductors, where the presence of two different atoms in the Bravais lattice breaks the inversion symmetry [25]. Through spin orbit interaction, inversion asymmetry results in different energies for spin-up and spin-down electrons, which is equivalent to a momentum-dependent internal magnetic field $\mathbf{B}(\mathbf{k})$. Typically the electron spin precession frequency (called the Larmor frequency) $\mathbf{\Omega}(\mathbf{k}) = e/m\mathbf{B}(\mathbf{k})$ is much smaller than the rate of ordinary scattering processes such as phonons, impurities and boundaries. Figure 1.4 (upper right) illustrates this situation. An electron with momentum $\mathbf{k}$ and a spin initially pointing in the z-direction precesses around $\mathbf{B}(\mathbf{k})$. After some time, but before a full precession has occurred, the electron scatters into momentum $\mathbf{k}'$ and the precession axis changes into $\mathbf{B}(\mathbf{k}')$. This small random change of precession angle and frequency dephases the spin ensemble.

The spin relaxation time due to DP mechanism is generally expressed as [30, 31, 32]:

$$\frac{1}{\tau_s} = Q\frac{\alpha_{CB}^2}{\hbar^2\varepsilon_g}\tau_p(k_BT)^3, \tag{1.5}$$

for bulk semiconductors and

$$\frac{1}{\tau_s} = \frac{\alpha_{CB}^2\langle p_z^2\rangle^2}{2\hbar^2m^2\varepsilon_g}\tau_p k_BT \tag{1.6}$$

for quantum well structures. α_{CB} describes the conduction band spin splitting due to lack of inversion symmetry, ε_g is the band gap, T is the temperature, Q is a numerical factor depending on the orbital scattering, $\langle p_z^2\rangle$ is the average square of momentum in the QW growth direction, and τ_p is the average momentum relaxation time [25].

1.2.2 Rashba effect

The Rashba effect originates from the spin-orbit interaction caused by the macroscopic electric field in a semiconductor quantum well. If the potential well in a 2DEG channel is asymmetric, the electrons are moving in an effective electric field $\mathbf{E}$, which the conducting electron or hole sees as a effective magnetic field $\mathbf{B}$. This magnetic field gives rise to a spin splitting. For applications it is essential that the strength of the Rashba effect and thus the spin splitting can be controlled by means of a gate electrode [11, 33].

1.2.3 Optical methods for measuring spin dynamics

In the solid state the average electron spin polarization P of a spin ensemble with average spin $\mathbf{S}$ is given as:

$$P = 2|\mathbf{S}|, \text{ where } |\mathbf{S}|_{Max} = 1/2. \tag{1.7}$$

Throughout this project light has been collected along an axis normal to the sample plane $\hat{\mathbf{z}}$. In this geometry the degree of circular polarized light P_L is given as [2]

$$P_L = \frac{I_+ - I_-}{I_+ + I_-} = \alpha S_z \tag{1.8}$$

where I_{+-} are the intensities of right (+) and left (-) circularly polarized light and α is determined by the optical polarization state of the radiative recombination process in the semiconductor. Through the selection rules shown in Figure 1.5 **S** has a direct connection with the net luminescence helicity of circular polarized light. The selection rules are schematically shown for semiconductors with zincblende structure (e.g. GaAs). The transitions (arrows) are only shown for photoexcitation, however, the magnitudes are the same for radiative recombination.

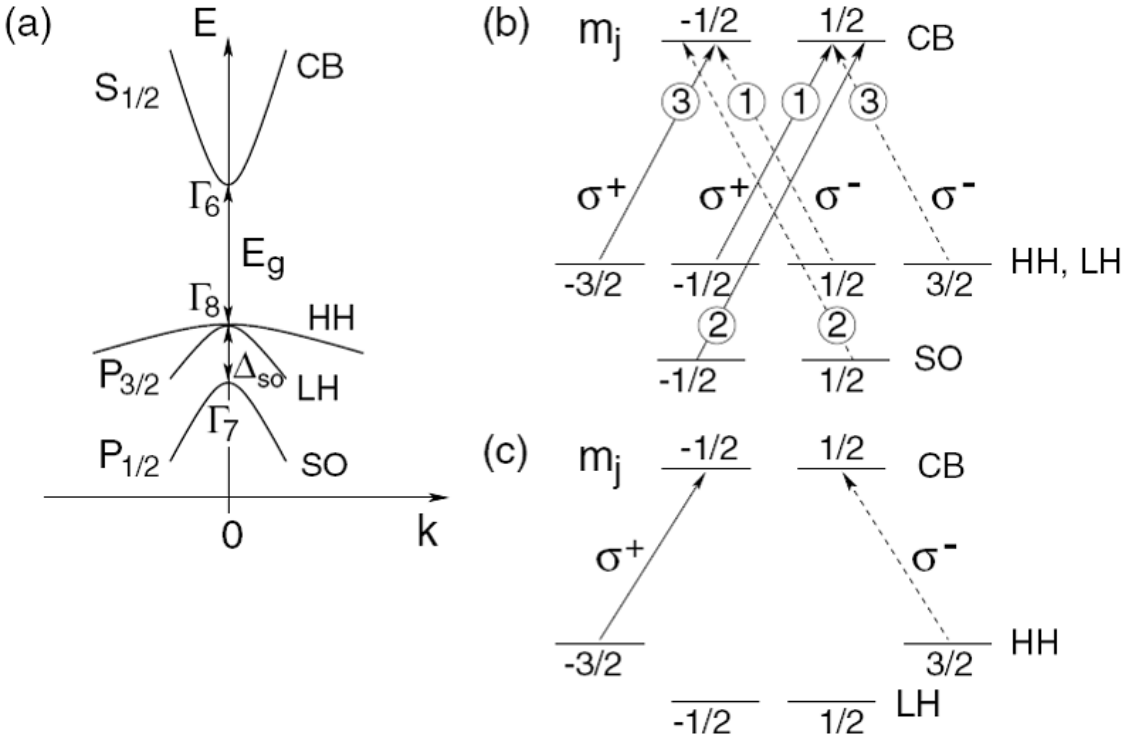

Figure 1.5: *Angular momentum selection rules for* Γ*-point interband transitions. The different bands are indicated with the s-like conduction band (CB), and the p-like valence bands with heavy-holes (HH), light-holes (LH), as well as spin-orbit split off holes (SO). The circular polarizations are dictated by the change in angular momentum,* $\Delta m_J = \pm 1$*. The transition amplitudes are shown circled numbers. (a) shows interband transitions for bulk GaAs. (c) shows interband transitions in a QW, where the degeneracy is lifted due to quantum confinement (and strain in* $In_xGa_{1-x}As$ *QW). Adapted from [28].*

[2] To distinguish between the spin polarization defined earlier as P and the degree of optical circular polarization, the latter will be denoted by a L (Luminescence).

The relevant transition amplitudes are determined by calculating the dipole matrix elements as described in [34]. Transitions which do not carry any momentum $\Delta m_J = 0$, are not depicted in Figure 1.5 because it corresponds to linearly polarized light with polarization axis parallel to the momentum.

In radiative recombination, excitations of the spin-orbit split off subband can be neglected due to the much larger band gap compared with heavy and light hole subbands. In bulk GaAs recombination process, α can be determined from equation (1.8) by considering completely polarized electrons resulting in a spin ensemble with $|\mathbf{S}| = 1/2$ recombining through the selection rules, shown in Figure 1.5,

$$\alpha_{Bulk} = 2 \cdot ((3-1)/(3+1)) = 1. \tag{1.9}$$

In QWs recombination process are dominated by heavy hole excitation due to an energy split of the heavy and light hole subband caused by energy confinement and strain in the QW [34]. Her from it follows that

$$\alpha_{QW} = 2 \cdot ((3-0)/(3+0)) = 2. \tag{1.10}$$

Though this connection (Equation 1.8), optical or electrical spin probing combined with optical detection techniques becomes a very sufficient tool for studying electron-spin dynamics in semiconductors. In order to determine the connection between S_z and $\mathbf{S}$ and thereby the connection between P and P_L, we have to find $\mathbf{S}$. Within the semiconductor the evolution of the average electron spin $\mathbf{S}$, with spin injection, spin scattering, and electron recombination processes taken into account, is described by a Bloch-type equation ([34])

$$\frac{d\mathbf{S}}{dt} = \frac{\mathbf{S}_0}{\tau} - \frac{\mathbf{S}}{T_s} + [\mathbf{\Omega} \times \mathbf{S}] \tag{1.11}$$

where $\mathbf{S}_0$ is the average spin injection (the average electron spin just after injection), τ is the radiative recombination lifetime of the electrons, T_s is the spin lifetime ($T_s^{-1} = \tau^{-1} + \tau_s^{-1}$, where τ_s is the spin scattering time), and $\mathbf{\Omega} = g^* \mu_B \mathbf{B}_{app}/\hbar$ is the Larmor precession frequency, where g^* is the effective electron g-factor, μ_B is the Bohr magneton , and $\mathbf{B}_{app}$ is the applied magnetic field. In steady state ($d\mathbf{S}/dt = 0$) the solution is very simple. Experimentally the model has been tested by two different configurations, namely Faraday and oblique Hanle. The geometries will be described in the following.

Faraday geometry

When helicity dependent Electro Luminescence (EL) measurements are performed with an applied magnetic field perpendicular to the sample plane, parallel to the direction of observation $\hat{\mathbf{z}}$ as depicted in Figure 1.6 (a), the S_z-component of the solution to [34] is given as

$$S_z = \eta \mathbf{S}_0 \cdot \hat{\mathbf{z}} \tag{1.12}$$

where η describes the longitudinal spin relaxation prior to recombination i.e. the spin detection efficiency in the semiconductor $\eta = T_s/\tau$.

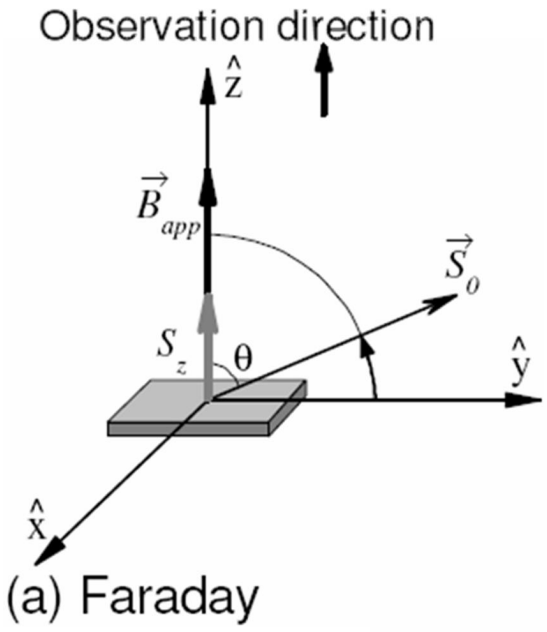

Figure 1.6: *Schematically drawn experiment in the Faraday configurations. Adapted from [35]*

This configuration is called the Faraday configuration. Figure 1.6 shows the influence of an applied perpendicular magnetic field. By increasing the applied magnetic field the magnetic moment will rotate out of the sample-plane and eventually saturate with $\mathbf{M}||\hat{\mathbf{z}}$ at $B_{app} \approx \mu_0 M$. By measuring P_{EL} at magnetic fields higher than the saturation field the average spin polarization in the semiconductor can be found by combining Equations (1.7), (1.8), and (1.12):

$$P = 2\eta S_0 = 2\alpha^{-1} P_{EL},\ B_{app} > \mu_0 M. \tag{1.13}$$

This configuration involves high applied magnetic fields to saturate the thin film out-of-plane typically $B_{app} > 2T$.

Hanle geometry

Another way of measuring the spin polarization of carriers in a semiconductor is using a more moderate applied magnetic field, is the Hanle configuration, where both electroluminescence (EL) and photoluminescence (PL) can be used to yield information about spin polarization of the carriers, but also the characteristic field scale for precession ΔB and thereby T_s and τ, and hence the spin polarization just after injection $P_0 = 2\alpha^{-1}|\mathbf{S_0}|$.

Again light is detected along an axis normal to the sample plane. By applying a moderate oblique magnetic field $\mathbf{B}(0, B_y, B_z)$ with an angle φ to the $\hat{\mathbf{z}}$-direction, precession of in-plane injected spins gives an average non-zero and measurable S_z-component. This component has a direct connection with $\mathbf{S}$ and thereby P.

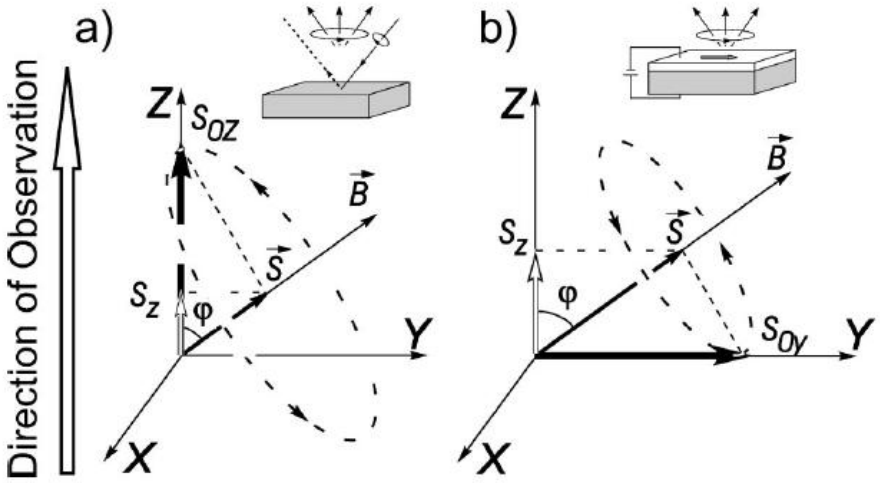

Figure 1.7: *Spin precession in the oblique magnetic field in the case of (a) optical spin injection and (b) electrical spin injection. Under steady state conditions the spin precession leads to averaging and vanishing of the component of* **S** *perpendicular to* **B** *. The remaining component is parallel to* **B** *and is accessible in measurements. Adapted from [36].*

Figure 1.7 depicts the Hanle geometry in (a) the optical spin injection (PL) and (b) electrical spin injection (EL) configuration. At first we look at the optical spin injection where no bias is applied to the LED-structure. By exciting with circularly polarized light we can polarize the carriers to have an average spin $\mathbf{S}_0(0, 0, S_{0z})$. The solution to Equation (1.11), in the steady state case, with respect to S_z is

$$S_z = S_{0z}\eta \frac{1 + (B/\Delta B)^2 \cdot \cos^2 \varphi}{1 + (B/\Delta B)^2}, \tag{1.14}$$

where $\Delta B = (\frac{g^* \cdot \mu_B}{\hbar} T_s)^{-1}$ is the Hanle curve half-width corresponding to the condition $\Omega T_s = 1$. Equation (1.14) shows that for zero applied magnetic field $B_{app} = 0$ we measure η directly because $S_z = S_{0z} \cdot \eta$, where S_{0z} is known from the incident light-polarization. By finding the Hanle curve half-width, information about T_s is found (if g^* is known). From this measurement all characteristic times in the spin system are measured. This works as a reference measurement for the electrical spin injection configuration described below.

In the case of in plane electrical injection, which means we define $\mathbf{S}_0(0, S_{0y}, 0)$, we get a new solution to Equation (1.11)

$$S_z = S_{0y}\eta \frac{(B/\Delta B)^2 \cdot \cos \varphi \sin \varphi}{1 + (B/\Delta B)^2}. \tag{1.15}$$

This time S_z is a function of S_{0y} which was precisely what we wanted with this approach. From Equation (1.15) it is found that S_z increases from 0 at $B = 0$ and saturates at $S_z = S_{0y}\eta \cos \varphi \sin \varphi$ for $B >> \Delta B$. This highly nonlinear effect gives an explicit way of

determining spin injection compared with side-effects which are linear or nearly linear with B. It can also be seen that the angle which yields the largest change in S_z is $\varphi = 45°$. To find the steady state polarization P we again use equation (1.7) and (1.8) together with the fact that we know $\mathbf{S}_0(0, S_{0y}, 0)$, i.e.,

$$P = 2|S| = 2\eta S_{0y} = 2S_{z,max}(\cos\varphi \sin\varphi)^{-1} = 2\alpha^{-1}P_{EL}(\cos\varphi.\sin\varphi)^{-1}, B >> \Delta B \tag{1.16}$$

Again we can use the Hanle curve half-width ΔB to give information about T_s, but on the contrary to the optical case, no direct information on τ is given. If optical reference measurement has been made or if τ has been measured by use of, for example, Time Resolved Photo Luminescence (TRPL) measurements, the spin polarization just after injection can be found by $P_0 = P/\eta$.

If the magnetization of the thin film in the oblique magnetic field tilts out of the plane this gives rise to the situation sketched in Figure 1.8.

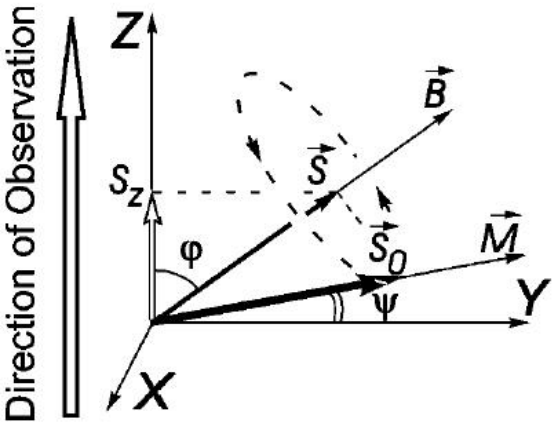

Figure 1.8: *Tilting of the magnetization* **M** *of the thin ferromagnetic film under application of the oblique magnetic field* $\mathbf{B}(0, B_y, B_z)$ *in the oblique Hanle effect experimental configuration[36]*

.

A new steady state solution to Equation (1.11) needs to be found. With $S_0(0, S^*_{0y}, S^*_{0z})$ where $S^*_{0y} = S_0 cos\psi$ and $S^*_{0z} = S_0 sin\psi$ the new solution is

$$S_z = S^*_{0y}\eta\frac{(B/\Delta B)^2\cos\varphi\sin\varphi}{1+(B/\Delta B)^2} + S^*_{0z}\eta\frac{1+(B/\Delta B)^2\cos^2\varphi}{1+(B/\Delta B)^2}. \tag{1.17}$$

From this solution the connection between the spin polarization P and the degree of circularly polarized light P_{EL} can be found.

Confounding effects

Mainly two confounding effects are present for both Faraday and Hanle geometries.

MCD The first effect arises from the fact that the obtained light propagates through the thin semitransparent magnetic film which may have some out-of-plane magnetization. The effect that comes into play is the Magneto-optical Circular Dichroism (MCD) which is a difference in absorption probability of right and left circularly polarized light. This effect is linear with B and can therefore quite easily be taken into account. By using unpolarized incident light in the optical injection configuration one can easily measure the MCD effect by simply measuring P_{PL} as a function of B. A detailed description of the phenomenon can be found in [36].

Zeeman splitting The side effect arises from the Zeeman splitting in the semiconductor. The side effect is most important in Faraday geometry, where the applied field typically is above 2T. The average electron spin corresponding the Zeeman splitting is given by

$$S_{Zeemann} = \frac{g^* \mu_B B}{4 k_B T}. \tag{1.18}$$

As seen from Equation (1.18) this effect is also linear with B and is therefore easy to take into account. A detailed description of the phenomenon can be found in [36].

Dynamic Nuclear Polarization (DNP)

Furthermore DNP can come into play through hyperfine interaction of electrons and nuclei [34]. The hyperfine interaction potential is given as:

$$V = \frac{16\pi}{3I} \mu_I \mu_B |\psi(\mathbf{R})|^2, \mathbf{I} \cdot \mathbf{S} \tag{1.19}$$

where $\psi(\mathbf{R})$ is the electronic wave function at the nucleus, $\mathbf{I}$ and $\mathbf{S}$ are the nucleus spin and electron spin respectively, and μ_I and μ_B are the nuclear and electron spin magnetic moments. The effect is observed as a change of the effective B-field due to the polarized nuclei ensemble $\mathbf{B} = \mathbf{B}_{app} + \mathbf{B}_N$. $\mathbf{B}_N$ is given by

$$\mathbf{B}_N = b_N \mathbf{I}_{av} / I \tag{1.20}$$

$$b_N = \frac{16\pi}{3 g v_0} \mu_I \eta_B \xi \tag{1.21}$$

$\mathbf{I}_{av}$ is the average nucleus spin, I is the nucleus spin, and b_N is the nuclear field, which would be observed in the case of complete nuclear polarization. ξ is the number of nuclei of the species considered in the unit cell, η_B is the Bloch amplitude at the site of the nucleus (unity in case of homogenous electron density), μ_I is the nuclear magnetic moment. Since the spin-lattice time T_1 is in the order of seconds to days, dependent on temperature and paramagnetic impurity content [34], DNP can be observed differently dependent on B-field sweep rate, and other time related experimental parameters. The effect is especially observed for a high spin injection efficiency [36, 35, 37]. A detailed description of the phenomenon is found in [34].

1.3 Spin injection theory

Previous section described spin processes and some experimental techniques to measure the spin quantities inside a semiconductor. This section will describe some electrical techniques to yield the spin polarization in a given metal by use of superconductors. Furthermore a diffusive model regarding spin injection into a semiconductor (or normal metal) will by given .

1.3.1 Ferromagnetic/Superconductor contacts

Methods combining superconducting and ferromagnetic materials to detect the spin polarization P in the ferromagnet, have been found to be rather powerful. Mainly two approaches have been followed, (1) the Tedrow and Meservey approach, based on Zeeman splitting of the electron level in a superconductor via a tunnel junction between a ferromagnetic and a superconductor thin film, and (2) Point contact Andreev reflection approach based on the coherent quantum mechanical phenomenons in a point contact between a ferromagnet and a superconductor.

Tedrow-Meservey approach

A non-equilibrium of spin states at the fermi energy results in an asymmetry of the tunneling conductance due to Zeeman splitting in the ferromagnet [38, 39, 40, 41, 42]. This asymmetry can be seen in Figure 1.9. Large applied magnetic field gives a large asymmetry. The spin dependent conductivities are:

$$\begin{aligned}\frac{dI}{dV} = \sigma(V) \sim &\int_{\infty}^{\infty} \frac{1+P}{2} N_s(E+\mu_z B) \frac{1/(k_B T)\exp(1/(k_B T)(E+eV))}{(1+\exp(1/(k_B T)(E+eV)))^2} dE \\ &+ \int_{\infty}^{\infty} \frac{1-P}{2} N_s(E-\mu_z B) \frac{1/(k_B T)\exp(1/(k_B T)(E+eV))}{(1+\exp(1/(k_B T)(E+eV)))^2} dE,\end{aligned} \tag{1.22}$$

where P is the spin polarization, T is the temperature, k_B is the Boltzmann constant, μ_z is the electron magnetic moment, B is the applied magnetic field, e is the electron charge, and N_s is the BCS normalized density of states [43]. Two assumptions are made when doing this analysis:

- The density of states of the superconductor for each spin direction in a given magnetic field has the same functional form and is merely displaced in energy by $\pm\mu B$. (we neglect spin-orbit and spin-flip scattering in the superconductor).
- There are no spin-flip tunneling processes.

Both assumptions are true for Al.

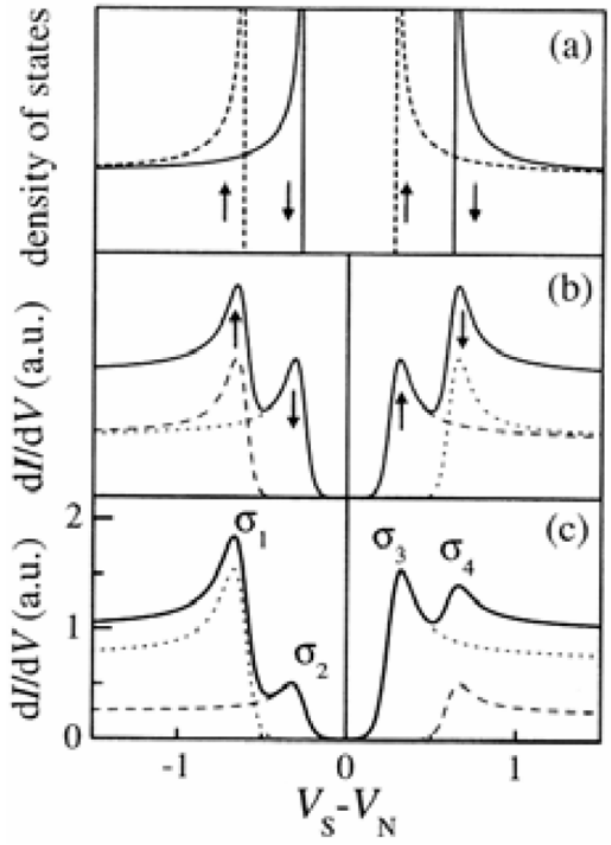

Figure 1.9: *Magnetic field splitting of the quasi-particle states into spin-up and spin-down density of states (a). Spin resolved conductances and resulting total conductance (solid line) of a N/I/S (b) and F/I/S (c) tunnel junctions. Adapted from [44].*

The spin polarization P can be calculated from the conductance "finger print". From the four local maximum values called $\sigma_{1..4}$, we get

$$P = \frac{(\sigma_4 - \sigma_2) - (\sigma_1 - \sigma_3)}{(\sigma_4 - \sigma_2) + (\sigma_1 - \sigma_3)}. \tag{1.23}$$

From these type of experiments Tedrow *et al.* have reported 40 ± 2 % in the case of Fe, 23 ± 3 % in the case of Ni, and 35 ± 3 % in the case of Ni [39].

Andreev reflection approach

In 1998 R. J. Soulen *et al.* [45] used a superconducting point contact to determine the contact spin polarization at the Fermi energy of several metals. The spin polarization is then determined from the conduction characteristic of the contact. The method does not need any applied magnetic field or any special constraints on the sample. Several different materials have been characterized within this method. Figure 1.10 shows the results of the work.

Material studied	Point	Base	N	P_T (%)	P_C (%)
NiFe	Nb	$Ni_{0.8}Fe_{0.2}$ film	14	25 ± 2	37 ± 5
Co	Nb	Co foil	7	35 ± 3	42 ± 2
Fe	Ta	Fe film	12	40 ± 2	45 ± 2
	Fe	Ta foil	14		46 ± 2
	Nb	Fe film	4		42 ± 2
	Fe	V crystal	10		45 ± 2
Ni	Nb	Ni foil	4	23 ± 3	46.5 ± 1
	Nb	Ni film	5		43 ± 2
	Ta	Ni film	8		44 ± 4
NiMnSb	Nb	NiMnSb film	9	–	58 ± 2.3
LSMO	Nb	$La_{0.7}Sr_{0.3}MnO_3$ film	14	–	78 ± 4.0
CrO_2	Nb	CrO_2 film	9	–	90 ± 3.6

Figure 1.10: *Summary of experimental results with Andreev reflection to determine P_c at E_F. Adapted from [45].*

As described earlier the spin polarization P can be defined as

$$P = \frac{n_\uparrow(E_F) - n_\downarrow(E_F)}{n_\uparrow(E_F) + n_\downarrow(E_F)}, \tag{1.24}$$

where $n_{\uparrow(\downarrow)}(E_F)$ is the spin depending density of states at the Fermi energy. The value of P is usually controlled by the extent of which the d and s band cross the Fermi surface [45]. For a typical transition metal ferromagnet the d bands are narrow and fully or partially spin polarized, while the s bands are broad and have a lesser degree of spin polarization. If the ferromagnet has an electronic structure at the Fermi surface which is primarily d-like, P will be high, while it can be both, if the electronic structure at the Fermi surface is s-like or s-d-hybridized [45].

The point contact Andreev reflection method does not measure P but a very close relative, i.e., the contact spin polarization efficiency

$$P_c = \frac{n_\uparrow(E_F)v_{F\uparrow} - n_\downarrow(E_F)v_{F\downarrow}}{n_\uparrow(E_F)v_{F\uparrow} + n_\downarrow(E_F)v_{F\downarrow}}, \tag{1.25}$$

where $v_{F\uparrow}$ and $v_{F\downarrow}$ are the spin dependent Fermi velocities. Since the spin dependent current $I_{\uparrow\downarrow}$ is proportional to $n_{\uparrow\downarrow}(E_F)v_{F\uparrow\downarrow}$, the contact spin polarization is

$$P_c = \frac{I_\uparrow - I_\downarrow}{I_\uparrow + I_\downarrow}. \tag{1.26}$$

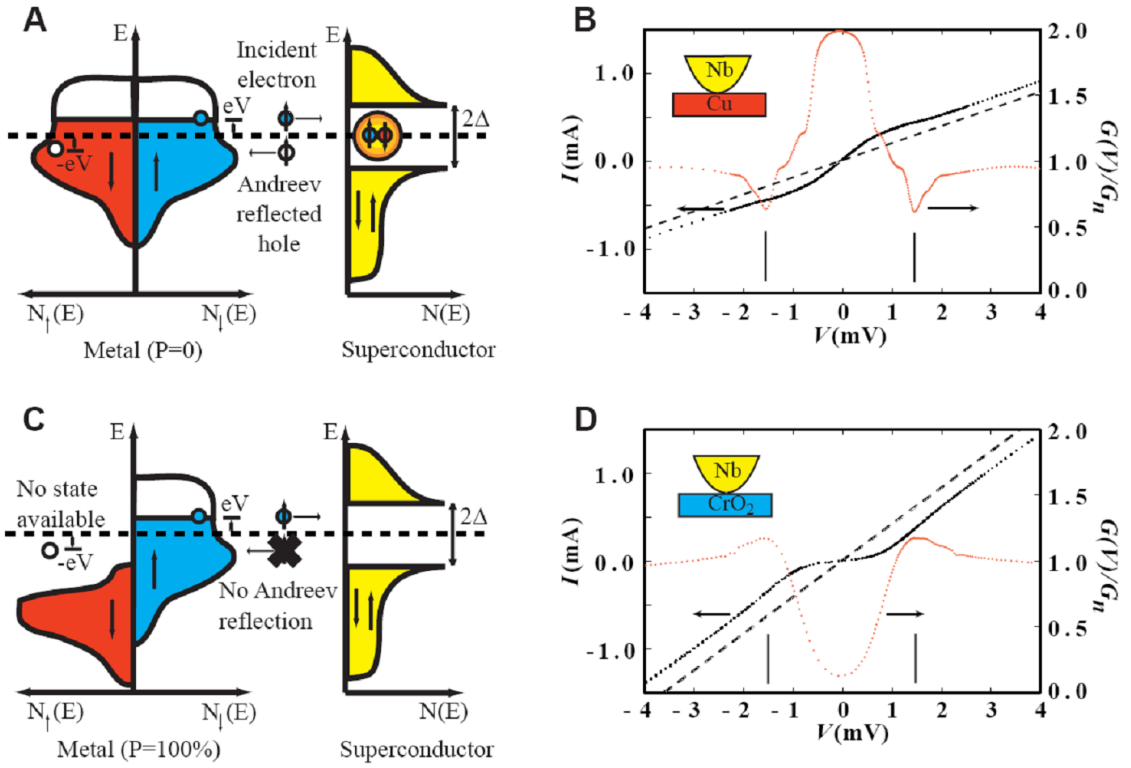

Figure 1.11: *A and C: Schematics of the process for $P = 0$ and $P = 100$ % . B and D: Measurements on Cu ($P_c = 0$) and measurements on CrO_2 ($P_c = 90$ %). Adapted from [45].*

.

Andreev reflection can be explained from Figure 1.11 where (A) shows the schematics of a metal with $P = 0$. An electron with spin up is propagating from the metal towards the superconductor. At the interface a so-called Cooper pair is made [43] which leads to a reflection of a hole with spin down. This hole-reflection acts like an additional conduction channel and gives a doubling of the normal state conductance. This is a second order process which dominates since the first order process is forbidden due to the energy gap in the superconductor. Figure 1.11 (B) shows the conductance as a function of applied bias for a Nb-Cu point contact. The doubling of the conductance inside the superconducting gap $\Delta(T = 0) = 1.5$meV marked with vertical lines is clearly seen. Figure 1.11 (C) shows the schematics of a metal with $P = 100$ %. An electron with spin up is propagating from the metal towards the superconductor. This time the formation of a Cooper pair is forbidden due to the lack of spin-down electrons in the metal. This results in a suppression of the conduction. For a 100 % spin polarized metal the conduction inside the superconducting gap Δ will be zero. Figure 1.11 (D) shows the conductance as a function of applied bias for a Nb-CrO_2 point contact. The suppression of the conductance inside the superconducting

gap marked with vertical lines is clearly seen. P_c was initially found from the fact that

$$\frac{1}{\sigma_n}\frac{dI}{dV}(eV \to 0, T \to 0, Z = 0) = 2(1 - P_c), \tag{1.27}$$

where Z is the interfacial scattering parameter. As long as Z is zero or at least small, this assumption is valid. If this is not the case another path must be chosen. Blonder, Tinkham, and Klapwijk (BTK) previously developed a theory for analyzing the conductance versus bias for normal metal/superconductor contacts [46, 47]. Strijkers *et al.* extended the model to include the spin polarization by decomposing the current into two parts namely the polarized I_p and the unpolarized I_u current [48]

$$I = (1 - P_c)I_u + P_c I_p. \tag{1.28}$$

The two currents are found by solving the following equation:

$$I_{u,p} = 2eCNv_F \int_{-\infty}^{+\infty} [f(E - eV, T) - f(E, T)][1 + A_{u,p} - B_{u,p}]dE, \tag{1.29}$$

where e is the electron charge, C is the cross-sectional area of the contact, N is the one-spin density of states at the Fermi energy, v_F is the Fermi velocity, f is the Fermi-Dirac distribution function, $A_{u,p}$ represents the Andreev reflection probability and $B_{u,p}$ the probability of normal reflection. The latter two are given in details as a function of energy by Strijkers *et al.* [48]. The model includes an interface superconducting layer with a gap energy Δ_1. This parameter is important when dealing with nonmagnetic metals [48]. By using this model the full conductance versus bias curve may be fitted.

1.3.2 Ferromagnet/Semiconductor contacts

A simple diffusive model can conceptually describe the physics in a ferromagnet/normal metal (F/N) or ferromagnet/semiconductor (F/SC) junction. The method used to analyze the model was developed by Fert and Jaffres [49] and is based on methods firstly described by van Son *et al.* [50]. Rashba *et al.* [51] continued the work to include a tunnel barrier as a possible solution to the conductivity mismatch problem. The methods are an electrochemical potential-based treatment of the system with the assumption that spin-scattering occurs on a much longer time scale than other electron scattering events. The system under consideration is the F/SC-junction .

Two electrochemical potentials $\mu_\uparrow$ and $\mu_\downarrow$ are defined at any point of the device. Under the assumption that the current flows only in the x-direction the electrochemical potentials are connected to the current via the conductivity σ, the diffusion constant D, and the spin-flip time constant τ_{sf} through Ohm's law and the diffusion equation

$$\frac{\partial \mu_{\uparrow,\downarrow}}{\partial x} = -\frac{e j_{\uparrow,\downarrow}}{\sigma_{\uparrow,\downarrow}}, \tag{1.30}$$

$$\frac{\mu_\uparrow - \mu_\downarrow}{\tau_{sf}} = \frac{D\partial^2(\mu_\uparrow - \mu_\downarrow)}{\partial x^2}, \tag{1.31}$$

where $j_\uparrow$ is the current density for spin-up, and $j_\downarrow$ is the current density for spin-down. The sum of the two spin dependent current densities gives the total current density $j = j_\uparrow + j_\downarrow$. D is the weighted average of the different diffusion constants for both spin directions. By solving the above equations and using the continuity of $j_\uparrow - j_\downarrow$ on each side of the F/SC-interface, we find the chemical potentials and thereby the spin polarized current densities as a function of x in each material ($x < 0$ for F and $x > 0$ for SC). Figure 1.12 (a) shows the electrochemical potentials anywhere in a F/SC device. Due to non-equilibrium of the spin states at the boundary a splitting of the electrochemical potentials occurs. The splitting is proportional to the total current density at the interface and decays exponentially inside the materials which results in zero difference at $\pm\infty$. A typical length scale for the decay is the spin-flip length $l_{sf} = \sqrt{D\tau_{sf}}$ of the material. Normally, the spin-flip length in the semiconductor l_{sf}^{SC} exceeds the spin-flip length in the ferromagnet l_{sf}^{F}. This is especially the case when using a degenerate semiconductor. The current density spin polarization at the boundary is found to be:

$$\frac{j_\uparrow - j_\downarrow}{j} = \frac{\beta + \gamma r_b^*/r_F}{1 + r_{SC}/r_F + r_b^*/r_F}, \tag{1.32}$$

where $\beta = (\sigma_\uparrow - \sigma_\downarrow)/(\sigma_\uparrow + \sigma_\downarrow)$ is the spin polarization of conduction electrons in the ferromagnet, $\gamma = (r_\uparrow - r_\downarrow)/(r_\uparrow + r_\downarrow)$ is the spin polarization of the interface, and $r_F = \rho_F/(1-\beta^2) \cdot l_{sf}$, $r_{SC} = \rho_{SC} l_{sf}^{SC}$, and $r_{b*} = r_b/(1-\gamma^2)$ are the effective resistances of the materials involved. Without interface resistance $r_b^* = 0$, $\gamma = 0$ the spin polarization at the interface

$$\frac{j_\uparrow - j_\downarrow}{j} = \frac{\beta}{1 + r_{SC}/r_F}. \tag{1.33}$$

From equation (1.32) the conductivity mismatch problem can be observed. If the resistance of the ferromagnet is much smaller than the resistance of the normal metal the spin injection vanishes. Rashba exploited the situation where the interface between the ferromagnet and the normal metal has a finite resistance and a spin polarization. This is the case for a tunnel barrier where the spin polarization is controlled by the non-equilibrium of spins on the ferromagnet-side of the barrier. From equation (1.32) it is seen that even in the case of conductivity mismatch $r_F/r_{SC} << 1$ some injection still remains which is controlled by the relation between r_{SC} and r_b^*. Figure 1.12 shows the chemical potentials in the case of (a) zero interface resistance and (b) finite interface resistance and polarization. Figure 1.12 (c) shows the corresponding current spin polarization.

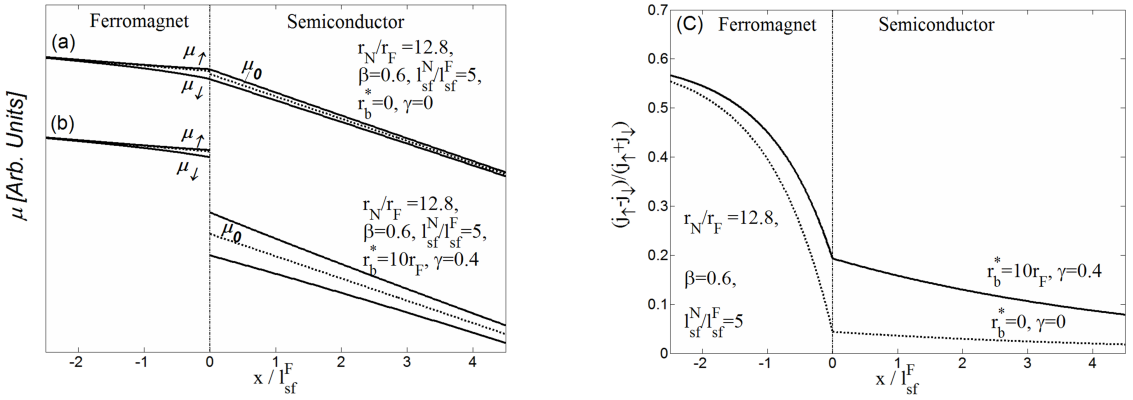

Figure 1.12: *Calculated electrochemical potentials at a ferromagnet/semiconductor interface shown in the case of (a) zero interface resistance and (b) finite interface resistance. (c) shows the corresponding spin polarized current. To enhance the splitting of the electrochemical potentials at the interface, some parameters are chosen unrealistically:* $\beta = 0.6$, $l^{SC}_{sf}/l^F_{sf} = 5$, $r_{SC}/r_F = 12.8$, *and in (b)* $\gamma = 0.4$, *and* $r^*_b = 10r_F$

The degree of spin injection is clearly enhanced by implementing a spin polarized interface resistance. The effect becomes even more significant when modeling more realistic ferromagnet/semiconductor junctions. Figure 1.13 shows the spin polarized current in such a junction with and without interface resistance. In the case of zero interface resistance $r^*_b = 0$ the current spin polarization rapidly goes to zero resulting in extremely low spin injection. In case of a finite interface resistance spin injection is observed.

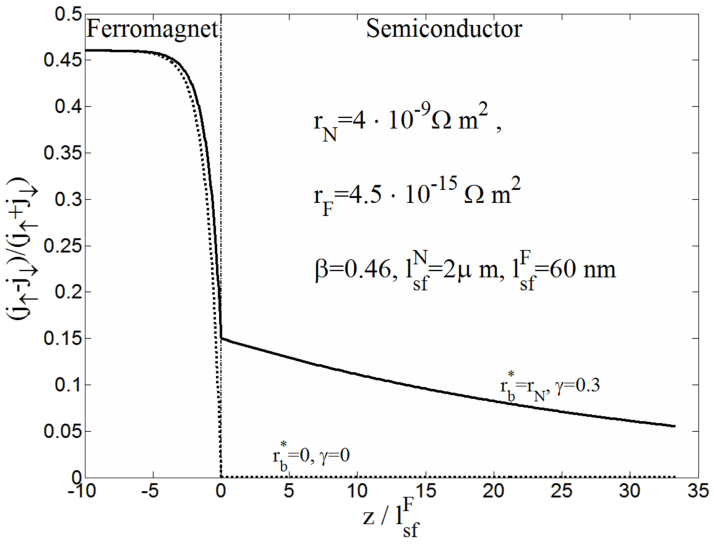

Figure 1.13: *Calculation of the spin polarized current of a ferromagnet/semiconductor interface shown in the case of zero interface resistance and finite interface resistance. The parameters are chosen realistic to:* $\beta = 0.46$, $l^{SC}_{sf} = 2\ \mu m$, $l^F_{sf} = 60\ nm$, $r_{SC} = 4 \cdot 10^{-6}$, $r_F = 4.5 \cdot 10^{-15}$, $\gamma = 0.4$, *and* $r^*_b = r_{SC}$

The diffusive model describes a simple approach to understanding F/SC interfaces. The model ignores important mechanisms such as non-linearities in the transport regime, which in case of tunneling could be highly non-linear and bias dependent. Any ballistic mechanism, such as e.g. band bending effects at the interface as described by Schmidt *et al.* [53], is also ignored.

1.4 Spin injection approaches

From the calculations in the previous section it seems that good efficient spin injection from a normal ferromagnetic metal into a semiconductor is rather complicated to achieve. By using a spin selective interface resistance one could "cheat" the conductivity mismatch, however, engineering such a barrier is difficult. In this section alternative roads to achieve spin injection into a semiconductor, will be presented.

If we could make a ferromagnet with the same conductance or even lower than the semiconductor, r_N/r_F would not dominate the denominator in Equation (1.32) and spin injection would indeed occur. This approach is possible. Dilute Magnetic Semiconductors (DMS) is the name of a family of semiconductors doped with a magnetic ion such as for example Mn^{2+}. The best known material is GaMnAs. The main problem with this approach is that compared with normal ferromagnetic metals, the Curie temperature is low $T_C \leq 120$ K. The highest spin injection into a semiconductor by this material is as mentioned in section 1.1.3 82 ± 10 % at 4 K [20].

Another interesting approach is g-factor engineered devices as proposed by [54]. Re-

cently Salis *et al.* [55] demonstrated a gate-voltage-mediated control of coherent spin precession over a 13-GHz frequency range in a fixed magnetic field of 6 T. The measurements revealed complete suppression of precession, reversal of the sign of $g*$, and operation up to room temperature.

1.4.1 Half metals

In a half metal, all charge carriers at the Fermi energy is either spin up or down. Having a half metal as spin injector material the conductivity mismatch would be irrelevant. In respect to equation (1.32) this would be the same as letting $r_F \rightarrow \infty$ due to the infinite spin-flip length in the ferromagnetic l^F_{sf}. Figure 1.14 shows a sketch of the spin dependent density of states for a half metal. One spin direction has a finite density of states at the Fermi energy (like in a 3d-metal) while the other spin direction has a gap (like in a semiconductor).

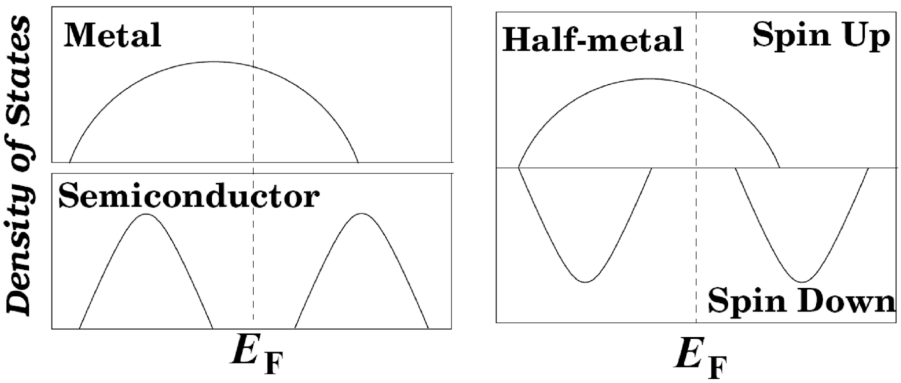

Figure 1.14: *Schematic representation of the density of states for a half-metal with respect to normal metals and semiconductors. Adapted from [56]*

.

Several theoretical predictions of half metal materials have been made. The best known candidate is CrO_2 [57]. A very high spin polarization $P = 0.96 \pm 0.01$ have been verified by Point Andreev Reflection Contacts [58]. Only a few functional devices has been realized with CrO_2, due to difficulties in synthesis. The material has a narrow stability range near 300 °C which extends to high oxygen pressure [59].

1.5 Heusler alloys

In 1983 Groot *et al.* [2] theoretically predicted the half Heusler alloys NiMnSb and PtMnSb to be half metals. This initiated both theoretical and experimental investigations of Heusler alloys.

The Heusler alloys were named after Frederich Heusler who, in 1903, found strong ferromagnetism in ternary alloys combined of weakly magnetic materials often with Mn

as one of the components [60]. There are two types of Heusler alloys: Full Heusler alloy which has the form X_2YZ placed in a $L2_1$ crystal structure and half Heusler alloy which has the form XYZ placed in a $C1_b$ crystal structure. The X and Y are elements of the transition metal group whereas the Z component belongs to the group III-V elements. The $L2_1$ crystal structure consists of four face-centered-cubic (fcc) sublattices. $C1_b$ differentiates itself from $L2_1$ by leaving one of the sublattices empty. Figure 1.15 shows the crystal structure of the full and half Heusler crystal.

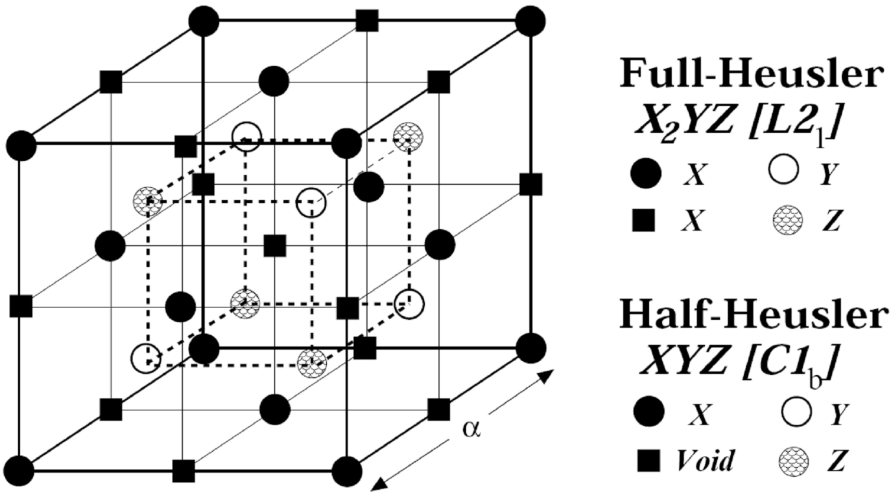

Figure 1.15: *$C1_b$ and $L2_1$ structures adapted by the half- and full-Heusler alloys. The lattice consist of 4 interpenetrating f.c.c. lattices. The unit cell is that of a fcc lattice with four atoms as basis, e.g. CoMnGa: Co at (000), Mn at (1/4 1/4 1/4), a vacant site at (1/2 1/2 1/2) and Ga at (3/4 3/4 3/4). In the case of the full Heusler alloys, e.g. Co_2MnGa also the vacant site is occupied by a Co atom. Note also that if all atoms were identical, the lattice simply would be the bcc. Adapted from [56].*

Some of the alloys are used as efficient focusing monochromators for polarized neutrons, due to the possibility of growth of very large single domain crystals. Monocrystalline Cu_2MnAl ingots have been successfully grown up to a length of 150 mm and a diameter of 60 mm [61]. As already mentioned, it was found theoretically that some Heusler alloys are Half metal candidates [2]. Most research on these alloys have been done on NiMnSb [62], [63], Ni_2MnGa[64, 65], Co_2MnGe [66, 67], and Co_2MnSi [68, 69, 70, 71, 72]. In the present study we have chosen to work with Co_2MnGa due to its nearly lattice match with GaAs (about 2.1 % mismatch) and InP (about -1.7 % mismatch) together with the fact that Toshiba Research Europe Ltd. Cambridge, who is our collaborator, had already done some growth and obtained promising measurements on this material [3, 4]. In 1970 P. J. Webster reported magnetic and structural characterization of some bulk heusler alloys, including Co_2MnGa [5]. Table 1.1 summarizes some of the results.

Lattice parameter [Å]	5.770
Curie temperature [K]	694 ± 3
Total magnetic moment pr. formula unit [μ_B]	4.05 ± 0.05
Magnetic moment pr. Co atom [μ_B]	0.52 ± 0.08
Magnetic moment pr. Mn atom [μ_B]	3.01 ± 0.16

Table 1.1: *Bulk properties of Co_2MnGa. Taken from [5]*

Bulk resistivities of Heusler alloys are found in the range of 20 − 120 $\mu\Omega$cm [73] at 300 K, which seem high compared with e.g. Cu (0.17 $\mu\Omega$cm) and Fe (9.7 $\mu\Omega$cm).

Only little information on Co_2MnGa thin films have been published. Recently Pechan *et al.* [74] have reported measurements of strain-induced magnetic anisotropy in epitaxial Co_2MnGa (001) films by epitaxial growth on GaAs/InP to introduce an in-plane compression/tension strain.

Chapter 2

Electronic structure: Numerical calculations

From theoretical predictions done by Ayuela *et al.* [6] and Fujii *et al.* [7], we knew at the beginning of this project that Co_2MnGa is not a half metal. During the growth optimization process of Co_2MnGa, we discovered the broad variation in stoichiometry in which epitaxial films could be grown. This gave us the hope in order to maximize the spin polarization by changing stoichiometry.

Several theoretical groups have studied the electrical and magnetic properties of Heusler alloys [6, 7, 75, 76, 77]. All of them are in good agreement with bulk measurements. Picozzi *et al.* report [75, 76] calculations of dislocation effects on Co_2MnGa and Co_2MnSi were made to some extent. To my knowledge no one has reported what effect site dislocations have on the bulk properties such as spin polarization and local magnetic moments of the full Heusler alloy Co_2MnGa. We wanted to explore this by ab-initio calculations. We have used a program developed by professor Hans L. Skriver (Department of Physics, DTU) to calculate stoichiometry effects, strain effects, and site dislocation effects.

2.1 The method

We use Density Functional Theory (DFT) within the Local Spin-Density Approximation (LSDA) to investigate the itinerant magnetism of the full Heusler alloy Co_2MnGa. In the calculations the Kohn-Sham equations are solved by the Exact Muffin-Tin Orbitals (EMTO) method in the spherical cell approximation using a Green Function technique. The random substitutional alloys are treated within the Coherent Potential Approximation (CPA) which allowed us to map out the magnitude of the magnetic moments of the individual atomic species and the spin polarization for a wide range of compositions.

2.1.1 Density Functional Theory (DFT)

We will here shortly introduce the concept of DFT theory [78, 79]. However, we will not get into the details of the program.

In 1964 P. Hohenberg and W. Kohn initiated what today is broadly used to compute material properties, in not only bulk materials but also for example in proteins and carbon nanotubes by stating the first Hohenberg-Kohn theorem [78]:

The external potential $v(\vec{r})$ is determined, within a trivial additive constant, by the electron density $n(\vec{r})$.

From this follows the possibility of replacing the number of electrons N and the external potential $v_{ext}(\vec{r})$ with the electron density $n(\vec{r})$. By considering the energy as a functional of the electron density the equation for the energy is

$$\begin{aligned} E[n] &\equiv \langle \Psi[n] | \hat{T} + \hat{U} + \hat{V} | \Psi[n] \rangle \\ &= \langle \Psi[n] | \hat{T} + \hat{U} | \Psi[n] \rangle + \int v_{ext}(\vec{r}) n(\vec{r}) d\vec{r} \\ &= F[n] + E_{ext}[n], \end{aligned} \tag{2.1}$$

where $\Psi[n]$ is the wave function, $\hat{T}$ is the kinetic energy operator, $\hat{U}$ is the electron-electron interaction operator, $\hat{V}$ is the external potential operator, and F[n] is an universal energy functional, which means that its form does not depend on the particular system under consideration. $E_{ext}[n]$ is the energy contribution from the interaction with the nucleus (in the case of a solid with no external field). The second Hohenberg-Kohn theorem is a variational principle:

For any given non-interactive trial density, $n(\vec{r})$, that integrates to the correct number of electrons, N, the true ground state energy E_0, satisfies the relation:

$$E_0 = min_n(E[n]) \tag{2.2}$$

The two theorems would result in exact solutions if only the form of $F[n]$ were known exactly.

2.1.2 Kohn Sham equations

In 1965 W. Kohn and L. Sham came up with an idea on how to get around the problem [79]. They treat $F[n]$ as the energy functional of a system with the same density as the real system but in which the electron-electron interaction is missing (this is also called an non-interacting electron system). To correct for the missing electron-electron interaction they implement an exchange-correlation part in which the differences between the real system and the non-interacting system are described

$$F[n] = T[n] + E_{Hartree}[n] + E_{xc}[n], \tag{2.3}$$

where T is the kinetic energy of electrons in a non-interacting electron system, $E_{Hartree}$ is the classical Coulomb interaction between electrons, and E_{xc} is the exchange-correlation energy. The exchange-correlation energy includes everything missing in the other energy contribution such as electron exchange, electron correlation, and kinetic energy.

Using Hohenberg-Kohns second theorem provides us with a self-consistent set of equations, the so called Kohn Sham equations

$$\Big(\frac{-\hbar}{2m}\nabla^2 + v_{eff}(\vec{r})\Big)\Psi_i(\vec{r}) = \varepsilon_i\Psi_i(\vec{r}), \tag{2.4}$$

$$v_{eff}(\vec{r}) = \int \frac{n(\vec{r'})}{|(\vec{r}) - (\vec{r'})|}d\vec{r'} + v_{ext}(\vec{r}) + v_{xc}(\vec{r}), \tag{2.5}$$

$$n(\vec{r}) = \sum_{i=1}^{N} |\Psi_i|^2, \tag{2.6}$$

$$E_0 = T[n] + E_{Hartree}[n] + E_{xc}[n] + E_{Ext}[n], \tag{2.7}$$

where $v_{xc} \equiv \delta E_{xc}/\delta n$. The effective potential is given by the functional derivative of $F[n]$ given in Equation (2.3), where the kinetic potential has been subtracted because it already is in the one-electron Equation (2.4). The equations are solved by the following steps:

1. Guess an electron density,
2. Calculate the effective potential, Equation (2.5) (for now we assume known exchange-correlation potential $v_{xc}(\vec{r})$),
3. Solve the one-electron equation, Equation (2.4),
4. Calculate a new electron density by using Equation (2.6) on the eigenfunctions from previous step.

Step 2 to 4 is repeated until wanted convergence criteria are established. The ground state energy is found by equation 2.7.

2.1.3 Local Spin Density Approximation (LSDA)

All terms in Equation (2.7) are exactly known except from the exchange correlation energy functional E_{xc}. This term needs to be approximated. The approximation used in this simulation is the Local Spin Density Approximation (LSDA). LSDA is based on the spin dependent exchange and correlation terms for a homogenous electron gas. To use this approximation the Kohn-Sham equations are solved for each of the two spin directions. From LSDA-solution estimates on other solutions solved by other approximations such as Gradient Generalized Approximation (GGA) and Local Airy Gas approximation (LAG) and can be made.

2.2 Co_2MnGa calculations

Our first test was to calculate on a stoichiometric crystal, and compare to other calculations on Heusler alloys. The calculated crystal parameters are seen in Table 2.1.

Method	LSDA	GGA	LAG	Experimental [5]
a[Å]	5.61	5.75 (5.72)	5.68	5.77

Table 2.1: *Calculated estimates of the lattice parameter a, compared with experimental data. The value in brackets are theoretical predictions reported by Ayuela et al.*

The numbers are in good agreement with experimental data [5] and with other calculations on the bulk Co_2MnGa crystal [6, 80]. The energy dependence calculated by GGA-methods seems to be closest to the experimental value. This knowledge will be used later where the GGA-estimated formation energies will be used to give an idea on which defects are most likely to happen.

The calculated spin dependent Density Of States (DOS) are shown in Figure 2.1 and corresponds nicely to other calculations [77].

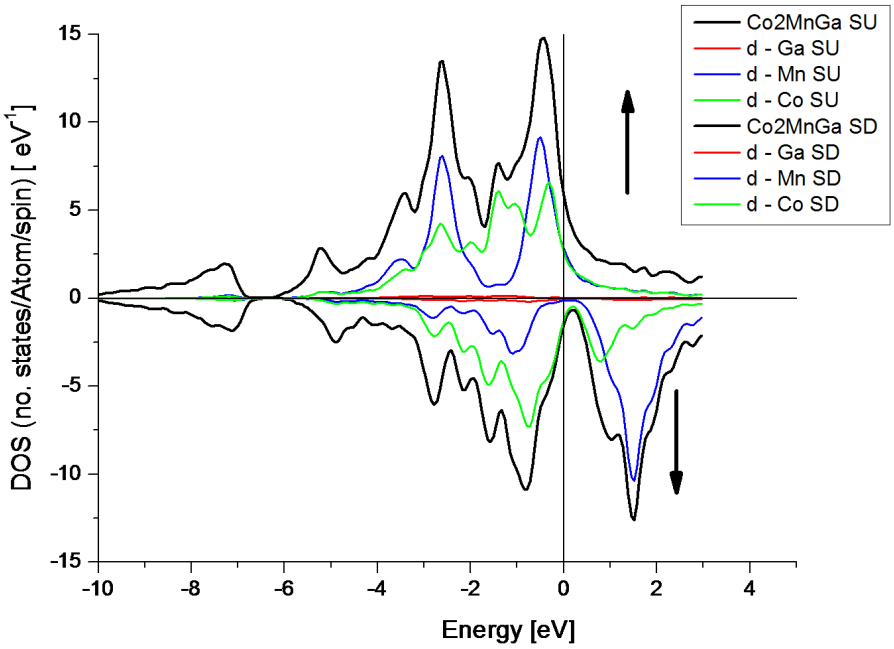

Figure 2.1: *Spin dependent DOS showing the contributions from d-bands in $Co_2Mn_1Ga_1$ to the total DOS.*

The main contributions to the DOS are from Mn and Co d-electrons. Contributions from s- and p-electrons are negligible. The spin calculated bulk spin polarization is given in Equation (2.8)

$$P = \frac{n_\uparrow(E_F) - n_\downarrow(E_F)}{n_\uparrow(E_F) + n_\downarrow(E_F)} = 63\ \%. \tag{2.8}$$

From the calculations local magnetic moments are given on each sub-lattice in the crystal. The local magnetic moments on the two Co-sites are the same. Table 2.2 shows the local and total magnetic moments per formula unit.

Atom	Ga	Mn	Co	Total (4.05μ_B [5])
Magnetic moment [μ_B]	-0.09	2.91	0.65	4.12
Magnetic moment [μ_B] [6]	-0.07	2.72	0.76	4.08
Magnetic moment [μ_B] [80]	-0.13	2.78	0.73	4.13

Table 2.2: *Calculated local and total magnetic moment per formula unit, Compared with calculations reported by Ayuela* et al. *[6], and Kurtulus* et al. *[80], and experimental data reported by Webster [5].*

From the above calculations it is seen that approximately 2/3 of the magnetic moment comes from the Mn-sites, and 1/3 comes from Co-sites.

2.3 Stoichiometry variation

Next step was to vary the stoichiometry. We decided to investigate this by making changes in two atom-sites at the same time. For example as shown in the following we defined an additional Ga-site on the same lattice site as Co, and likewise an additional Co-site on the same lattice-site as Ga. The total number of atoms on each site is kept at one. The formalism used to describe the change in stoichiometry has been chosen as below

$$Co_{2-x}Mn_1Ga_{1+x}. \tag{2.9}$$

The color denotes the sublattice (atom site), while the index numbers denotes stoichiometry, in this case Co and Ga. If for example $x = -0.2$ the formalism: $Co_{2--0.2}Mn_1Ga_{1+-0.2}$ tells us that the stoichiometry is $Co_{2.2}Mn_1Ga_{0.8}$ and that the extra Co is situated on Ga sites.
Changing the stoichiometry has mainly three effects:

1. Change in lattice parameter a
2. Change in spin polarization P
3. Change in the magnitude of the local magnetic moments

The effects are described in the following in the case of changes in Co/Ga and Co/Mn stoichiometry. In comparison changes due to stoichiometry changes of Mn/Ga are smaller and can be found in Appendix A.

2.3.1 Variation of Co/Ga-Stoichiometry

Table 2.3 shows the relative change of a when varying the composition of Co and Ga. Both excess Ga and Co results in an increase of the lattice parameter a, as expected.

Composition	GGA change in lattice parameter a
$Co_{2.1}Mn_1Ga_{0.9}$	+0.73 %
$Co_{1.9}Mn_1Ga_{1.1}$	+0.61 %

Table 2.3: *GGA estimates $a = 5.75$ Å for $Co_2Mn_1Ga_1$.*

Figure 2.2 shows the change in spin polarization and total magnetic moment and Figure 2.3 illustrates the change in local magnetic moment.

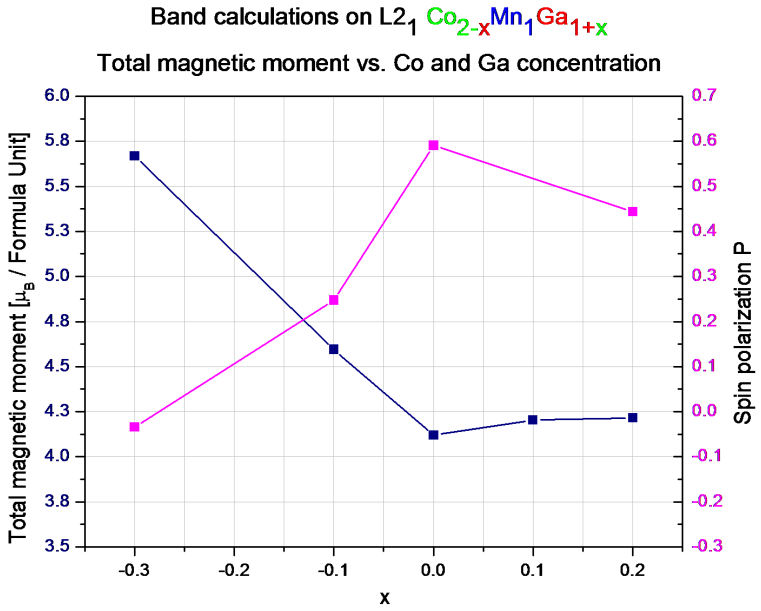

Figure 2.2: *Calculation of spin polarization and total magnetic moment vs. Co-Ga ratio*

A drastic change in both spin polarization and magnetic moment is seen. The spin polarization even changes sign. The reason is that the DOS of the d-electrons from Co on Ga-sites has a peak very close the the Fermi energy. This may be seen in Figure 2.4

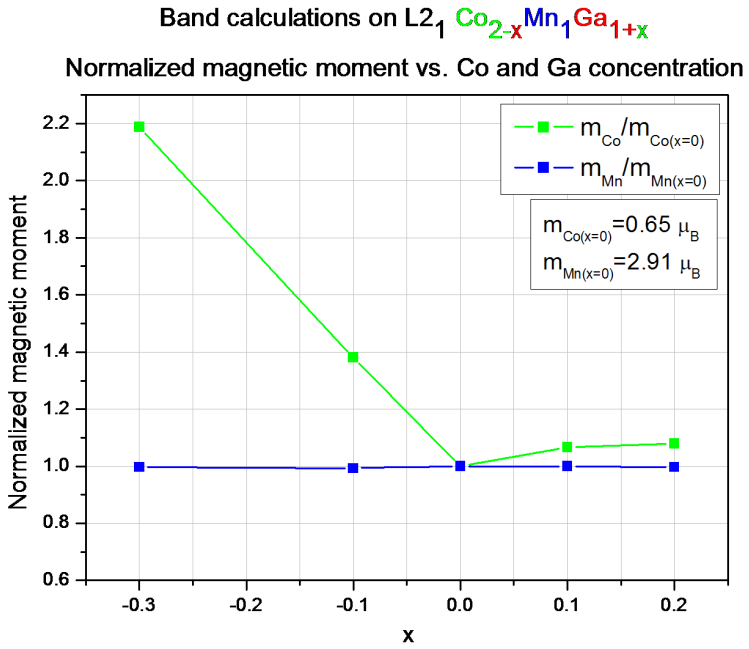

Figure 2.3: *Co and Mn magnetic moments vs. Co-Ga ratio.*

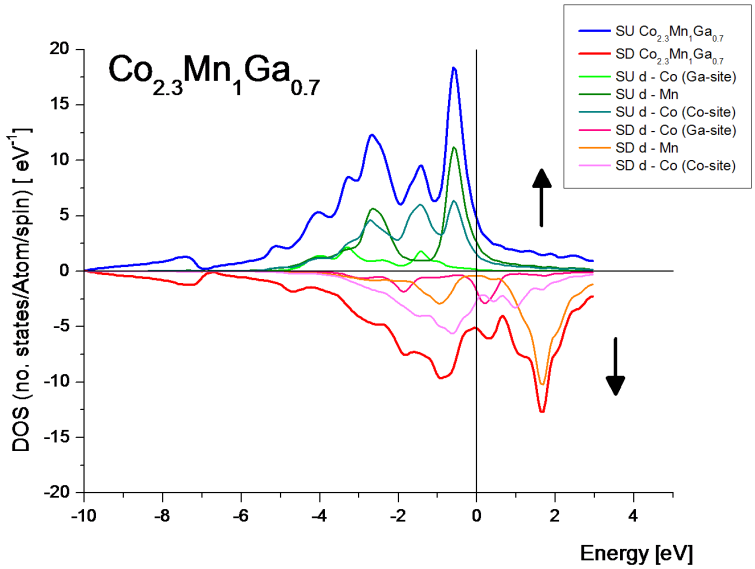

Figure 2.4: *Spin dependent DOS showing the contributions from d-electrons in* $Co_{2.3}Mn_1Ga_{0.7}$.

Table 2.4 illustrates the local magnetic moments on each atom-site in the crystal when calculated in the case of $Co_{2.3}Mn_1Ga_{0.7}$.

Sublattice	Ga		Mn	Co		Total
Atom	Ga (0.7)	Co (0.3)	Mn (1)	Co (2)	Ga (0)	
Magnetic moment [μ_B]	-0.11	1.95	2.90	1.13	-0.05	5.67

Table 2.4: *Local and total magnetic moment for* $Co_{2.3}Mn_1Ga_{0.7}$

The local moment from Co on Co-sites has increased with a factor of 1.73 which together with the moment from Co on Ga-sites adds up to a factor of 2.2. This can as well be in Figure 2.3. Only little effect is seen on the Mn-moment. In case of excess Ga only a small magnetic change is observed.

2.3.2 Variation of Co/Mn-stoichiometry

The variation of Co/Mn-stoichiometry has no effect on the lattice parameter, but as it was the case with Co/Ga, changes are clearly seen on the spin polarization and the magnetic moments. Figure 2.5 shows the spin polarization and the total magnetic moment as a function of Mn-concentration.

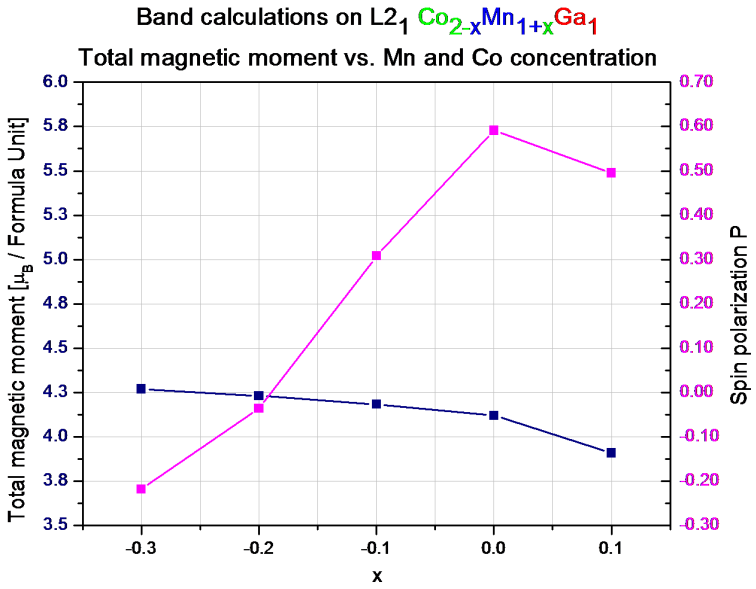

Figure 2.5: *Calculation of spin polarization and total magnetic moment vs. Co-Mn composition.*

Again it is found that excess Co is destructive for the spin polarization and this time the DOS for the d-electrons from Co on Mn-sites is situated exactly at the Fermi energy This is seen in Figure 2.7 for the case of $Co_{2.3}Mn_{0.7}Ga_1$.

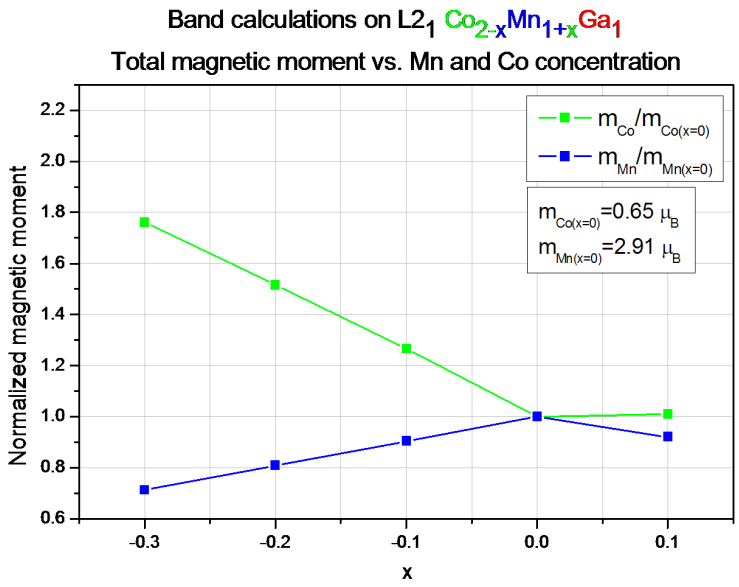

Figure 2.6: *Co and Mn magnetic moments vs. Co-Mn composistion.*

The local magnetic moments change as seen in Figure 2.6 and in the case of $Co_{2.3}Mn_{0.7}Ga_1$ in Table 2.5. Co-moments on Co-sites change with a factor of 1.3, which together with the moment from Co on Mn-sites add up to a factor of 1.76 as also seen in Figure 2.6.

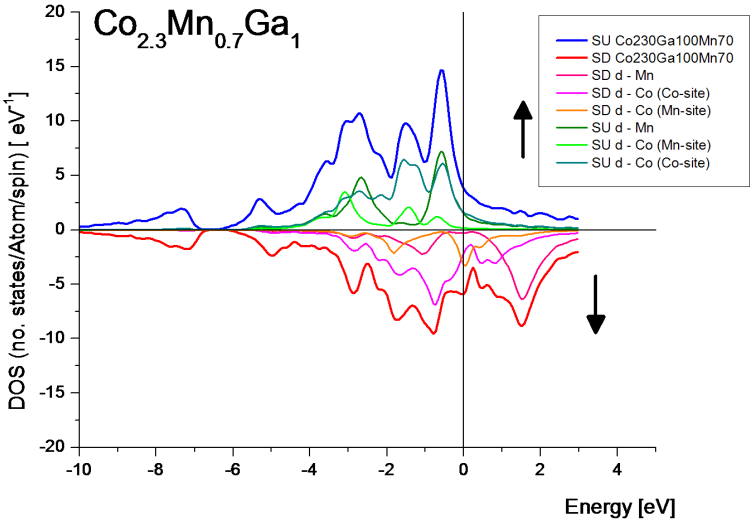

Figure 2.7: *Spin dependent DOS showing the contributions from d-electrons in $Co_{2.3}Mn_{0.7}Ga_1$.*

In case of excess Mn the local moment per Mn decreases. The reason for this is that Mn on Co sites orders itself antiferromagnetically, as seen in Table 2.6.

Sublattice	Ga	Mn		Co		Total
Atom	Ga (1)	Mn (0.7)	Co (0.3)	Co (2)	Mn (0)	
Magnetic moment [μ_B]	-0.09	2.96	1.83	0.87	-2.37	4.27

Table 2.5: *Local and total magnetic moments calculated for* $Co_{2.3}Mn_{0.7}Ga_1$

Sublattice	Ga	Mn		Co		Total
Atom	Ga (1)	Mn (1)	Co (0)	Co (1.9)	Mn (0.1)	
Magnetic moment [μ_B]	-0.08	2.91	2.43	0.69	-2.32	3.91

Table 2.6: *Local and total magnetic moments calculated for* $Co_{1.9}Mn_{1.1}Ga_1$

2.4 Atomic-"Swap" calculations

Next step was to calculate the influence of atom-swapping. Stoichiometry is kept constantly on $Co_2Mn_1Ga_1$ while the sites of the involved atoms are "swapped". We investigate for changes in the same effect as described in section 2.3. Again the effects are only weakly dependent on the Mn-Ga swap. The results can be seen in Appendix A. The formalism used in the following to describe the swapping has been chosen as follows

$$Co_{2-y}Ga_yMn_1Ga_{1-y}Co_y. \tag{2.10}$$

The color denotes the sublattice (atom-site), while the y denotes the swap(y>0), in this case between Co and Ga. If for example $y = 0.2$ the formalism: $Co_{1.8}Ga_{0.2}Mn_1Ga_{0.8}Co_{0.2}$ tells us that 10 % of the Co is on Ga-sites and that 20 % of the Ga is on Co-sites.

2.4.1 Variation of Co-Ga swaps

The influence of Co-Ga swaps on spin polarization and total magnetic moment is depicted in Figure 2.8, while influence on the local magnetic moment of Mn and Co is seen in Figure 2.9.

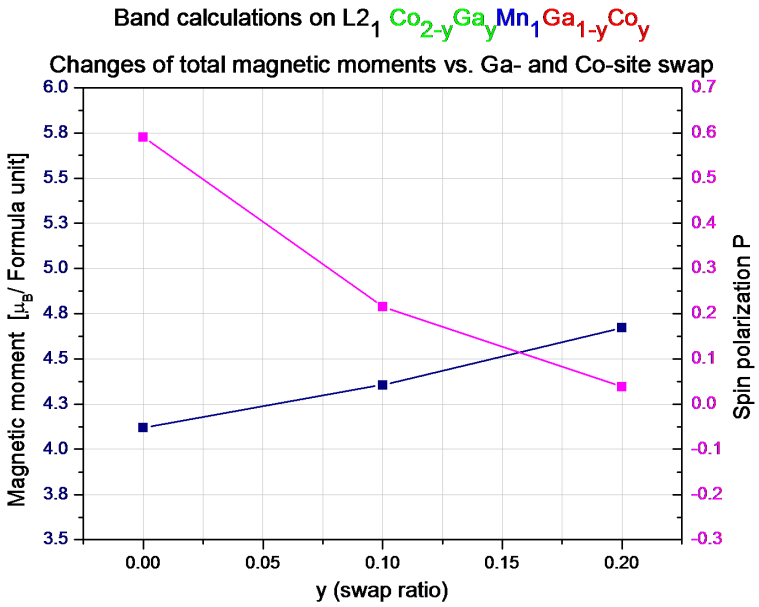

Figure 2.8: *Calculation of spin polarization and total magnetic moment vs. Co-Ga swaps.*

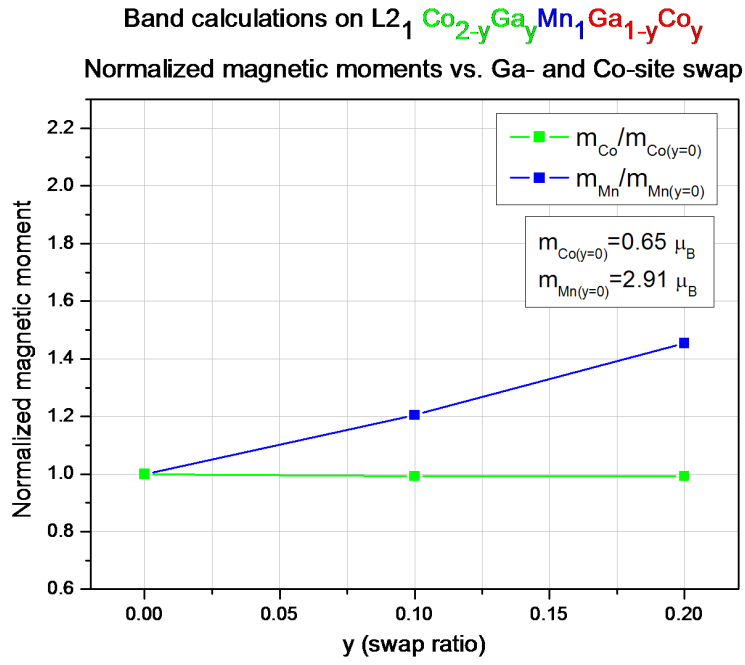

Figure 2.9: *Co and Mn magnetic moments vs. Co-Ga swaps.*

Again Co on Ga-sites destroys the spin polarization as in the case of the off-stoichiometry calculations. The change of Co-moment is in good agreement with the results from the

off-stoichiometric calculations. The total magnetic moment changes with approximately a factor of 1.1 in the case where 20 % of the Mn has swapped site with 10 % of the Co-atoms.

2.4.2 Variation of Co-Mn swaps

The influence of Co-Mn swaps on spin polarization and total magnetic moment is seen in Figure 2.10, while influence on the local magnetic moment of Mn and Co is illustrated in Figure 2.11.

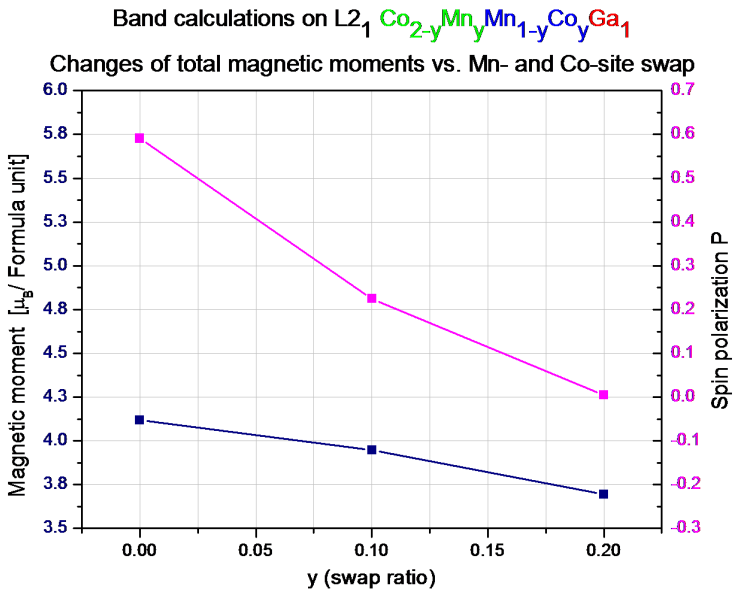

Figure 2.10: *Calculation of spin polarization and total magnetic moment vs. Co-Mn swaps.*

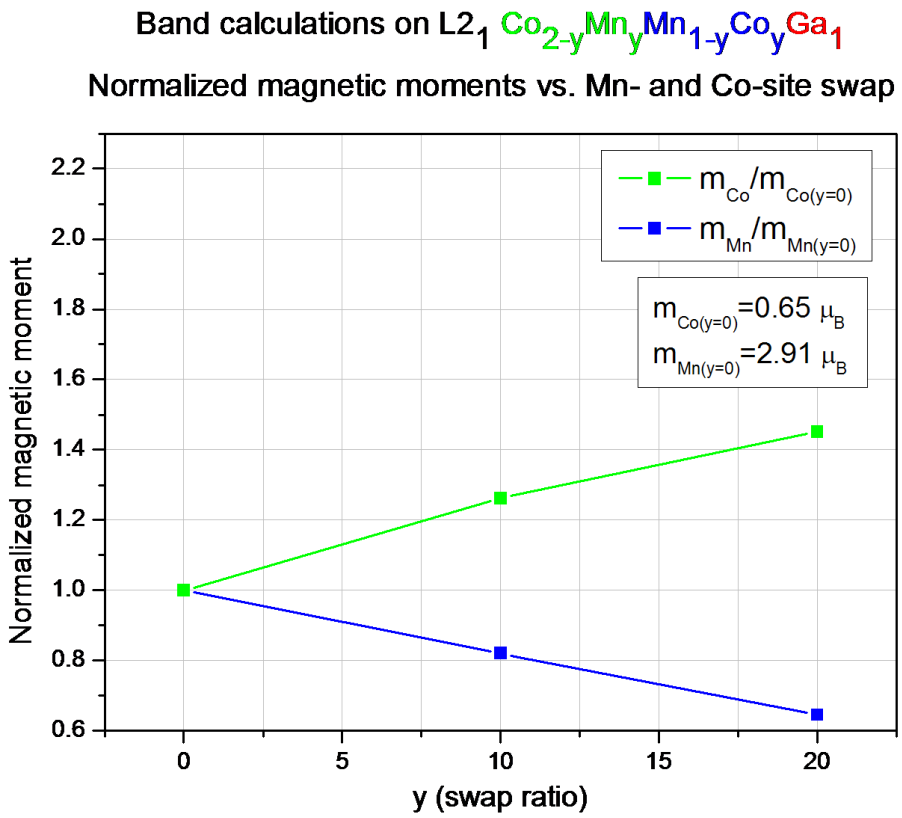

Figure 2.11: *Co and Mn magnetic moments vs. Co-Ga swaps.*

The polarization is destroyed again. This time the total magnetic moment decreases with increasing swapping rate. The reason is the antiferromagnetic ordering of the Mn. As seen by the decrease of the relative local magnetic moment in Figure 2.11.

2.5 Strain calculations

Finally, we wanted to investigate the influence of in-plane strain. When growing on GaAs a mismatch of approximately 2 % is present at least until the thin film is relaxed. The strain was introduced in the calculations by defining a new tetragonal crystal structure, which in the cubic case($c/a = 1$, where c and a are the length of the sides in the unit cell) is identical to the L21 structure. Figure 2.12 shows that even a 5 % change in the ratio between the sides of the crystal unit cell only changes the spin polarization with a small fraction. However if we are able to compress all sides of the unit cell the spin polarization increases up to approximately 85 % for a decrease in the lattice parameter of 5 %.

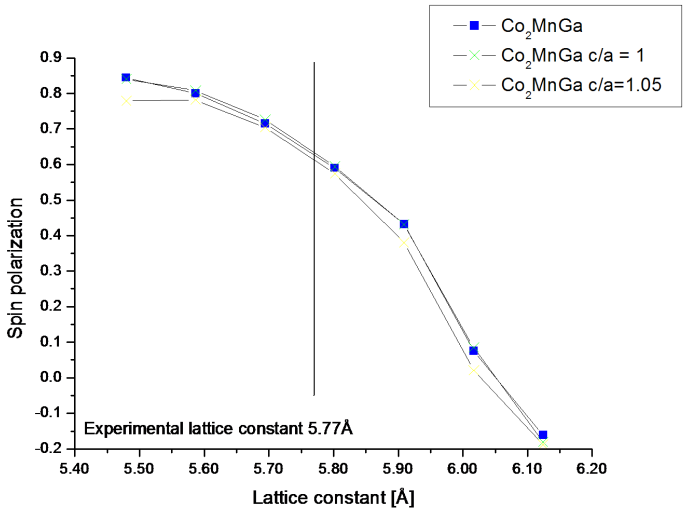

Figure 2.12: *Calculations of the crystal shape- and size-dependence on the spin polarization. To confirm the strain calculations, calculations in the traditional L21 (c/a=1) crystal structure have been plotted (in squares), to compare with calculations on the tetragonal structure with c/a=1.*

Calculations on the traditional cubic L21 crystal structure have been plotted (in squares) to compare with the calculations on the tetragonal structure with $c/a = 1$. The results are in good agreement, implying that the strain calculations are valid.

2.6 Defect formation energies

To estimate which defect process is most likely to happen we have gathered the formation energy differences per defect in Table 2.7.

Defect	ΔeV/Defect
	GGA
Co on Ga-sites	1.40
Co on Mn-sites	0.84
Mn on Co-sites	0.20
Mn on Ga-sites	0.76
Ga on Co-sites	0.84
Ga on Mn-sites	0.08
Co-Mn swapping	0.92
Co-Ga swapping	1.92
Mn-Ga swapping	0.76

Table 2.7: *GGA estimates on the difference in formation energy per defect.*

Again we use the ground state estimates. A good control of the calculations is to compare the swapping formation energy with the sum of the two corresponding stoichiometry defects. The results are in good agreement. We find that Mn on Co-sites and Ga on Mn-sites are most likely to happen among the stoichiometric defects. Among the swapping defects we find Mn-Ga to be most likely. The formation energies correspond nicely to calculation done by Picozzi *et al.* [76] on Co_2MnSi and Co_2MnGe. The results are shown in Table 2.8.

	Co_2MnSi		Co_2MnGe	
	ΔE	M_{tot}	ΔE	M_{tot}
Co antisite	0.80	38.01	0.84	38.37
Mn antisite	0.33	38.00	0.33	38.00
Co-Mn swap	1.13	36.00	1.17	36.00
Mn-Si swap	1.38	40.00		

Table 2.8: *Formation energy (in eV) and total magnetic moments (in Bohr magnetons) for the different defects in Co_2MnGe and Co_2MnSi hosts. Anti-sites refers to Co and Mn-sites only. Adapted from [76].*

To estimate the equilibrium concentration of defects at temperature T, a Boltzmann-like distribution can be used [75] for low defect concentrations

$$D_{def} = N_{sites} \exp(-\frac{\Delta E}{k_B T}). \tag{2.11}$$

At growth temperatures around $T \approx 600\ K$ the antisite concentration is estimated to 2 % for Mn on Co-sites, and to 21 % for Ga on Mn-sites which is outside the limits of the model.

2.7 Discussion of the calculations

Both the investigation of stoichiometry-variation and swapping-defects showed that the alloy with the highest spin polarization is the stoichiometric alloy $Co_2Mn_1Ga_1$. We did find some trends to look for experimentally in the total magnetic moment for each of the defects but the changes are reasonably small and diverse in magnitude. This means that it is difficult to extract anything from measurements of the total magnetic moment itself.

From the formation energies it seems like this particular alloy has some very low defect formation energies making the point of eutecticum difficult to determine. To confirm the calculations experimentally we need measurements of:

- Spin polarization vs. stoichiometry
- Measurements of defect-type and density

- Local magnetic moments vs. stoichiometry

These types of measurements are indeed possible and some of them are to some extend, performed in this project. Spin polarization has been measured (see section 3.6 and 4), but due to the time consuming and difficult measurements there are no systematic results on spin polarization vs. stoichiometry.

Several techniques exist to measure the disorder effect. Neutron Diffraction (ND), NMR-techniques, and Extended X-ray-Absorption Fine-Structure (EXAFS) measurements are some of them. Studies on Co_2MnSi [70, 69] grown at $T = 700 - 1000$ K show no Mn-Si disorder but extensive Co-Mn disorder as much as 14 % of Mn sites are occupied by Co atoms and 5-7 % of Co sites are occupied by Mn atoms. Similar results were found by the same group on high temperature growth $T = 700 - 1100$ K of Co_2MnGe where 12.7 % of the Mn sublattice were occupied by Co. Van Roy *et al.* [81] report very low disorder less than 1 % for each disorder defect in epitaxial NiMnSb thin films grown at $T = 230$ °C.

In 2004 we did contact the group in Warszawa who performed the NMR-measurements in [81]. The time of measurements is very long (and thereby also costly). The crystal quality was at that time poor compared to other Heuslers measured by that group. This made us reconsider the measurement. We have now indeed learned how to grow better films in both stoichiometry and structure as described in chapter 3, but due to economical reasons, we have not pursued this characterization.

2.8 X-ray Magnetic Circular Dichroism (XMCD) measurements

Another technique that, we have pursued, to quantify the local magnetic moments is X-ray magnetic Circular Dichroism (XMCD). The technique, results, and comparisons with other characterization measurements are discussed in detail in Appendix B. In this section, results directly comparable to the previous described theoretical predictions are presented.

2.8.1 XMCD collaboration

Three batches of samples were grown specifically for analyses of the average magnetic moments of the Co and the Mn atoms in the thin films of Co_2mnGa/GaAs(100) by measurements of the X-Ray Magnetic Circular Dichroism (XMCD). Growth parameters for the involved samples are presented in Tables B.1 and B.2. The work has been made in a collaboration involving DTU, the Univ. of York. UK, the Daresbury Synchrotron Radiation Source (SRS), Warrington, UK, and Toshiba Research Europe, Ltd., Cambridge Research Lab., Cambridge, UK. The XMCD measurements were carried out in Dec. 2004 and in April and Oct. 2005 by a group at the Spintronics Laboratory, Department of Electronics, University of York: J.S. Claydon, Y.B. Xu and S. Hassan, in collaboration with a group at the Daresbury SRS: N.J. Farley, N.D. Telling and G. van der Laan.

2.8.2 Method

The samples were measured at room temperature. The XMCD technique is element specific as it is based on X-ray absorption spectroscopy of electron core states of the atoms (the L2,3 absorption edges are used). The samples are placed with the sample plane at an angle of 45 °(see Figure 2.13) or 90 ° to the incident X-ray synchrotron beam which is aligned with an applied magnetic field of approximately 0.8 T.

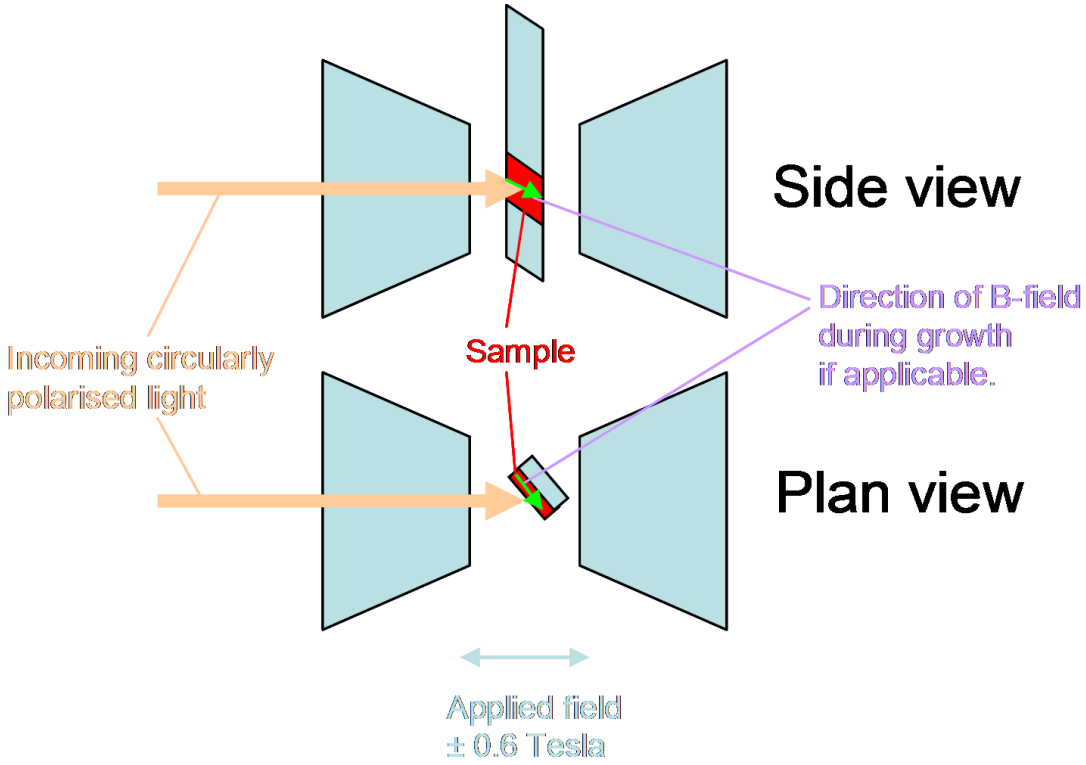

Figure 2.13: *Schematically representation of the XMCD setup. In the sketched configuration the sample is placed with the sample plane at an angle of 45 degrees to the incident X-ray synchrotron beam which is aligned with an applied magnetic field of approx. 0.8 Tesla.*

During the measurement the field is reversed and the difference between the absorption lines for the two field directions may be used to calculate the average local moments (both orbital and spin parts).

The method is only probing the magnetic moments in the sample down to about 5 nm. Therefore rather thin film samples were used (from 2 to 20 nm nominal thickness).

Three batches of Co_2MnGa/GaAs samples were grown under varying conditions (19 samples in total). First two samples were grown with a nominal thickness of 20 nm (VG05-077). This pair of samples were grown at $T(substrate)$ = 300 ° and at a total of rate of about 2.4 nm/min. These samples were not capped. The XMCD analyses showed signs of oxidation of the Mn. The next two batches were capped with Al after growth:

VG05-041 with Fe + Al and VG05-040 with 1.0 nm of Al (in all 8 samples with different CoMnGa thicknesses) and when this Al cap thickness was found to be insufficient (i.e. some of the Mn was still found to be oxidized) the batches VG05-088, VG05-089, and VG05-090 were capped with 1.5-1.7 nm of Al (in all 9 samples with different CoMnGa thicknesses).

Bulk Mn is anti-ferromagnetic. Bulk Co is ferromagnetic with $m_l = 0.153\ \mu_B$ and $m_s = 1.55\ \mu_B$, Chen *et al.* [82]. The distribution of magnetic moments within the Co_2MnGa structure is at low temperature expected to be: Co: 0.65 μ_B, Mn: 2.91 μ_B, and Ga: -0.09 μ_B.

From temperature dependent measurements on bulk Co_2MnGa, Webster *et al.* [5], we expect the local magnetic moments values to decrease with a factor of approximately 10 % at 300 K. i.e. magnetic moment is expected to move from Co to Mn.

The spin and orbital moments have been calculated using the XMCD sum rules as described in Chen et. al. [82], see the Table below. The moments are proportional to the number of 3d holes per atom which are estimated to be: $n_h = 2.2$ for Co and $n_h = 4.5$ for Mn, Schmalhorst *et al.* [83].

2.8.3 Results

Examples of raw data are shown in Figure B.2 and B.3 in Appendix B. Figure 2.14 shows a overview of the measured m_{tot} values from samples VG05-088, VG05-089, and VG05-090.

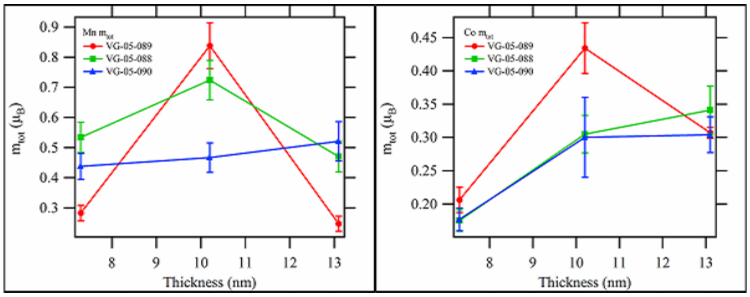

Figure 2.14: *XMCD data for Mn at 300 K (courtesy J. Claydon et al). Samples VG05-088+089+090. All thicknesses are nominal.*

Tables B.1 and B.2 in Appendix B summarizes the sample parameters and estimates of the stoichiometry.

2.8.4 XMCD Discussion and conclusions

In order to validate the calculations, a systematic study of the local spin and orbital moments on samples with different thickness and stoichiometry was done. The obtained results did not exhibit the expected systematic change.

All analyses of the XMCD data on the Co_2MnGa thin films show magnetic moments on the Mn atoms which are much smaller than expected. On average the Mn moments are 4-5 times smaller than expected in a well ordered Co_2MnGa crystal at low temperature:

At 300 K the measured average value of m_{tot} for Mn falls between 0.25 μ_B and 0.85 μ_B, the theoretical value is 2.91 μ_B and measured bulk value is 3.01 μ_B, Webster *et al.* [5].

The measured values of the Co moments at 300 K lies between 0.1 μ_B and 0.45 μ_B and thereby on average fall abelow the expected theoretical value of 0.65 μ_b, and the experimental bulk value 0.52 μ_B with a factor of 2. All in all the XMCD data indicates that at 300 K the grown Co_2MnGa thin films do not exhibit the expected magnetic properties of a Heusler alloy: the hypothesis that a large magnetic moment is transferred from Co to Mn is not supported by the XMCD analyses of our samples. At 300 K the average Co moment is indeed reduced from its bulk value but the expected corresponding increase of the average Mn moment is not found. No significant difference was observed between VG05-088, VG05-89, and VG05-090, even though the stoichiometries are quite different: VG05-088: $Co_{1.86}Mn_{0.99}Ga_1$, VG05-089: $Co_{1.95}Mn_{0.98}Ga_1$, and VG05-090: $Co_{1.97}Mn_{0.96}Ga_1$.

The reasons for these discrepancies are at present not fully understood. The behavior cannot be explained by the calculations alone. Even though we theoretically found that Mn-defects on Co-sites anti-aligns itself with the applied field, one needs a very high Mn on Co-site defect-concentration of approximate 38 % to explain the missing Mn moment. One explanation could be that the Heusler alloy is not fully saturated. But as in our case where a magnetic field incident with 45 ° to the sample plane, is applied with a magnitude of 0.8 T, the thin film should indeed be saturated.

As mentioned earlier the XMCD-technique is expected to probe approx. 5 nm, which corresponds to the thinnest part of VG05-088, VG05-089, and VG05-090 (t_{nom} = 7.3 nm), which in addition to the 1.5nm Al-cap is more than the technique can probe. We therefore expect the measured thickness dependency to be a result of the coupling with an eventually stronger magnetization beneath the probing depth. Structurally and magnetically characterizations have been performed on VG05-088 and VG05-089. A comparison and a discussion of the results are given in section 3.3.4.

The conclusion of the comparison with magnetization measurements, Auger spectroscopy, and XRD measurements, is that we expect Mn to diffuse towards the surface into the 1.5 nm Al cap layer, or/and As-bonding from the substrates to destroy the local magnetic moments on Mn. More measurements are needed to determine the dynamics of the local magnetic moments.

Chapter 3

Growth and characterization of ferromagnetic thin films

This chapter describes the techniques used for synthesis of Co_2MnGa thin films and it presents the characterization techniques and measurements. The optimized growth recipe based on the measurements is described in Appendix C.

The main purpose of growth was to develop a good spin injector on a semiconductor. A direct way to measure this quality is by optical methods and is described in chapter 4. As this technique is very time consuming, we have had to establish additional characterization techniques with faster feedback to the growth procedure. First of all we needed to be sure that we actually grew the correct material. This was mainly done with feedback from stoichiometry measurements, crystal structure measurements, and magnetic properties. The methods are described in section 3.2. To get a good understanding of the parameters involved in the growth, we made a study with focus on the following five parameters:

1. Growth temperature
2. Annealing procedure
3. Stoichiometry
4. Strain - choice of bufferlayer and substrate
5. Film thickness

The results are given in section 3.3. Furthermore investigations on magnetic and electrical properties were done and can be seen in section 3.4 and 3.5 respectively. Measurements of bulk spin polarization was done to estimate the effective spin-loss during the injection process. The method and the results are described in section 3.6.

3.1 Growth technique

We started out by following the recipe of Dong *et al.*[64]. They describe a Molecular Beam Epitaxy (MBE) technique where epitaxial growth of the full Heusler alloy Ni_2MnGa is done pseudomorphically by use of a relaxed NiGa interlayer on GaAs(001). We adapted the technique and used CoGa as an interlayer. The interlayer has two purposes:

1. to prevent interdiffusion between the Heusler alloy and the semiconductor,
2. to reduce the effect of the lattice mismatch between the semiconductor and the Heusler alloy

Not only GaAs (001) has been investigated. Several different substrates-materials and preparation of substrates have been tried. Table 3.1 is meant as a guide to the reader on which substrates have been used in the characterization process. Furthermore thin films have been grown on As-capped, MBE-grown p-i-n substrates with a Quantum Well (QW) in the intrinsic region designed for spinLEDs. These substrates will be described in section 5.1.

Substrate description	produced by:	MBE-name
Epi-ready GaAs (100)	WT	
Epi-ready n-doped GaAs (100)	WT	
Epi-ready n-doped InAs (100)	WT	
Si (001)	Topsil	
As-capped MBE-grown GaAs on Epi-ready GaAs (100)	NBI	NBI#8
As-capped MBE-grown δ-doped GaAs on Epi-ready GaAs (100)	NBI	NBI#7, NBI#10, NBI#21
As-capped MBE-grown $In_{0.28}Ga_{0.72}As$ on Epi-ready GaAs (100)	NBI	NBI#41

Table 3.1: *WT stands for Wafer Technologies, UK. Topsil is located in DK. NBI stands for Niels Bohr Institute, Copenhagen University, DK.*

3.1.1 Growth chamber

The MBE growth chamber was delivered by VG Special Systems ltd. in 1990, and was originally used for fabrication of high temperature superconductors.

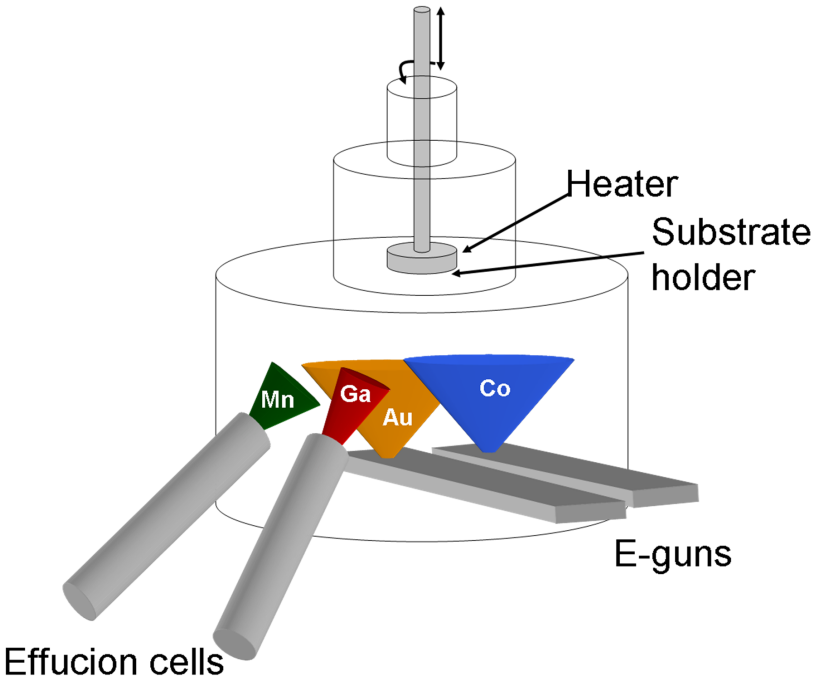

Figure 3.1: *Schematic illustration of the deposition chamber.*

The base pressure is about 10^{-10}mbar. The chamber has four sources in the growth chamber, two Effusion Cells (EC) and two Electron Beam (EB) sources:

Source	Material
EB#1	Co
EB#2	Au or Al
EC#1	Mn
EC#2	Ga

Table 3.2: *List of the sources and materials located in the deposition chamber.*

They are designed for co-evaporation processes. The sample can be investigated during growth by use of Reflected High Energy Electron Diffraction (RHEED) system from Oxford Applied Research Ltd. (type RH-200), and a Quadropole Mass Spectrometer (QMS) from Balzers (type Prisma) which monitors the masses and relative concentrations of atoms and molecules in the chamber. A primitive thermal source has been installed in the loadlock to enable evaporation of other materials than the four located in the sources in the growth chamber.

3.2 Characterization methods

3.2.1 Stoichiometry

Three different techniques have been used for characterizing the stoichiometry of our thin films. Our first approach was Energy Dispersive X-ray Spectroscopy (EDS), which is based on detection of intensity and energy of x-rays generated in the sample by a focused electron beam. The technique is non-destructive, which in thin film characterization and device development is a major benefit. One drawback by this method is the large sampling depth 1-2 μm, compared to the thin film thickness 10-100nm. It was not possible by this or any of the following methods to measure the amount of Ga in Heusler thin films grown on GaAs, due to the existing Ga in the substrate. Our solution to the problem was to assume identical stoichiometry-properties on thin films grown on Si and then compare Co and Mn relations with thin films grown on GaAs to validate the assumption. This was indeed observed (see Appendix D). The measured amount of Co and Mn in both GaAs and Si corresponded nicely. After a year of search for other available chemical mapping techniques we found that Risø National Laboratory offers analysis by Inductively Coupled Plasma Optical Emission Spectroscopy (ICP-OES). The technique is based on dissolving the Heusler thin films in acid. The solution is injected and vaporized at a controlled rate into a low-pressure inductively-driven plasma. The atomic spectral lines emitted from the plasma are resolved and detected and the concentration of atoms is determined to within 10^{-5} mol/g. Further description of the method can be found in Appendix D. Also this technique is limited to thin films grown on substrates with elements other than Co, Mn, or Ga such as Si. In principle it should be possible, but due to difficulties in dissolving only the thin film and not the substrate, we chose Si as substrate, with the same argument as used in the EDS-approach. A comparison between EDS and ICP-OES showed a systematic difference, see Appendix D.4). Table D.4 shows some typical differences between the two types of characterization. From measurements on bulk standards delivered by Goodfellow, we found that measurements done by ICP-OES correspond very nicely to the expected values for bulk samples to within ±2 % . The reasons for the failure of the EDS-method to determine the stoichiometry of Co_2MnGa are at present unknown. Since ICP-OES is a destructive characterization method, we did try to correct the EDS measurements by using the ICP-OES measurements as a reference. This was not possible as reproducibility of EDS-results was too poor. Other techniques have been tried and excluded: Rutherford Backscattering Spectroscopy (RBS) due to the difference between the energy of the backscattered He^+ on Co and Mn being too small, 1.535 MeV and 1.506 MeV respectively, for the setup to resolve. Auger Electron Spectroscopy (AES) was also not efficient due to its limiting sampling depth. The stoichiometry characterization throughout this thesis is based on ICP-OES measurements. To make sure the stoichiometry did not drift during growth ICP-OES samples were regularly grown either during same growth or just after growth of device wafers. As an example ICP-OES determines the stoichiometry of a 0.1 mg thin-film sample (VG-05-062) to be Co(1.96 ±0.02) Mn(1.00 ±0.01) Ga(1.00 ±0.01).

3.2.2 Crystal structure

By observing in-situ RHEED patterns during growth, an initial determination of crystal quality was obtained. For further investigations we used X-ray diffraction techniques. Mainly two different setups have been used:

1. A Philips X-ray Diffractometer PW1050 in the Bragg-Brentano geometry with graphite monochromator, $\theta - 2\theta$ step scanning. XRD patterns were recorded with Cu K α radiation. The setup is installed at Department of Physics, DTU, and has been used for fast characterization.

2. For high resolution measurement, the 3-axis BW2 synchrotron beamline at Hasylab, Hamburg, has been used for both $\theta - 2\theta$-scans and ω-scans also called rocking curves. Figure 3.2 shows a schematic drawing of the diffractometer with the different available sample- and detector-movement options.

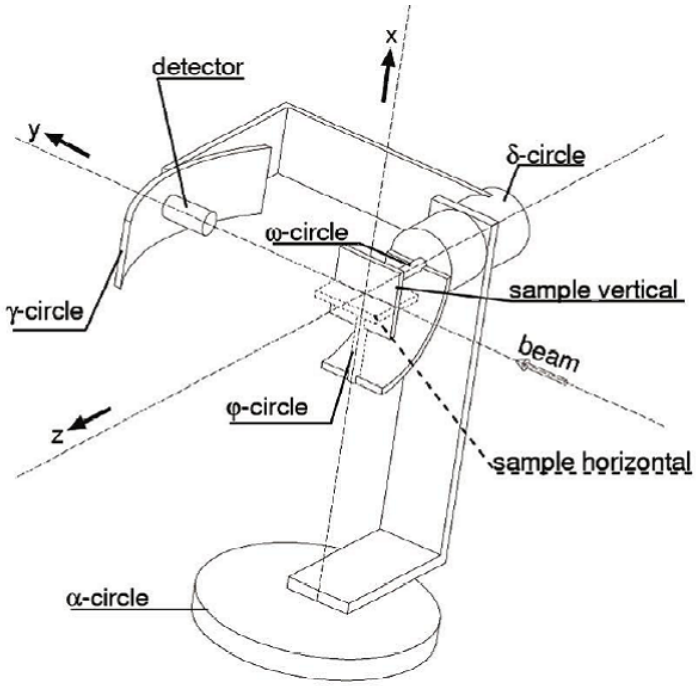

Figure 3.2: *A schematic drawing of the diffractometer. Adapted from [84].*

$\theta - 2\theta$-scans reveals x-ray reflection due to Bragg's law, see Equation 3.1, which basically is the condition for constructive interference of an electromagnetic wave with an angle of incidence θ to a crystal with lattice planes distanced by the parameter d.

$$m\lambda = 2d \sin\theta \tag{3.1}$$

m is an integer and λ is the wavelength of the electromagnetic wave. In k-space equation (3.1) has the following form:

$$m = d\frac{k}{2\pi}. \tag{3.2}$$

Figure 3.3 shows Bragg diffraction schematically.

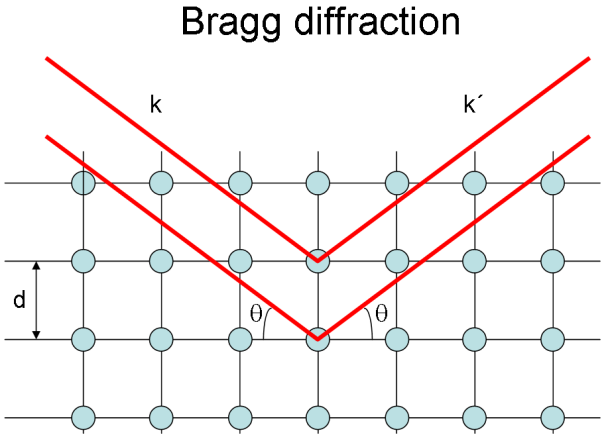

Figure 3.3: *Schematical example on Bragg diffraction.*

Practical $\theta - 2\theta$ scans are performed by keeping the source fixed and rotating the sample-angle ω by θ and the sensor-angle δ by 2θ. The scan gives information on the distance between the crystal planes perpendicular to the normal of the thin film surface, by interpreting the value of θ corresponding to local maxima of reflection.

ω-scans or rocking-curves are performed by keeping δ fixed on a specific Bragg diffraction peak $\delta = 2\theta_B$ and then rotating ω through θ_B. ω-scans reveal information on the homogeneity of the crystal. The width of the rocking curve is a measure of the range of orientation present in the irradiated area of the crystal.

At the BW2-line at Hasylab, Hamburg, it is possible to correct for any misalignment during sample-mounting by changing the sample angles φ and ω see Figure 3.2. The alignment procedure is described by Oliver Bunk in [85]. The setup at Department of Physics, DTU does not have the option to change ω independent from δ, which simply means omega-scans are impossible to do and further more makes sample mounting very crucial since any misalignment will remain during the measurements.

To identify obtained reflections, positions and amplitudes from $\theta - 2\theta$ scans are compared with powder diffraction data in [86].

From the Full Width Half Maxima (FWHM in radians) of the reflections, an estimate on the crystallite size can be given from following relation [87]:

$$FWHM = \frac{\lambda}{D\cos\theta'}, \tag{3.3}$$

where λ is the wavelength and D is the crystallite size. In high intensity x-rays sources such as the BW2 beamline another thickness dependent effect appears namely thickness

oscillations or Kiessig fringes [88, 89]. The phenomenon is caused by the interference of waves reflected from top and bottom interfaces. The relation between the oscillation period Δk measured in k-space [Å^{-1}], and the film thickness t is given by the relation

$$\Delta k = \frac{2\pi}{t}. \tag{3.4}$$

Furthermore information on the interface can be found with high intensity x-rays by a technique based on the interference of the diffraction of the film with the crystal truncation rods [90]. This analysis is yet to be done due to lack of time.

3.2.3 Magnetic properties

Magnetic properties of the grown thin films gives, together with stoichiometry and structural information, a very good feed back to growth parameters. We have obtained information on the magnetic properties by several very efficient techniques: Magneto Optical Kerr Effect (MOKE), Vibrating Sample Magnetometry (VSM), Magnetic Force Microscopy (MFM), and X-ray Magnetic Circular Dichroism (XMCD). Each of them has its own advantages and disadvantages. In the brackets after the method, the location of the setup is mentioned. Only a small part of the characterization is actually made at Department of Physics, Technical University of Denmark. Most of the characterization is made through setups installed at our collaborators. MOKE (Department of Physics Technical University of Denmark, and Toshiba Research Laboratories Cambridge) has generally been used for magnetic anisotropy measurements due to the easiness of aligning the sample in a given direction. VSM (Department of Physics, and Department of Micro and Nanotechnology, Technical University of Denmark) has generally been used for measuring saturation moments. MFM (Niels Bohr Institute, Copenhagen University) has been used to see domain structures at room temperature. XMCD (Daresbury Synchrotron via York University) has been used to measure local moments on the individual atom sites in the crystal lattice.

3.3 Results on growth parameter investigation

In the following a study of the five growth parameters will be presented. When comparing magnetic properties of different films with different stoichiometries with bulk magnetization values it is important to know the exact film thickness. A nominal film thickness t_{nom} is determined after each growth. Information on the relation between the nominal and real film thickness t_{real} have been estimated from ICP-OES mass determinations, assuming bulk densities, and confirmed by thickness oscillations from high intensity X-ray diffraction measurements. Figure 3.4 shows t_{real}/t_{nom} as a function of film thickness.

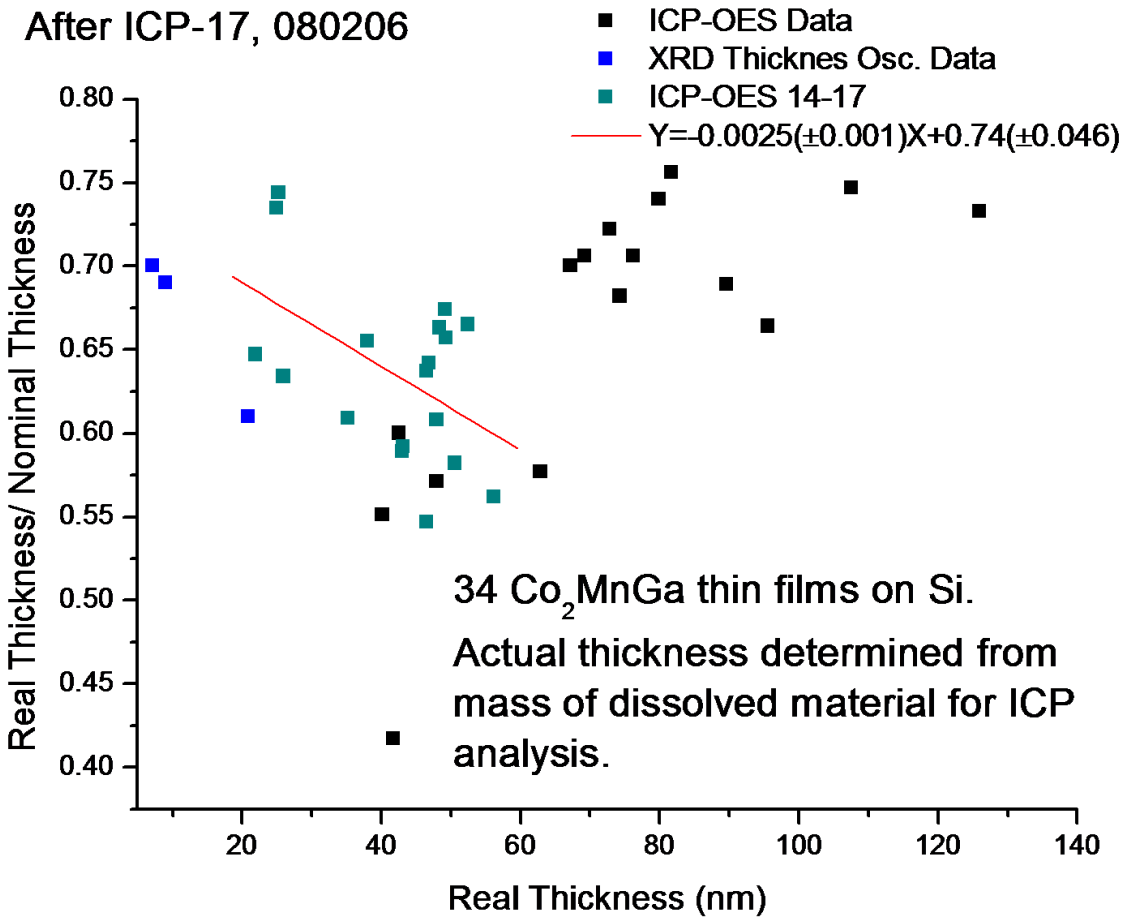

Figure 3.4: *Ratio t_{real}/t_{nom} vs. actual thickness measured by ICP-OES and XRD technique.* $t_{real} = 0.74t_{nom}/(1 + 0.0025t_{nom})$.

The shown data includes films with different growth parameters. This could be the explanation for the large dispersion. By focussing on the 4 latest ICP-analysis, which are done on films with t_{real} =20-60 nm a linear trend is found and confirmed with thickness measurements done by high intensity XRD-measurements. This dependence $t_{real} = 0.74t_{nom}/(1 + 0.0025t_{nom})$ will be used to estimate the real thickness of films, which has not been measured by XRD-techniques.

3.3.1 Growth temperatures

An intuitive model for growth temperature dependence on Heusler thin films can be described by a low temperature region where the thin film has many structural defects, such as dislocations and anti-sites, and a high temperature region where the crystal has only a few defects but due to diffusion the interface between substrate and film is smeared out. With spintronic devices in mind a clean interface is very important due to magnetic scattering events. The optimum growth temperature is in our opinion

Sample name	t_{nom} [nm]	Nominal growth rate [nm/h]	Cap	T_{growth} [^{o}C]	Substrate	Stoichiometry Co:Mn:Ga
VG-CoMnGa-05-052	73	29	no cap	300	GaAs*, Si	2.33:1.02:1
VG-CoMnGa-05-053	75	29	no cap	300	GaAs*, Si	2.56:1.00:1
VG-CoMnGa-05-059	100	29	no cap	300	GaAs, InAs, Si	1.91:0.90:1
VG-CoMnGa-05-060	73	29	no cap	300	GaAs, InAs, Si	2.02:0.95:1
VG-CoMnGa-05-062	34	29	no cap	300	GaAs, Si	2.04:1.00:1
VG-CoMnGa-05-063	79	29	no cap	300	GaAs, Si	1.96:1.00:1
VG-CoMnGa-05-073	53	29	Al(4nm)	300	NBI#10*, NBI#41*, InAs*, Si*	1.97:0.97:1
VG-CoMnGa-05-074	58	29	Al(3nm)	300	NBI#10*, NBI#41*, Si*	1.92:1.01:1
VG-CoMnGa-05-079	58	29	no cap	200	NBI#10*, NBI#41*	2.46:1.03:1
VG-CoMnGa-05-080A	39	29	no cap	200	NBI#10*	2.12:1.03:1
VG-CoMnGa-05-080B	34	29	no cap	300	NBI#10*	1.94:1.03:1
VG-CoMnGa-05-083	34	29	Au(4.5nm)	40	NBI#21	2.02:0.98:1
VG-CoMnGa-05-088	7.3, 10.2, 13.1	29	Al(1.5nm)	250	GaAs(Si)*	1.86:0.99:1
VG-CoMnGa-05-089	7.3, 10.2, 13.1	29	Al(1.5nm)	250	GaAs(Si)*	1.95:0.98:1
VG-CoMnGa-05-090	7.3, 10.2, 13.1	29	Al(1.5nm)	250	GaAs(Si)*	1.97:0.96:1
VG-CoMnGa-05-093	34	29	no cap	250	NBI#10*	2.08:0.93:1
VG-CoMnGa-06-002	15.7, 31.4, 62.8, 125.6	145	no cap	250	NBI#119*	1.92:0.98:1

Table 3.3: *List of growth parameters and stoichiometry measurements (green) and estimates (blue). * refers to the substrate being bonded with In.*

the highest temperature without any confirmed interface diffusion layer. From Auger Electron Spectroscopy (AES) data we find that T_{growth} = 450 °C is too high indeed, due to massive inter-diffusion between the substrate and the thin film. Further details can be found in Appendix E. An approach to experimentally verify the model described above is by measuring the saturation magnetization M_s on films grown at different temperatures, but with other growth conditions as constant as possible.

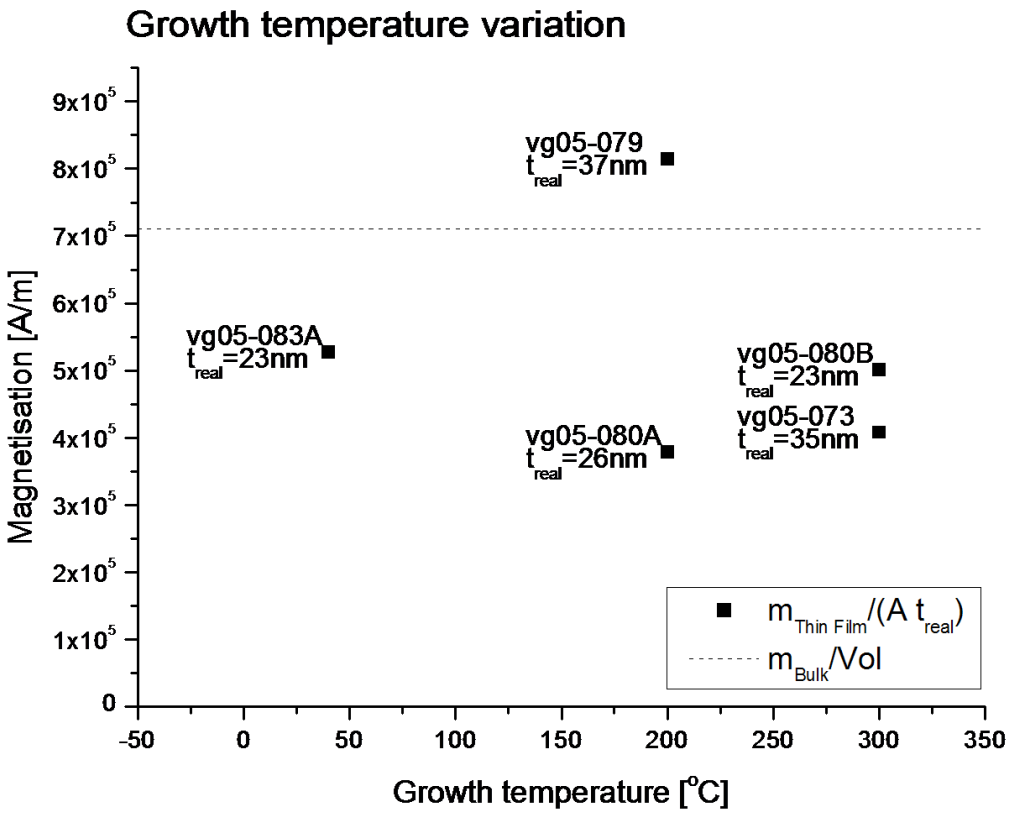

Figure 3.5: *Magnetization vs. growth temperatures. The real film thickness have been estimated from t_{nom} by the linear dependence shown in Figure 3.4. All samples are grown on GaAs-substrates.*

The effect is not clearly seen. The reason for this is probably the magnetization dependence on stoichiometry. From the estimates shown in Table 3.3, VG05-079 has more than 20 % extra Co, which explains the very high saturation magnetization. The rest of the samples shown in the graph deviates less than 6 % from the 2:1:1 stoichiometry relation.

By comparing XRD-scans in Figure 3.6 the growth temperature effect is clearest seen by a shift of the Heusler (400) and (200) reflections.

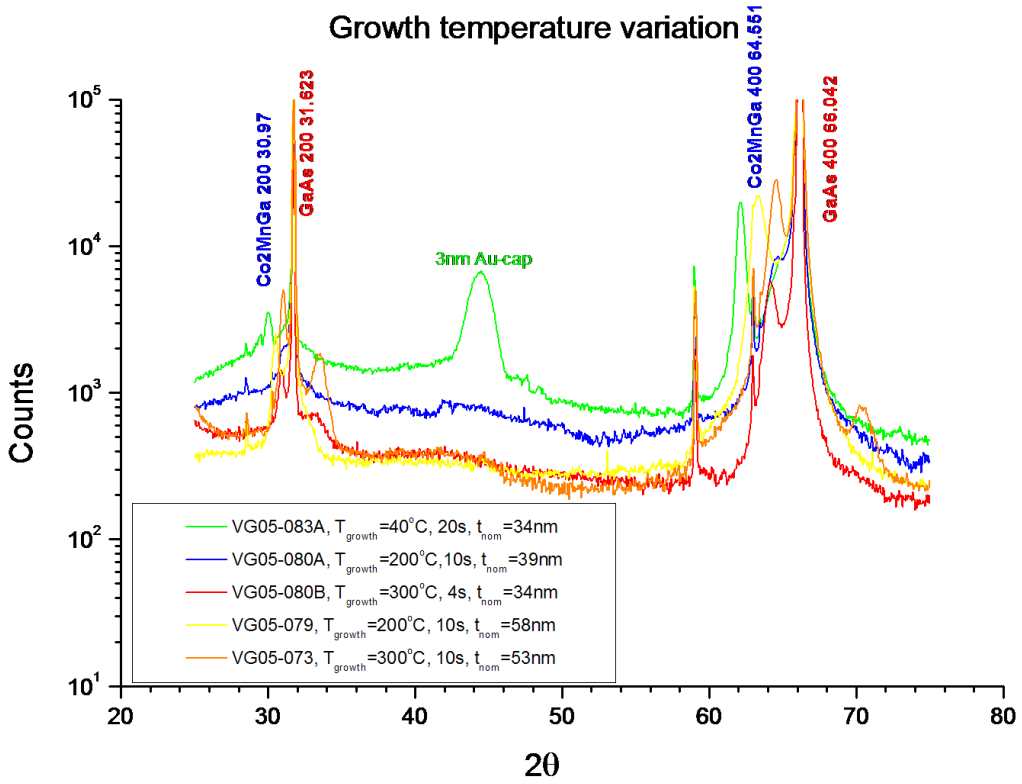

Figure 3.6: *XRD spectra for different growth temperatures. The very sharp peaks at* $2\theta = 28.5\,^{\circ}$, $59\,^{\circ}$, *and* $63\,^{\circ}$ *are artifacts from the substrate.*

By calculating the out-of-plane lattice parameter from the position of the reflections (Equation 3.1) as done in Figure 3.7 an interesting dependence is seen.

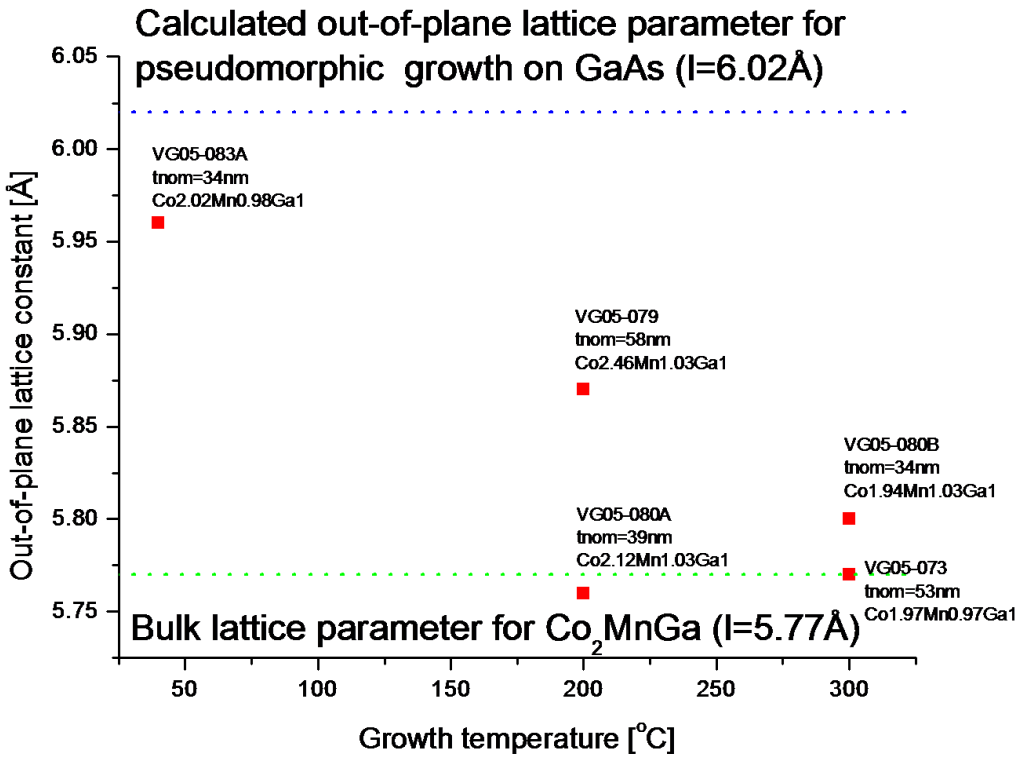

Figure 3.7: *Out-of-plane lattice parameter vs. growth temperatures.*

At low growth temperatures the measured out-of-plane lattice parameter is found to be very close to the expected value for a Co_2MnGa strained on the GaAs lattice. By assuming a constant volume of the unit cell the expected out-of-plane lattice parameter is given by $a = (5.77)^3/(5.65^2)$ Å = 6.02 Å. At T_{Growth} = 200 °C it seems like the lattice parameter have found its minimum very close to the bulk value 5.77 Å. VG05-079 is neglected due its 23 % extra amount of Co. At T_{Growth} = 300 °C the lattice parameter is around the expected bulk lattice parameter. It seems like high content of Co either increases the relaxed lattice parameter or enhance the ability to grow pseudomorphic (same in-plane lattice parameter) on GaAs. The explanation for this behavior is at the moment unknown. To enlighten this topic an in-plane lattice parameter study is needed. This have not yet been done.

From the above we must conclude that we have not obtained real significant data on the optimal growth temperature. The used techniques are indeed capable of providing such information, but due to difficulties in reproducibility of films with same stoichiometry, the approach seems to fail. This is the reason for us choosing the same growth temperature as reported by other Heusler-growth groups: NiMnSb [62, 63], Ni_2MnGa [64], Co_2MnGe[24] and Co_2MnSi[71, 72]. The most used technique described in the

literature for finding the highest growth temperature without inter-diffusion reactions is Transmission Electron Microscopy pictures (TEM). Most films have been grown at a temperature between T_{growth} =200 °C-300 °C.

3.3.2 Annealing temperatures

A way to minimize the formation of a diffusion layer and on the same time obtain a low defect density could be to grow the thin film in the low temperature region and then relax the structural defects by short time annealing the thin film in vacuum. Figure 3.8 shows three samples from the same growth but with different annealing temperatures. The sample was capped with ≈ 4nm Au. The annealing time is 10 minutes for all samples.

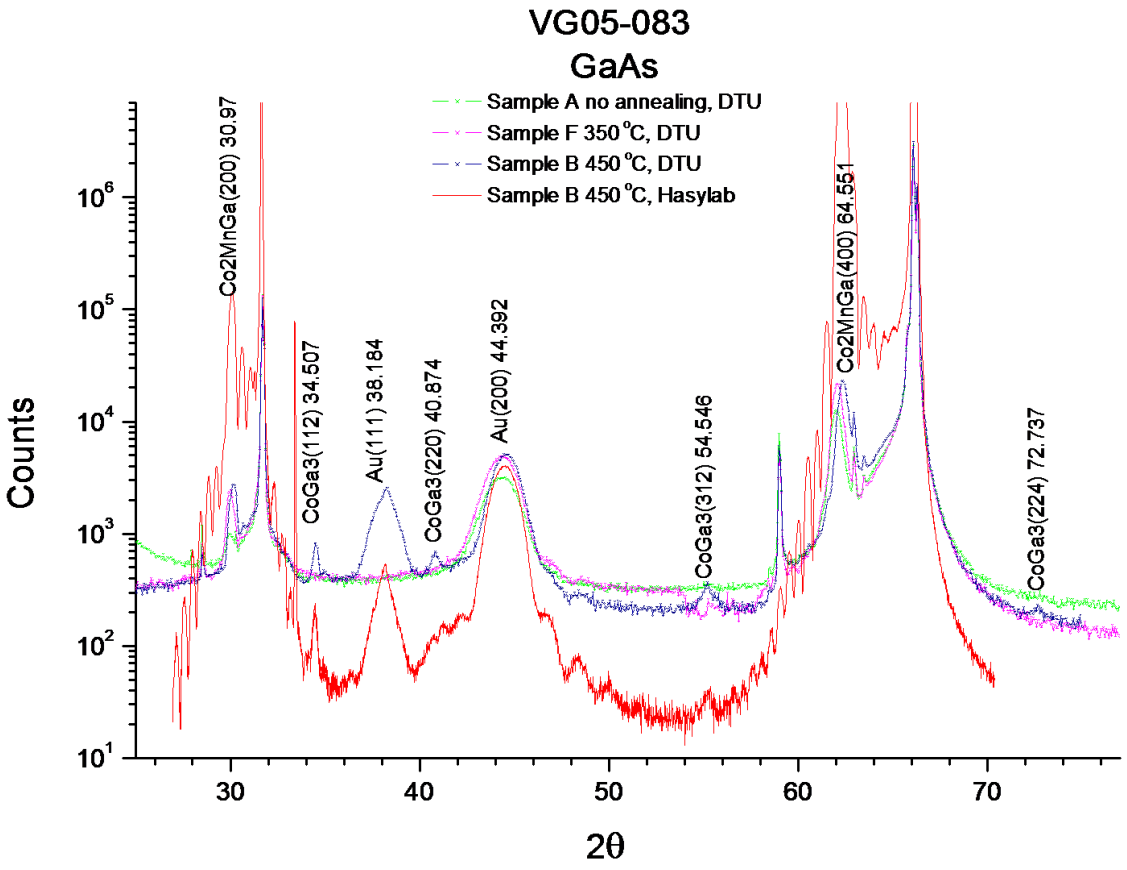

Figure 3.8: *XRD spectra vs. annealing temperatures.*

From the structural measurements it seems that short time annealing only has limited effect when the temperature is below 350 °C. At 450 °C several new reflections are observed. Figure 3.9 shows synchrotron measurements. From rocking curves it is found that only the reflection at k = 2.666 Å^{-1}(θ = 38.2 °) has epitaxial behavior, while the rest of the defect-reflections are powder-peaks.

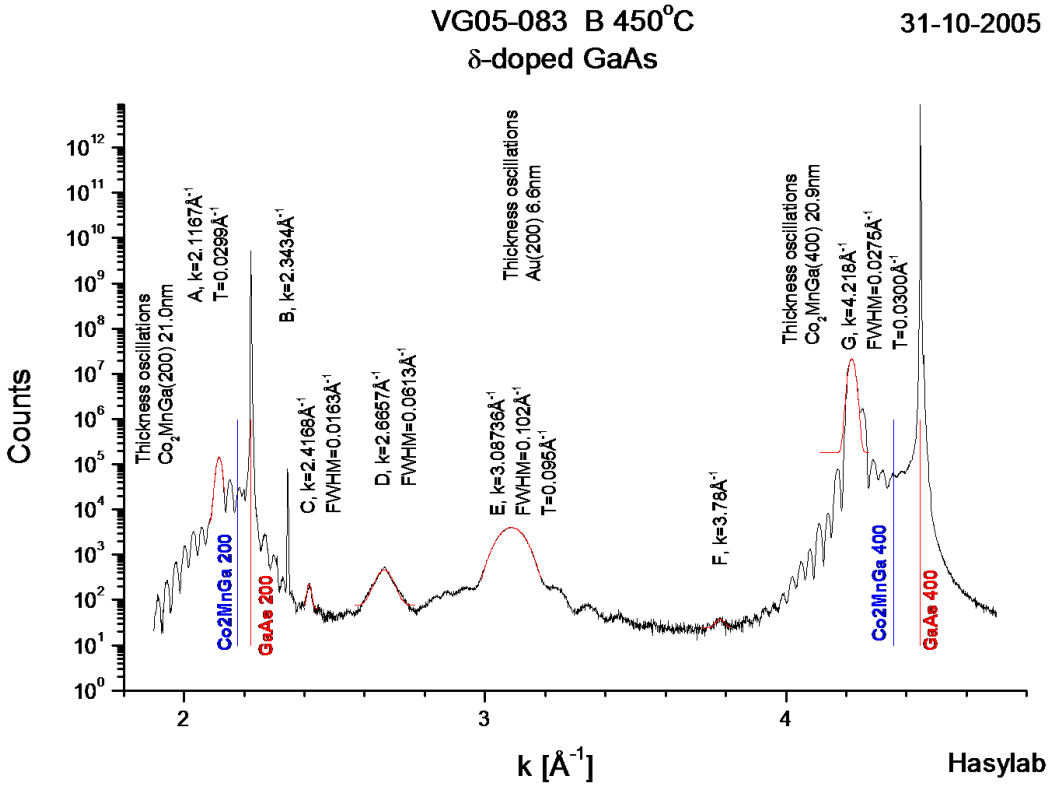

Figure 3.9: *Synchrotron measurements: VG05-083 annealed at 450 °C for 10 minutes.*

Table 3.4 summarizes the structural results. From the thickness oscillations the film thickness can be estimated to ≈ 21 nm. Some efforts have been made to determine the composition of the new phases seen in the 450 °C annealed samples. From powder diffraction data [86], we have come up with a hypothesis, which due to priorities has yet to be validated. The hypothesis is: When annealing the thin films capped with Au, two processes happen:

1. A segregation and recrystallization of some of the Au(200) into Au (111)
2. A segregation of polycrystalline $CoGa_3$ a=6.235 Å and c=6.454 Å

The "new" reflections and angles are indicated in Figure 3.9. The last column in table 3.4 shows the difference between the position of powder diffraction data and the measurements. From studies on epitaxial grown Fe thin films on GaAs and InP, we know that As is very reactive. This is not observed in this study due to either the methods we are using, which means that eventual As-phases are very thin or amorphous, or As-diffusion is not an issue in this alloy.

Magnetic behavior depends to some extent on the annealing temperature. The magnetic saturation moment does not seem to change while the coercive field does. Figure 3.10 shows hysteresis curves of the annealed samples.

VG05-083 setup	Reflection [Degrees]	FWHM [radians]	Thickness [nm]	lattice par. a [Å]	Osc.-period [$Å^{-1}$]	Thickness [nm]	Reflection guess	Angle [Degrees]	Difference [Degrees]
A no ann. - DTU	30.040	0.0158	10.1	5.94	-	-	Co2MnGa(200)	30.92	-0.88
A no ann. - DTU	31.700	-	-	5.64	-	-	GaAs(200)	31.623	0.077
A no ann. - DTU	44.317	0.0346	4.8	-	-	-	Au(200)	44.392	-0.07455
A no ann. - DTU	62.030	0.0106	16.9	5.98	-	-	Co2MnGa(400)	64.551	-2.52054
A no ann. - DTU	66.077	-	-	5.65	-	-	GaAs(400)	66.042	0.0346
F 350 °C - DTU	29.993	0.0073	21.7	5.95	-	-	Co2MnGa(200)	30.92	-0.92717
Aa 350 °C - Hasylab	29.959	0.0057	28.0	5.96	0.0310	20.3	Co2MnGa(200)	30.92	-0.961
F 350 °C - DTU	31.700	-	-	5.64	-	-	GaAs(200)	31.623	0.077
F 350 °C - DTU	44.324	0.0330	5.0	-	-	-	Au(200)	44.392	-0.0684
F 350 °C - DTU	62.077	0.0101	17.7	5.98	-	-	Co2MnGa(400)	64.551	-2.4742
Aa 350 °C - Hasylab	62.007	0.0084	21.5	5.98	0.0300	20.9	Co2MnGa(400)	64.551	-2.544
F 350 °C - DTU	66.077	-	-	5.65	-	-	GaAs(400)	66.042	0.0346
B 450 °C - DTU	30.144	0.0077	20.7	5.92	-	-	Co2MnGa(200)	30.92	-0.776
B 450 °C - Hasylab	30.080	0.0053	30.2	5.94	0.0299	21.0	Co2MnGa(200)	30.92	-0.83987
B 450 °C - DTU	31.700	-	-	5.64	-	-	GaAs(200)	31.623	0.077
B 450 °C - Hasylab	31.629	-	-	5.65	-	-	GaAs(200)	31.623	0.006
B 450 °C - DTU	34.503	0.0052	31.1	-	-	-	CoGa3(112)	34.507	-0.004
B 450 °C - Hasylab	34.453	0.0048	33.7	-	-	-	CoGa3(112)	34.507	-0.054
B 450 °C - DTU	38.187	0.0231	7.0	-	-	-	Au(111)	38.184	0.003
B 450 °C - Hasylab	38.140	0.0144	11.3	-			Au(111)	38.184	-0.044
B 450 °C - DTU	40.832	0.0074	22.3	-	-	-	CoGa3(220)	40.874	-0.042
B 450 °C - DTU	44.555	0.0285	5.8	-	-	-	Au(200)	44.392	0.163
B 450 °C - Hasylab	44.481	0.0277	6.0	-	0.0950	6.6	Au(200)	44.392	0.089
B 450 °C - DTU	55.200	0.0107	16.3	-	-	-	CoGa3(220)	54.546	0.654
B 450 °C - Hasylab	55.228	0.0074	23.4	-	-	-	CoGa3(220)	54.546	0.682
B 450 °C - DTU	62.259	0.0105	17.1	5.96	-	-	Co2MnGa(400)	64.551	-2.292
B 450 °C - Hasylab	62.282	0.0069	26.1	5.96	0.0300	20.9	Co2MnGa(400)	64.551	-2.269
B 450 °C - DTU	66.077	-	-	5.65	-	-	GaAs(400)	66.042	0.035
B 450 °C - DTU	72.602	0.0113	16.9	-	-	-	CoGa3(224)	72.737	-0.135

Table 3.4: *XRD-parameters: Measurements on VG05-083. The annealing was 10 minutes.)*

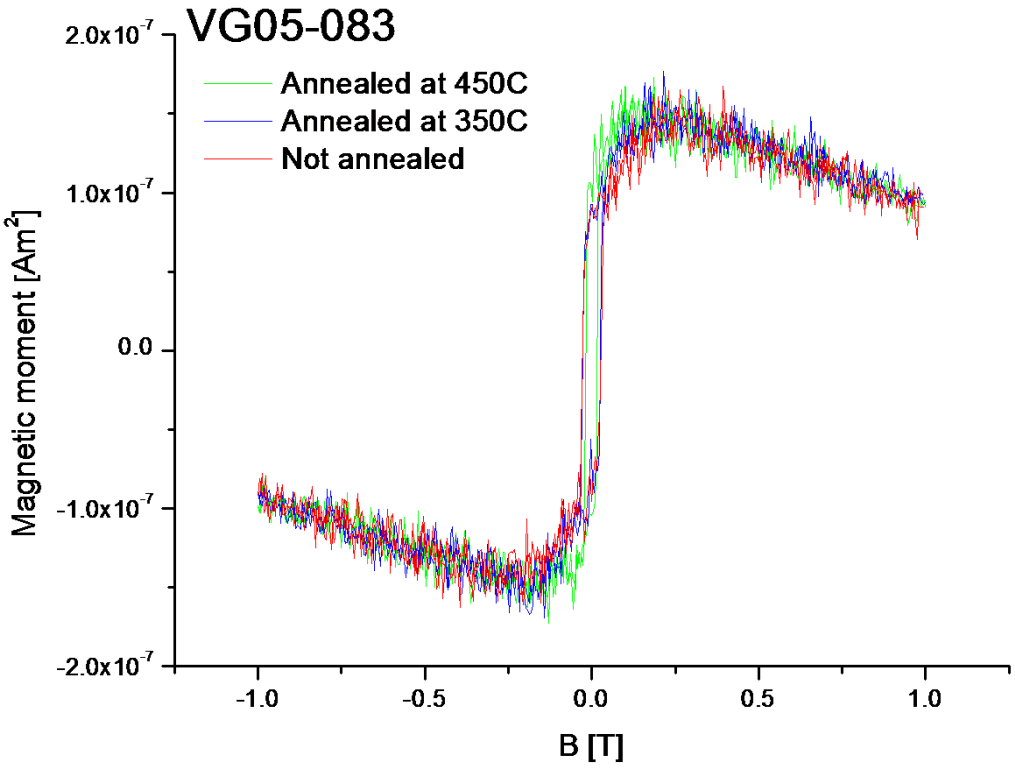

Figure 3.10: *Magnetic moment vs. annealing temperature*

A increased squareness with annealing temperature is observed. This behavior implies that by annealing the homogeneity of the film is improved as expected. The influence of inter-diffusion observed by XRD for T_{growth} = 450 °C is absent in the VSM measurements.

3.3.3 Stoichiometry

We have mainly focused on the Co/Mn ratio. Two approaches have been chosen to investigate how stoichiometry influences on structure and magnetic properties:

1. Large change in Co-Mn ratio (0-30 %) by changing the material flux and comparing samples from different growths, see Figure 3.11
2. Small changes in Co/Mn ratio (0-10 %) by using the flux-gradient in non-rotated samples, and comparing samples from same growth, see Figure 3.13

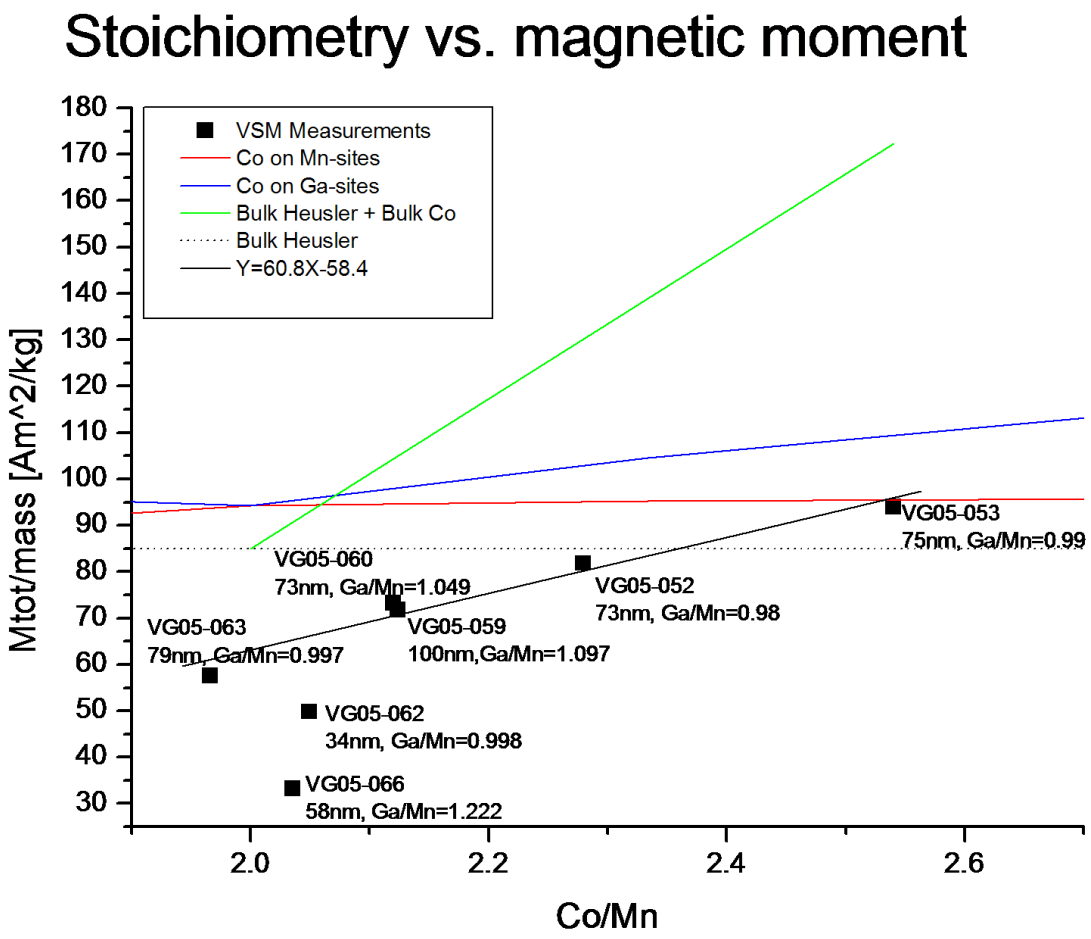

Figure 3.11: *Magnetic saturation moment vs. Co/Mn Stoichiometry variations. The thicknesses written in the graph are nominal thicknesses 3.4.*

Accurate mass measurements from ICP-OES make it possible to scale the magnetic saturation moments, between samples with different stoichiometry and therefore different densities. A linear trend is clearly seen for $Co/Mn > 2$. Ratios where $Co/Mn < 1.96$ have not been made. First of all it is observed that the size of the magnetic saturation moment is around 10 % less than bulk samples. Furthermore it is seen that the magnetic saturation moment is increasing with increasing Co/Mn ratio. To understand this, three models have been plotted as lines. One is a simple bulk Co_2MnGa added up with bulk hexagonal Co (185 Am^2/kg), where it is assumed that the excess amount of Co is segregated out of the Heusler lattice. The two other models are adopted from the DFT-calculations. One assuming Co on Mn sites and one assuming Co on Ga sites. From the slopes the bulk model seems to be the best one to explain Co/Mn dependence. To obtain the right slope with the bulk model, Co must have a saturation moment about 60 % of the saturation moment of hexagonal Co (185 Am^2/kg), which makes sense since the segregated Co will have a limited crystallographic order. Co-atoms on Ga-sites combined with Co-segregation

could also be an explanation.

To compensate for the difficulties in growing CoMnGa-alloys with the correct 2:1:1 stoichiometry we came up with the idea to use the natural stoichiometry gradient when not rotating the sample during growth. Figure 3.12 shows a drawing of the sample seen from the sources.

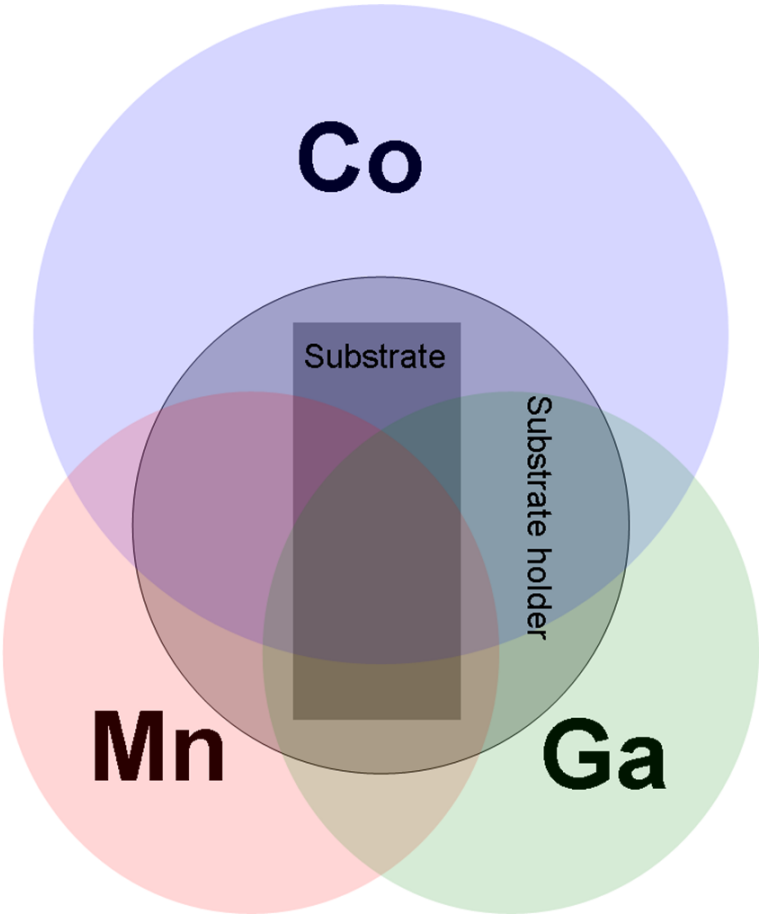

Figure 3.12: *Drawing of the sample holder seen from the sources. When not rotating the sample a change of* ±10 % *in Co-concentration over 35 mm is observed.*

From ICP-OES measurements it was found that the Co-concentration changes ±10 % over 35 mm. Figure 3.13 shows the magnetic saturation moments measured in Co-rich and Co-poor ends of a 35 mm long sample grown on Si, GaAs and lattice matched InGaAs (a=5.77 Å).

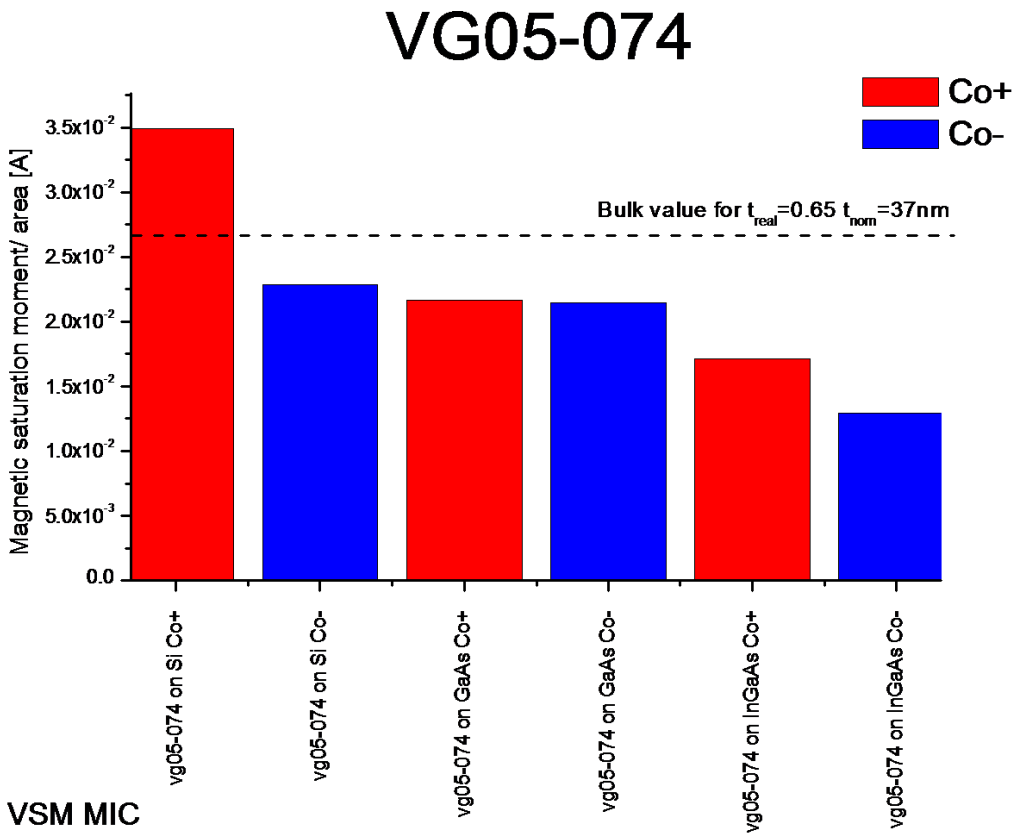

Figure 3.13: *Magnetic saturation moment vs. Stoichiometry variations. The film has a nominal thickness t_{nom} = 58nm, which corresponds to a real thickness of approximately t_{real} = 37 nm. The horizontal line illustrates the expected magnetic moment calculated from bulk properties.*

An effect is clearly seen in Si and InGaAs samples. From XRD measurements on films grown on Si-substrates and lattice matched InGaAs presented later in section 3.3.5, we know that these films do not grow entirely epitaxially. In the case of Si the film is nanocrystalline. In the case of lattice matched InGaAs grown on a GaAs substrate some parts are indeed grown epitaxially, which is seen by XRD, but at the cross hatch dislocations caused by the relaxation of InGaAs [91, 92] the films must also be polycrystalline. This makes segregation easier and could be an explanation for the significant difference in the magnetic saturation moment m_{sat}, with a difference in Co-content on 10 %. In this section only the magnetic changes on films grown on GaAs-substrate will be considered. For GaAs samples the effect is much smaller. The effect is within the same amplitude as the reproducibility of the measurements. Even though the magnetic saturation moment does not seem to change very much the hysteresis curves indeed do.

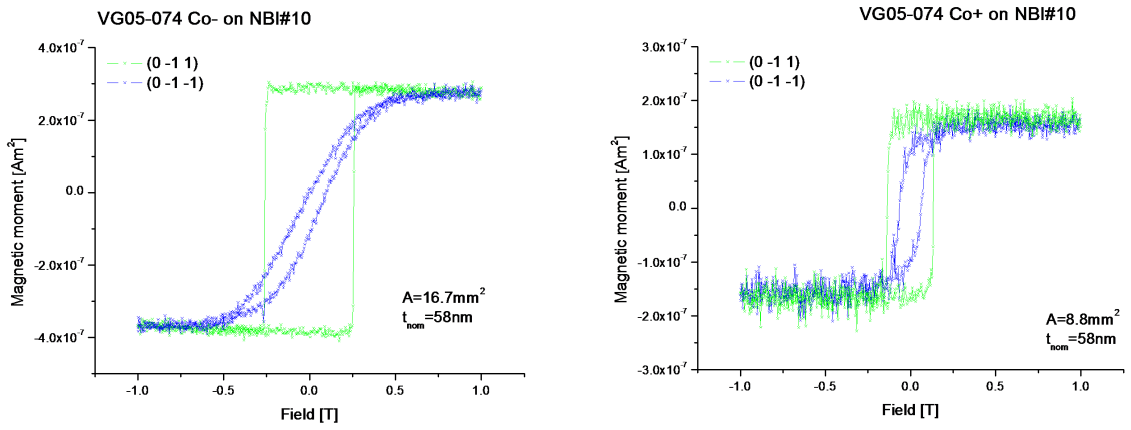

(a) Co- (b) Co+

Figure 3.14: *Magnetic hysteresis curves for each end of a film on GaAs with a difference in stoichiometric of 10 %. The film has a nominal thickness* $t_{nom} = 58$ *nm.*

Figure 3.14 shows a film which is grown on a GaAs-substrate MBE-overgrown with 1μm GaAs and capped with amorphous As to achieve a high quality GaAs surface, with only a small concentration of dislocations. Just before CoMnGa-growth the As was desorbed in-situ through the procedure described in Appendix C, which results in a 2×4 Ga-rich reconstruction of the GaAs surface. This was confirmed by RHEED patterns. Figure 3.15 shows the hysteresis curve for a film with same thickness, and a close to 2:1:1 stoichiometry. Contrary to VG05-074, the As-cap was desorbed at a lower temperature 450 °C, which prevents the reconstruction of the surface.

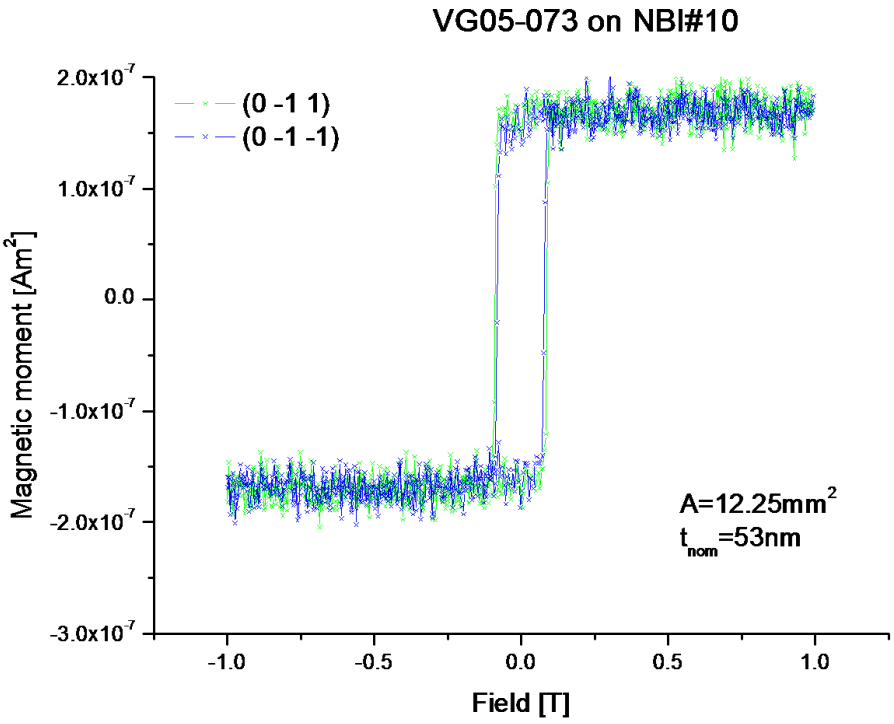

Figure 3.15: *Magnetic hysteresis curves for VG05-073. The film has a nominal thickness* $t_{nom} = 53\ nm$.

The differences between the shape (squareness) of the three hysteresis curves are remarkable, considering the only difference being stoichiometry with ±5 % and As desorption process. XRD measurements of sample VG05-074 are shown in Figure 3.16

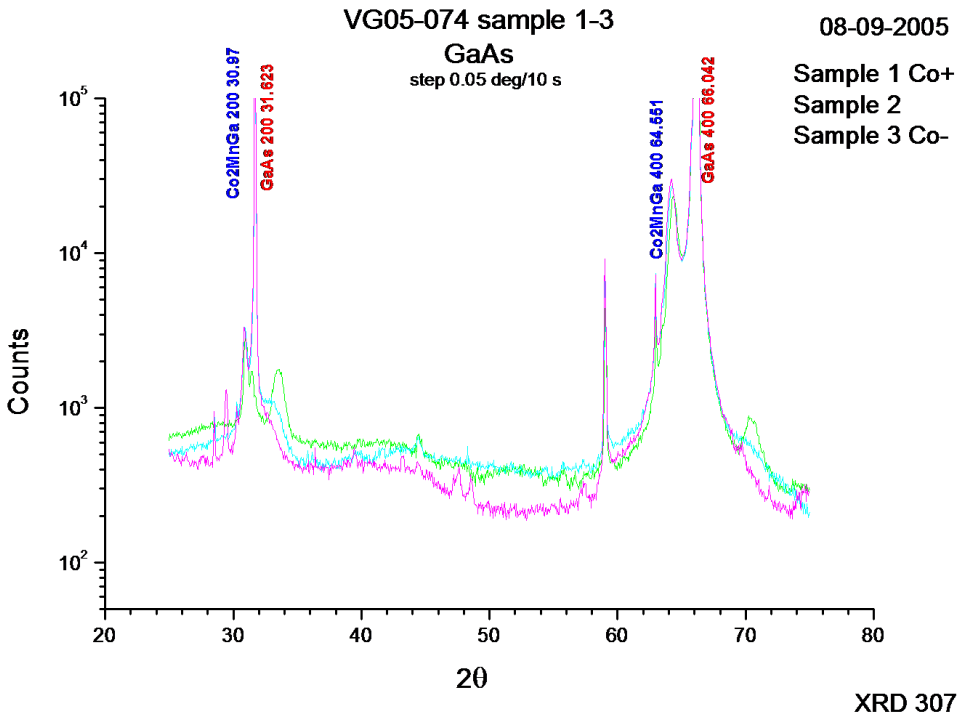

Figure 3.16: *XRD spectra vs. stoichiometry gradient sample. Sample 1 is Co-rich sample 2 is very close to the right stoichiometry and sample 3 is Co-poor. The very sharp peaks at* $2\theta = 28.5\,^\circ$, $59\,^\circ$, *and* $63\,^\circ$ *are artifacts from the substrate.*

Table 3.5 shows the observed crystal parameters obtained from the $\theta - 2\theta$-scans.

VG05-074 Setup	Reflection [Degrees]	FWHM [radians]	Thickness [nm]	lattice parameter [Å]	Guess	Angle [Degrees]	Difference [Degrees]
Co+ - hasylab	31.586	-	-	5.66	GaAs(200)	31.623	-0.037
Co+ - DTU	31.685	-	-	5.64	GaAs(200)	31.623	0.062
Co+ - hasylab	30.892	-	-	5.78	Co2MnGa(200)	30.92	-0.028
Co+ - DTU	30.980	-	-	5.77	Co2MnGa(200)	30.92	0.060
Co+ - hasylab	33.250	0.0171	9.4	2.69	Mn(100)	33.51	-0.26
Co+ - DTU	33.510	0.0159	10.1	2.67	Mn(100)	33.51	0
Co+ - hasylab	44.268	0.0067	24.8	-	Co2MnGa(220)	44.37	-0.102
Co+ - hasylab	64.155	0.0092	19.9	5.80	Co2MnGa(400)	64.551	-0.396
Co+ - DTU	64.380	0.0124	14.7	5.78	Co2MnGa(400)	64.551	-0.171
Co2MnGa - DTU	64.262	0.0096	19.0	5.79	Co2MnGa(400)	64.551	-0.289
Co- - DTU	64.214	0.0104	17.5	5.80	Co2MnGa(400)	64.551	-0.337
Co+ - hasylab	65.958	-	-	5.66	GaAs(400)	66.042	-0.084
Co+ - DTU	66.115	-	-	5.65	GaAs(400)	66.042	0.073
Co+ - hasylab	70.236	0.0239	7.9	2.68	Mn(200)	70.42	-0.184
Co+ - DTU	70.420	0.0212	8.9	2.67	Mn(200)	70.42	0

Table 3.5: *XRD-parameters for sample VG-05-074.*

A new phase with reflections at 2θ = 33.5 ° and 2θ = 70.4 ° appears in the Co-rich end of the sample. Again a hypothesis has been made yet to be validated. The reflections fit reasonably well with tetragonal Mn (100) and (200) reflection. This can be explained by the excess Co and makes it more energetically favorable to bind Ga, than the Heusler phase and by this process leave Mn in clusters. The crystallite size estimated from the FWHM value obtained with high resolution measurement is very large t = 9.4 nm compared to the crystallite size of the Heusler film t = 19.9 nm. If this hypothesis is correct some reflections from some CoGa alloy should be observed. Cubic CoGa has a (100 θ = 31.1 °) and a (200 θ = 64.8 °) reflection very close to Co_2MnGa (200 2θ = 30.9 °) and (400 2θ = 64.5 °), which means that the hypothesis cannot be validated by use of XRD only.

CoGa is in general nonmagnetic at room temperature [93], which does not correspond to the measurements shown in Figure 3.11. We do not completely understand the obtained data, but since this was a study to optimize growth parameters we conclude that the reflections at 30.9 ° and 70.2 ° are a sign of a film with too much Co.

From the measurements above it seems like the Co-content has a great influence on the hysteresis curve shape and the saturation magnetization.

3.3.4 Thickness

By moving a shutter very close to sample during growth, samples with same stoichiometry but varied thickness have been made. A picture of the shutter can be seen in Figure 3.17.

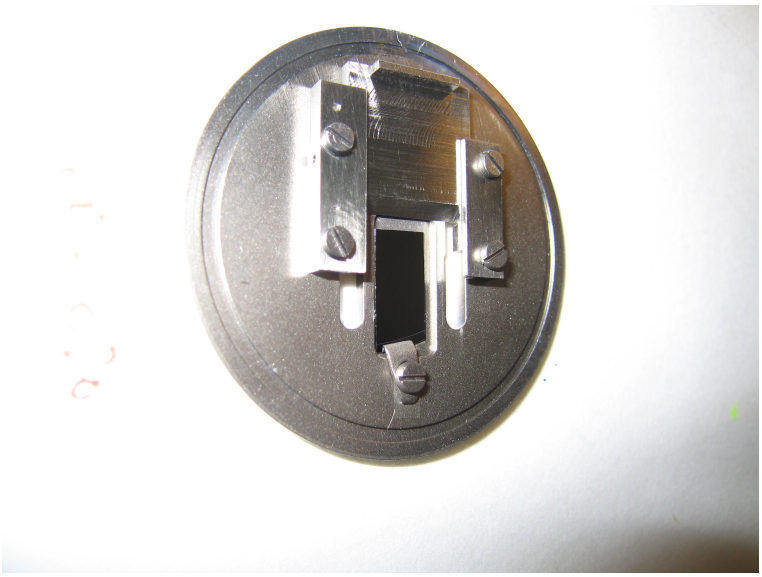

Figure 3.17: *Picture of the modified sample holder. By use of the wobble stick in the deposition chamber the shutter can be pushed or pulled in-situ.*

Two of such samples have been magnetically and structurally characterized, (VG05-088 and VG05-089), and one has been magnetically characterized (VG06-002). The sample

parameters can be seen in Table 3.3. Table 3.6 shows the obtained parameters from MOKE, VSM and XRD measurements on VG05-088 and VG05-089. Figure 3.18 shows the XRD-measurements.

		Magnetisation measurements					XRD							
		MOKE		VSM			Co2MnGa 200-reflection			Co2MnGa 400-reflection				
Sample	Piece	Hc (0-11) [mT]	Hc(0-1-1) [mT]	Hc (0-11) [mT]	Hc(0-1-1) [mT]	Hsat/Volume [kA/m]	Thickness osc. Period [A^-1]	Corr. Thickness [nm]	Interaction effect	Corr. Lattice parament k [A^-1]	Corr. Lattice parament er [A]	Thickness osc.	FWHM [A^-1]	Corr. Thickness [nm]
VG05-088	a, tnom=7.3 nm	-	-	0	0	67	No	-	Yes	4.34	5.79	No	0.106	5.93
	b, tnom=10.2nm	1.6	1.3	1.7	1.7	182	No	-	Yes	4.34	5.79	No	0.1	6.28
	c, tnom=13.1nm	3.9	1.4	3.8	3.8	235	Yes	-	Yes	4.31	5.83	No	0.073	8.61
VG05-089	a, tnom=7.3 nm	-	-	0	0	80	No	-	No	-	-	No	-	-
	b, tnom=10.2nm	1.4	1.3	1.4	1.2	322	0.088	7.14	Yes	4.268	5.89	Yes	0.0928	6.77
	c, tnom=13.1nm	1.7	3.3	2.5	2.9	367	0.07	8.98	Yes	4.262	5.90	Yes	0.0706	8.90

Table 3.6: *Samples: VG05-088 and VG05-089. Parameters from MOKE, VSM and XRD measurements.*

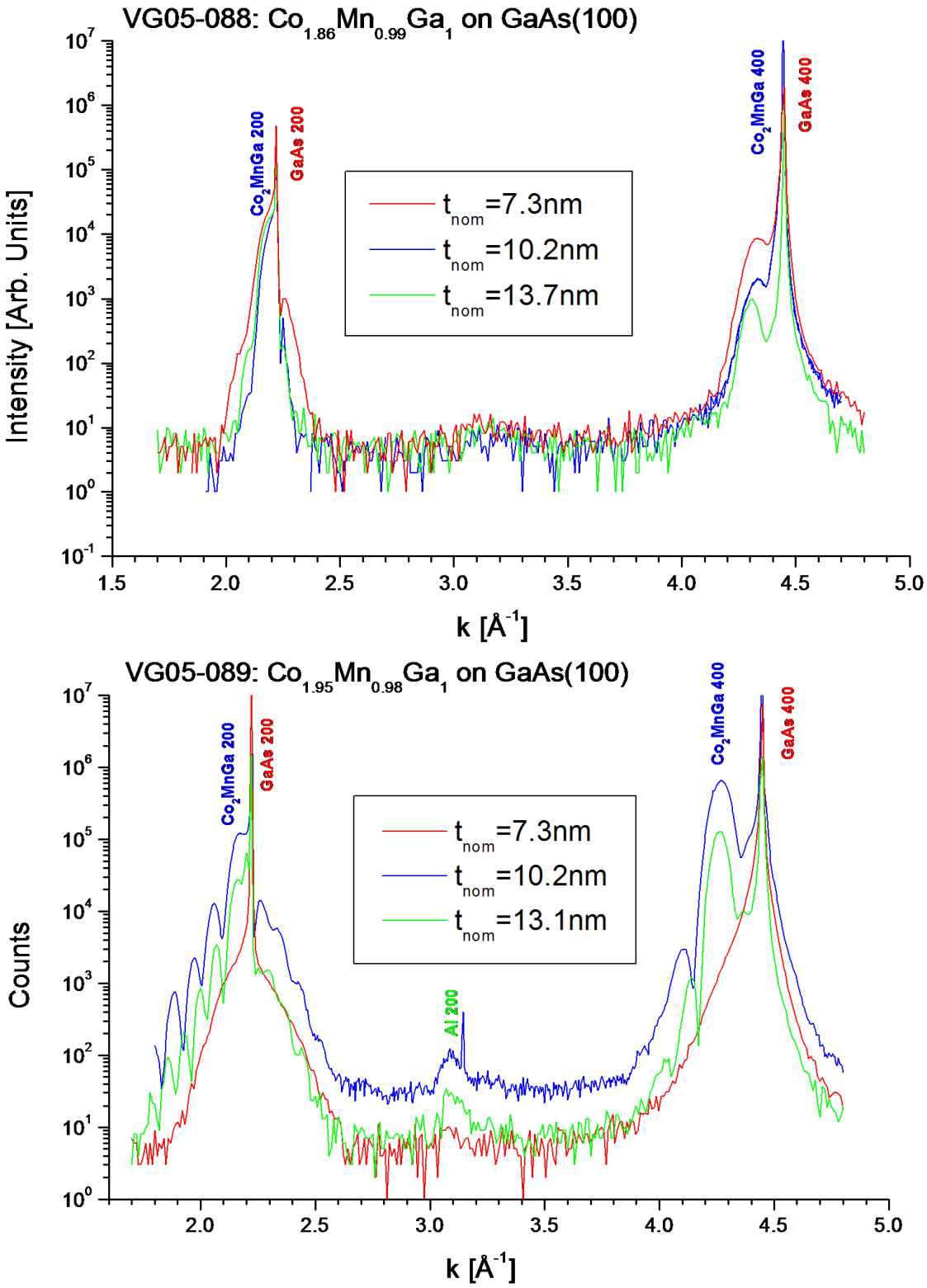

Figure 3.18: *Synchrotron XRD-measurements on thin films with different thickness and stoichiometry.*

We suspect the film to evolve from a strained film with in-plane lattice parameters matched with GaAs a = 5.65 Å into a relaxed film with bulk lattice constant a = 5.77 Å. Since we by normal $\theta - 2\theta$-scans probe the out-of-plane lattice parameter we suspect to see a lattice parameter close to a = 6.02 Å (assuming that the crystal lattice keeps a fixed volume) for very thin films and a = 5.77 Å for thicker films, where a relaxation of the strain has been established by dislocation in an intermediate region between the substrate and relaxed film. Dislocations are expected up through the film.

This trend is only seen to some extent in the measurements above as an increase, relative to the film thickness, in the FWHM value in the thinnest part of VG05-088. The reason for not observing the relaxation process should rather be found in the quality of the substrate crystal. VG05-088 and VG05-089 are part of the XMCD study and were grown on epi-ready GaAs substrates treated with the oxide-removing process described in Appendix C.

Films grown on As-capped high quality GaAs-substrates show to some extent the expected pseudomorphic growth. Figure 3.19 illustrates this.

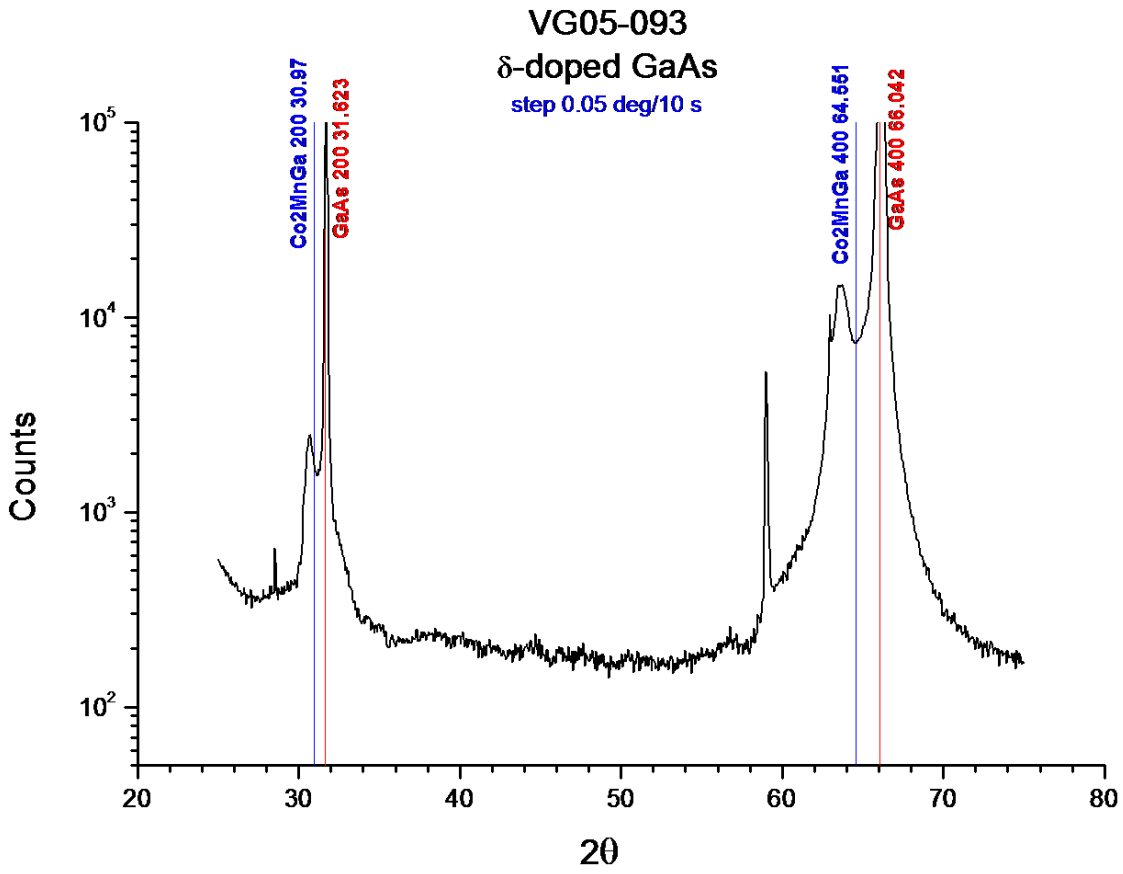

Figure 3.19: *XRD-measurements VG05-93,* t_{nom} = 34 *nm. The very sharp peaks at* 2θ = 28.5 °, 59 °, *and* 63 ° *are artifacts from the substrate.*

The Heusler lattice parameter is measured to a = 5.84 Å. This number can be understood if the Heusler crystal is not strained in both in-plane directions, but only in one of them. The expected out-of-plane lattice parameter should then be $a = 5.77^2/(5.65)$ Å = 5.89 Å. The magnetic behavior of the sample shown in Figure 3.19 is yet to be determined. By use of high intensity x-ray source incident from a shallow angle, the in-plane lattice parameter can be determined. Due to limited time on the synchrotron facility, this has only been done on VG05-083 annealed at T = 450 °C (denoted B), and only in one of the two major in-plane directions ((0 $\bar{1}$ 1) and (0 $\bar{1}$ $\bar{1}$)). The measurements seemed to reveal a relaxed Co_2MnGa lattice parameter of a = 5.76 Å. The in-plane XRD-measurements are shown in Figure 3.20

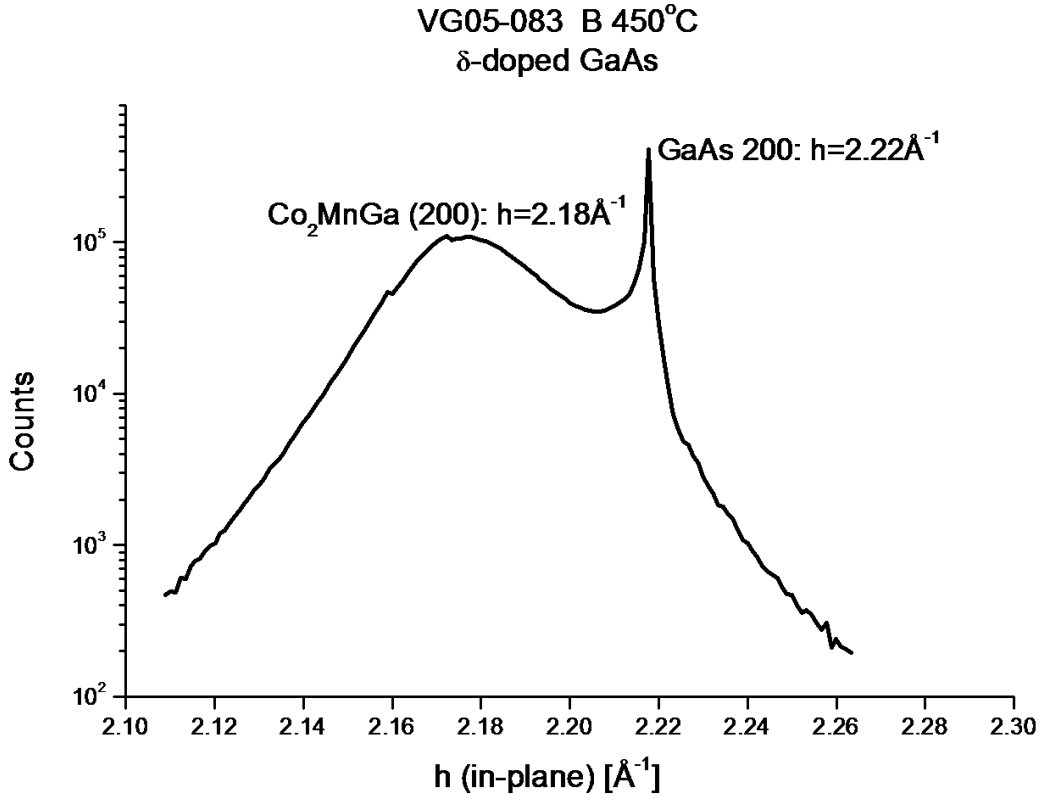

Figure 3.20: *In-plane XRD-measurements on VG05-083, annealed at 450 °C for 10 minutes,* t_{real} = 21 *nm.*

Very recently, new 2D data on same sample VG05-083 but annealed at 350 °C for 10 minutes (denoted Aa) have been obtained. The measurements revealed that the thin film indeed has the same in-plane lattice constant as GaAs, but also a very wide peak corresponding to a higher lattice constant as seen with VG05-083B (see Figure 3.20). The

data is shown in Figure 3.21

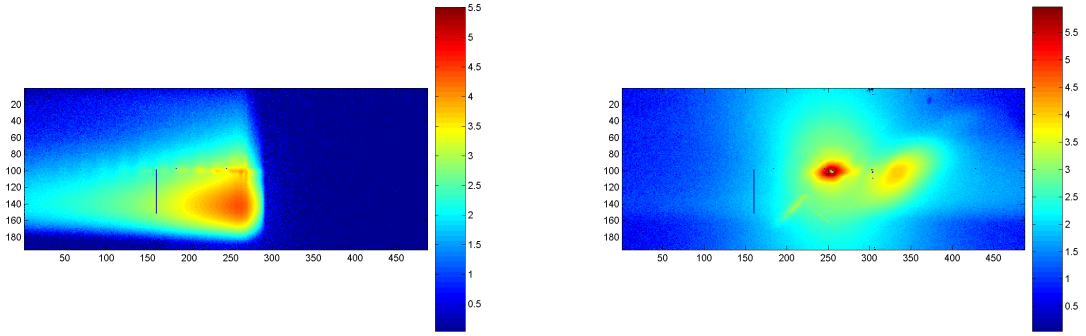

(a) GaAs(020) Bragg point at (250,100)

(b) GaAs(202) Bragg point at (250,100)

Figure 3.21: *2D XRD-measurements on VG05-083, annealed at 350 °C for 10 minutes,* t_{real} = 21 *nm.*

The scan shown in Figure 3.20 would correspond to a vertical line through the GaAs (020) Bragg point, shown in Figure 3.21 (a). The reason that we conclude that the thin film is lattice matched to the substrate in this particular film is the clear oscillations observed in the horizontal line through the GaAs (020) Bragg point. From the oscillation period the film thickness has been estimated to 24 nm which corresponds nicely to a previously estimated thickness on same film 21 nm (see Table 3.4). Figure 3.21 illustrates a 2D picture with the GaAs (202) Bragg point at (250,100). The figure shows that the out-of-plane lattice constant of the thin film is longer than the GaAs lattice parameter. We expect the wide peak to be due to disorder-scattering, but as mentioned earlier the measurements are obtained very recently and yet to be analyzed further.

From measurements on VG05-083, which were grown at 40 °C and subsequently annealed at 350 °C for 10 minutes, the thin film seems to be strained by the substrate up till a thickness of at least 21 nm. From out-of-plane measurements it seems like the critical thickness is $\leq$ 20 nm.

To conclude on the general structural dynamics of thin film growth, more in-plane measurements are needed on samples grown with different growth parameters. Especially the influence of growth temperature and usage of bufferlayer would be interesting to study.

Figure 3.22 shows a plot of the magnetic saturation magnetization and the coercive field vs. nominal thickness for three different samples.

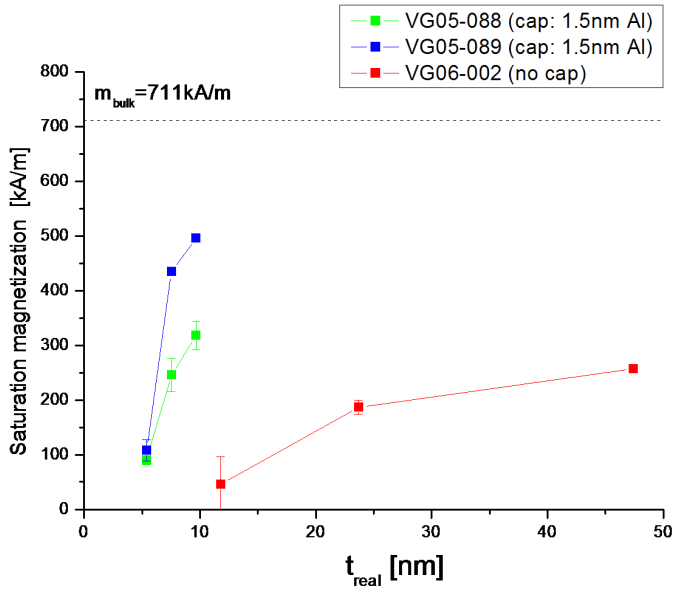

(a) M_{sat}

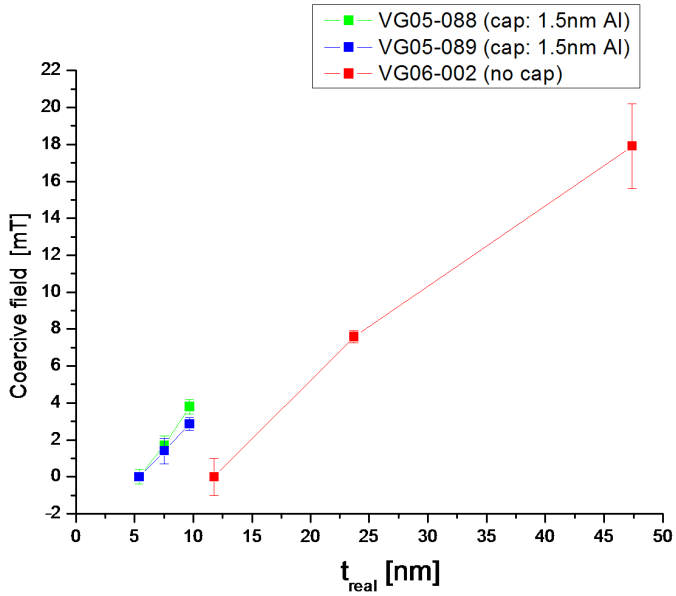

(b) H_c

Figure 3.22: *Magnetic behavior measured on thin films with different thickness, substrate quality and capping. a) shows the saturation magnetisation M_{sat}. t_{real} (scaling the x-axis, and denominates the y-axis)has been estimated by use of the thickness dependence shown in Figure 3.4. b) shows the coercive fields as a function of t_{real}.*

VG05-089 (1.95:0.98:1) and VG06-002(1.92:0.98:1) are both very close to the correct stoichiometry 2:1:1. There are two differences in growth conditions. 1) lack of cap layer on VG06-002 , and 2) VG06-002 is grown on a high quality As-capped GaAs substrate contrary to VG05-088 and VG05-089. From Figure 3.22 an estimate on the thickness of a dead magnetic layer due to e.g. oxidation of VG06-002 can be given. The figure shows the estimated saturation magnetization M_s, where the film thickness has been calculated from the nominal thickness by use of the linear dependence of thickness shown in Figure 3.4. VG06-002 seems to saturate at a saturation magnetization of 43 % of the bulk value. This corresponds to 22 nm nonmagnetic thin film. The very slow saturation could be explained by variations in the depth of the oxidation.

The only difference between VG05-088 (1.86:0.99:1) and VG05-089(1.95:0.98:1) is the stoichiometry. As also described in section 3.3.3 we find that Co-rich films show a higher magnetization than the stoichiometric films. Even after an estimated real thickness of 7.6 nm the measured saturation magnetization VG05-088 shows approximate 57 % of the bulk value. This corresponds to 3.3 nm nonmagnetic thin film. The origin of such a lack should be found from either:

- The assumption of bulk magnetic moment is wrong, or
- Chemical reactions and diffusion at the ferromagnetic thin film/Al interface, or
- Chemical reactions and diffusion at the ferromagnetic thin film/semiconductor interface

Based on depth profiling Auger-data, see Appendix E, we have found that Mn tends to diffuse towards the surface into Al. Comparison of magnetization measurements of VG05-088 and VG05-089 with the local magnetic moments measured by XMCD (see section 2.8) are summarized in Table 3.7.

Sample:	t_{real} [nm]	XMCD $\frac{m_{Mn}+2m_{Co}}{m_{bulk}}$	VSM $\frac{Co_2MnGa}{M_{bulk}}$
VG05-088:	5.3	0.24	0.13
VG05-088:	7.6	0.36	0.34
VG05-088:	9.7	0.31	0.45
VG05-089:	5.3	0.19	0.15
VG05-089:	7.6	0.46	0.61
VG05-089:	9.7	0.23	0.70

Table 3.7: *Comparison of XMCD measurements of the local magnetic moments from Co and Mn, compared with VSM saturation magnetization measurement. The measurements are performed at* 300 *K.* m_{bulk} = 3.71 μ_B *has been chosen to* 90 % *of the theoretically expected low temperature value.* M_{bulk} *is chosen to 711 KA/m, Webster* et al. *[5]. Stoichiometries: VG05-088 is estimated to be* $Co_{1.86}Mn_{0.99}Ga_1$ *and VG05-089 is estimated to be* $Co_{1.95}Mn_{0.98}Ga_1$.

A fairly good agreement for both samples is observed for the thinnest films, while

the magnetization measurements are higher for the thickest films. This behavior can be explained if oxide has penetrated the 1.5 nm Al-cap and oxidized the top Co_2MnGa layer.

But the XMCD measurements showed no evidence of oxidation, on the contrary the Mn L3 peaks were very clean in appearance. Another explanation could be an impurity layer caused by diffusion and chemical reactions, which not include oxygen. We approximate this layer to be between 3nm and 10nm, due to the fact that $m_{Mn} + 2m_{Co}$ (XMCD) does not seem to increase from t_{real} = 7.6 nm to t_{real} = 9.7 nm, implying that a coupling with the non-diffused Heusler layer is constant. Furthermore we expect the layer to act strongly on Mn compared to Co, due to the relative larger decrease in Mn moment, compared to Co moment. This is in good agreement with Auger spectroscopy measurements (see section E), where measurements have shown that Mn tends to diffuse towards the surface, even though the structure is capped with approximately 2 nm Al. Furthermore As-bonding at the substrate interface is known to significantly change the local magnetic moments in e.g. Fe/GaAs structures [94, 95].

More measurements are needed in particular on samples with other cap layers and complementing experimental techniques should be applied to the same samples used for the XMCD study, as it has been done with VG05-088 and VG05-089:

- the crystal structure should be checked by XRD
- the magnetic properties should be checked by magnetometry

Furthermore it would be interesting to compare the XMCD results with the nature and the density of defects, analyzed using NMR (e.g. looking for Mn- and Co-antisites).

3.3.5 Strain

The strain in the film can be varied by using different substrates materials (and the possibility of a bufferlayer). One must bear in mind that diffusion processes also are substrate dependent. To compare the influence of strain, samples were made during the same growth but on four substrates with different lattice constants.

substrate	lattice parameter [Å]	mismatched to Co_2MnGa [%]
GaAs	5.65	-2.1
InAs	6.06	+5.0
Si	5.43	-5.9
$In_{28.8\ \%}Ga_{70.2\ \%}As$	5.80 (intended to be 5.77)	+0.5

Table 3.8: *Substrate information.*

Figure 3.23 shows the magnetic saturation moment from two different growths on four and two different substrates, respectively.

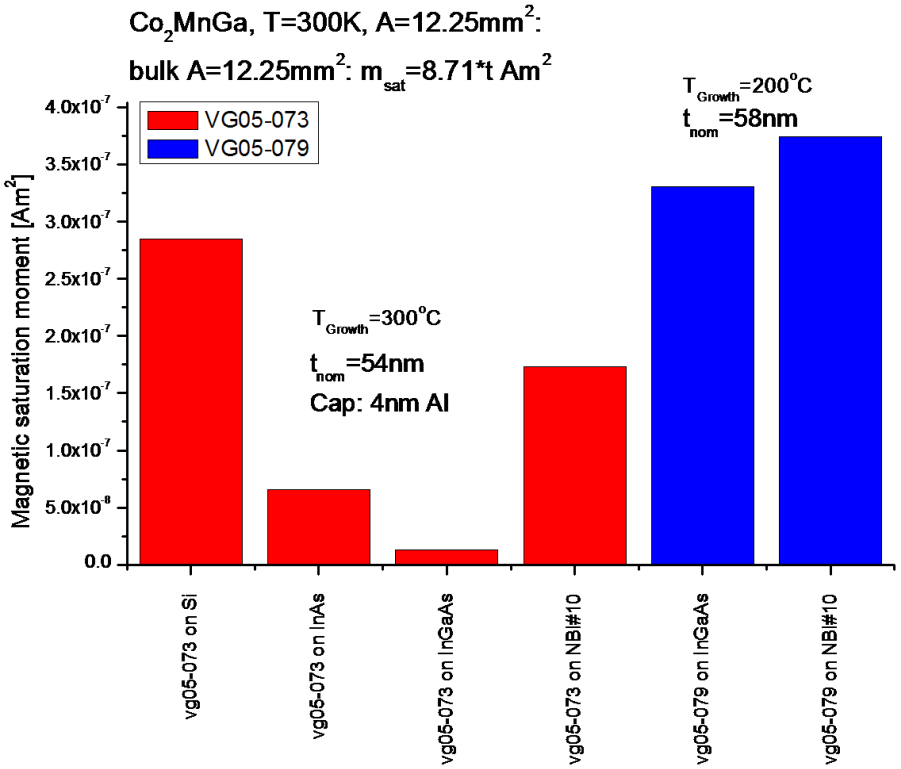

Figure 3.23: *Magnetic saturation moment vs. substrate and growth temperature. NBI#10: As-capped MBE-grown δ-doped GaAs on Epi-ready GaAs (100).*

The growth has been made at different growth temperatures to give an idea of the diffusion process involved. The magnetic saturation moment seems to be much less on films grown at 300 K on substrates with In, suggesting that diffusion processes are enhanced when In is involved at the interface. The effect is clearly seen. No films with a good stoichiometry grown on CoGa have been characterized. The films grown on CoGa-buffer layers were made at the beginning of the growth and characterization study which means that the stoichiometry was not optimal.

Figure 3.24 shows XRD-measurements on films from same MBE-growth but on Si, GaAs, InAs, and InGaAs lattice matched to a = 5.77 Å.

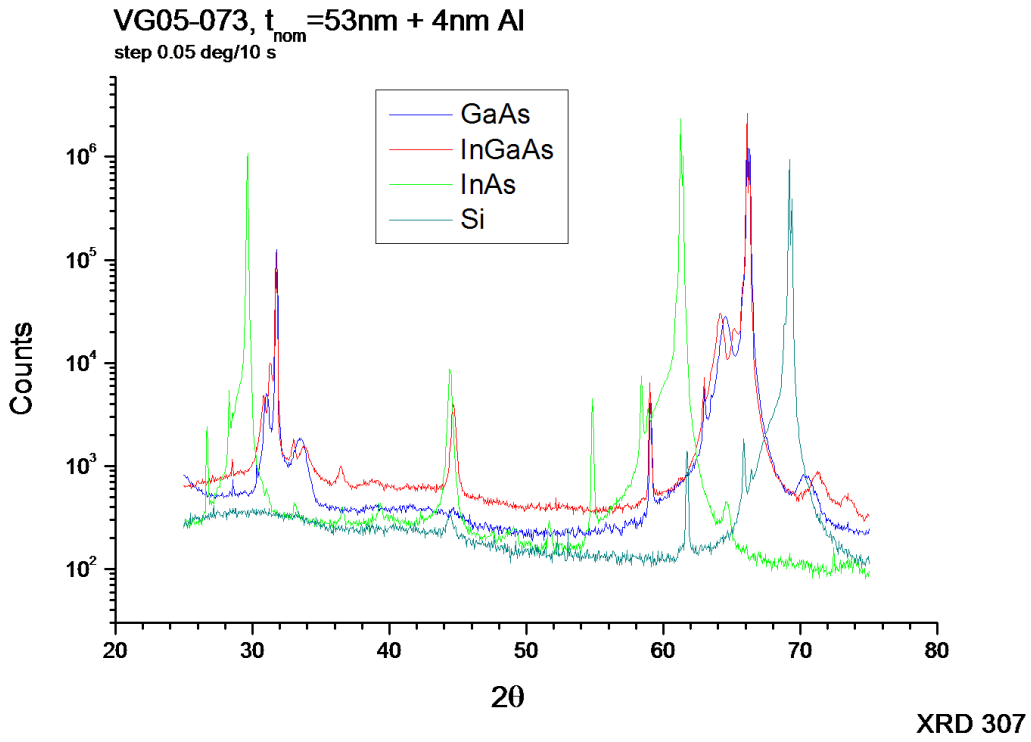

Figure 3.24: *XRD-measurements on films from MBE growth on Si, GaAs, InAs, and lattice matched InGaAs.*

To summarize the results only a few reflections are observed in the case of Si. The reflection corresponds to Co_2MnGa (220) reflections, which is the strongest reflection in powder diffraction measurements. We suspect the film on Si to be polycrystalline. The same is the case with InAs. The observed reflections are clearer. Peaks are observed for (200), (220) and (400) reflections. The ratio between the amplitudes of the (220) and (400) reflections are measured to be (220)/(400) = 24 compared to 8 measured on a powder-sample [96].

The data on GaAs shows a relaxed out-of-plane lattice parameter a = 5.77 Å. In the case of InGaAs we observe a shorter lattice parameter a = 5.71 Å as compared to bulk. From XRD measurements on a reference sample with the As-cap desorbed, the out-of-plane lattice parameter was found to a = 5.80 Å (since the InGaAs is relaxed on the underlying GaAs substrate we expect same lattice parameter for in- and out-of-plane directions). The expected out-of-plane parameter, when elongating the Heusler in-plane-lattice parameters is as observed 5.71 Å. In this case the lattice mismatch is only 0.5 %. We have not been able to estimate how much the film is ordered compared with how much it is disordered due to disorder defects in the relaxed InGaAs-layer. To do this in a correct manner high intensity in- and out-of-plane measurements should be done. But by

use of the intensity of the (220)-reflection observed, and using this as a measurement on how ”many” randomly oriented lattice planes exist in the films, we have estimated this to be 8 % of the material. We have made the estimate on the basis of the relation between the amplitudes of the (220) and (400) reflections (220)/(400) = 0.7 compared to a powder diffraction relation of 8 [96].

3.4 Magnetic properties

Most magnetic properties have already been described in the previous section. The results are shortly summarized in the following.

- Films rich on Co seems to have a higher saturation moment than stoichiometric films. Annealing improves the homogeneity of the films, resulting in increased squareness in the hysteresis curve.
- Anisotropy is very dependent on the reconstruction of the substrate surface and the stoichiometry. Near stoichiometric films grown on GaAs surfaces which are not reconstructed, show no anisotropy while films grown on reconstructed GaAs surfaces exhibit anisotropy. Films deficient in Co seems to have a very strongly defined anisotropy with $[0\bar{1}1]$ as the easy axis.
- Oxidation reduces the magnetization of the thin films.
- The coercive field depends linearly on the film thickness.
- Films grown on Si-substrates have the highest saturation moment compared to GaAs and InGaAs-substrates, implying that some interface diffusion occur for GaAs and InGaAs or that polycrystalline films segregates Co easier than single crystalline films.

Only a few low temperature magnetization measurements have been carried out. Figure 3.25 shows SQUID-magnetometer measurements on VG04-015 at different temperatures, and with the applied field in both parallel (easy axis) and perpendicular (hard axis) direction to the sample plane.

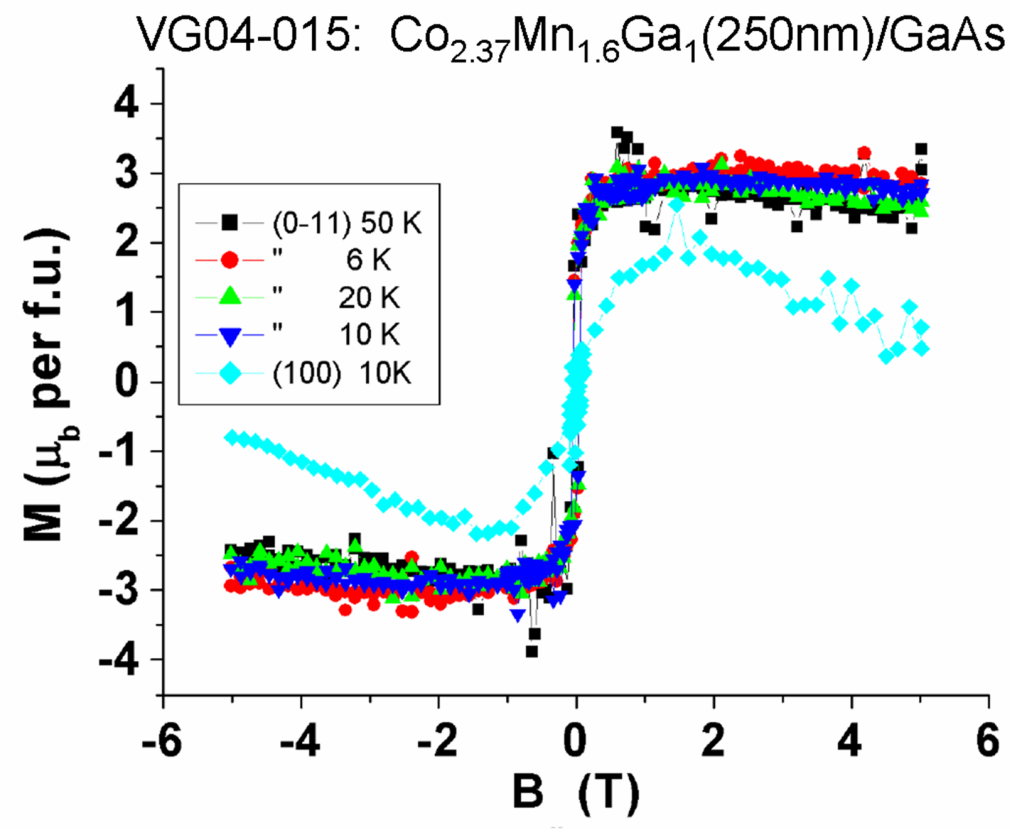

Figure 3.25: *SQUID magnetometer measurements of magnetic moment at 6 K-300 K, on VG04-015($Co_{2.37}Mn_{1.6}Ga_1$(t_{nom}=250 nm)/GaAs (100), the thickness are nominal).*

Only a small change in the magnetic moment is observed from 6 K to 50 K. The alignment of thin films perpendicular to the applied magnetic field, have shown to be a bit difficult in the SQUID setup. We expect this to be the reason for the negative slope in the case of perpendicular applied field shown with diamonds. Still the conclusion is that in-plane magnetization is indeed the easy axis compared with out-of-plane magnetization. The measurements are in good agrement with VSM measurements (where alignment is easier controlled) on VG04-065, with a more moderate Co-concentration. The data is seen in Figure 3.26

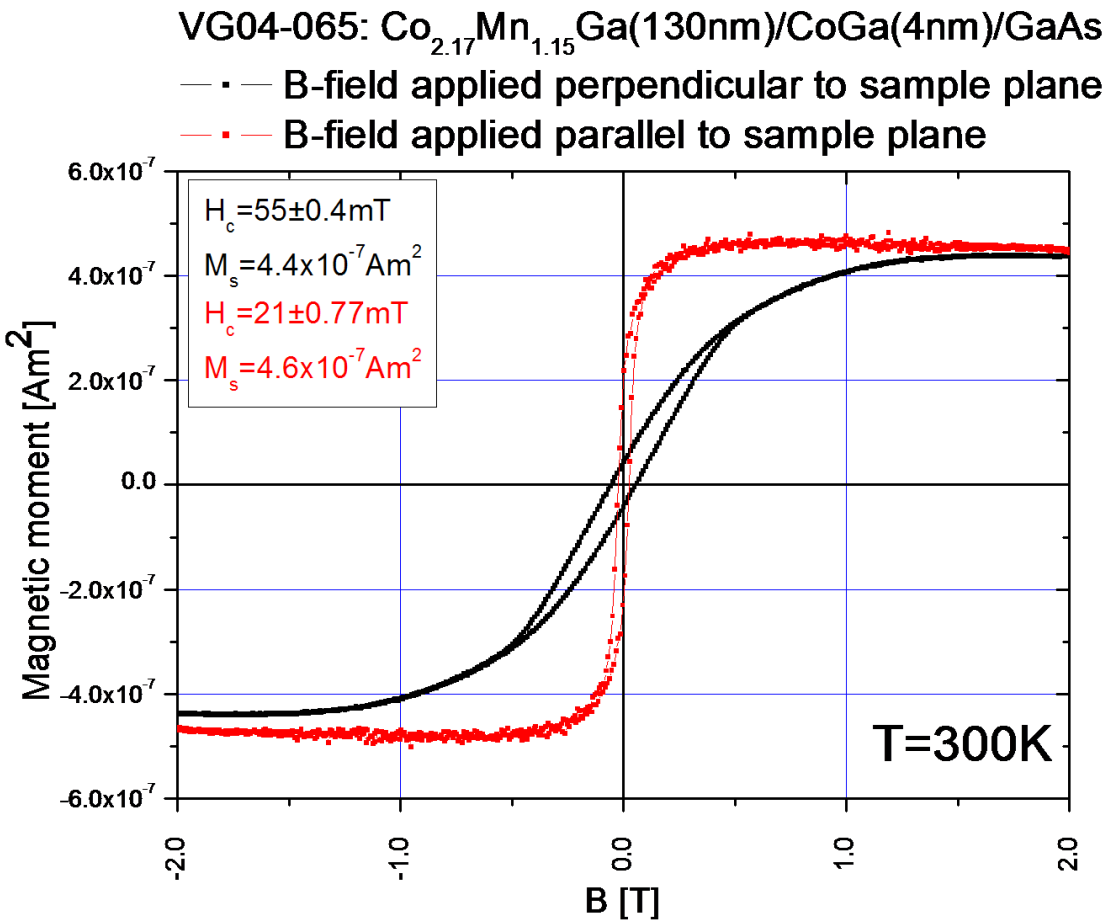

Figure 3.26: *Vibrating Sample Magnetometer measurements of magnetic moment at 300 K, on VG04-065($Co_{2.17}Mn_{1.15}Ga_1$(t_{nom}=130 nm)/CoGa(t_{nom}=4 nm)/GaAs (100), the thickness are nominal).*

To saturate the samples with an applied magnetic field perpendicular to the sample plane, a magnitude of 1-2 T is needed.

Figure 3.27 shows MFM pictures of VG06-002b and c.

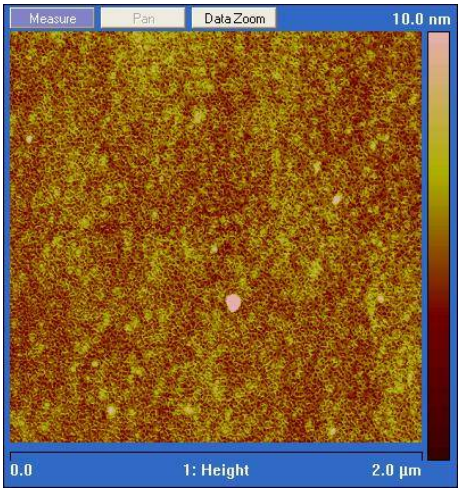

(a) VG06-002b: Topography scan (AFM)

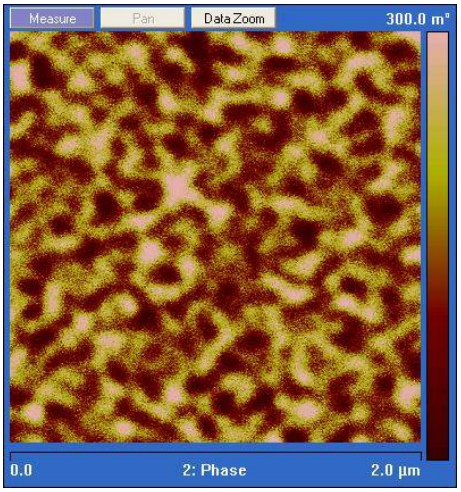

(b) VG06-002b: Magnetic domain scan (MFM)

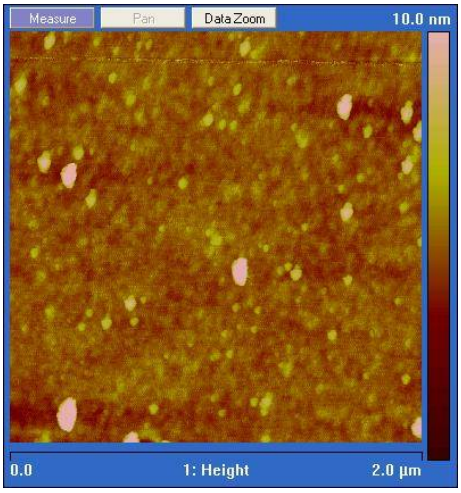

(c) VG06-002c: Topography scan (AFM)

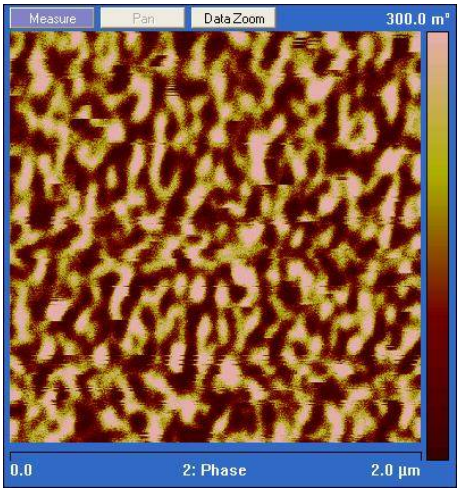

(d) VG06-002c: Magnetic domain scan (MFM)

Figure 3.27: *AFM/MFM scans of VG06-002b(t_{nom}=62.8 nm) and VG06-002c(t_{nom}=31.4 nm). The lift height is 20 nm.*

The observed magnetic domain sizes are in average approximately 300 nm in sample VG06-002b, and 200 nm in sample VG06-002c which are quite long compared to the thicknesses of the films t_{real}=40 nm and 20 nm respectively. From the topography measurements the roughness of the surfaces are observed to ±3 nm for VG06-002b and ±1.5 nm for VG06-002c. Some nano sized structures are clearly seen on the topography graph for VG06-002b. The origin of these approximately 25 nm sized structures are at the moment not known. We expect it to be the signature of an oxidized surface layer, and the reason that it is not observed for sample VG06-002c is the differences in resolution.

Very recently AFM/MFM measurements on a Au capped thin film have been obtained. The pictures are shown in Figure 3.28.

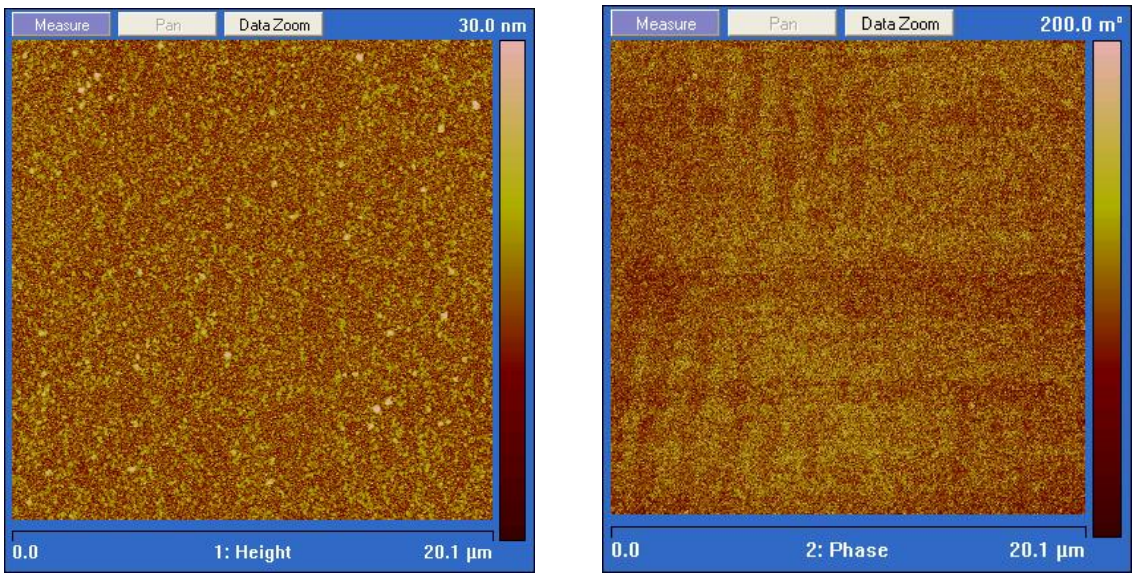

(a) Topography scan (AFM) (b) Magnetic domain scan (MFM)

Figure 3.28: *AFM/MFM scans of VG04-071(t_{nom}=20 nm) capped with 3 nm Au. The stoichiometry is estimated to $Co_{1.91}Mn_{1.1}Ga$. The lift height is 40 nm.*

Figure 3.28 (a) depicts the roughness of the film (±10 nm). Figure 3.28(b) exhibit a much more ordered magnetic behavior than observed in the case of VG06-002. We expect the nice ordered magnetic structure to be due to the Au cap preventing oxidization of the thin film. Further measurements on Au capped samples are needed to validate this.

3.5 Electrical properties

The electrical properties were investigated by conventional Hall-bar and transmission line measurements. The processing details used for fabricating Hall bars and TLM samples may be seen in Appendix F. The main idea of Hall-bar measurements was to compare the resistivity with bulk values e.g. to get information on a critical minimum thickness. The methods and the results are given in section 3.5.1. The purpose of the transmission line measurements was to measure the barrier resistance between the thin film and the substrate, and study this when changing growth parameters such as substrate barrier-type or thin film growth temperature. The methods and the results can be seen in section 3.5.2.

3.5.1 Hall bar measurements

The electrical properties of the thin films have been characterized by normal Hall bar techniques. Further description can be found in Appendix G. High applied magnetic field (12 T) measurements were done at Toshiba Research Laboratories, Cambridge. The purpose of the measurements was to obtain information on the general electrical properties such as resistivity and Hall behavior but also information on the critical thickness for conduction. A picture of a typical Hall bar is seen in Figure 3.29

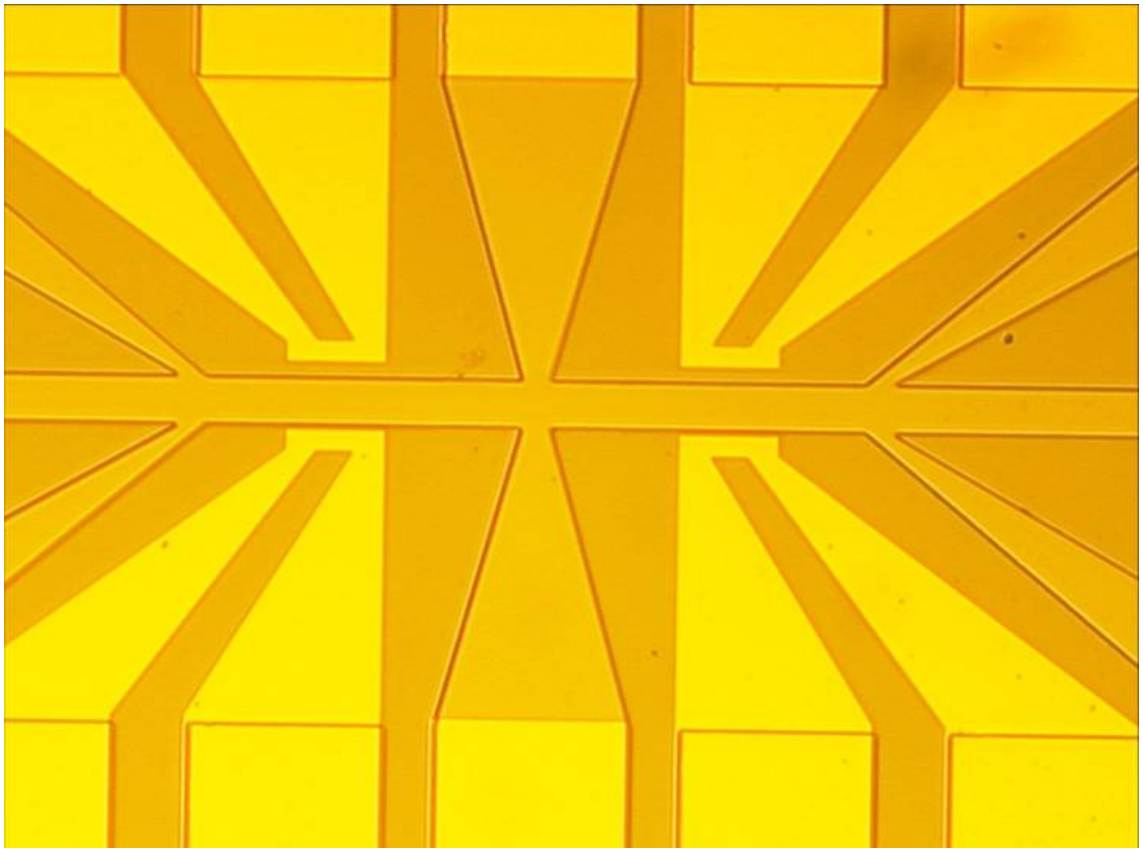

Figure 3.29: *Picture of a typical Hall bar. The mesa is* 50μ*m wide and 670* μ*m long.*

Three different samples have been characterized. Each sample has been grown with 4-5 different thickness. The details are seen in table 3.9.

Sample name	T_{growth}	Growth rate [nm/s]	Buffer layer	Substrate	Stoichiometry	Piece	$t_{nom}[nm]$	Comment
VG-05-070	300	0.00958	none	GaAs	Co2.06Mn0.95Ga1	A	23.2	Lost during processing
						B	11.6	Measured
						C	5.8	Measured
						D	2.9	Not measured
VG04-069	300	0.0118	none	n-GaAs	Co1.91Mn1.10Ga1	A	25	Measured
						B	15	Measured
						C	10	Measured
						D	15	Measured
Vg04-030	300	0.06	CoGa 5nm	n-GaAs	Co1.96Mn0.84Ga1	A	128	Measured
						B	64	Measured
						C	32	Measured
						D	16	Measured
						E	8	Measured

Table 3.9: *hall bar Sample details.*

The general measurement procedure for all samples are described by:

1. Temperature dependence [1.8 K;300 K]
2. R_{xx} and R_{xy} vs. applied perpendicular magnetic field [-8 T;8 T]
3. R_{xx} and R_{xy} vs. applied parallel magnetic field [-1 T;1 T]

Experimental details can by found in Appendix G. Figure 3.30 shows room temperature resistivity vs. film thickness. There seems to be a critical thickness around a nominal thickness of 10 nm. At larger thickness the resistivity seems to saturate at 350 $\mu\Omega$cm. Resistivity measurements on a bulk sample delivered by Goodfellow with correct stoichiometry show $\rho = 120 \pm 30$ $\mu\Omega$cm, while measurements on other Heusler thin films show $\rho \approx 90..160$ $\mu\Omega$cm [65, 67]. The enhanced resistivity in thin films could be due to structural defects induced by the strain from the substrate, contamination of the surface, or impurity defects.

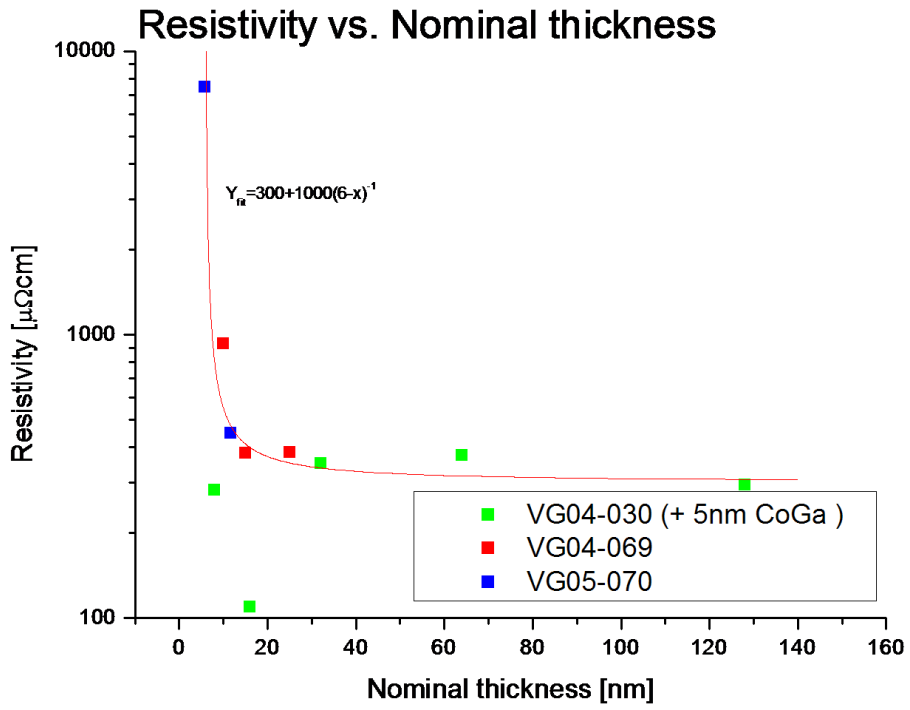

Figure 3.30: *Resistivity vs. nominal film thickness at room temperature*

When applying a magnetic field, perpendicular to the film plane the resistance dependence is highly nonlinear. In Figure 3.31 the Magneto Resistance (MR) R_{xx} and the Hall-resistance R_{xy} vs. magnetic field applied perpendicular to the film plane at low temperature T=1.8 K are shown. The thickness of the film is estimated to be 10.7 nm from a nominal thickness of 15 nm. The actual thickness of the conducting thin film is difficult to determine due to a natural oxide on the surface of the thin films.

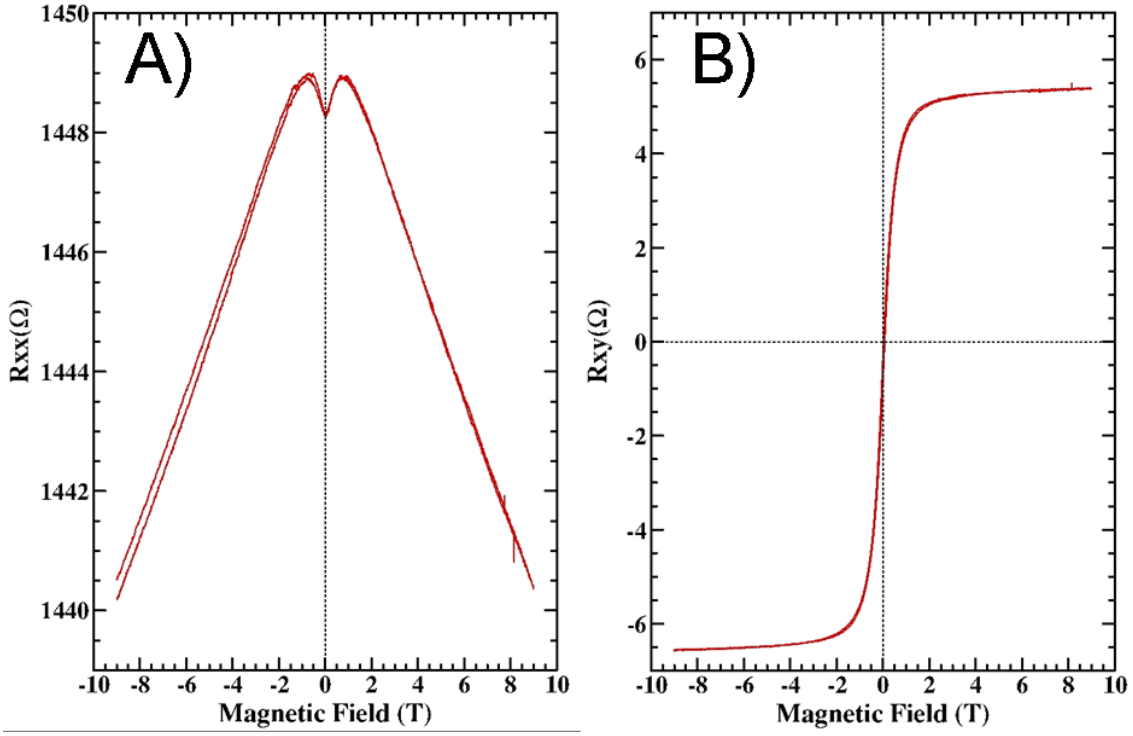

Figure 3.31: *Sample VG04-069b, t_{nom}=15 nm, T = 1.8 K: A) Magneto resistance vs. Applied magnetic field perpendicular to the film plane. B)Hall resistance vs. Applied magnetic field perpendicular to the film plane.*

Figure 3.31 A) shows a clear decrease in magneto resistance for $|B| > 2$ T. This corresponds to a negative MR ratio $MR = (R(B) - R(0))/R(B)$. At B =9 T the MR is approximately -0.6 %. The same dependence has been reported by Lund *et al.* [65] in Ni_2MnGe, Ni_2MnGa, and Ni_2MnAl thin films. They interpret that the effect is not related to spin effect but common to all Heusler systems. Negative MR ratios has also been observed in NiMnSb, and PtMnSb [97] but also in other systems such as CrO_2 [98, 99] and Fe_3O_4 [100]. The origin of this effect is unclear. At lower fields $|B| < 2$ T the MR ratio is positive. The process observed is similar to the in-plane AMR effect. The change in resistance is due to the hysteretic shift from an out-of-plane magnetization to an in-plane magnetization.

Figure 3.31 B) shows the Hall effect described by $\rho_{Hall} = \mu_0(R_0 B_\perp + R_S M_\perp)$ [101]. Here $R_0 = 1/(ne)$ is the ordinary Hall coefficient, and n is the carrier density. R_S is the anomalous Hall coefficient. Again $|B| = 2$ T determines a shift where the Hall effect goes from being dominated by the magnetization ($M_\perp$) to the applied magnetic field $B_\perp$. Figure 3.32 shows the temperature dependence on the resistivity and the sheet carrier density calculated from the ordinary Hall-constant. At low temperature a modest mobility of order $1 cm^2/Vs$ results.

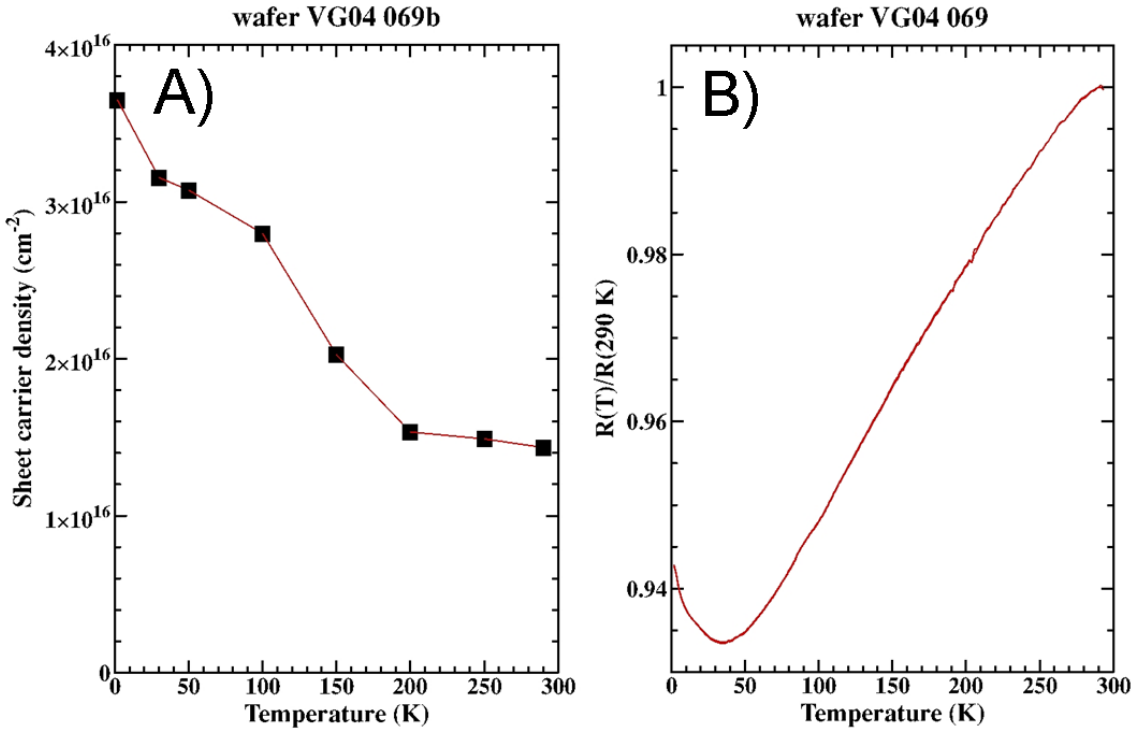

Figure 3.32: *Sample VG04-069b, t_{nom}=15 nm: A) Sheet carrier density vs. temperature. B) Normalized resistivity vs. temperature R(290 K)=390 $\mu\Omega$cm.*

The temperature dependence on resistivity is small. From RT to 40 K the dependence seems metallic from the fact that the resistance decreases for decreasing temperature. The resistivity below 40 K is increasing slightly with decreasing temperature suggesting some magnetic ordering effect such as e.g. Kondo-effect [102, 103].

By applying a magnetic field in the film plane, parallel and perpendicular to the current , a small Anisotropic Magneto Resistance (AMR) ratio has been measured to approximately 0.062 % (here defined as $AMR = (R_{\parallel} - R_{\perp})/R_{\perp}$). The measurements are shown in Figure 3.33.

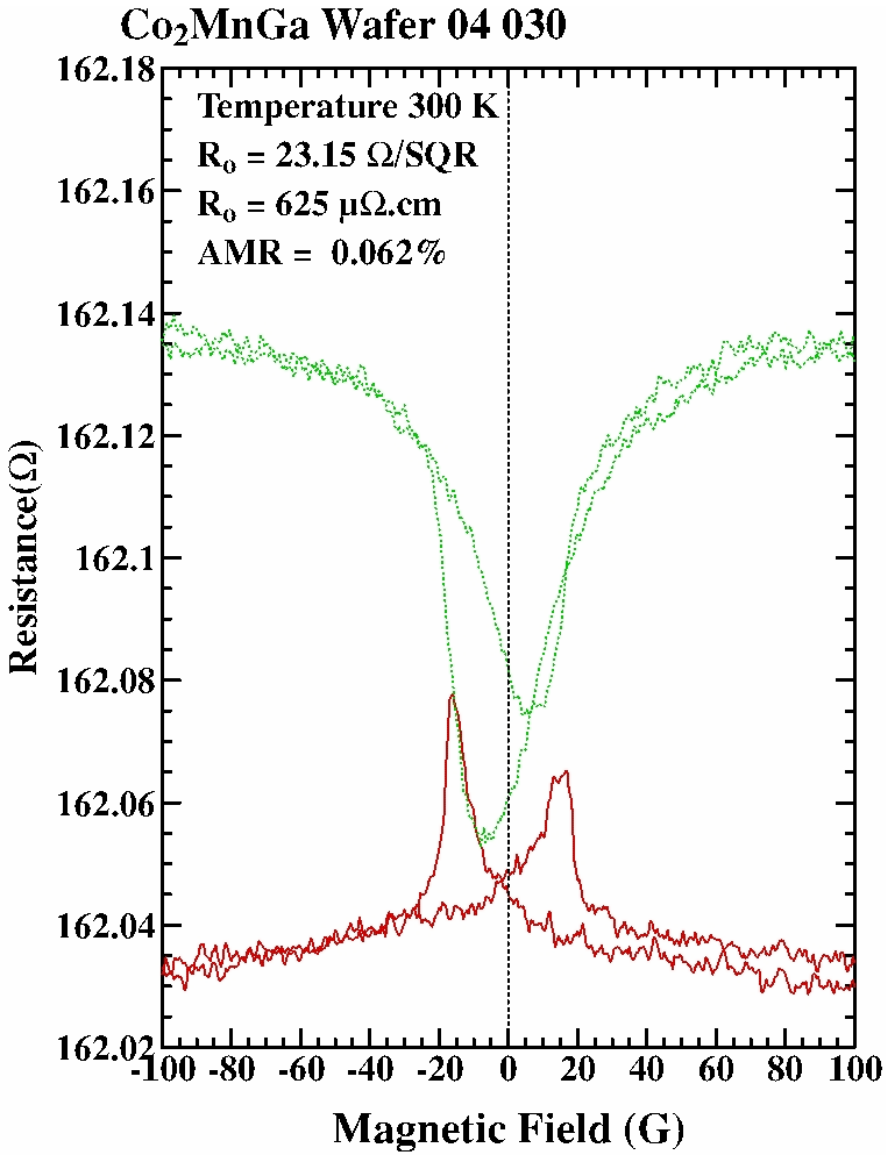

Figure 3.33: *Sample VG04-030a, t_{nom}=128 nm, T = 300 K: The green curve corresponds to a magnetic field in the film plane, parallel to the current direction, while the red curve corresponds to a magnetic field in the film plane, perpendicular to the current direction. The small AMR-ratio is measured to be 0.062 %.*

3.5.2 Transmission line measurements (TLM)

TLM devices have been used to determine typical contact resistances and conductance of mesas with different kinds of interface between the ferromagnetic thin-films and GaAs. The layout is sketched in Figure 3.34, which shows a top view of the mesa of approximate size 570×50 μm^2.

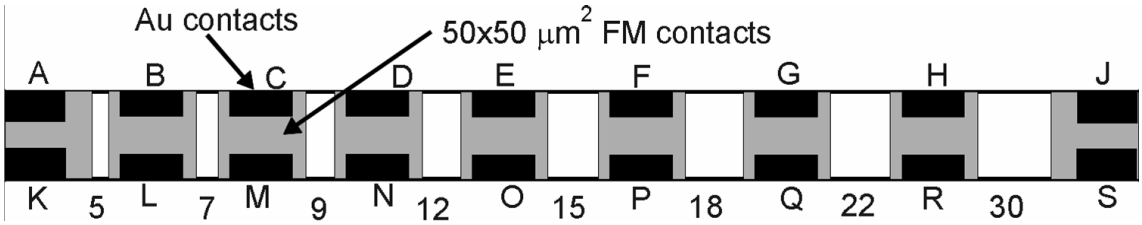

(a) The numbers shown are the lengths of the bare GaAs channel parts in μm

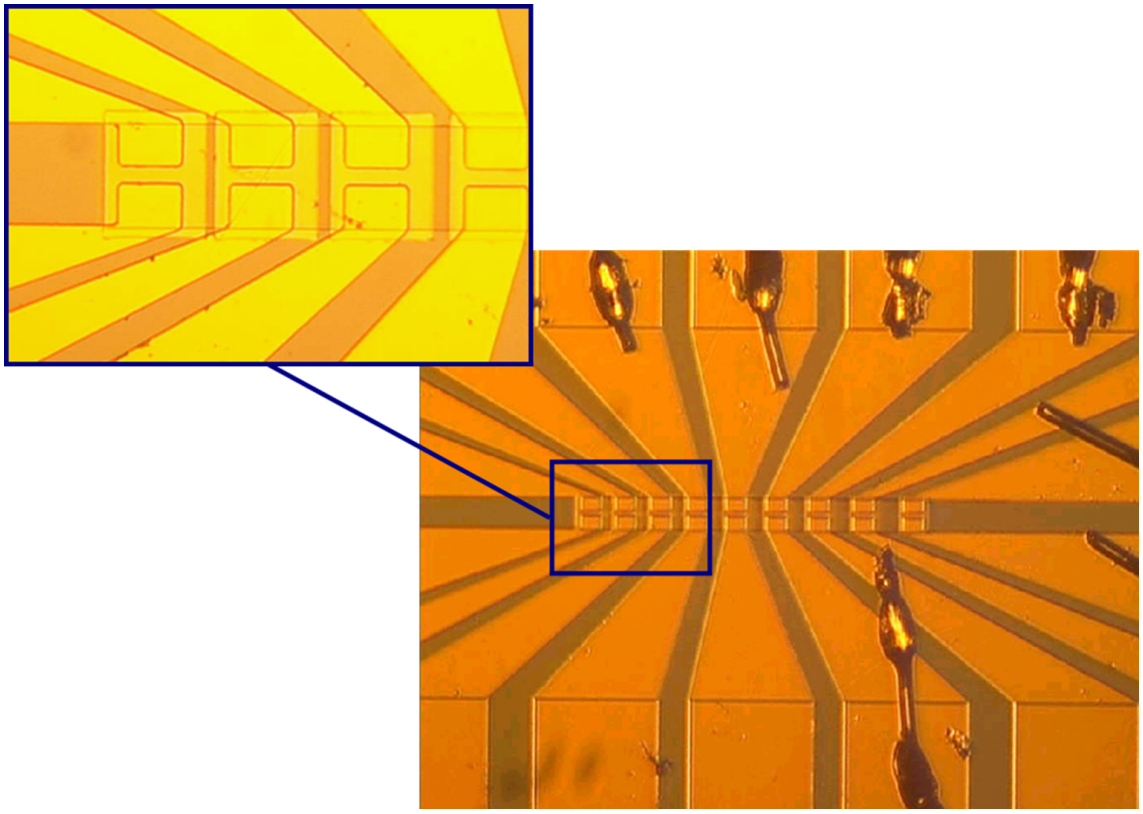

(b) Picture of a bonded TLM sample, made with an optical microscope

Figure 3.34: *Top view of TLM mesa.*

The principal purpose of the TLM is to separate the resistances of the contact islands and the bare GaAs channel. This is done by sending a current from e.g. A to J and measure the voltage drops between B and C, C and D, D and E, E and F, F and G, and G and H and plot the corresponding resistances versus the length of the bare GaAs (these lengths are given in μm in the sketch). The resistances consist of the series combination of a contact island and a piece of bare channel. Each of these contributions can in turn be considered parallel combinations of resistances corresponding to the various materials and various doping levels and/or quantum wells in the GaAs. Thus a quantitative comparison is not trivial. Rather a qualitative agreement can be taken as an indication that the sample is uniform and that the lithographic processing is of good quality.

As a single example Figure 3.35 shows a TLM plot for a device, where the ferromagnetic contacts consist of 35 nm Co_2MnGa on GaAs with a large near surface doping (δ-doping).

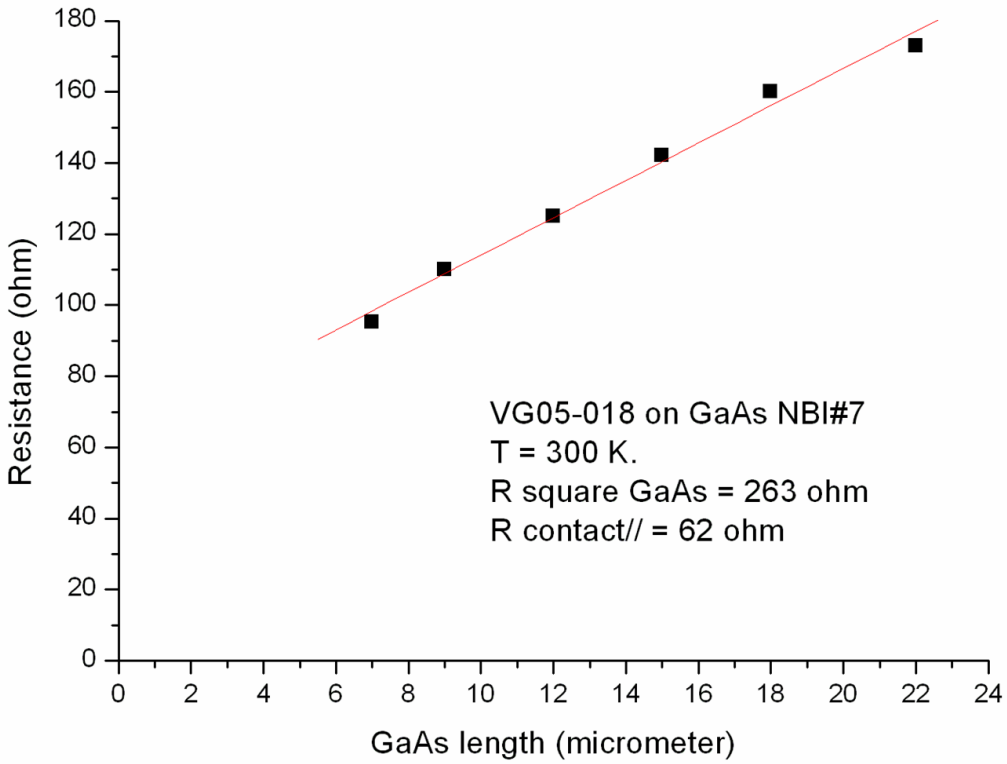

Figure 3.35: *Linear fit to TLM data for a selected sample. Derived resistances are given on the figure.*

In addition to the standard TLM fit, important information on the electrical contact perpendicular to the film plane may be obtained. A two probe measurement at e.g. B and L will give the interface resistance Au-FM plus some FM resistance, while two probe measurements like B and C involves the interface between FM and GaAs twice. A measuring arrangement where current is injected at A and taken out at C, while the potential is measured between B and C, allows the characterization of a single GaAs-FM interface, although to some (unknown) extent, the GaAs is included.

The two and three probe measurements have been performed on a large number of devices. A list of the measured values can be seen in Appendix G. The main conclusions are as follows:

1. The low current interface resistance in δ-doped GaAs-FM is typically 0.02-0.1 Ωmm^2 for Fe and Co contacts but is 2 orders of magnitude higher for the Heusler contacts

(Co_2MnGa). Correspondingly the IV-characteristics measured in a 3 probe configuration are nearly ohmic for Fe and Co, while some asymmetry is found for Heusler contacts (of order 10-30 % for 50 μA (J= 2A/cm^2)). In comparison contact resistances between a metal like Al and δ-doped GaAs have been reported to be as low as 10^{-4} Ωmm^2 [104] and in selected wafers even lower.

2. A number of TLM devices were fabricated using GaAs wafers with InGaAs quantum wells 100 to 300 nm below the surface. The wafers were mainly intended for spin-LEDs and had doping profiles corresponding to Schottky barriers at the surface. In these devices a large spread in interface resistances is found, but both for Fe and the Heusler alloy the low current value is of order 1 to several 100 Ωmm^2. Two devices with Heusler contacts were picked for measuring IV-characteristics. The data are shown in Figure 3.36.

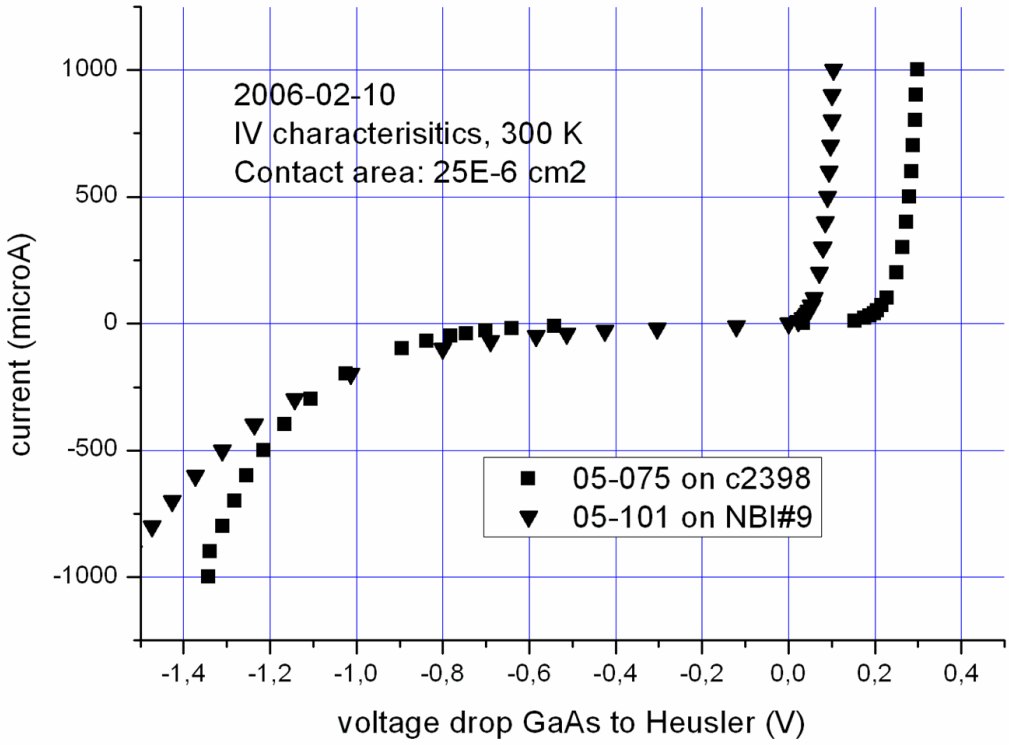

Figure 3.36: *Room temperature IV characteristics for TLM devices with Heusler alloy on wafers with quantum well and Schottky barrier.*

As may be expected the characteristics are much more asymmetric than for δ-doped GaAs, but the rectifying behavior looks more like arising from the p-n junction

around the quantum well than what would be expected for the Schottky barrier. Thus the current may to a large extent spread to the p-layer below the quantum well.

3. In all properly processed samples the resistance between Au and FM is found to be insignificant, as expected for metal to metal contacts.

3.6 Spin polarization measurements

Point Contact Andreev Reflection (PCAR) has been used as a method to measure the spin polarization P. The theory is described in section 1.3.1. PCAR related measurements can be seen in Appendix H. The section will end with a discussion of the measurements. Measurements shown here are made on VG04-015: $Co_2.4Mn_{1.6}Ga$(250 nm)/CoGa(5 nm)/GaAs film.

In order to find the spin polarization of the samples, a numerical fit of the data is done by using the model described by Equation 1.29 (see section 1.3.1). In order to check the technique, normal metal films were made of Au and Cu.

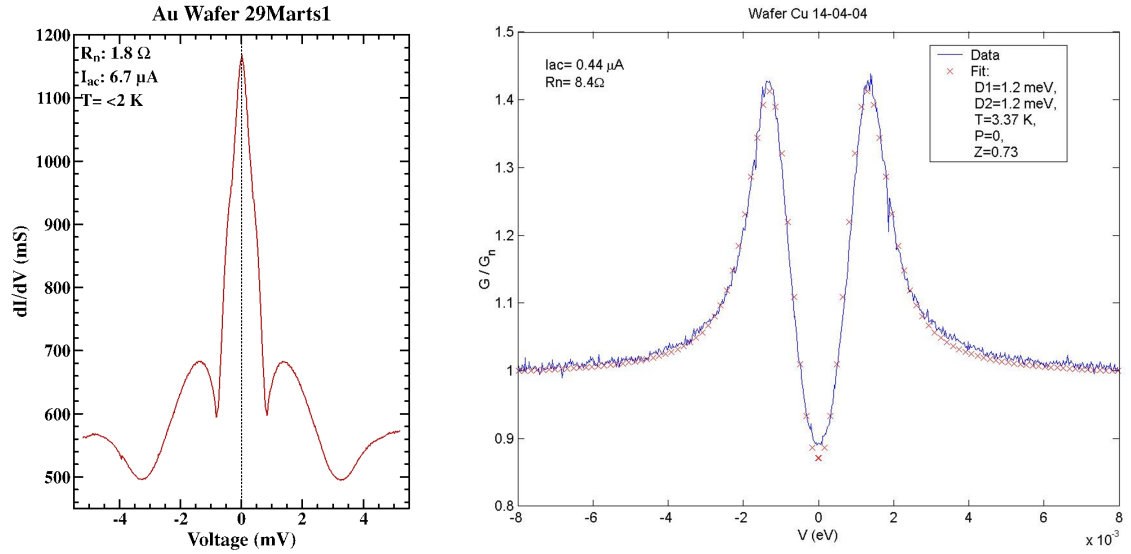

(a) Au (b) Cu

Figure 3.37: *PCAR measurements on a) Au(300 nm)/Ti(30 nm)/GaAs(substrate), and b) Cu(120 nm) /NiCr(5 nm)/GaAs(substrate), $T < 2$ K. The blue line is the data and the red cross are the fit using Equation 1.29 as the model.*

The measurements on Au could not be fitted (Figure 3.37 a) due to the strange structures around $V = 1.5$ mV $- 4.5$ mV. But still a factor of approximately two is seen between G_N at $V > |5$ mV$|$ and $G(0)$ as predicted in Equation (1.27). By using Equation (1.27) the spin polarization of the Au-film is found to be $P \approx 0$ %. Measurements on

Cu could be fitted. The fitting parameters seem realistic. The two superconducting gap parameters are very close, implying that the proximity effect in this system is low. This time the factor of two is missing. The reason is the nonzero interface parameter Z. The fitted temperature seems quite high. The measurements were done below 2 K and still the fitting temperature is 3.37 K. This was a problem which appeared constntly during the measurements. After finishing the measurements on Co_2MnGa, the error was found and corrected by changing how the sample was thermally anchored to the surroundings. Next step was to measure a ferromagnetic film with a generally known spin polarization. We chose Co. Figure 3.38 show measurements on a 250 nm Co-film.

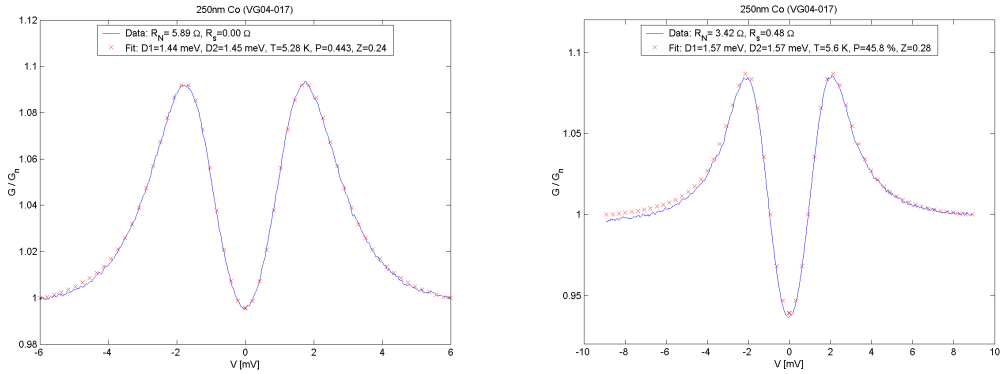

(a) First achieved contact

(b) Second achieved contact

Figure 3.38: *Two different measurements on a Co(250 nm)/GaAs(substrate) at T = 4 K. The left data were taken first.*

The two measurements in Figure 3.38 are made during the same cool down. The data to the left was taken first. None of the fitting parameters change much except the resistance at $V >> \triangle$, R_N, and the resistance in series with the contact. The reason could be that we, due to plastic deformation of the needle, are out of the Sharvin limit (Sharvin limit: the radius of the point contact is less than the mean free path [105]) and therefore measures more than just interface-effects. The spin polarization measured (P=44-46 %) is in good agreement with earlier measurements [45, 48].

Measurements on a Heusler film is seen in Figure 3.39.

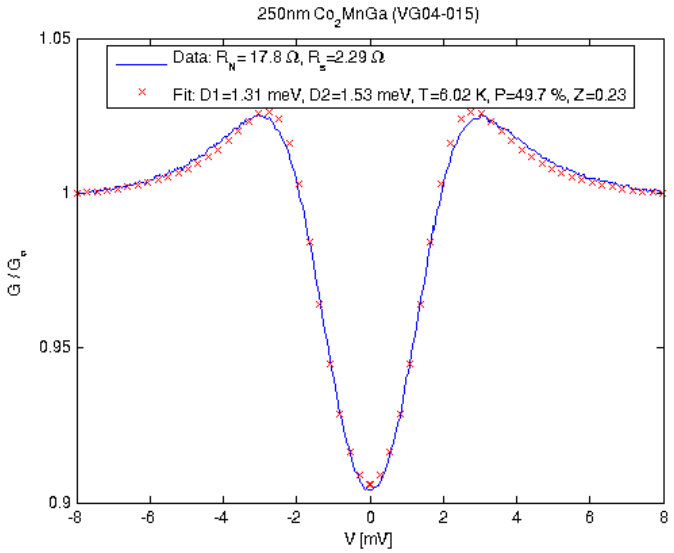

(a)

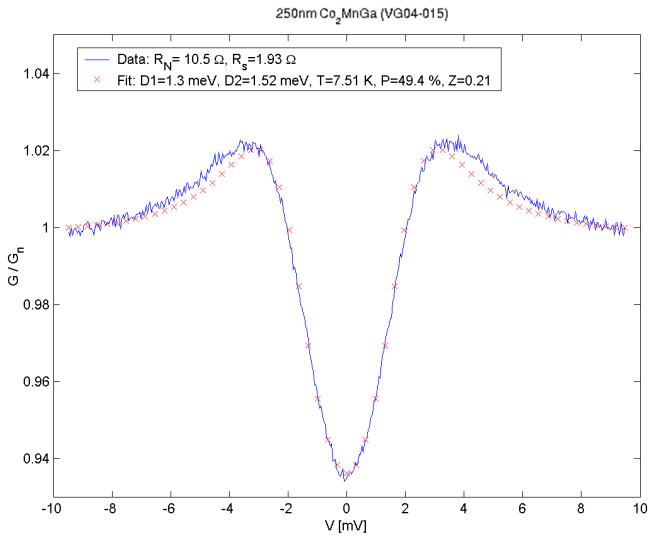

(b)

Figure 3.39: *Two measurements on VG04-015 $Co_2.4Mn_{1.6}Ga$(250 nm)/CoGa(5 nm)/GaAs. Both measurements are done at $T = 4$ K.*

The spin polarization is fitted to $P = 49.7$ % and $P = 49.4$ %.

3.6.1 Discussion on PCAR results

Looking at the statistics of general PCAR-measurements ~50 % is often the result [45]. The reason is probably that the technique does not measure the bulk spin polarization P, but

some surface-polarization instead, which most likely can have a reduced value. However, the measured magnitude is in good agreement with the calculations done in Chapter 2. The bulk spin polarization was calculated to 63 %, and from theoretical stoichiometry variations we saw that especially Co and Mn defects could rapidly decrease the spin polarization.

The quantity we really want to know is the spin polarization measured at the interface with the semiconductor. The best technique to actually do this are spinLED-measurements in either Faraday or Hanle geometry as described later, with reference measurements on injector materials with a known spin polarization such as e.g. Fe or Co.

3.7 Other considered devices

Several devices have been considered and tried out at different levels. The first choice of device was the Tedrow-Meservey SC-I-F junction to reveal information on the spin polarization P at the interface with an insulator and to practice growth of Heusler hetero-junctions. The recipe is seen in Appendix I. None of the devices seemed to work properly. Some of the measurements can be seen in Figure 3.40:

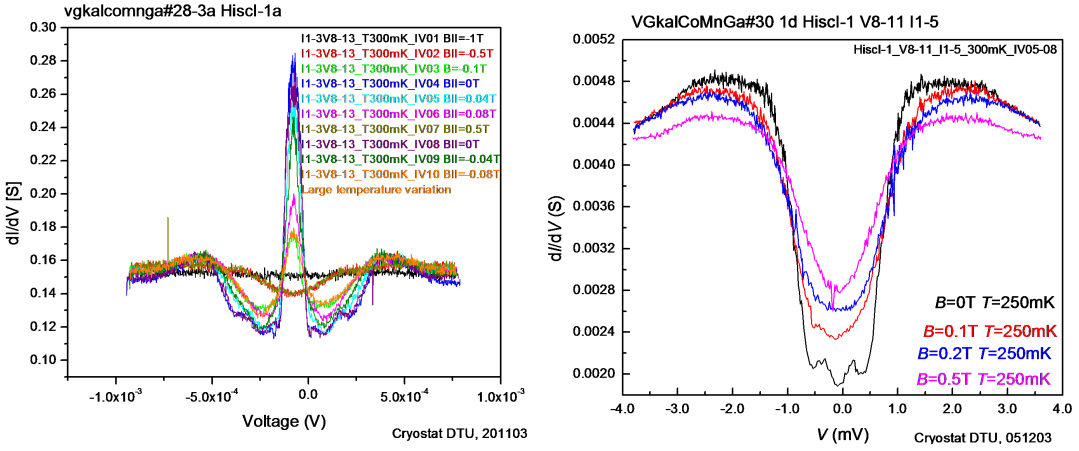

(a) (b)

Figure 3.40: *Measurements on Al/AlOx/Co_2MnGa at* T = 400 mK.

Clearly magnetic and bias dependencies are seen. But the data cannot be explained by the model described in section 1.3.1. The measurements look more like the expected dependency of a point contact, even though some of the expected features are seen in Figure 3.40 b). We explain the results by poor quality of the oxide layer. In this type of junction the oxide layer needs to be of high quality without any pin-holes. This is normally done by following procedure:

1. Growth of an epitaxial thin film of Al (2-4 nm)
2. 2-3 repetitions of 1 nm Al growth followed by complete oxidation

3. Growth of ferromagnetic thin film

To ensure a good single crystal Heusler film, we chose to begin with Heusler-growth and end up with Al deposition. The chosen Heusler thickness was 100 nm. We suspect the surface of a 100 nm Heusler film to be rather rough, which clearly decreases the quality of the Al_xO_y layer. Tedrow-Meservey reports [41] a low yield of reasonably good tunnel junctions on less than 5 % when producing devices as described above.

After realizing this we have tried to make devices with Co_2MnGa grown on Al_xO_y. The recipe can be seen in Appendix I. We have not yet obtained any data on these devices.

The next considered device was "Non-local measurements of spin injection à la Jedema *et al.* [106]". The measured effect in this type of device is a traditional GMR-effect, but measured with voltage-probes in a controlled distance, away from the path of the spin polarized current. This is an approach to measure not only the spin injection but also the spin lifetime in the selected spin transport layer. The lithography process relies on a well-controlled sub-micrometer technique, such as SEM-lithography. The development of the device was stopped even before test measurements were made due to very time consuming optimization of processing. A further description of the problems encountered can be seen in Appendix J.

Chapter 4

Spin Light Emitting Diodes (spinLEDs): Experimental

Our goal was to explore spinLEDs as a tool to investigate the spin injection from Co_2MnGa thin films, and furthermore optimize the spin injection by varying growth parameters. This chapter describes the fabrication of spinLEDs, and the experimental set-up used for characterizing spinLEDs. Furthermore we wanted to analyze the spinLEDs in both Hanle and Faraday geometry, but due to lack of time only Hanle geometry has been used. We are still working on the Faraday setup.

4.1 Device structure

Three different p-i-n structures with incorporated QWs in the intrinsic region have been designed and tested with Au, Fe and Co_2MnGa thin films as injectors. Contrary to other published work based on GaAs/AlGaAs QWs [21, 35, 107, 108, 109] or bulk GaAs intrinsic region [20, 36] , our structures are based on InGaAs/GaAs QWs like [110, 111]. We chose the $In_xGa_{1-x}As$/GaAs QWs for the following reasons:

1. The system is highly useful for g-factor engineering applications. g=-0.44..-15 for x=0..1.

2. InGaAs forms a strained layer on GaAs, which forms optimum growth conditions for self-assembled InAs quantum dots (QDs), for future spin light emitting diodes based on QDs. The radiative life time is expected to be shorter than in QWs, due to the 3D carrier confinement. Recently Itskos *et al.* has reported studies on QD SpinLEDs [23].

3. If the D'yakonov-Perel' mechanism is dominant, the lower mobility in InGaAs compared to GaAs should result in a longer spin lifetime.

There are several challenges in designing an efficient p-i-n heterostructure for detection of spin injection. The first challenge is to establish a Schottky barrier with reasonable

height and width, to ensure that injection by tunneling dominates (see section 1.3.2). The second challenge is to make sure the electrons move to the quantum well experiencing as few spin scattering events as possible.

The structures are described in detail in Appendix K. For comparison the growth parameters are shown in Table 4.1.

Layer	Material	Thickness [nm]	Dopant	Density [cm^{-3}]	Comment
C2294					
0	GaAs (100)	4E5			Substrate
1	GaAs	500	Be	1.00E18	Nominal doping level
2	GaAs	500			
3	InGaAs	5			20 % In
4	GaAs	200			
5	GaAs	100	Si	1.00E18	
6	AlGaAs	15	Si	1.00E18	x=0.33 alloying Schottky barrier
7	AlGaAs	15	Si	3.33E18	x=0.33 alloying Schottky barrier
8	GaAs	1			Nominal GaAs interrupt before As cap
9	As				Cap
C2398					
0	GaAs (100)	4E5	Be	1E18	Substrate
1	GaAs	500	Be	1.00E18	Nominal doping level
2	GaAs	100			
3	InGaAs	10			20 % In
4	GaAs	100			
5	InGaAs	5			20 % In
6	GaAs	50			
7	GaAs	50	Si	1.00E18	
8	AlGaAs	15	Si	1.00E18	x=0.33 alloying Schottky barrier
9	AlGaAs	15	Si	5.00E18	x=0.33 alloying Schottky barrier
10	GaAs	1			Nominal GaAs interrupt before As cap
11	As				Cap
NBI 9					
0	GaAs (100)	4E5	Zn	1E19	Substrate
1	GaAs	1000	Be	1E18	Nominal doping level
2	GaAs	150			
3	InGaAs	10			17.8 % In
4	GaAs	40			
5	GaAs	200	Si	1.00E17	
6	GaAs	15	Si	1.00E17-5.00E18	Schottky barrier graded doping
7	GaAs	15	Si	5.00E18	Schottky barrier
8	As	~2E3			Cap

Table 4.1: *List of growth parameters for the three different spinLED-substrates.*

Two structures (C2294 and C2398) have been designed and grown at the Cavendish Laboratory Cambridge, and one (NBI#9) has been designed and grown at Niels Bohr Institute (NBI) Copenhagen. All structures were in situ capped with amorphous As to prevent surface oxidation during transport between growth chambers. The main difference between the heterostructures is the design of the schottky barrier. The Cavendish wafers are based on a highly doped AlGaAs barrier while the NBI structure is based on a graded doping of GaAs. Band diagram calculations in case of C2294 and NBI#9 are shown in Figure 4.1

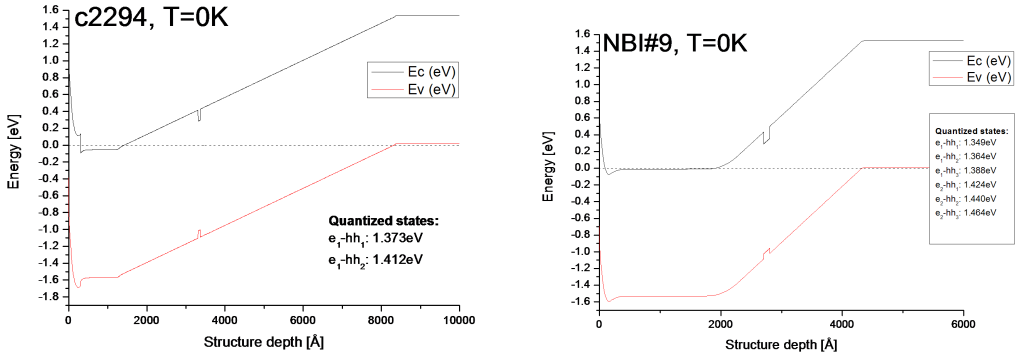

(a) C2294 (b) NBI#9

Figure 4.1: *Band diagram calculations in case of C2294 and NBI#9. The inserts show calculated recombination energies.*

Estimates of the radiative lifetime τ in the QW have been made by time resolved photoluminescence spectroscopy measured on reference samples (c2475 and NBI#119) without barrier and doping profiles. Reference samples without barrier and doping profiles were used in order to maximize the photoluminescence signal. Figure 4.2 shows the time-resolved photoluminescence measurements.

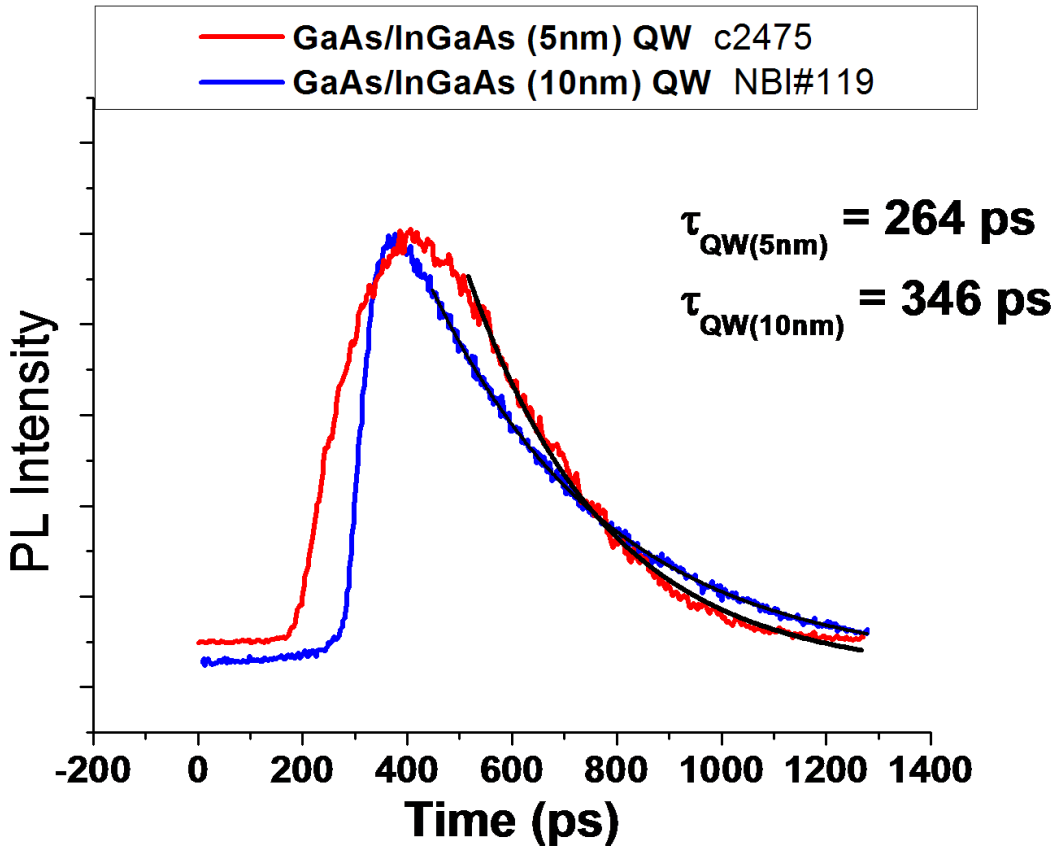

Figure 4.2: *Time-resolved photoluminescence measurements at T=5 K. The samples are reference samples, without barrier and doping in the cladding layers, as the only difference to the spinLED structures.*

Very similar results obtained at low temperature have been reported by Haiping *et al.* [112]. Neither the temperature dependence nor the magnetic field dependence of the radiative lifetimes have been measured due to lack of time.

4.2 Device fabrication

We focused on a quick and reproducible processing method. Figure 4.3 shows the process schematically:

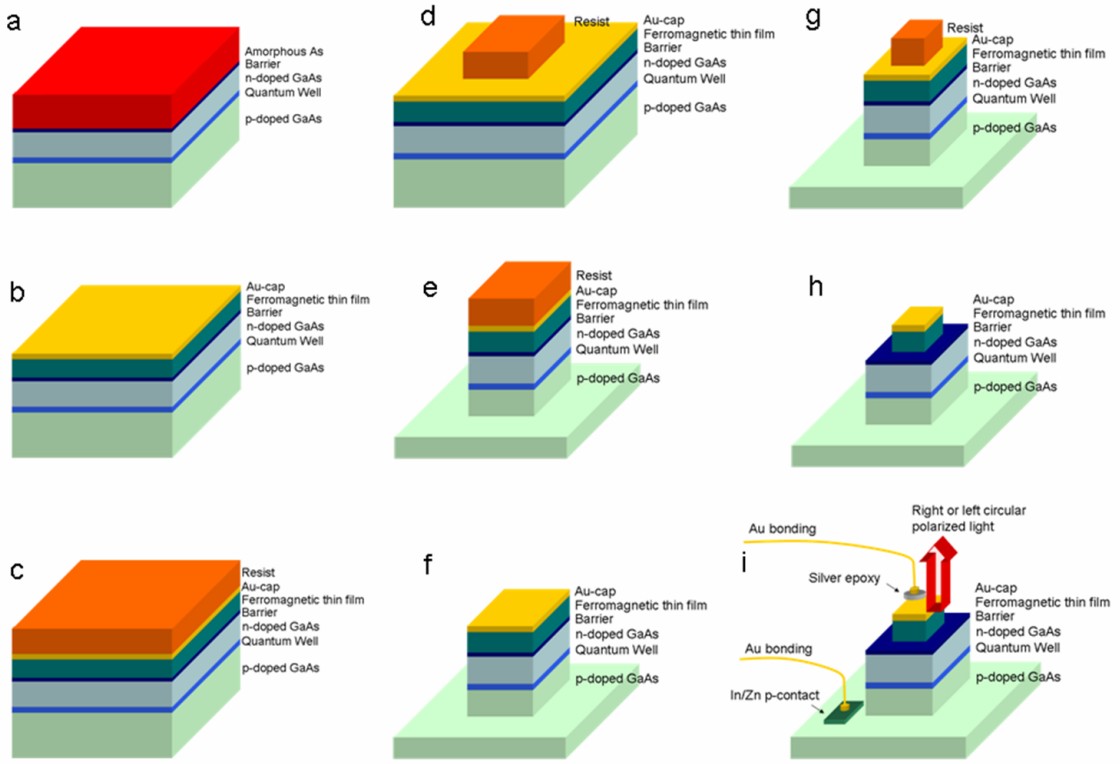

Figure 4.3: *Device processing drawn schematically. The semiconductor mesa is* 500μm *on each side and the contact mesa is* 240μm *on each side.*

Figure 4.3 (a) illustrates the p-i-n structure after growth. After As-desorption as described in Appendix C a Ga-rich surface is obtained. 10 nm of Co_2MnGa capped with 2 nm Au is grown (Figure 4.3 (b)). Resist is spun on (Figure 4.3 (c)) and a mesa (500 μm $\times$ 500 μm) is defined with UV-lithography techniques (Figure 4.3 (d)). The mesa etch is made with a low voltage ion gun. The etch rate is approximately 1.8 nm/s. The etch is stopped when the p-doped layer is reached (Figure 4.3 (e)). After removing the excess resist (Figure 4.3 (f)), early devices were bonded after this process step. Later devices were processed further by defining a new mesa 240 μm on each side in resist on top of the first mesa (Figure 4.3 g). Again an etch is performed. This time the etch is stopped just after the Co_2MnGa layer (Figure 4.3 h). The reason for the second mesa is to increase the amount of surface emitted light. By this approach we expect most of the detected light to be emitted from the edge of the second mesa. The amount of detected light did increase after this process step. The bonding procedure was performed at the Cavendish cleanroom. The P-contact was established by a piece of In/Zn foil annealed at 180 °C for 10 minutes. To contact the thin Au layer on the top of the 240 μm mesa a small amount of silver epoxy was placed in a corner of the mesa using of a probe-tip baked at 150 °C for 45 minutes. By normal bonding techniques Au-wires was bonded to the silver epoxy and the In/Zn foil to establish electrical contacts to top and bottom of the device. A typical

IV-curve can be seen in figures 4.4 and 4.5.

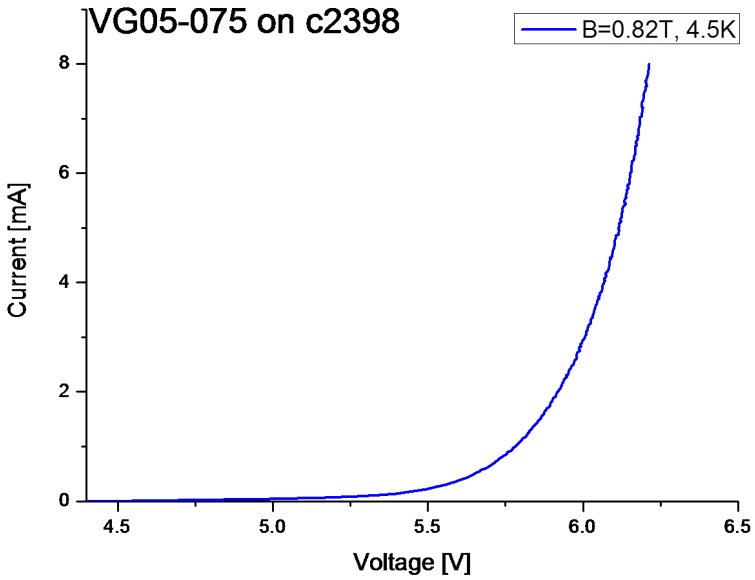

Figure 4.4: *Typical IV-curves of the spinLED devices at 4.5 K: Two point measurements of the devices.*

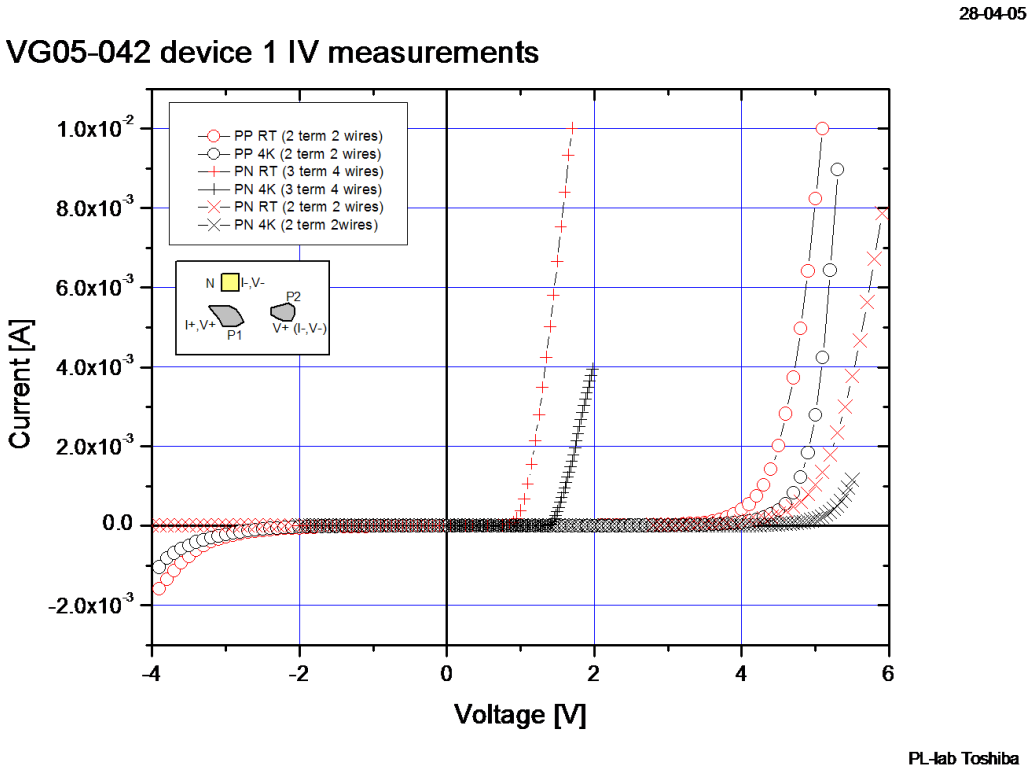

Figure 4.5: *NBI#9:IV curve of VG05-042 (Co_2MnGa on NBI#9) at 300 K and 4 K: By two point probe technique the I-V dependence has been measured on two P-contacts (∘). By 3-points measurements the p-contacts have been neglected, revealing the IV-dependence of the n-contact in series with the Schottky-diode and the p-i-n-diode (+).*

4.3 Electrical setup

The p-i-n devices are operated by biasing the P-region positively. In semiconductor terms the p-i-n device is forward biased, while the Schottky diode at the interface is reversed biased. The device is probed by 2 or 3 wires. Four point probe techniques have not been possible due to limited free area on the top contact. I-V measurements of two typical P-contacts in series are shown by (∘) in Figure 4.5. The complete structure opens up at voltages around 4-6 V. Due to the unknown contribution from the n-contact and the Schottky-barrier, we do not know what bias this corresponds to over the p-i-n diode itself. From the data shown in Figure 4.5 it is seen that the the main diode-contribution comes from the p-contact. By 3-points measurements the p-contacts have been neglected, revealing the IV-dependence of the n-contact in series with the Schottky-diode and the p-i-n-diode. The structure opens up around 1V and 1.5V for T=300 K and T=4 K, respectively.

4.4 Optical setup

Two different techniques have been used. A "manual" setup where the intensity of right and left circularly polarized light is measured individually by manually rotating a linear polarizer ±45 ° relative to the fast axis of a quarter-wave plate. The emitted light is detected normal to the sample plane.

Figure 4.6 schematically shows the setup.

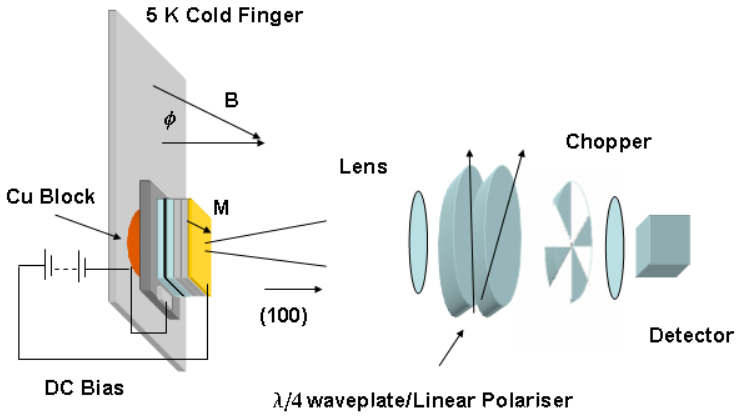

Figure 4.6: *Schematic representation of the "manual" setup*

The other "automatic" setup is automatically able to shift between detection of right and left circular polarized light by use of a variable wave retarder adding or subtracting a phase shift of 90° followed by a linear polarizer with fixed vertical polarization angle. See Appendix L for more information about the calibration of the variable wave retarder. The setup can schematically be seen in Figure 4.7. In Appendix L.2 Jones calculus have been used to verify the setups for measuring circular polarized light. By use of a lock-in amplifier locked to the frequency of the wave retarder($f1$ = 2Hz, maximum frequency) the difference between right and left circular polarized light can be measured as one quantity. The integration time was chosen to 3 s. Half of the magnitude of the total intensity was measured by use of another lock-in amplifier locked to a chopper-frequency ($f2$ = 200Hz). The integration time was chosen to 3 s.

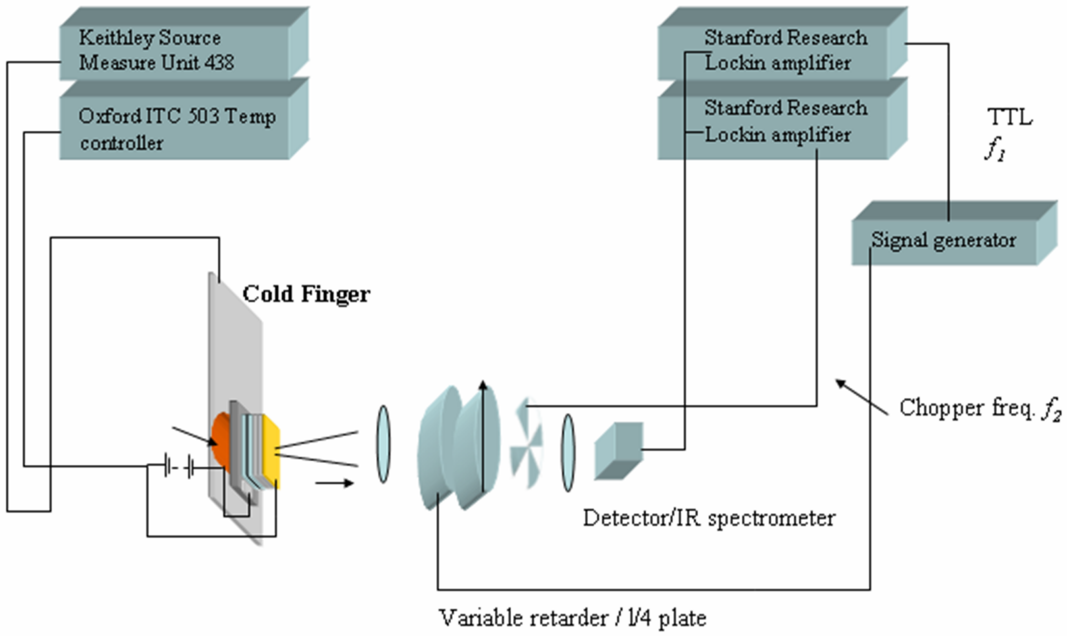

Figure 4.7: *Schematic representation of automated setup, with the variable retarder plate.*

In both setups the intensities are measured with either a Thorlabs DET-110 Si-photodetector (0.6 A/W at λ =900 nm) or a Bruker Optics Equinox 55 Fourier Transform Infrared Spectrometer(FTIR) based on a Michelson-Morley interferometer system. The latter device is able to spectrally resolve the emitted light.

4.5 Magnetic setup

The magnetic field was applied with a water-cooled electromagnet. The maximum applied magnetic field was 0.82 T. The magnetic poles were positioned approximately 15 cm apart to enable enough space for the cryostat and a Hanle angle $\varphi = 60\,^{\circ}$. If a Hanle angle of $\varphi = 45\,^{\circ}$ was to be used, the maximum magnetic field would be approximate 0.5 T. The default sweep rate was around 0.01 T/s.

4.6 Cryogenic setup

The samples were cooled using a continuous flow cryostat (nitrogen or helium, Oxford Instruments). The sample was attached to a cold finger. To ensure optimum cooling the chip carriers were equipped with a copper cylinder providing a thermal link between sample and cold finger. However, the samples were exposed to 300 K radiation through the window.

Data acquisition was made by a routine written in Labview. Figure 4.8 shows pictures of the setup.

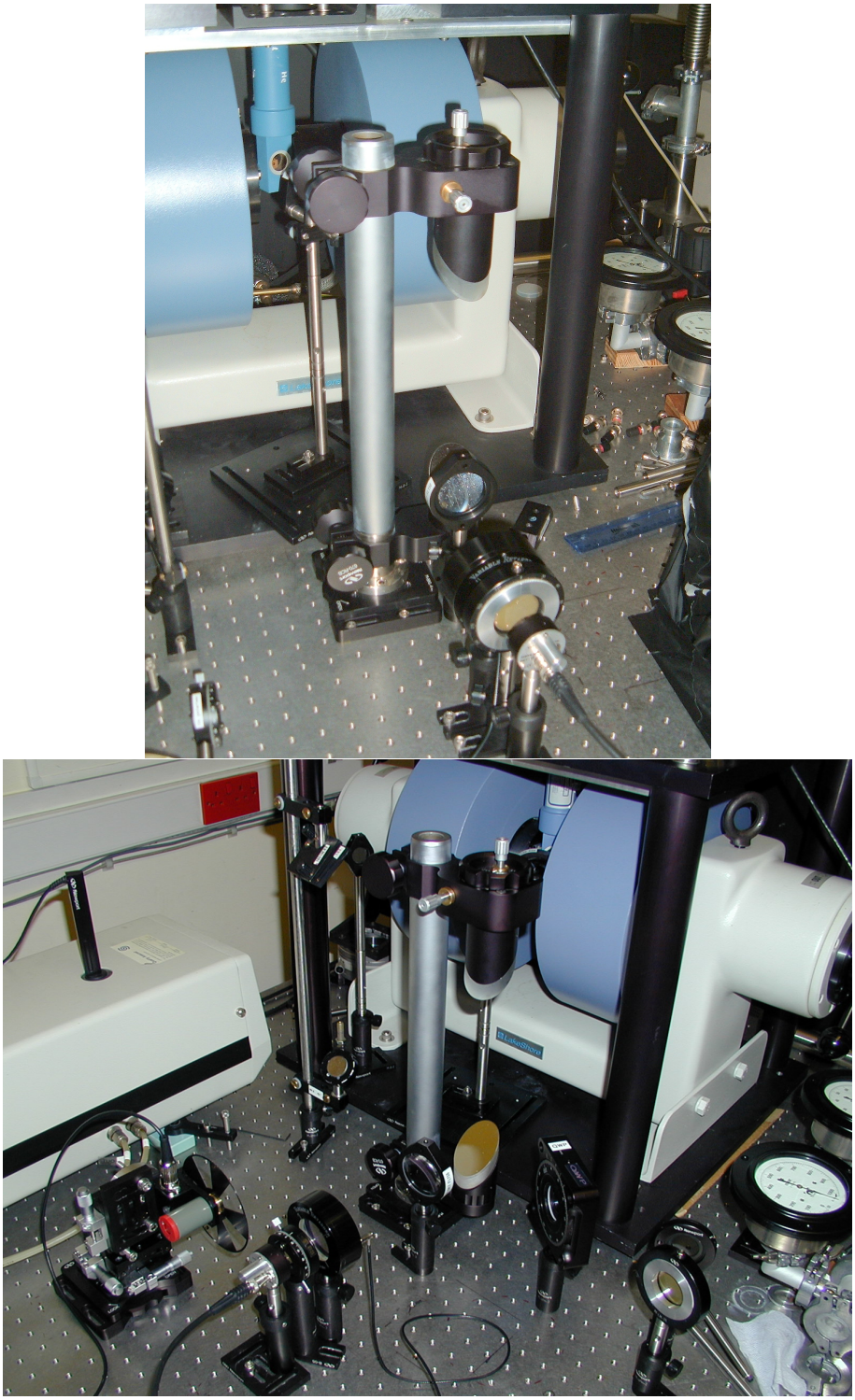

Figure 4.8: *Pictures of the setup used for Hanle geometry measurements.*

Chapter 5

SpinLED measurements

In the following chapter the obtained spinLED results will be presented. Fe SpinLEDs have been used as reference to compare with Co_2MnGa spinLEDS.

Table 5.1 shows an overview of the characterized samples together with an estimate of the stoichiometry.

Injector type	Co2MnGa(10 nm):CoGa(2 nm)	Co2MnGa(10 nm)			Fe(5 nm)		Au(5 nm)
Growth number ⟶	VG04-002	VG04-013	VG05-064	VG05-075	M53	VG05-048	Au:C2294
Wafer ↓: C2294	x	x			x		x
C2398			x	x		x	
NBI#9			x	x		x	
Stoichiometry	Co(2.4)Mn(1.6)Ga(1)	Co(2.16)Mn(1)Ga(1)	Co(2.25)Mn(1.02)Ga(1)	Co(1.97)Mn(1.03)Ga(1)	Fe	Fe	Au

Table 5.1: *Overview of the measured samples shown in this chapter.*

5.1 Electroluminescence spectra

The expected emission energy of the $In_xGa_{1-x}As/GaAs$ QW has been calculated by use of a 1d Poisson/Scrödinger solver made by G. Snider [113]. Further details can be found in Appendix M. The calculations were reproduced by a web-solution offered by the Ioffe institute [114]. Figure 5.1 shows the emitted light as a function of energy for all three spinLED structures. The lines show the calculated e_1-hh_1 (lowest energy) recombinations.

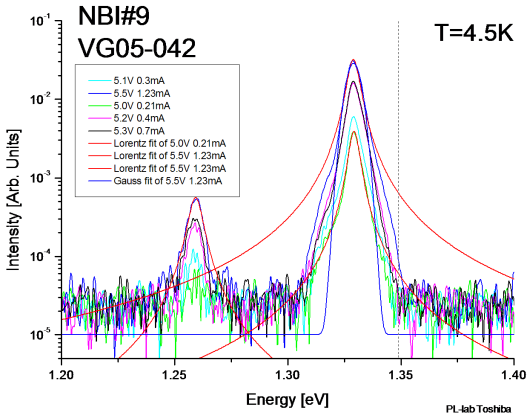

(a) Energy spectra of light emitted from NBI#9. At T=4.5 K peaks are observed E=1.329 eV and E=1.259 eV.

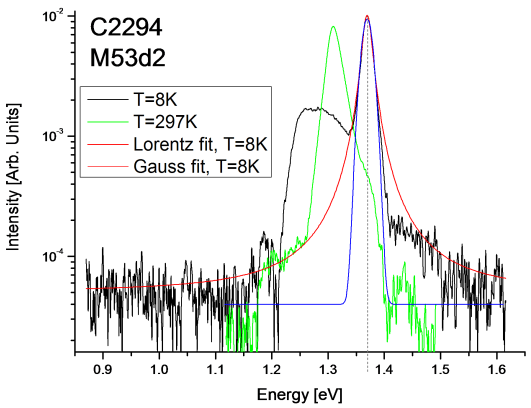

(b) Energy spectra of light emitted from C2294. At T=4 K, the main peak is observed at E=1.370 eV

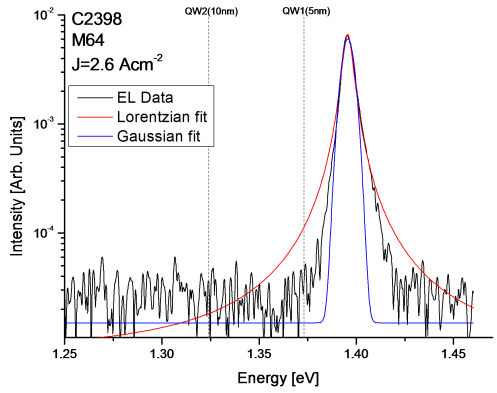

(c) Energy spectra of light emitted from C2398. At T=4 K, the main peak is observed at E=1.396 eV

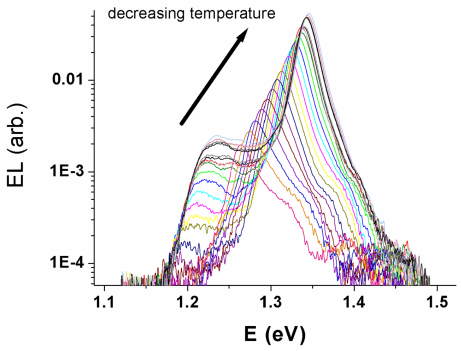

(d) C2294-spectra, J=3 Acm^{-2}: Temperature variation from 5 K to 300 K

Figure 5.1: *Detected intensity of the far-infrared emitted light as a function of energy for the spinLED structures. The lines show the calculate energy of e_1-hh_1 recombinations.*

The emission peaks are narrower at lower temperatures as a result of suppression of electron-phonon scattering. Below 80 K the emission arises mainly from the e_1-hh_1 recombination. Lorentz and Gauss fits have been made for the low temperature spectra. In

all cases the line width is best described by some intermediate distribution. A theoretical study of the line shape is given by T. Ohtoshi in [115]. The faster decay than described by a Lorentzian is due to so-called non-Markovian relaxation processes. The FWHM of C2398 and NBI#9 are 6meV, while C2294 is 20 meV.
The small peak at E=1.259 eV in NBI#9, seems to appear from the noise level at biases above 5.0V. We expect this to be due to a defect band with energies just below the InGaAs bandgap. Similar behavior is reported by Haiping *et al.* [112, 116], with approximate the same energy difference. Haiping *et al.* explain the splitting by Indium segregation in the QW.
The reason for the rather wide line width of C2294 is not fully understood. The same is the case for the rather large shoulder observed around 1.3 eV. Indium segregation could be the case even though the observed energy difference between the shoulder peak and the main peak seems a bit too large (approximate a factor of two). The observed behavior could also be explained by inhomogeneities in the QW thickness. Measurements on other pieces of the wafer show some deviation in the observed main peak position, and the magnitude of the shoulder peak, indicating that the wafer is not homogeneous. The observed shoulder seem to increase when decreasing the temperature. Figure 5.1 illustrates this.

Only one peak is observed in the energy spectra of C2398, even though there are two QWs in the structure. From comparison with the calculations we expect the emitted light to come from the 5 nm QW. We have no explanation to why we do not see emitted light other than at that bias it seems like all recombination happens in the 5 nm QW. We do expect to see emitted light from the 10 nm QW at higher biases. We realized this after the measurements were finished, and therefore it has not been done.

The small differences in calculated and measured energies can be explained by uncertainty in thickness and doping-concentration. For example calculations of e_1-hh_1 in a 10 nm $In_{0.195}Ga_{0.805}As$ QW would give the energy observed in case of NBI#9 and, a 5 nm $In_{0.18}Ga_{0.82}As$ QW would give the energy observed in case of C2398.

5.2 Spin injection with Fe as injector material

Our first attempt to inject electron spins were made with Fe as an injector. As a reference a device was made with Au as an injector. The electroluminescence spectra for both devices for each helicity of circularly polarized light are shown in Figure 5.2.

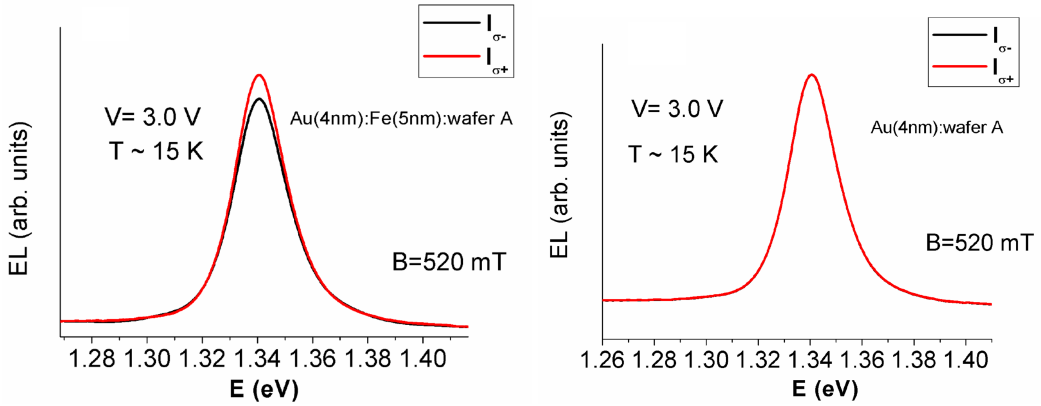

(a) M53: Au(4 nm):Fe(5 nm):C2294 (b) Au(4 nm):C2294

Figure 5.2: *Electroluminescence spectra for spinLEDs with Fe and Au as injectors. The temperature is T=15 K, the current density is J=3 Acm^{-2}, and the Hanle angle is φ = 60 °.*

The B-field variation of P_{EL}, the difference between right and left circularly polarized light for the Fe-device is shown in Figure 5.3

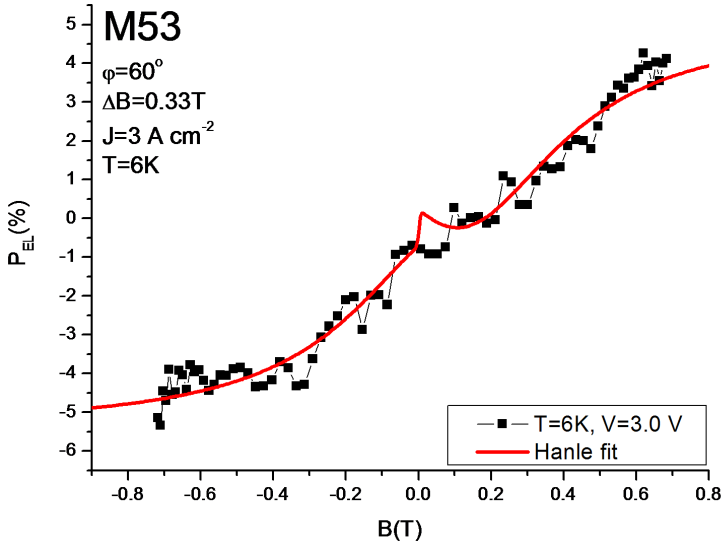

Figure 5.3: *M53 on C2294: Optical polarization P vs. applied magnetic field B. The temperature is T=15 K, the current density is J=3Acm^{-2}, and the Hanle angle is φ = 60 °. The solid line is a Hanle curve fit.*

The Au-reference device showed zero spin injection as expected while the Fe-device exhibit an electroluminescence Hanle behavior. A description of the model used in the fitting procedure is given in Appendix N. From Equation 1.16 with $\alpha = 1$, $g^* = -1.8$ (linear interpolation from bulk measurements [54]), Hanle angle φ = 60 °, T_s given by

the Hanle-fit and the radiative lifetime τ given by the time-resolved photoluminescence measurements to 264ps, a total spin injection is found to $P_0 = P_{EL}/(\cos\varphi \sin\varphi)\tau/T_s = 146$ %. The reason for this unrealistic value must be found among:

1. The approach which uses the radiative lifetime measured on an undoped reference sample is not suitable, or
2. The assumption that the bulk value $g* = -1.8$ can be used for strained QWs is incorrect, or
3. The measurements are dominated by confounding effects such as MCD or Zeemann splitting.

We are convinced that the reason is due to a combination of 1 and 2, with 2 as the main reason. A discussion of this will be given later. For now let us consider which information we can subtract from the measurements: If the Hanle signal is saturated, we have the same information as found in the Faraday-geometry measurements i.e. the steady state spin polarization in the well $P = P_0 T_s/\tau$, which in QWs at low temperatures is given by $P = P_{EL}/(\cos\varphi \sin\varphi)$, due to the selection rules described in 1.2.3. To keep the same formalism throughout this chapter we will use the average value measured for $\mid B \mid = 0.8$ T to determine the steady state polarization P. This is an approximation since it is difficult to determine if P_{EL} is saturated. Furthermore we will write the fitted Hanle width in the graphs. In the discussion 5.4 we will compare the Hanle width and estimate the spin injection P_0.

At 6 K the Hanle curve saturates at a magnitude of $P_{EL} = 4.1$ %, given a steady state spin polarization $P = 9.5$%.

This particular Fe device M53 also showed spin injection at room temperature. Figure 5.4 illustrates the results.

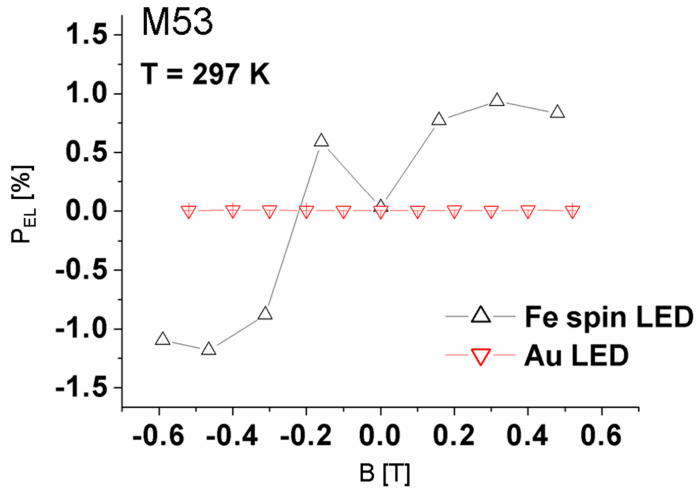

Figure 5.4: *M53 on C2294: Optical polarization P vs. applied magnetic field B.*

The reason for the fewr points in these measurements is that in order to use the right value of α we need to measure the circular polarization of a known recombination process either e-hh or e-lh. As a result of this the full electroluminescence spectra was measured for both helicities and for each value of the applied magnetic field. The Hanle curve seems to saturate with a magnitude of P_{EL} = 1 %, giving a steady state spin polarization P = 2.3 %.

Later results on other devices from the same growth showed injection of comparable efficiency. At 15 K the Hanle curve saturates with a magnitude of P_{EL} = 2.8 %, given a steady state spin polarization P = 6.5 %. Figure 5.5 illustrates this.

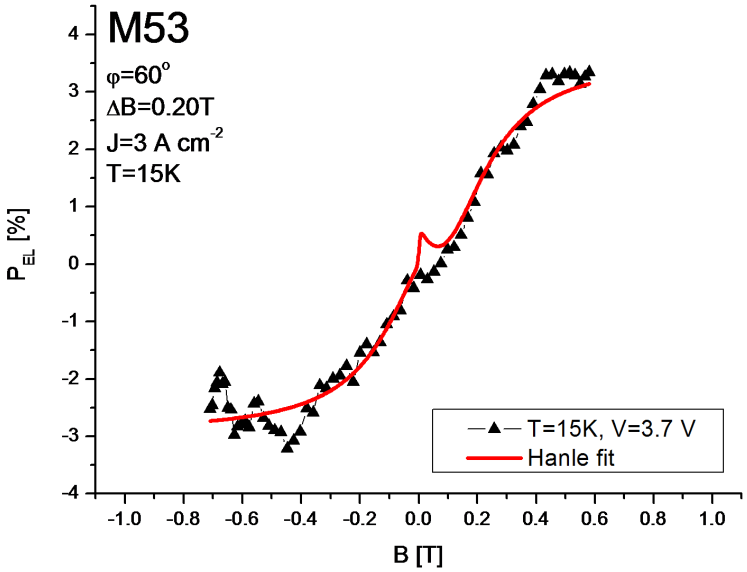

Figure 5.5: *M53 on C2294, J=3Acm^{-2}: Optical polarization P_{EL} vs. applied magnetic field B at T=15 K. The solid line is a fit to the Hanle curve.*

From the fits of the above measurements at low temperatures, a horizontal offset is observed. This can be explained by Dynamic Nuclear Polarization (DNP) through hyperfine field interactions between the electron and nuclear spin as described in section 1.2.3. The offset is 0.1 T and 0.06 T at T = 6 K and T = 15 K, respectively. The relaxation of nuclear spins can be much slower (minutes) compared to electron spin relaxations (ps). To observe nuclear polarization the magnetic field sweep should be slow compared to the nuclear spin relaxation. In our experiments we have not studied the dependence of sweep direction, but we did see the expected offset-dependence on the magnetic sweep rate. In both low temperature sweeps the rate was 0.002 T/s (5 times slower than the default rate).

Bias dependence investigations were done on VG05-048 grown on C2398 at T = 77 K. The dependence can be seen in Figure 5.6.

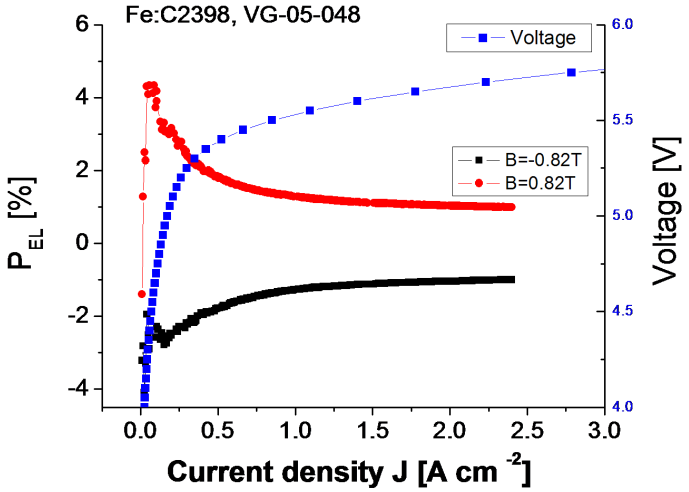

Figure 5.6: *VG05-048 on C2398: Bias dependence and IV-curve at T=77 K.*

The applied magnetic field was kept on the maximum applied field B=0.82 T during the bias sweep. At high bias the spin polarization seems to saturate at P_{EL} = 1 % resulting in a steady state polarization of P = 2.3 %. Since we do not have photoluminescence measurements we are not able to really clarify the origin of the measured spin polarization at high biases. By looking at the magnitudes of the known confounding effects such as MCD and Zeeman-splitting and their magnitude, one finds that at 0.8 T the Zeeman-splitting is negligible. MCD-effects from a $Co_{90}Fe_{10}$(2 nm)/$Ni_{80}Fe_{20}$(8 nm) heterostructure have been reported to less than ≈0.4 % at B=0.5 T by Motsnyi *et al.* [36]. Strand *et al.* [37] report similar results, less than 1 % at B=2.1 T for a 5 nm Fe film. From these results we can estimate the MCD effect in our 5 nm Fe film at B=0.8 T to be less than 0.6 % in worst case. We expect the majority of the emitted light to come from the edge of the contact mesa due to the etch of a second mesa on top of the semiconductor mesa (see Figure 5.7), and therefor not exhibit MCD-effects. The intensity of the emitted light as a function of position on the sample has been measured by a CCD camera on one sample (VG05-075 on NBI#9). It clearly shows more intensity along the Heusler mesa.

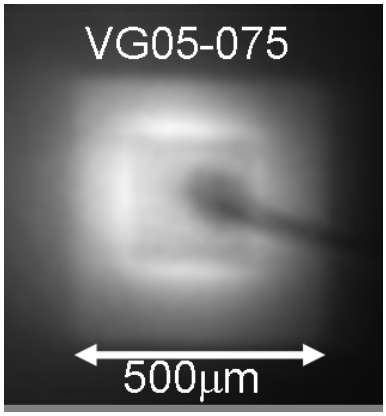

Figure 5.7: *VG05-075 on NBI#9), The applied bias is 2 V and the integration time: 1000 ms.*

The large polarization P_{EL} at high biases cannot be explained by the MCD-effect only even though all emitted light goes through the Fe film. An interesting explanation could be hot-electron spin injection. To investigate this it would be essential to measure the spin lifetime as a function of bias. Hot electron spins are expected to have a shorter lifetime due to spin scattering events and loss of coherence during thermalization processes [34, 117]. This study is yet to be done.

Further details on the Fe-spinLEDs can be found in [118, 119].

5.3 Spin injection with Co_2MnGa as injector material

Our first attempt to inject spins by Co_2MnGa were done on samples including a CoGa-buffer layer. As described in section 3.1 the buffer layer was made to prevent diffusion of Mn into the semiconductor structure and to relax some of the strains introduced from the substrate. Injection was observed. Figure 5.8 shows the measurements and the corresponding fit. The inset shows in-plane MOKE measurements.

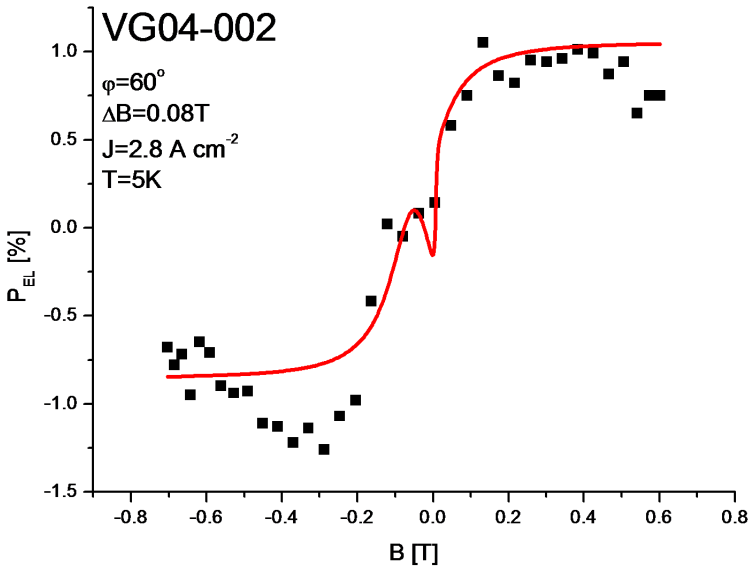

Figure 5.8: *VG04-002 on C2294, J=0.8Acm^{-2}, T=5 K: Optical polarization P_{EL} vs. applied magnetic field B. The solid line is a fit to the Hanle curve.*

The steady state spin polarization in the QW was found to be $P \approx 2.3$ % at 5 K. The temperature dependence reveals a fast decreasing trend as compared to Fe-devices as described in [119]. This is not really understood. In this particular sample the spin injection disappears around $T \approx 20$ K.

As described in Appendix E, Auger spectroscopy showed no evidence of Mn-diffusion and we decided to try without growth of buffer-layer. Figure 5.9 shows P_{EL} as a function of applied magnetic field.

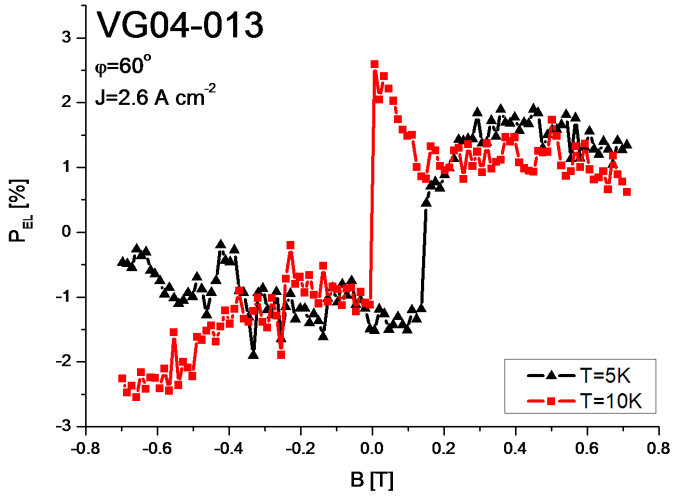

Figure 5.9: *VG04-013 on C2294, J=2.6Acm^{-2}, T1=5 K and T2=10 K: Optical polarization P_{EL} vs. applied magnetic field B.*

VG04-013 showed a magnitude of the steady state polarization of $P \approx 3.5$ %. In both measurements the magnetic field is swept upwards with the same sweep rate 0.002 Ts^{-1} (default sweep rate 0.01 T^{-1}). The measurements exhibit a sharp shift, and a very drastic temperature dependence. At T=5 K the shift is observed at 0.14 T, while at T=10 K the shift has changed to zero. The observation of a much sharper shift than expected from Bloch theory, has also been made by Strand *et al.* [35]. They explain the observation by DNP through hyperfine field interactions between the electron spin and the nucleus. They do not observe a horizontal shift at low temperatures. We do not fully understand this behavior. Since the relaxation times of the nucleus spin can be very long (minutes), it would have been interesting to investigate this sample at even lower sweep rates and in both sweep directions to get more information on the cause of the horizontal offset.

Figure 5.10 shows P_{EL} from another Co_2MnGa sample without a CoGa buffer layer. In this case an offset in the helicity dependent EL signal is observed.

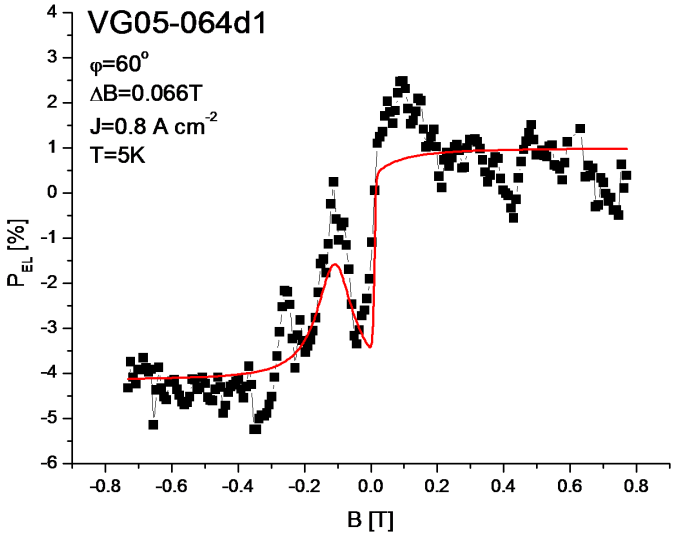

Figure 5.10: *VG05-064d1 on C2398, J=0.8Acm^{-2}, T=5 K: Optical polarization P vs. applied magnetic field B. The solid line is a fit to the Hanle curve.*

The measurements are very noisy due to the low intensity of emitted light at that current density $J = 0.8$ Acm^{-2}. The steady state spin polarization is found to $P = 5.3$ % at 5 K. Measurements on a sample from the same growth (VG05-064) but on another processed device showed the same injection efficiency but with a much wider Hanle curve and without the switching around zero applied magnetic field. Figure 5.11 shows two Hanle curves at different current densities (bias).

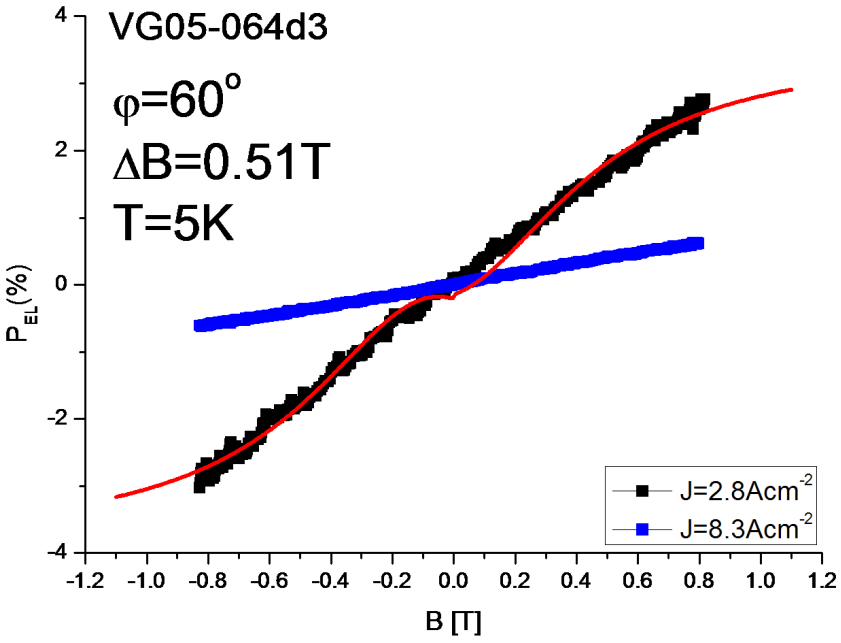

Figure 5.11: *VG05-064d3 on C2398, J=2.8 Acm*$^{-2}$&8.3 *Acm*$^{-2}$*, T=5 K: Optical polarization* P_{EL} *vs. applied magnetic field B. The solid line is a fit to the Hanle curve a J=2.8 Acm*$^{-2}$.

The effect is clearly seen. The bias dependence seems very interesting because of its ability to control the spin injection and thereby the spin polarization in the well. We decided to study this effect more carefully. By sweeping the bias at $B = \pm 0.8\ T$, the bias influence on P_{EL} and thereby on the steady state spin polarization P can be found. The results are shown in Figure 5.12 and show similar trends as seen in the Fe-sample.

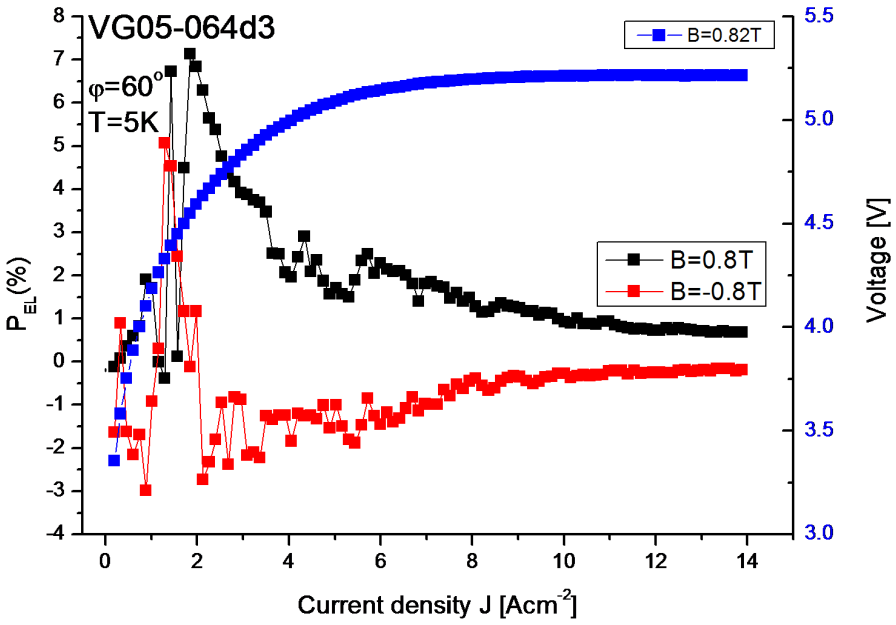

Figure 5.12: *VG05-064d3 on C2398: Optical polarization P_{EL} vs. current density J. T=5 K .*

The reason that we use the current density J instead of the applied bias is to make the comparison between samples easier. The bias is measured with two point technique, which includes the contribution from n and p-contacts. From a single three point measurement we know that the main contribution is coming from the p-contact (see Figure 4.5).

It is clear that the spin polarization in the QW decreases with increasing bias. Our explanation is that the injected electrons are in the tunneling regime at low bias and out of the tunneling regime for higher biases. If we had accurate measurements of the p-i-n junction itself, comparisons with the expected height of the Schottky barrier would have been possible. But this has not been done due to the simple processing technique. For $J < 1.5$ Acm^{-2}, the signal to noise ratio is very poor due to the intensity of the emitted light. At current densities above $J \approx 10$ Acm^{-2}, the steady state polarization saturates at $P \approx 1.2$ %. Since we expect only very little tunneling to happen resulting in very little efficient spin injection to follow, this value could be an artifact arising from confounding effects mainly Magnetooptical Circular Dichroism (MCD) in the ferromagnetic film. As was the case of the Fe device the spin polarization magnitude is larger than expected for the MCD-effect even though no MCD-reference measurements have been done on Co_2MnGa thin films. Again hot electron spin injection could be an interesting explanation, but again more measurements should be done. Another point in this measurement is that the voltage dependence seems to saturate around 5.2V. The reason for this is due to Joule heating of the device. This was the measurement that made us decide to thermally link the device to the cold finger using a small Cu-cylinder. The magnitude of the heating is a matter of a few K, which should not change P_{EL} drastically. The temperature of the cold

finger was measured to increase 0.2 K.

In this particular growth we also had a piece of the NBI#9 wafer. Figure 5.13 shows the results. Compared to C2398-wafer the current density at which maximum spin polarization is observed is much smaller (J = 2.8 Acm^{-2} vs. J = 0.2 Acm^{-2}). This could be explained by a higher and/or wider Schottky barrier. Furthermore the optical polarization and thereby the steady state polarization $P \approx 1.2$ % is also small. Since the QW- structures are very similar in all three wafers we expect the difference to stem from the difference in barrier design.

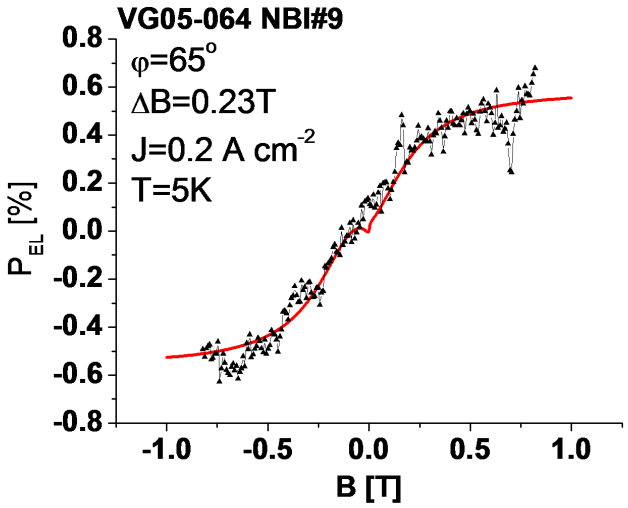

Figure 5.13: *VG05-064 on NBI#9, J=0.2 Acm^{-2}, T=5 K: Optical polarization P_{EL} vs. applied magnetic field B. The solid line is a fit to the Hanle curve.*

From the bias dependence measurements shown in Figure 5.14, for $B = 0.8\ T$ it is also clear that the "bias"-window of efficient spin injection (J=0.15..0.8 Acm^{-2}) is also much smaller compared to the C2398-wafer (J=1.5..10 Acm^{-2}).

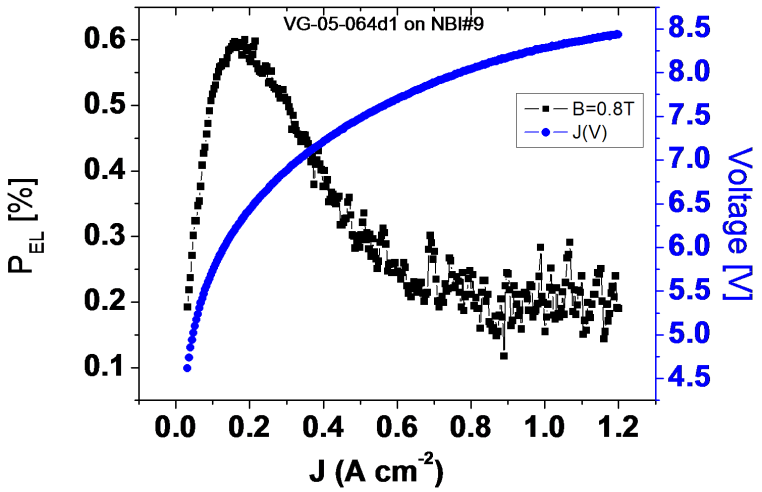

Figure 5.14: *VG05-064 on NBI#9, B=0.8 T, T=5 K: Optical polarization P_{EL} vs. current density J.*

The steady state spin polarization at large current densities is measured to $P = 0.5$ %, which is less than observed in C2398. The magnitude is comparable to the expected MCD-effect.

Sample VG05-075 shows similar effects. This device is based on the C2398-wafer. The steady state spin polarization is measured to $P \approx 1.8$ % at T=5 K and J=1.7 Acm^{-2}, which compared to VG05-064 on the same wafer is a bit low.

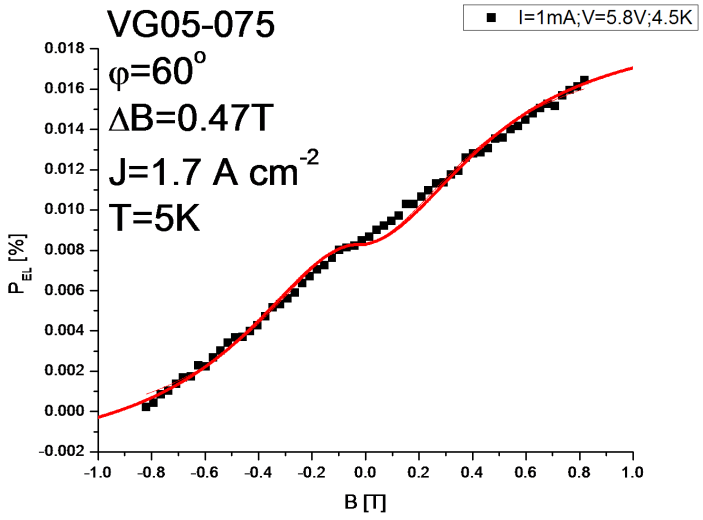

Figure 5.15: *VG05-075 on C2398, J=1.7 Acm^{-2}, T=4.5 K: Optical polarization P_{EL} vs. applied magnetic field B.*

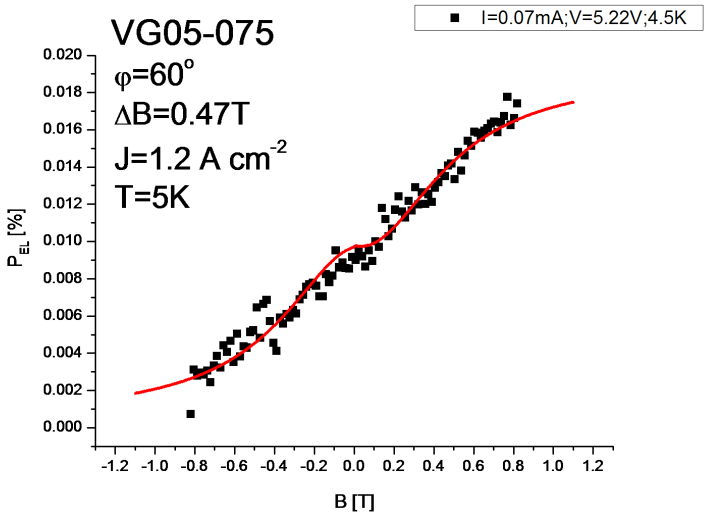

Figure 5.16: *VG05-075 on C2398, J=1.2 Acm^{-2}, T=4.5 K: Optical polarization P_{EL} vs. applied magnetic field B. The solid line is a fit to the Hanle curve.*

When comparing Figure 5.15 and 5.16, the change in polarization due to voltage bias, is only seen as a lower signal to noise ratio. The effect is best seen in Figure 5.17, which shows the current dependence of P_{EL} for $B = \pm 0.8\ T$

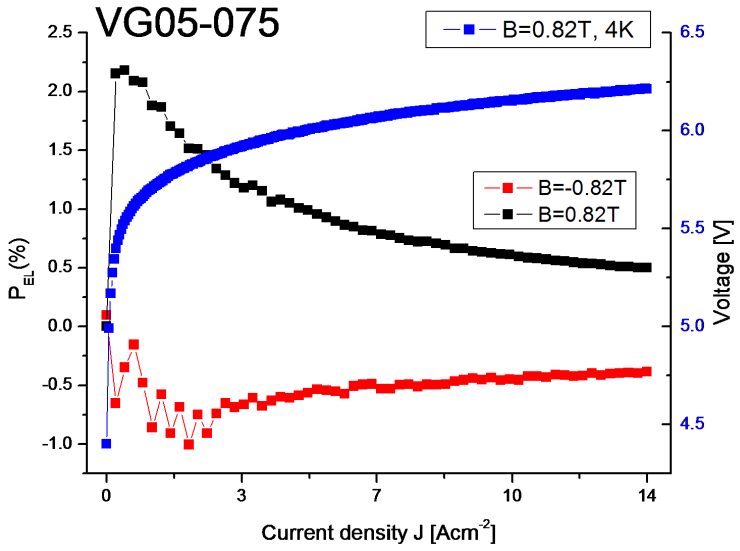

Figure 5.17: *VG05-075 on C2398, T=4.5 K: Optical polarization P_{EL} vs. current density J.*

The steady state spin polarization measured at current densities $J > 10\,\mathrm{Acm}^{-2}$ is $P \approx 1.1\,\%$. This time no Joule heating is observed, neither in the temperature measurement

nor in the IV-dependence.

5.4 Discussion and comparison

In this section a discussion and comparison will be given on the basis of the steady state spin polarization P measurements. Hereafter we will discuss the analysis of the spin injection efficiency P_0.
Table 5.2 shows a summary of the results.

The observed optimum bias, estimated from the current density and the individually measured IV-curves, is around 4 V-6 V at $T = 5$ K, which corresponds to approximate 1.5 V-2 V measured over the FM/Schottky/p-i-n structure.

5.4.1 Spin injector: Fe vs. Co_2MnGa

The highest measured steady state polarization is observed in the Fe device M53 at T=6 K with a magnitude of $P \approx 9.5$ %. The steady state polarization remains up to room temperature with a magnitude of $P \approx 2.3$ %. The highest steady state spin polarization measured with Co_2MnGa as injector was $P \approx 6.4$ % at $T = 5$ K. No spin polarization was observed at temperatures above $T = 20$ K. Since the two samples were grown on wafers (C2294 vs. C2398) a good comparison is not possible, even though the p-i-n structures are very similar with respect to barrier and QW. The best comparison of the two injector materials would be M53 ($P \approx 9.5$ %) vs. VG04-013 ($P \approx 3.5$ %). PCAR results show bulk spin polarization $P = 50$ % in CoMnGa alloys with stoichiometries close to VG04-013. Fe is known to have a bulk polarization $P = 44$ %. The reason for the lower spin injection and thereby lower obtained steady state spin polarization in the QW could be due to interface scattering. This would correlate nicely with TLM measurements where Fe or Co grown on δ-doped GaAs typically show resistances of 0.02-0.1 Ωmm^2, while it is 2 orders of magnitude higher for the Co_2MnGa-contacts. The reason for this large difference could be explained by chemical reactions at the interface of the Co_2MnGa/GaAs contact. This could also be the reason for the faster decease in steady state spin polarization as a function of temperature observed in Co_2MnGa compared to Fe.

A more direct method to get information on the spinLED-ferromagnet contact would be to do TLM investigations on the spinLED structures or from comparison of four point measurements of the IV-dependence on the different devices. We did carry out TLM studies on C2398 and NBI#9 and found interface resistances between 1 to several 100 Ωmm^2.

Similar bias dependencies are observed for both injector materials and for all spinLED structures. The region in which tunneling happens is different but the trends seems to be the same. One must bear in mind that not only the electron energy is dependent on the bias but also the radiative life times. Which one of the effects is dominating the picture is not possible to determine from the information we have at this moment. To look into this τ should be determined as a function of bias. Strand *et al.* [35] report very similar bias dependence to ours.

Sample name	Description	Experimental details					Spin polarization	Fit parameters		Spin injection		
		φ [DEG]	J [Acm-2]	T [K]	Horizontal offset [T]	$max(P_{EL})$ [%]	steady state P [%]	ΔB [T]	prefactor	T_s [ps]	τ [ps]	P_0 [%]
M53	Fe:C2294	60	3	15	0.06	2.8	6.5	0.20	3.2E-02	32	264	60.4
M53	Fe:C2294	60	3	300	-	1.0	2.3	-	-	-	-	-
M53	Fe:C2294	60	3	6	0.1	4.1	9.5	0.33	4.6E-02	19	264	145.5
VG05-048	Fe:C2398	60		77	-	3	6.9	-	-	-	-	-
VG04-002	Co2MnGa:C2294	60	2.8	5	-0.05	0.95	2.2	0.08	9.5E-3	80	264	7.2
VG04-013	Co2MnGa:C2294	60	2.6	5	0.14	1.5	3.5	0.08	-	-	-	-
VG04-013	Co2MnGa:C2294	60	2.6	10	0	1.5	3.5	0.08	-	-	-	-
VG05-064d1	Co2MnGa:C2398	60	0.8	5	-0.1	2.6	6.0	0.07	2.6E-02	94	264	16.7
VG05-064d3	Co2MnGa:C2398	60	2.8	5	-0.05	2.8	6.4	0.51	3.7E-02	12	264	181.3
VG05-064d3	Co2MnGa:C2398	60	8.3	5	-	0.61	1.4	-	-	-	-	-
VG05-064nbi	Co2MnGa:NBI#9	65	0.2	5	-0.05	0.52	1.4	0.23	5.5E-03	27	350	18.3
VG05-075	Co2MnGa:C2398	60	1.7	4.5	-0.02	0.80	1.9	0.47	9.0E-03	14	264	40.6
VG05-075	Co2MnGa:C2398	60	1.2	4.5	-0.04	0.70	1.6	0.52	1.1E-02	12	264	55.0

Table 5.2: *Summary of spinLED measurements, T_s and P_0 is estimated from the Hanle fit with a effective g-factor of $g = -1.8$.*

Group	P	Detector	Barrier	Injector	Setup
Strand* *et al.* 2005 [35]	3.1 % (6.7%) at T = 20 K	GaAs/$Al_{0.1}Ga_{0.9}As$ QW	higly doped $Al_{0.1}Ga_{0.9}As$ Schotkky barrier	Fe	Hanle (Faraday)
Adelmann* *et al.* 2005 [107]	27 % at T = 2 K and 10% at T = 295 K	GaAs/$Al_{0.1}Ga_{0.9}As$ QW	higly doped $Al_{0.1}Ga_{0.9}As$ Schotkky barrier	Fe	Faraday
Dong* *et al.* 2005 [64]	13 % at T = 2 K	GaAs/$Al_{0.1}Ga_{0.9}As$ QW	higly doped $Al_{0.1}Ga_{0.9}As$ Schotkky barrier	Co_2MnGe	Faraday
Zhu *et al.* 2001 [110]	2.2 % at T = 25 K	$In_{0.2}Ga_{0.8}As$/GaAs QW	n-doped GaAs	Fe	Faraday
Hanbicki *et al.* 2002 [109]	13 % at T = 4.5 K	GaAs/AlGaAs QW	$Al_{0.08}Ga_{0.92}As$	Fe	Faraday
Jiang *et al.* 2005 [21]	57 % at T =100 K and 47 % at T =290 K	GaAs/$Al_{0.08}Ga_{0.92}As$ QW	MgO	$Co_{70}Fe_{30}$	Faraday

Table 5.3: *SpinLED measurements with Fe as an injector and a QW as detector, reported by other groups. * is from the same group at University of Minnesota.*

5.4.2 SpinLED efficiency

Some reported studies on spinLED structures are given in Table 5.3: it is seen from the steady state polarization, that our structure does not seem to be as efficient as especially the structure reported by Jiang *et al.* based on $Co_{70}Fe_{30}$ as injector, MgO as tunnel barrier, and GaAs/$Al_{0.08}Ga_{0.92}As$ QW as detector. Also the Minnesota group (Strand, Dong, Adelmann), reports good results on all semiconductor designed barrier and detector structure. They have focused on a highly doped $Al_{0.1}Ga_{0.9}As$ Schottky barrier and a GaAs/$Al_{0.1}Ga_{0.9}As$ QW as spin polarization detector. Their observed steady state polarizations are approximately a factor of 5 larger than our results. Why is this? To find the answer, we have to look into the following issues:

1. Spin injector material: The spin injector material should have a spin polarization as high as possible together with an abrupt and clean interface towards the spinLED structure. Chemical reactions and inter diffusion destroys the magnetism and thereby the polarization of the injected spins.

2. Spin injection: The barrier need to be high and thin for tunneling events to happen at a reasonable bias, at which electroluminescence is easily observed.

3. Spin detection efficiency: The spin detection efficiency $\eta = T_s/\tau$, where T_s is the spin life time and τ is the radiative life time should be as high as possible. To get a high spin detection, T_s needs to be high and the radiative lifetime needs to be short.

We expect 3) to be the main reasons for rather low observed steady state spin polarization P, together with 1) in case of Co_2MnGa as injector material. The observed radiative lifetime on our structures is comparable to other measurements on both InGaAs/GaAs

($\tau \approx 230 - 330$ps[112]) and GaAs/AlGaAs ($\tau \approx 200$ps [120]) QWs. When comparing τ measured on reference sample to both NBI#9 and C2398, and C2294, the latter two are the best ones due to the lower $\tau = 264ps$. To investigate the optimum of τ and T_s vs. In content more wafer and measurements are needed. We expect both τ and T_s to decrease with increasing In content due to strain. For now it seems to be the case that 20 % In is better than 18 %.

By comparison of VG05-064 grown on C2398 and NBI#9 we can compare the efficiencies of the barriers (case 2). It seems like the highly doped $Al_{0.2}$Ga0.8As Schottky barrier is most efficient compared to the highly doped GaAs. This could be due to the difference in depletion depths.

5.4.3 Measurement configuration

The Hanle configuration is ideal for measuring spinLEDs, compared to Faraday, due the moderate needed applied magnetic field, and due to the possibility of finding the spin life time T_s. But in our case it has been a problem, that we have not been able to saturate the observed P_{EL} even at the maximum field of 0.8 T. The reason for this beside of T_s being very short could be due to a small effective g factor. The Hanle curve width is given by $\Delta B = \hbar/(g\mu_B T_s)$. As also mentioned in the text the fitted values of T_s shown in Table 5.3 are all calculated by use of an effective g-factor (-1.8), interpolated from bulk measured effective g-factors in GaAs (g=-0.44) and $In_{0.53}Ga_{0.47}As$ (g=-3.95). This is only a very simple approximation, due to the energy confinement in the QW and due to strain. Malinowski *et al.* [121] report effective electron g-factors of $In_{0.11}Ga_{0.89}As$/GaAs between $-0.44.. - 0.6$ for QW with widths between 3 nm..20 nm and Kowalski *et al.* [122] report g=-0.8 in a 14.3 nm wide $In_{0.21}Ga_{0.79}As$/GaAs QW with the B-field applied $\sim 30\,^\circ$ to the growth axis of the QW (As is the case for the majority of Hanle-measurements in this thesis). Figure 5.18 shows the results:

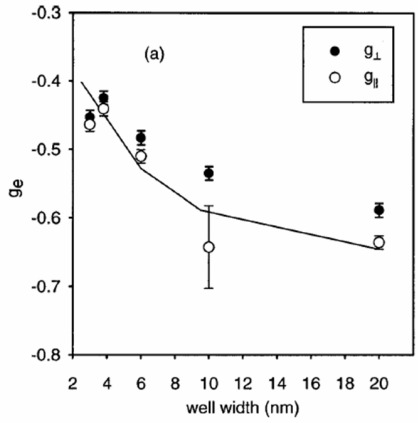

(a) Adapted from [121]

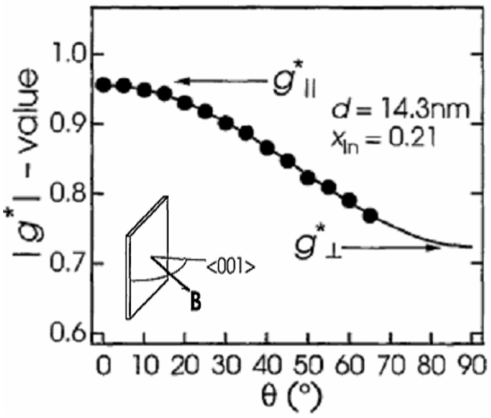

(b) Adapted from [122]

Figure 5.18: *Measurements of the g-factor anisotropy and QW-width.$g^*_{||}$ and $g^*_\perp$ are the effective g-factors parallel and perpendicular to the QW growth direction respectively. (a) :Results from time resolved, polarization-sensitive, pump-probe measurements at $T = 10$ K. (b): Results from optical detected spin resonance measurements at $T = 5$ K.*

From the two references an estimate of the g-factor can be given as g=-0.63 and g=-0.73 respectively for a 5 nm and 10 nm $In_{0.2}Ga_{0.8}As$/GaAs QW By using a g-factor ~2.5-3 times smaller than the used bulk approximation ($g = -1.8$) the spin life times T_s are increased, and more realistic values of the spin injection P_0 are obtained (a factor of 2.5-3 less than written in the P_0-column. see Table 5.4).

Sample name	Description	Temperature	Spin injection		
		T [K]	T_s [ps]	τ [ps]	P_0 [%]
M53	Fe:C2294	15	80	264	24.5
M53	Fe:C2294	300	-	-	-
M53	Fe:C2294	6	47	264	59
VG05-048	Fe:C2398	77	-	-	-
VG04-002	Co2MnGa:C2294	5	198	264	2.9
VG04-013	Co2MnGa:C2294	5	-	-	-
VG04-013	Co2MnGa:C2294	10	-	-	-
VG05-064d1	Co2MnGa:C2398	5	231	264	6.8
VG05-064d3	Co2MnGa:C2398	5	31	264	73.5
VG05-064d3	Co2MnGa:C2398	5	-	-	-
VG05-064nbi	Co2MnGa:NBI#9	5	78	350	6.4
VG05-075	Co2MnGa:C2398	4.5	33	264	16.5
VG05-075	Co2MnGa:C2398	4.5	30	264	22.3

Table 5.4: *Re-analysis of spinLED measurements, where T_s and P_0 are estimated from the Hanle fit with a effective g-factor of $g = -0.63$ and $g = -0.73$ for NBI#9 and C2294/C2398 respectively.*

To validate this approach, reference measurements on T_s or the effective g-factor should be done.

Chapter 6

Conclusion and Outlook

This chapter will summarize the conclusions drawn in the different parts of this thesis. This will include material device properties as well as the methodological aspects. Furthermore the project will be described from an outlook perspective.

6.1 Theoretical calculations

Density Functional Theory (DFT) within the Local Spin-Density Approximation (LSDA) has been used to investigate the itinerant magnetism of the full Heusler alloy Co_2MnGa. Local magnetic moments have been calculated for a stoichiometric crystal, and correlates nicely to measurements on bulk samples. Furthermore spin polarization P has been calculated and compared with PCAR measurements with some success: PCAR exhibit $P = 50$ %, while the calculations expects $P = 63$ %. Furthermore calculations were made on off-stoichiometric crystals, and stoichiometric crystals with swapping-defects. Both studies have given trends to look for in the dependence of the local magnetic moment and the spin polarization on stoichiometry variations and site-swapping. It was found that disorder involving especially Co on Ga or Mn sites cause a significant decrease of spin polarization. None of these trends were identified from XMCD studies. From an estimate based on the calculated defect formation energies it is found that Mn on Co-sites are likely to exist with a concentration of 2 %, while Ga on Mn-sites are likely to exist with a concentration of 21 %. Mn on Co-sites could explain the $P = 50$ % observed by PCAR, but surface contamination of the Heusler alloy is more likely the explanation of "low" polarization measured by PCAR measurements.

In an outlook perspective, more measurements on either the local magnetic moments or the spin polarization are needed to compare with the calculations. SpinLEDs could be a good candidate as a characterization method for this study. Furthermore NMR measurements which could determine the identity of the defects and corresponding concentrations would be a good way of validating the calculation of defect formation energies.

6.2 Growth and characterization

We have had great difficulties with the growth process during this project. Our approach was first to obtain the right stoichiometry, then optimize the crystal structure by changing growth temperature or annealing process, and finally fine tune the growth parameters based on feedback from spin injection measurements on spinLEDs. However, several difficulties have slowed down the progress and a direct feedback from spinLEDs has never been made.

A recipe for epitaxial growth of the full Heusler alloy Co_2MnGa have been developed (see Appendix C). The reproducibility is approximately within 2 % of the correct stoichiometry. The technical reason which cause this deviation is the feedback control of the Co evaporated from an E-beam source. Furthermore epitaxial growth of hetero structures of Co_2MnGa and Al and Al_xO_y layers has been performed. Devices (GMR or Tedrow-Meservey) are yet to be made from these grown samples.

A reliable and efficient way of determining the stoichiometry of thin films grown on GaAs has been found. From EDS measurements we have confirmed same measured stoichiometry on samples from same growth on Si and GaAs. By using this knowledge combined with ICP-OES supplemented with reference measurements on bulk Co_2MnGa, we are able to measure the stoichiometry to within 1-2 %. The measured stoichiometry is non-linearly dependent on the individual Co,Mn, and Ga rates, which made the growth parameter study very difficult.

The crystal structure study was done by XRD-methods. There are Indications that the thin films grow pseudomorphically on GaAs up till a critical thickness of at least 20 nm, but more measurements and analyses are needed to confirm this. The lattice parameter has been observed to be very dependent on the stoichiometry. This would normally be feasible as a feedback to the growth parameters, but in our case this has been difficult to do, due to difficulties in making systematical changes in the growth. We explain this by the eutecticum being very shallow, which results in the growth of off-stoichiometric alloys. Furthermore the 2×4 Ga-rich reconstruction of the GaAs surface is clearly observed as anisotropy in in-plane magnetization, while no anisotropy is observed for near stoichiometry thin films on an ordinary GaAs surface. Different substrates Si, InAs, $In_{0.28}Ga_{0.72}As$, and GaAs have been used to establish different strains in the thin films. A dependence is clearly observed, but whether it is due to strain or diffusion/chemical reaction on the surface is still to be determined with e.g. TEM-studies. Furthermore InP should be added to the list of substrates, due to its small lattice mismatch (1.7 %).

From high temperature annealing/growth and XRD/VSM/AES-techniques, the formation and detection of interphase diffusion layers have been studied without great success. Some new phases were observed by XRD. By AES measurements on samples annealed at 450° for 10 minutes, showed that Mn tends to diffuse both towards the surface and into the substrate. A more direct way of studying interphase properties would be by TEM-techniques, but due to costs and lack of time, this technique has not been pursued. From an outlook perspective this should indeed be done.

The magnetic properties from nearly stoichiometric films grown on GaAs exhibited saturation magnetizations lower than measured in bulk samples. From XMCD measure-

ments, it seems that especially the Mn does not carry the same moment as the theoretically predicted and as in bulk measurements. We explain the missing Mn moment by two reasons: 1) Mn diffusion: From AES we expect Mn to diffuse towards the surface. This implies that XMCD really probed some diffusion layer rather than the pure Co_2MnGa alloy. However, to verify this more measurements are needed, and complementing experimental techniques should be performed. The thin films exhibit small in plane coercive fields typically 1-10 mT. On the contrary a magnetic field of 1-2 T is needed to saturate the thin films in the out of plane direction. From AFM scans a surface roughness has been measured to 3 nm for a 50 nm film, and 1.5 nm for a 25 nm film. Both thin films were not capped and therefore oxidized. MFM-scans reveals domain sizes of 200-300 nm respectively for 25 nm and 30 nm thin films without capping. AFM/MFM measurements of a capped sample to prevent oxidation and following change in surface magnetism is yet to be done.

Future measurement should include magnetization measurements at high temperatures $T > 600$ K to determine the Curie temperature of the Heusler thin films and in case of other magnetic phases reveal their presence.

The electrical characterizations reveal resistivities around $\rho = 350\ \mu\Omega$cm, and a critical thickness around $t_{nom} = 10$ nm, which corresponds to a real thickness $t_{real} = 7\ nm$ at 300 K. The resistivity of a a bulk sample was measured to approximately a factor of 3 less $\rho = 120\mu\Omega$cm. In comparison with measurements on other Heusler thin films our value also seems to be high. We expect surface contamination and strain in the film to be the main reasons for this. It would be interesting to cap the hall bars to prevent contamination in future samples. Generally, the near stoichiometric films have a very weak temperature dropping slightly when cooled.In good agreement with other reported studies on Heusler alloys thin films negative MR has been observed. Furthermore a small AMR has been measured to 0.062 %. Sheet carrier densities have been measured to $1.5\text{-}3.6{\cdot}10^{16}$ cm^{-2} with a decreasing tendency with increasing temperature. From TLM measurements the low current interface resistance in δ-doped GaAs-Ferromagnet is found to typically 0.02-0.1 Ωmm^2 for Fe and Co contacts but is 2 orders of magnitude higher for the Co_2MnGa contacts. Correspondingly the IV-characteristics measured in a 3 probe configuration are nearly ohmic for Fe and Co, while some asymmetry is found for Heusler contacts (of order 10-30% for 50 μA (J=2 A/cm^2)). In comparison contact resistances between a metal like Al and δ-doped GaAs have been reported to be as low as 10^{-4} Ωmm^2. A number of TLM devices were fabricated using GaAs wafers with InGaAs quantum wells 100 to 300 nm below the surface. The wafers were mainly intended for spin-LEDs and had doping profiles corresponding to Schottky barriers at the surface. In these devices a large spread in interface resistances is found, but both for Fe and the Heusler alloy the low current value is of order 1 to several 100 Ωmm^2.

Measurements to characterize the thin film spin polarization were tried with both PCAR and Tedrow-Meservey spectroscopy. The latter with no success. We explain the difficulties by poor quality tunneling barriers. We are still working on this approach now where synthesis have been improved compared to the first Tedrow-Meservey samples. The PCAR measurements showed good agreement with other reported studies on Au, Cu, and Co. Measurements on Co_2MnGa revealed P=50 %. As already mentioned this

is less than the theoretical expected value $P = 63$ %. We expect surface contamination of the Heusler alloy cause the "low" polarization. In an outlook perspective PCAR measurements should be made on capped samples to prevent contamination.

6.3 SpinLEDs

Surely spin injection is observed. The highest measured steady state polarization is observed in the Fe device M53 at T=6 K with a magnitude of $P \approx 9.5$ %. The steady state polarization remains up to room temperature with a magnitude of $P \approx 2.3$ %. The highest steady state spin polarization measured with Co_2MnGa as injector was $P \approx 6.4$ % at $T = 5$ K. No spin polarization has been observed at temperatures above $T = 20$ K. We explain the lower steady state polarization in the QW by: 1) Interface scattering, which correlate nicely with TLM measurements where Fe or Co grown on δ-doped GaAs typically show resistances of 0.02-0.1 Ωmm^2, while it is 2 orders of magnitude higher for the Co_2MnGa-contacts. We explain the reason for this large difference by diffusion/chemical reactions at the interface of the Co_2MnGa/GaAs contact. We expect this to cause considerable scattering and also be the reason for the faster decrease in steady state spin polarization as a function of temperature observed in Co_2MnGa compared to Fe.

Similar bias dependencies are observed for both Fe and Co_2MnGa materials and for all spinLED structures. The region in which tunneling happens is different but the trends are the same. The large steday state spin polarization at high biases on $P \approx 1.2$ % cannot be explained by the Magneto-optical Circular Dichroism effect especially because we know that most of the emitted light is from the contact mesa edge which does not shine through the injector material Co_2MnGa or Fe. An interesting explanation could be hot-electron spin injection. To investigate this it would be essential to measure the spin lifetime as a function of bias. Hot electron spins are expected to have a shorter life time due to spin scattering events and loss of coherence during thermalization process.

The observed radiative lifetime on our structures are $\tau \approx 230 - 330$ ps and comparable to other measurements on both InGaAs/GaAs and GaAs/AlGaAs QWs. When comparing τ measured on reference samples to both NBI#9 and c2398, and c2294, the latter two are the best ones in respect to a efficient spinLED due to the lower $\tau = 264$ ps. From comparison of the used spinLED structures we conclude that 20 % In is better than 18 % to achieve an efficient spin detection.

By comparison of samples from same growth on c2398 and NBI#9 we can compare the efficiencies of the barriers. We conclude that the highly doped $Al_{0.2}Ga_{0.8}As$ Schottky barrier is most efficient compared to the highly doped GaAs. We explain this by the difference in depletion depths.

In an outlook perspective, higher magnetic fields should be applied to saturate the Hanle signal. Furthermore Faraday measurements should be done to confirm the Hanle measurements. It is a drawback by the Hanle technique that τ is approximated from measurements on a un-doped reference wafer.

In good agreement with other studies we have found that interpolating bulk electronic g-factors in the QW, results in unrealistic high spin injection efficiencies (P_0 >100 %).

From Malinowski *et al.* [121] and Kowalski *et al.* [122] we estimate the effective electronic g-factor in the QW to g=-0.63 and g=-0.73 respectively for a 5 nm and 10 nm $In_{0.2}Ga_{0.8}As$/GaAs QW. By use of these factors the fitted spin life times T_s are increased, and more realistic values of the spin injection P_0 are obtained P_0 <30 % in general but with two outliers on 73.5 % and 59 %. We expect that the reason for these unrealistic values should be found in the fitting of the Hanle curve. Due to the very linear dependence or noisy good valid fitting parameters are difficult to determine.

Several additional issues in the spinLED characterization are still to be studied and verified compared to the above described hypothesis.

1. Magnetization switching and Hanle fitting of the low magnetic field dependence. To achieve as few fitting parameters as possible, magnetic hysteresis behavior should be measured on the spinLED itself by focused MOKE,

2. Dynamic nuclear polarization dependence on sweep direction and rate should by studied in more details,

3. The effective g-factor should be measured, by zeeman splitting measurements on the spinLED structure itself.

It is our opinion that in order to optimize the device, another sample design is needed, with the possibility of four electrical probes to enable four point measurement techniques and thereby the possibility to reveal more information from the IV-dependence on the tunnel barrier height. Furthermore spinLED based on QDs, should be grown as an approach to develop a spin detector with a short recombination time.

6.4 Overall achievements

We have succeeded in growing the full Heusler alloy Co_2MnGa epitaxially on GaAs. We have developed a methodology to optimize the thin films. The techniques include theoretical calculations, stoichiometric analyses, structure studies, and characterization of electrical and magnetic properties as well as specific techniques to measure the degree of spin polarization achieved.

Spin injection into a semiconductor has been observed, but with a lower efficiency than seen on a Fe reference sample. The main problem areas by use of Co_2MnGa as spin injector and in spintronics in general are:

1. The bulk spin polarization is estimated to P = 63 % and measured to P = 50 %, which is not significant higher than other well known materials (Fe, Co, Ni, FeNi).

2. There are indications of increased surface scattering, due to diffusion and chemical reactions near surfaces and interfaces.

3. It has proven difficult to control stoichiometry.

Heusler alloys are very interesting alloys, both theoretically and experimentally. If Heusler alloys are to succeed in spintronics we speculate that the Heusler candidate should exhibit high crystal quality and no diffusion of any kind from or towards surface and substrate.

In an outlook perspective, future optimization of growth should be done to reduce disorder and chemical reactions near the substrate interface. Furthermore a screening of other Heusler alloys with higher predicted spin polarization, but still lattice matched to appropriate semiconductor should be done.

Nomenclature

Physical notation

α	Factor deterined by the selection rules. $\alpha_b ulk = 1$ and $\alpha_b ulk = 2$
α_{CB}	Conduction band spin splitting due to lack of inversion symmetry
β	Spin polarization of conduction electrons in a FM
χ	Static susceptibility
ΔB	The Hanle curve half-width
Δ	Superconducting gap
η	The longitudinal spin relaxation prior to recombination (or the spin detection efficiency)
γ	Electron gyromagnetic ratio ($\gamma = \mu_B g^*/\hbar$)
γ	Spin polarization of F/SC interface
$\hat{T}$	kinetic energy operator
$\hat{U}$	Electron-electron interaction operator
$\hat{V}$	External potential operator
$\hbar$	Reduced Planck's constant $h/(2\pi)$ (1.0546^{-34} m^2kg/s)
$\mathbf{\Omega}$	Larmor frequency
B	Magnetic field
E	Electric field
I	Nucleus spin
k	Momentum
M	Magnetization

$\mathbf{m}$	Magnetic moment
$\mathbf{S}$	intrinsic angular momentum (Spin)
μ	Chemical potential
μ_B	Bohr magneton ($9.2740 \cdot 10^{-24}$ JT^{-1})
μ_i	Nuclear spin magnetic moment
μ_z	Electron spin magnetic moment
ν	Potential
π	3.1416
Ψ	Wave function
ρ	resistivity
σ	Conductivity
τ	Radiative recombination lifetime
τ_c	Correlation time(interaction time)
τ_p	momentum scattering time
τ_s	Spin scattering time
τ_{sf}	Spin flip time
v_F	Fermi velocity
ε_g	Semiconductor band gap
φ	The Hanle angle
A	Andreev reflection probability
$a,\ c$	Lattice constants
B	Normal reflection probability
C	Cross-sectional area
D	Diffusion constant
e	Electron state
e	Elementary charge
$E[n]$	Energy functional

E_F Fermi energy

f Fermi-Dirac distribution

G Conductivity

g Electronic g-factor

g^* effective electronic g-factor

hh heavy hole state

I_{+-} The right and left circular polarized intensities

$I_{\uparrow\downarrow}$ Spin dependent current

J Spin dependent current density

$j_{\uparrow\downarrow}$ Spin dependent current density

l_{sf} Spin flip length

m mass

m_j Angular momentum

N One-dimensional spin density of states at the Fermi energy

n Electron density

P Spin polarization coefficient

P_0 Spin injection (prior to spin relaxation events)

P_c Contact spin polarization efficiency

P_L Degree of helicity polarization of circularly polarized light (Luminescence)

p_z Momentum in the QW growth direction

P_{EL} Degree of helicity polarization of circularly polarized light excited electrically (Electro Luminescence)

P_{PL} Degree of helicity polarization of circularly polarized light excited optically (Photo Luminescence)

Q A numerical factor depending on the orbital scattering

R Electrical resistance

r Effective resistance

S_0 Average injected electron spin

S_z z-component of the spin state **S**

T Temperature

t Thickness

T_1 Spin relaxation time

T_2 Spin dephasing time

T_C Curie Temperature

T_s The spin lifetime

V Hyperfine interaction potential

Abbreviation

2DEG Two Dimensional Electron Gas

AES Auger Electron Spectroscopy

BAP Bir-Aronov-Pikus

BCS Theory described in 1957 by J. Bardeen, L. Cooper, and R. Schrieffer

BTK Blonder, Tinkham and Klapwijk

CB The s-like conduction band

CPA Coherent Potential Approximation

CRL Cambridge Research Laboratory

DFT Density Functional Theory

DMS Dilute Magnetic Semiconductor e.g. GaMnAs

DNP Dynamic Nuclear polarization

DOS Density Of States

DP D'yakonov-Perel'

DTU Technical University of Denmark

EB Electron Beam source

EC Effusion Cell

EDS Energy Dispersive X-ray Spectroscopy

EL Electroluminescence

EMTO Exact Muffin-Tin Orbitals

EXAFS Extended X-ray-Absorption Fine-Structure

EY Elliot-Yafet

F Ferromagnet

FET Field Effect Transistor

GGA Gradient Generalized Approximation

GMR Giant Magneto Resistance

HFI HyperFine-Interactions

HH The p-like valence bands with heavy-holes

ICP-OES Inductively Coupled Plasma Optical Emission Spectroscopy

LAG Local Airy Gas approximation

LH Light-holes

LSDA Local Spin Density Approximation

MCD Magneto-optical Circular Dichroism

MFM Magnetic Force Microscopy

MOKE Magneto Optical Kerr Effect

MRAM Magnetic Random Access Memory

MTJ Magnetic Tunnel Junction

N Normal metal

NBI Niels Bohr Institute (Copenhagen University)

ND Neutron Diffraction

NMR Nuclear magnetic Resonans

p-i-n p-type semiconductor - intrinsic region - n-type semiconductor

PL Photoluminescence

QMS Quadropole Mass Spectrometer

QW Quantum Well

S Superconductor

SC Semiconductor

SO Spin-orbit split off holes

SpinFET Spin Field Effect Transistor

SpinLED Spin Light Emitting Diode

TLM Transmission Line Measurements

TMR Tunnel Magneto Resistance

TREL Toshiba Research Europe Ltd.

TRPL Time Resolved Photoluminesccence

VSM Vibrating Sample magnetometry

XMCD X-ray Magnetic Circular Dichroism

XRD X-ray Diffraction Spectroscopy

List of Figures

List of Tables

Publications

Journals

1. M.C. Hickey, C.D. Damsgaard, I. Farrer, S.N. Holmes, J.B. Hansen, C.S. Jacobsen, D. A. Ritchie, R.F. Lee, G.A.C. Jones, and M. Pepper,*"Spin photo-electronic devices based on Fe and the Heusler alloy Co_2MnGa,"* Oxford-Kobe seminars on spintronic materials and technology (2004) (in press).

2. M.C. Hickey, C.D. Damsgaard, I. Farrer, S.N. Holmes, J.B. Hansen, C.S. Jacobsen, D. A. Ritchie, R.F. Lee, G.A.C. Jones, and M. Pepper,*"Spin injection between $Co_{2.4}Mn_1$.6Ga and a InGAs quantum well,"* Applied Physics Letters, **86** 252106 (2005) and Virtual Journal of Nanoscale Science and Technology **11** issue 25 (2005).

3. C.D. Damsgaard, H.P. Gunnlaugsson, G. Weyer, J. Bindslev Hansen, C.S. Jacobsen, J.L. Skov, I. Rasmussen, and S. Mørup, *"Fe-contacts on InAs(100) and InP(100) characterised by conversion electron Mossbauer spectroscopy,"* Solid State Communications **133** 579 (2005).

4. C.D. Damsgaard *et al.*, *" Epitaxiel growth and magnetic properties of Co_2MnGa on GaAs(001)" (in preparation)*

Conferences

1. M.C. Hickey, C.D. Damsgaard, I. Farrer, S.N. Holmes, J.B. Hansen, C.S. Jacobsen, D. A. Ritchie, R.F. Lee, G.A.C. Jones, and M. Pepper, *"Spin injection from a Heusler alloy into an InGaAs quantum well,"* O-8 (talk), Spintech III, Awaji, Japan (2005).

2. C.D. Damsgaard, M.C. Hickey, A. Husmann, S.N. Holmes, C.S. Jacobsen, and J. Bindslev Hansen, *"Magnetic and electrical properties of Co_2MnGa epitaxially grown on GaAs(001),"* P-48 (poster), Spintech III, Awaji, Japan (2005).

Bibliography

[1] S. Datta and B. Das, "*Electronic analog of the electro-optic modulator*," Applied Physics Letters **56**, 665–7 (1990).

[2] R. A. de Groot and F. M. Mueller, "*New class of materials: half-metallic ferromagnets*," Phys. Rev. Lett. **50**, 2021 (1983).

[3] S. Holmes and M. Pepper, "*Magnetic and electrical properties of Co_2MnGa grown on GaAs (001)*," Applied Physics Letters **81**, 1651–3 (2002).

[4] S. N. Holmes and M. Pepper, "*Cobalt-Based Heusler Alloys for Spin-Injection Devices*," Journal of Superconductivity: Incorporating Novel Magnetism **16**, 191–194 (2003).

[5] P. Webster, "*Magnetic and chemical order in Heusler alloys containing cobalt and manganese*," Journal of the Physics and Chemistry of Solids **32**, 1221–31 (1971).

[6] A. Ayuela, J. Enkovaara, K. Ullakko, and R. Nieminen, "*Structural properties of magnetic Heusler alloys*," Journal of Physics: Condensed Matter **11**, 2017–26 (1999).

[7] S. Fujii, S. Sugimura, S. Ishida, and S. Asano, "*Hyperfine fields and electronic structures of the Heusler alloys Co_2MnX (X=Al, Ga, Si, Ge, Sn)*," Journal of Physics: Condensed Matter **2**, 8583–9 (1990).

[8] J. Nitta and H. Takayanagi, "*Gate control of spin-orbit interaction in an InAs-inserted $In_{0.53}Ga_{0.47}As/In_{0.52}Al_{0.48}As$ heterostructure*," Physica E **2**, 527–531 (1998).

[9] D. Grundler, "*Large Rashba splitting in InAs quantum wells due to electron wave function penetration into the barrier layers*," Physical Review Letters **84**, 6074–6077 (2000).

[10] S. Yamada, Y. Sato, S. Gozu, and T. Kikutani, "*Large and anisotropic zero-field spin-splittings in $In_xGa_{1-x}As/In_yAl_{1-y}As$ (x,y¿0.6) heterojunctions*," Physica E **7**, 992–996 (2000).

[11] D. D. Awschalom, D. Loss, and N. E. Samarth, *"Semiconductor Spintronics and Quantum Computation,"* (Springer, 2002).

[12] M. Baibich, J. Broto, A. Fert, F. Nguyen Van Dau, F. Petroff, P. Etienne, G. Creuzet, A. Friederich, and J. Chazelas, "*Giant magnetoresistance of (001)Fe/(001)Cr magnetic superlattices*," Physical Review Letters **61**, 2472–5 (1988).

[13] G. Binasch, P. Grunberg, F. Saurenbach, and W. Zinn, "*Enhanced magnetoresistance in layered magnetic structures with antiferromagnetic interlayer exchange*," Physical Review B (Condensed Matter) **39**, 4828–4830 (1989).

[14] G. A. Prinz, "*Magnetoelectronics*," Science **282**, 1660–1663 (1998).

[15] S. Wolf and D. Awschalom, "*Spintronic: A Spin-Based electronics Vision for the Future*," Science **294**, 1488–1495 (2001).

[16] S. Parkin, Z. Li, and D. Smith, "*Giant magnetoresistance in antiferromagnetic Co/Cu multilayers*," Applied Physics Letters **58**, 2710–12 (1991).

[17] C. Tsang, R. Fontana, T. Lin, D. Heim, V. Speriosu, B. Gurney, and M. Williams, "*Design, fabrication and testing of spin-valve read heads for high density recording*," Magnetics, IEEE Transactions on **30**, 3801 –3806 (1994).

[18] D. D. Djayaprawira, K. Tsunekawa, M. Nagai, H. Maehara, S. Yamagata, N. Watanabe, S. Yuasa, Y. Suzuki, and K. Ando, "*230 % room-temperature magnetoresistance in CoFeBMgOCoFeB magnetic tunnel junctions*," Applied Physics Letters **86**, 1–3 (2005).

[19] C. Ruster, C. Gould, T. Jungwirth, J. Sinova, G. Schott, R. Giraud, K. Brunner, G. Schmidt, and L. Molenkamp, "*Very large tunneling anisotropic magnetoresistance of a (Ga,Mn)As/GaAs/(Ga,Mn)As stack*," Physical Review Letters **94**, 027 203/1–4 (2005).

[20] P. Van Dorpe, Z. Liu, W. Van Roy, V. Motsnyi, M. Sawicki, G. Borghs, and J. De Boeck, "*Very high spin polarization in GaAs by injection from a (Ga,Mn) as zener diode*," Applied Physics Letters **84**, 3495–3497 (2004).

[21] X. Jiang, R. Wang, R. Shelby, R. Macfarlane, S. Bank, J. Harris, and S. Parkin, "*Highly spin-polarized room-temperature tunnel injector for semiconductor spintronics using MgO(100)*," Physical Review Letters **94**, 056 601/1–4 (2005).

[22] R. Wang, X. Jiang, R. Shelby, R. MacFarlane, S. Parkin, S. Bank, and J. Harris, "*Increase in spin injection efficiency of a CoFeMgO (100) tunnel spin injector with thermal annealing*," Applied Physics Letters **86**, 1–3 (2005).

[23] G. Itskos, E. Harbord, and S. K. Clowes, "*Oblique Hanle measurements of InAs/GaAs quantum dot spin-light emitting diodes.*" Applied Physics Letters **88**, 1–3 (2006).

[24] X. Dong, C. Adelmann, J. Xie, C. Palmstrom, X. Lou, J. Strand, P. Crowell, J.-P. Barnes, and A. Petford-Long, "*Spin injection from the Heusler alloy Co_2MnGe into $Al_{0.1}Ga_{0.9}As$/GaAs heterostructures*," Applied Physics Letters **86**, 102 107–1–3 (2005).

[25] I. Zutic, J. Fabian, and S. Das Sarma, "*Spintronics: fundamentals and applications*," Reviews of Modern Physics **76**, 323–410 (2004).

[26] F. Bloch, "*Nuclear induction*," Physical Review **70**, 460–474 (1946).

[27] H. Torrey, "*Bloch equations with diffusion terms*," Physical Review **104**, 563–565 (1956).

[28] S. E. Maekawa, *"Concepts in Spin Electronics,"* (Oxford University Press, 2006 Not Yet Published due Mar 15).

[29] J. Fabian and S. Sarma, "*Spin relaxation of conduction electrons*," Journal of Vacuum Science and Technology B (Microelectronics and Nanometer Structures) **17**, 1708–15 (1999).

[30] V. Puller, L. Mourokh, N. Horing, and A. Smirnov, "*Electron spin relaxation in a semiconductor quantum well*," Physical Review B (Condensed Matter and Materials Physics) **67**, 155 309 (2003).

[31] M. D'yakonov and V. Perel, "*On spin orientation of electrons in interband absorption of light in semiconductors*," Zhurnal Eksperimental'noi i Teoreticheskoi Fiziki **60**, 1954–65 (1971).

[32] M. D'yakonov and V. Kachorovskii, "*Spin relaxation of two-dimensional electrons in noncentrosymmetric semiconductors*," Fizika i Tekhnika Poluprovodnikov **20**, 178–81 (1986).

[33] E. Rashba, "*Properties of semiconductors with an extremum loop. I. Cyclotron and "combinational" resonance in a magnetic field perpendicular to the plane of the loop*," Fizika Tverdogo Tela **2** (1960).

[34] F. Meier and B. Zakharchenya, *"Optical orientation,"* (North-Holland, 1984).

[35] J. Strand, X. Lou, C. Adelmann, B. D. Schultz, A. F. Isakovic, C. J. Palmstrom, and P. A. Crowell, "*Electron spin dynamics and hyperfine interactions in Fe/$Al_{0.1}Ga_{0.9}As$/GaAs spin injection heterostructures*," Physical Review B (Condensed Matter and Materials Physics) **72**, 155 308 (2005).
http://link.aps.org/abstract/PRB/v72/e155308

[36] V. Motsnyi, P. Van Dorpe, W. Van Roy, E. Goovaerts, V. Safarov, G. Borghs, and J. De Boeck, "*Optical investigation of electrical spin injection into semiconductors*," Physical Review B (Condensed Matter and Materials Physics) **68**, 245 319–1–13 (2003).

[37] J. Strand, B. Schultz, A. Isakovic, C. Palmstrom, and P. Crowell, "*Dynamic nuclear polarization by electrical spin injection in ferromagnet-semiconductor heterostructures*," Physical Review Letters **91**, 036 602/1–036 602/4 (2003).

[38] P. Tedrow and R. Meservey, "*Spin polarization of electrons tunneling from films of Fe, Co, Ni, and Gd*," Physical Review B (Solid State) **7**, 318–26 (1973).

[39] R. Meservey and P. Tedrow, "*Spin-polarized electron tunneling*," Physics Reports **238**, 173–243 (1994).

[40] R. Meservey, P. Tedrow, and P. Fulde, "*Magnetic field splitting of the quasiparticle states in superconducting aluminum films*," Physical Review Letters **25**, 1270–2 (1970).

[41] R. Meservey, D. Paraskevopoulos, and P. Tedrow, "*Correlation between spin polarisation of tunnel currents from 3d ferromagnets and their magnetic moments*," Physical Review Letters **37**, 858–60 (1976).

[42] R. Meservey, P. M. Tedrow, V. R. Kalvey, and D. Paraskevopoulos, "*Studies of ferromagnetic metals by electron spin polarized tunneling*," Journal of Applied Physics **50**, 1935–1939 (1979).

[43] J. Bardeen, L. Cooper, and J. Schrieffer, "*Theory of superconductivity*," Physical Review **108**, 1175–1203 (1957).

[44] V. Motsnyi, *"Optical Investigation of Electrical Spin Injection into Semiconductors,"*, Ph.D. thesis, Universiteit Antwerpen, Faculteit wetenschappen, Departement Natuurkunde (2003).

[45] J. Soulen, R.J., J. Byers, M. Osofsky, B. Nadgorny, T. Ambrose, S. Cheng, P. Broussard, C. Tanaka, J. Nowak, J. Moodera, A. Barry, and J. Coey, "*Measuring the spin polarization of a metal with a superconducting point contact*," Science **282**, 85–8 (1998).

[46] G. Blonder, M. Tinkham, and T. Klapwijk, "*Transition from metallic to tunneling regimes in superconducting microconstrictions: excess current, charge imbalance, and supercurrent conversion*," Physical Review B (Condensed Matter) **25**, 4515–4532 (1982).

[47] G. Blonder and M. Tinkham, "*Metallic to tunneling transition in Cu-Nb point contacts*," Physical Review B (Condensed Matter) **27**, 112–18 (1983).

[48] G. J. Strijkers, Y. Ji, F. Y. Yang, C. L. Chien, and J. M. Byers, "*Andreev reflections at metal/superconductor point contacts: Measurement and analysis* ," Physical Review B **63**, 104 510 (2001).

[49] A. Fert and H. Jaffres, "*Conditions for efficient spin injection from a ferromagnetic metal into a semiconductor*," Physical Review B **64**, 184 420 (2001).

[50] P. van Son, H. van Kempen, and P. Wyder, "*Boundary resistance of the ferromagnetic-nonferromagnetic metal interface*," Physical Review Letters **58**, 2271–3 (1987).

[51] E. Rashba, "*Theory of electrical spin injection: Tunnel contacts as a solution of the conductivity mismatch problem*," Physical Review B **62**, R16 267–70 (2000).

[52] S. E. Andresen, *"Spin polarised tunnelling in magnetic semiconductor structures,"*, Ph.D. thesis, University of Copenhagen, Niels Bohr Institute (2004).

[53] G. Schmidt, C. Gould, P. Grabs, A. Lunde, G. Richter, A. Slobodskyy, and L. Molenkamp, "*Spin injection in the nonlinear regime: Band bending effects*," Physical Review Letters **92**, 226 602–1–226 602–4 (2004).

[54] H. Kosaka, A. Kiselev, F. Baron, K. W. Kim, and E. Yablonovitch, "*Electron g factor engineering in IlI-V semiconductors for quantum communications*," Electronics Letters **37**, 464–465 (2001).

[55] G. Salis, Y. Kato, K. Ensslin, D. Driscoll, A. Gossard, and D. Awschalom, "*Electrical control of spin coherence in semiconductor nanostructures*," Nature **414**, 619–622 (2001).

[56] I. Galanakis and P. H. Dederichs, "*Half-metallicity and Slater-Pauling behavior in the ferromagnetic Heusler alloys*," arXiv:cond-mat p. 0408068 (2004).

[57] S. Lewis, P. Allen, and T. Sasaki, "Band structure and transport properties of CrO_2," Physical Review B (Condensed Matter) **55**, 10 253–10 260 (1997).

[58] Y. Ji, G. Strijkers, F. Yang, C. Chien, J. Byers, A. Anguelouch, G. Xiao, and A. Gupta, "*Determination of the spin polarization of half-metallic CrO_2 by point contact Andreev reflection*," Physical Review Letters **86**, 5585–5588 (2001).

[59] J. M. D. Coey and M. Venkatesan, "*Half-metallic ferromagnetism: Example of CrO2 (invited)*," Journal of Applied Physics **91**, 8345–8350 (2002).

[60] F. Heusler, W. Starck, and E. Haupt, "*Some magnetic alloys of manganese*," Verhandlungen der Deutschen Physikalischen Gesellschaft **5** (1903).

[61] P. Courtois, "*Characterization of Heusler crystals for polarized neutrons monochromators*," Physica B **267**, 363–366 (1999).

[62] W. Van Roy, G. Borghs, and J. De Boeck, "*Epitaxial growth of the half-metallic ferromagnet NiMnSb on GaAs(001)*," Journal of Crystal Growth **227-228**, 862–866 (2001).

[63] E. Girgis, P. Bach, C. Ruster, C. Gould, G. Schmidt, and L. Molenkamp, "*Giant magnetoresistance in an epitaxial NiMnSb/Cu/CoFe multilayer*," Applied Physics Letters **86**, 142 503–1–3 (2005).

[64] J. Dong, L. Chen, J. Xie, T. Muller, D. Carr, C. Palmstrom, S. McKernan, Q. Pan, and R. James, "*Epitaxial growth of ferromagnetic Ni_2MnGa on GaAs(001) using NiGa interlayers*," Journal of Applied Physics **88**, 7357–9 (2000).

[65] M. Lund, J. Dong, J. Lu, X. Dong, C. Palmstrom, and C. Leighton, "*Anomalous magnetotransport properties of epitaxial full Heusler alloys*," Applied Physics Letters **80**, 4798–4800 (2002).

[66] J. Dong, J. Lu, J. Xie, L. Chen, R. James, S. McKernan, and C. Palmstroem, "*MBE growth of ferromagnetic single crystal Heusler alloys on (0 0 1)Ga/sub 1-x/In/sub x/As*," Physica E **10**, 428–432 (2001).

[67] T. Ambrose, J. Krebs, and G. Prinz, "*Epitaxial growth and magnetic properties of single-crystal Co_2MnGe Heusler alloy films on GaAs (001)*," Applied Physics Letters **76**, 3280–3282 (2000).

[68] U. Geiersbach, A. Bergmann, and K. Westerholt, "*Preparation and structural properties of thin films and multilayers of the Heusler compounds Cu2MnAl, Co2MnSn, Co2MnSi and Co2MnGe,*," Thin Solid Films **425**, 225–232 (2003).

[69] M. Raphael, B. Ravel, M. Willard, S. Cheng, B. Das, R. Stroud, K. Bussmann, J. Claassen, and V. Harris, "*Magnetic, structural, and transport properties of thin film and single crystal Co_2MnSi*," Applied Physics Letters **79**, 4396–4398 (2001).

[70] B. Ravel, M. Raphael, V. Harris, and Q. Huang, "*EXAFS and neutron diffraction study of the Heusler alloy Co_2MnSi*," Physical Review B (Condensed Matter and Materials Physics) **65**, 1–8 (2002).

[71] L. J. Singh, Z. H. Barber, Y. Miyoshi, W. R. Branford, and L. F. Cohen, "*Structural and transport studies of stoichiometric and off-stoichiometric thin films of the full Heusler alloy Co2MnSi*," Journal of Applied Physics **95**, 7231–7233 (2004).

[72] L. J. Singh, Z. H. Barber, A. Kohn, A. K. Petford-Long, Y. Miyoshi, Y. Bugoslavsky, and L. F. Cohen, "*Interface effects in highly oriented films of the Heusler alloy Co_2MnSi on GaAs(001)*," Journal of Applied Physics **99**, 013 904 (2006). http://link.aip.org/link/?JAP/99/013904/1

[73] W. Schreiner, D. Brandao, F. Ogiba, and J. Kunzler, "*Electrical resistivity of Heusler alloys*," Journal of the Physics and Chemistry of Solids **43**, 777–80 (1982).

[74] M. Pechan, C. Yu, D. Carr, and C. Palmstrom, "*Remarkable strain-induced magnetic anisotropy in epitaxial Co_2MnGa (001) films*," Journal of Magnetism and Magnetic Materials **286**, 340–345 (2005).

[75] S. Picozzi, A. Continenza, and A. J. Freeman, "*Role of structural defects on the half-metallic character of Co2MnGe and Co2MnSi Heusler alloys*," Physical Review B **69**, 94 423 (2004).

[76] S. Picozzi, A. Continenza, and A. J. Freeman, "*Co2MnX (X = Si, Ge, Sn) Heusler compounds: An ab initio study of their structural, electronic, and magnetic properties at zero and elevated pressure*," Physical Review B **66**, 94 421 (2002).

[77] I. Galanakis, P. H. Dederichs, and N. Papanikolaou, "*Magnetism - Slater-Pauling behavior and origin of the half-metallicity of the full-Heusler alloys*," Physical Review B **66**, 174 429 (2002).

[78] P. Hohenberg and W. Kohn, "*Inhomogeneous electron gas*," Physical Review **136**, B864–B871 (1964).

[79] W. Kohn and L. Sham, "*Self-consistent equations including exchange and correlation effects*," Physical Review **140**, A1133–A1138 (1965).

[80] Y. Kurtulus, R. Dronskowski, G. Samolyuk, and V. Antropov, "*Electronic structure and magnetic exchange coupling in ferromagnetic full Heusler alloys*," Physical Review B **71**, 14 425–1–12 (2005).

[81] W. Van Roy, M. Wojcik, E. Jedryka, S. Nadolski, D. Jalabert, B. Brijs, G. Borghs, and J. De Boeck, "*Very low chemical disorder in epitaxial NiMnSb films on GaAs(111)*," Applied Physics Letters **83**, 4214–4216 (2003).

[82] C. Chen, Y. Idzerda, H.-J. Lin, N. Smith, G. Meigs, E. Chaban, G. Ho, E. Pellegrin, and F. Sette, "*Experimental confirmation of the X-ray magnetic circular dichroism sum rules for iron and cobalt*," Physical Review Letters **75**, 152–155 (1995).

[83] J. Schmalhorst, S. Kammerer, M. Sacher, G. Reiss, A. Hutten, and A. Scholl, "*Interface structure and magnetism of magnetic tunnel junctions with a Co_2MnSi electrode*," Physical Review B (Condensed Matter and Materials Physics) **70**, 24 426 (2004).

[84] O. Bunk and M. Nielsen, "*Angle calculations for a z-axis/(2S+2D) hybrid diffractometer*," Journal of Applied Crystallography **37**, 216–22 (2004).

[85] http://www.fys.risoe.dk/public/bw2/bw2_notes.pdf.

[86] Powder Diffraction File Database (2001), *"The Powder Diffraction File (PDF) is a collection of single-phase X-ray powder diffraction patterns in the form of tables of the interplanar spacings and relative intensities characteristic of the compound. The PDF has been used for almost six decades, and today the International Center for Diffraction Data (ICDD) maintains the PDF by continually adding new and updated diffraction patterns to the file.*

[87] L. Gerward, "*X-ray Analytical Methods*," Tech. rep., Technical University of Denmark, Kongens Lyngby (2001).

[88] H. Kiessig, "*Interference of X-rays in thin films*," Annalen der Physik **10** (1931).

[89] J. Als-Nielsen and D. McMorrow, *"Elements of Modern X-Ray Physics,"* (John Wiley and Sons, Ltd., Chichester, 2001).

[90] I. Robinson, R. Tung, and R. Feidenhansl, "*X-ray interference method for studying interface structures*," Physical Review B **38**, 3632 (1988).

[91] P. Bhattacharya, *"Properties of lattice-matched and strained Indium Gallium Arsenide,"* (INSPEC, 1993).

[92] C. Ferrari, M. Bruni, F. Martelli, and M. Simeone, "*InGaAs/GaAs strained single quantum well characterization by high resolution x-ray diffraction*," Journal of Crystal Growth **126**, 144–150 (1993).

[93] M. Meisel, W.-S. Zhou, J. Owers-Bradley, Y. Ochiai, J. Brittain, and W. Halperin, "*Magnetic properties of CoGa alloys and the transition from spin glass to ferromagnetism*," Journal of Physics F (Metal Physics) **12**, 317–331 (1982).

[94] S. C. Erwin, S.-H. Lee, and M. Scheffler, "*Surface physics, low-dimensional systems, and related topics - First-principles study of nucleation, growth, and interface structure of Fe/GaAs (10 pages)*," Physical Review B **65**, 205 422 (2002).

[95] S. Mirbt, B. Sanyal, C. Isheden, and B. Johansson, "*Surface physics, low-dimensional systems, and related topics - First-principles calculations of Fe on GaAs(100) (9 pages)*," Physical Review B **67**, 155 421 (2003).

[96] Powder Diffraction File Database (2001), co_2MnGa PDF#32-0389.

[97] J. Moodera and D. Mootoo, "*Nature of half-metallic ferromagnets: transport studies*," Journal of Applied Physics **76**, 6101–3 (1994).

[98] K. Suzuki and P. Tedrow, "*Resistivity and magnetotransport in CrO_2 films*," Physical Review B (Condensed Matter) **58**, 11 597–11 602 (1998).

[99] S. Watts, S. Wirth, S. Von Molnar, A. Barry, and J. Coey, "*Evidence for two-band magnetotransport in half-metallic chromium dioxide*," Physical Review B (Condensed Matter) **61**, 9621–9628 (2000).

[100] S. Ogale, K. Ghosh, R. Sharma, R. Greene, R. Ramesh, and T. Venkatesan, "*Magnetotransport anisotropy effects in epitaxial magnetite (Fe_3O_4) thin films*," Physical Review B (Condensed Matter) **57**, 7823–7828 (1998).

[101] R. O'Handley, *"Modern Magnetic Materials,"* (John Wiley and Sons, 1999).

[102] J. Kondo, "*Resistance minimum in dilute magnetic alloys*," Progress of Theoretical Physics **32** (1964).

[103] G. Apostopoulos and C. Papastaikoudis, "*The influence of thickness on the Kondo effect in Cu(Fe) thin films*," Solid State Communications **99**, 277–281 (1996).

[104] R. Taboryski, T. Clausen, J. Bindslev Hansen, J. Skov, J. Kutchinsky, C. Sorensen, and P. Lindelof, "*Andreev reflections at interfaces between delta-doped GaAs and superconducting Al films*," Applied Physics Letters **69**, 656–658 (1996).

[105] Y. Sharvin, "*Observation of dynamic intermediate state of superconductors with the aid of microcontacts*," Zhurnal Eksperimental'noi i Teoreticheskoi Fiziki, Pis'ma v Redaktsiyu **2** (1965).

[106] F. Jedema, H. Heersche, A. Filip, J. Baselmans, and B. van Wees, "*Electrical detection of spin precession in a metallic mesoscopic spin valve*," Nature **416**, 713–16 (2002).

[107] C. Adelmann, X. Lou, J. Strand, C. Palmstrom, and P. Crowell, "*Spin injection and relaxation in ferromagnet-semiconductor heterostructures*," Physical Review B (Condensed Matter and Materials Physics) **71**, 121 301 (2005).

[108] T. Manago and H. Akinaga, "*Spin-polarized light-emitting diode using metal/insulator/semiconductor structures*," Applied Physics Letters **81**, 694–696 (2002).

[109] A. Hanbicki, B. Jonker, G. Itskos, G. Kioseoglou, and A. Petrou, "*Efficient electrical spin injection from a magnetic metal/tunnel barrier contact into a semiconductor*," Applied Physics Letters **80**, 1240–1242 (2002).

[110] H. Zhu, M. Ramsteiner, H. Kostial, M. Wassermeier, H.-P. Schonherr, and K. Ploog, "*Room-temperature spin injection from Fe into GaAs*," Physical Review Letters **87**, 016 601/1–016 601/4 (2001).

[111] S. Andresen, B. Sorensen, F. Rasmussen, P. Lindelof, J. Sadowski, C. Guertler, and J. Bland, "*Spin-polarized electron tunneling across a Si delta-doped GaMnAs/n-GaAs interface*," Journal of Applied Physics **94**, 3990–3994 (2003).

[112] Y. Haiping, C. Roberts, and R. Murray, "*Exciton recombination dynamics in InxGa1-xAs/GaAs quantum wells*," Physical Review - Section B - Condensed Matter **52**, 1493–1496 (1995).

[113] http://www.nd.edu/~gsnider.

[114] http://www.ioffe.rssi.ru/SVA/NSM/Level/index.php.

[115] T. Ohtoshi and M. Yamanishi, "*Optical line shape functions in quantum-well and quantum-wire structures*," Quantum Electronics, IEEE Journal of **27**, 46–53 (1991).

[116] Y. Haiping, C. Roberts, and R. Murray, "*Influence of indium segregation on the emission from InGaAs/GaAs quantum wells*," Applied Physics Letters **66**, 2253–2255 (1995).

[117] A. and V. Safarov, "*Influence of spin relaxation of 'hot' electrons on the effectiveness of optical orientation in semiconductors*," JETP Letters **13**, 700–704 (1971).

[118] M. C. Hickey, *"Spin polarised tunnelling in magnetic semiconductor structures,"*, Ph.D. thesis, University of Cambridge, Cavendish Laboratory and Toshiba Research Europe LTD (2005).

[119] M. C. Hickey, C. D. Damsgaard, I. Farrer, S. N. Holmes, A. Husmann, J. B. Hansen, C. S. Jacobsen, D. A. Ritchie, R. F. Lee, G. A. C. Jones, and M. Pepper, "*Spin injection between epitaxial Co2.4Mn1.6Ga and an InGaAs quantum well*," Applied Physics Letters **86**, 252 106 (2005).

[120] J. Martinez-Pastor, A. Vinattieri, L. Carraresi, M. Colocci, P. Roussignol, and G. Weimann, "*Temperature dependence of exciton lifetimes in GaAs/AlGaAs single quantum wells*," Physical Review B (Condensed Matter) **47**, 10 456–10 460 (1993).

[121] A. Malinowski, D. Guerrier, N. Traynor, and R. Harley, "*Larmor beats and conduction electron g factors in $In_xGa_{1-x}As$/GaAs quantum wells*," Physical Review B (Condensed Matter) **60**, 7728–7731 (1999).

[122] B. Kowalski, V. Zwiller, C. Wiggren, P. Varekamp, M. Miller, M. Pistol, P. Omling, and L. Samuelson, "*Conduction band spin splitting in $In_xGa_{x-1}As$/GaAs quantum wells*," Japanese Journal of Applied Physics **37**, 4272–4276 (1998).

[123] J. Song, N. Pryds, K. Glejbol, K. Morch, A. Tholen, and L. Christensen, "*A development in the preparation of sharp scanning tunneling microscopy tips*," Review of Scientific Instruments **64**, 900–3 (1993).

[124] A. H. Sorensen, U. Hvid, M. W. Mortensen, and K. A. Morch, "*Preparation of platinum/iridium scanning probe microscopy tips*," Review of Scientific Instruments **70**, 3059–3067 (1999).

[125] J. Samuelsson, *"The fine scale microstructure of tunnelbarriers in Al/AlOx/Al tunneljunctions,"*, Master's thesis, Chalmers university of Technology (2003).

Appendix A

Calculations of changes in stoichiometry and swaps of Mn/Ga

A.1 Variation of Mn/Ga-Stoichiometry

Composition	GGA change in lattice parameter a
$Co_2Mn_{1.1}Ga_{0.9}$	-0.12 %
$Co_2Mn_{0.9}Ga_{1.1}$	+0.14 %

Table A.1: *GGA estimates* $a = 5.75$ *Å for* $Co_2Mn_1Ga_1$.

Figure A.1 shows the change in spin polarization and total magnetic moment, Figure A.2 shows the change in local magnetic moment.

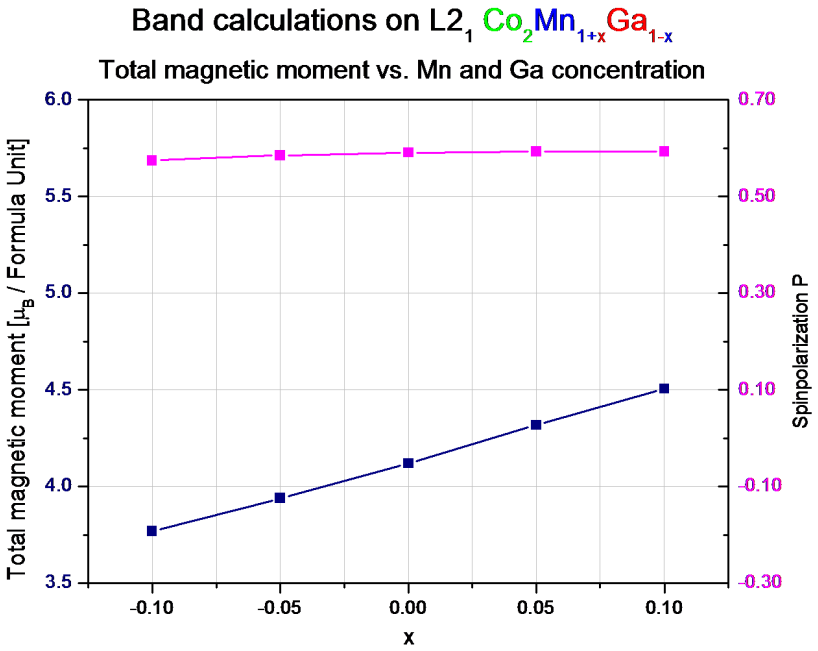

Figure A.1: *Calculation of spin polarization and total magnetic moment vs. Mn-Ga ratio*

Only a small change in both spin polarization and magnetic moment is seen.

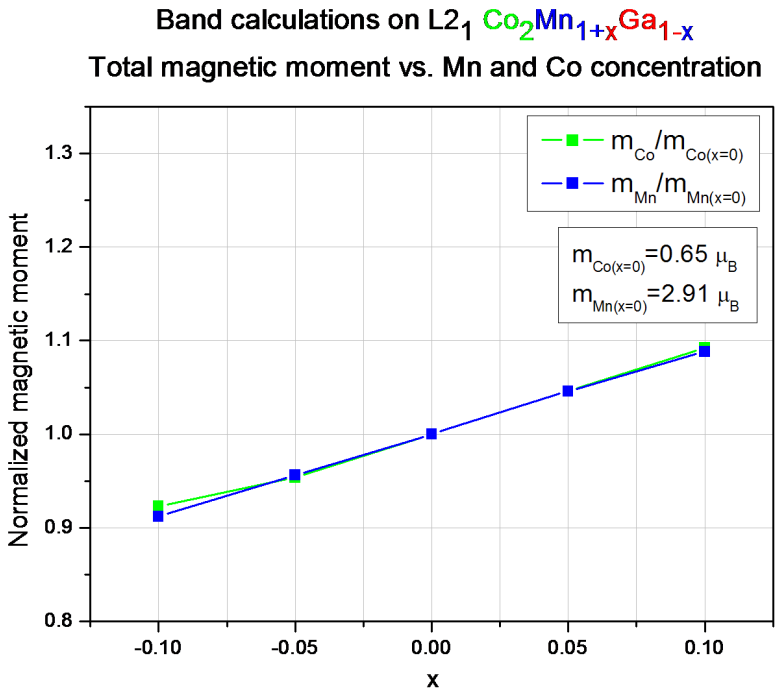

Figure A.2: *Co and Mn magnetic moments vs. Mn-Ga ratio*

Table A.2 shows the local magnetic moments on each atom-site in the crystal, calculated in the case of $Co_2.0Mn_{0.9}Ga_{1.1}$.

Sublattice	**Ga**		**Mn**		**Co**	**Total**
Atom	**Ga (1.0)**	**Mn (0)**	**Mn (0.9)**	**Ga (0.1)**	**Co(2)**	
Magnetic moment [μ_B]	-0.08	2.93	2.95	-0.06	0.6	3.77

Table A.2: *Local and total magnetic moment for $Co_{2.0}Mn_{0.9}Ga_{1.1}$*

A.1.1 Variation of Mn-Ga swaps

The influence of Mn-Ga swaps on spin polarization and total magnetic moment is seen in Figure A.3, while influence on the local magnetic moment of Mn and Ga is seen in Figure A.4

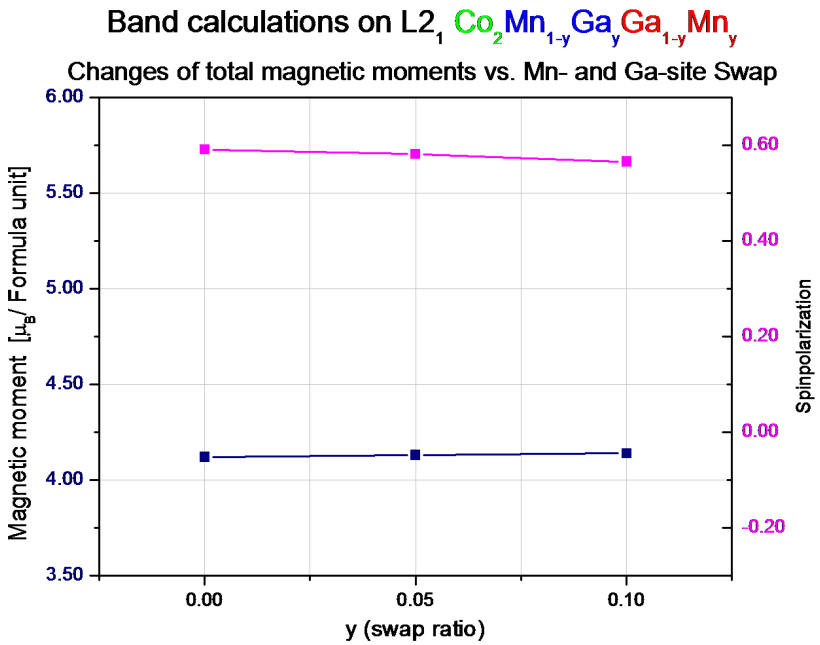

Figure A.3: *Calculation of spin polarization and total magnetic moment vs. Mn-Ga swaps.*

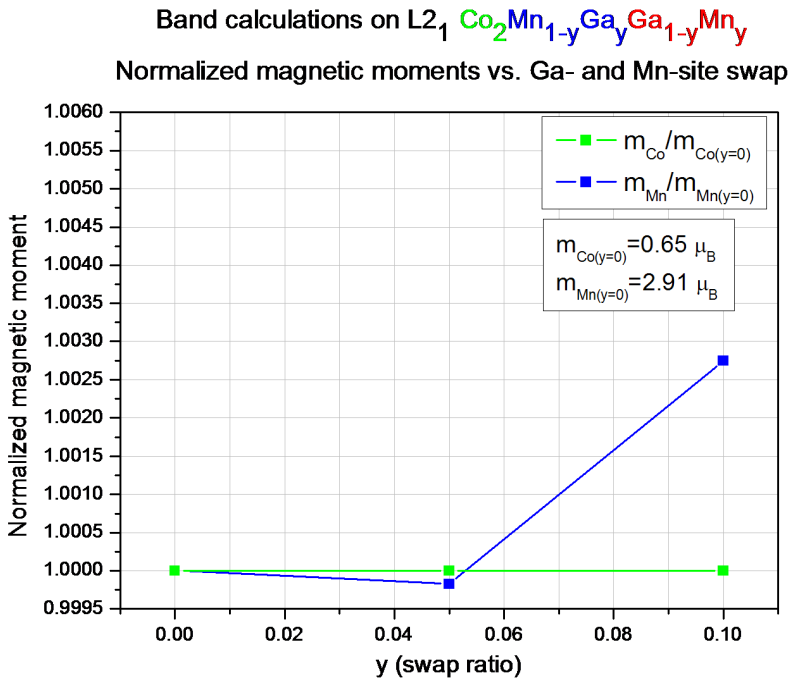

Figure A.4: *Co and Mn magnetic moments vs. Mn-Ga swaps.*

Again the changes are only small.

Appendix B

X-ray Magnetic Circular Dichroism (XMCD) measurements on Co-Mn-Ga thin films grown on GaAs

B.1 XMCD collaboration

Three batches of samples were grown specifically for analyses of the average magnetic moments of the Co and the Mn atoms in the thin films of Co_2mnGa/GaAs(100) by measurements of the X-Ray Magnetic Circular Dichroism (XMCD). This work was made in a collaboration involving DTU, the Univ. of York. UK, the Daresbury Synchrotron Radiation Source (SRS), Warrington, UK, and Toshiba Research Europe, Ltd., Cambridge Research Lab., Cambridge, UK. The XMCD measurements were carried out in Dec. 2004 and in April and Oct. 2005 by a group at the Spintronics Laboratory, Department of Electronics, University of York: J.S. Claydon, Y.B. Xu and S. Hassan, in collaboration with a group at the Daresbury SRS: N.J. Farley, N.D. Telling and G. van der Laan.

B.2 Method

The samples were measured at room temperature. The XMCD technique is element specific as it is based on X-ray absorption spectroscopy of electron core states of the atoms (the L2,3 absorption edges are used). The samples are placed with the sample plane at an angle of 45 °(see Figure B.1) to the incident X-ray synchrotron beam which is aligned with an applied magnetic field of approximately 0.8 T.

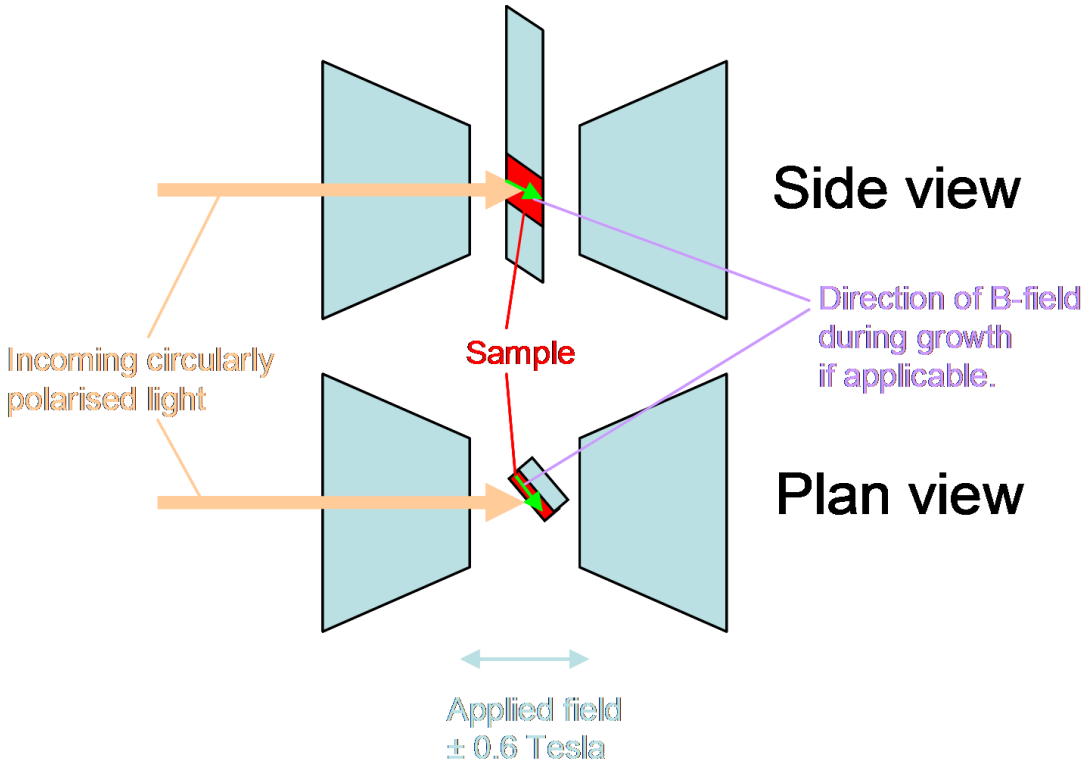

Figure B.1: *Schematically representation of the XMCD setup. In the sketched configuration the sample is placed with the sample plane at an angle of 45 degrees to the incident X-ray synchrotron beam which is aligned with an applied magnetic field of approx. 0.8 T.*

During the measurement the field is reversed and the difference between the absorption lines for the two field directions may be used to calculate the average local moments (both orbital and spin parts).
The method is only probing the magnetic moments in the sample down to about 5 nm. Therefore rather thin film samples were used (from 2 to 20 nm nominal thickness).
Three batches of Co_2MnGa/GaAs samples were grown under varying conditions (19 samples in total). At first two samples were grown with a nominal thickness of 20 nm (VG05-077). This pair of samples were grown at $T(substrate)$ = 300 C and at a total of rate of about 2.4 nm/min. These samples were not capped. The XMCD analyses showed signs of oxidation of the Mn. The next two batches were capped with Al after growth: VG05-041 with Fe + Al and VG05-040 with 1.0 nm of Al (in all 8 samples with different CoMnGa thicknesses) and when this Al cap thickness was found to be insufficient (i.e. some of the Mn was still found to be oxidized) the batches VG05-088, VG05-089, and VG05-090 were capped with 1.5-1.7 nm of Al (all in all 9 samples with different CoMnGa thicknesses).
Bulk Mn is anti-ferromagnetic. Bulk Co is ferromagnetic with m_l =0.153 μ_B and m_s = 1.55 μ_B, Chen *et al.* [82]. The distribution of magnetic moments within the Co_2MnGa

structure is at low temperature expected to be: Co: 0.65 μ_B, Mn: 2.91 μ_B, and Ga: -0.09 μ_B.

From temperature dependent measurements on bulk Co_2MnGa, Webster *et al.* [5], we expect the local magnetic moments values to decrease with a factor of approximately 10 % at 300 K. i.e. magnetic moment is expected to move from Co to Mn.

The spin and orbital moments have been calculated using the XMCD sum rules as described in Chen et. al. [82], (see the Table below). The moments are proportional to the number of 3d holes per atom which are estimated to be: n_h = 2.2 for Co and n_h = 4.5 for Mn, Schmalhorst *et al.* [83].

B.3 Results

Examples of raw data are shown in figure B.2 and B.3.

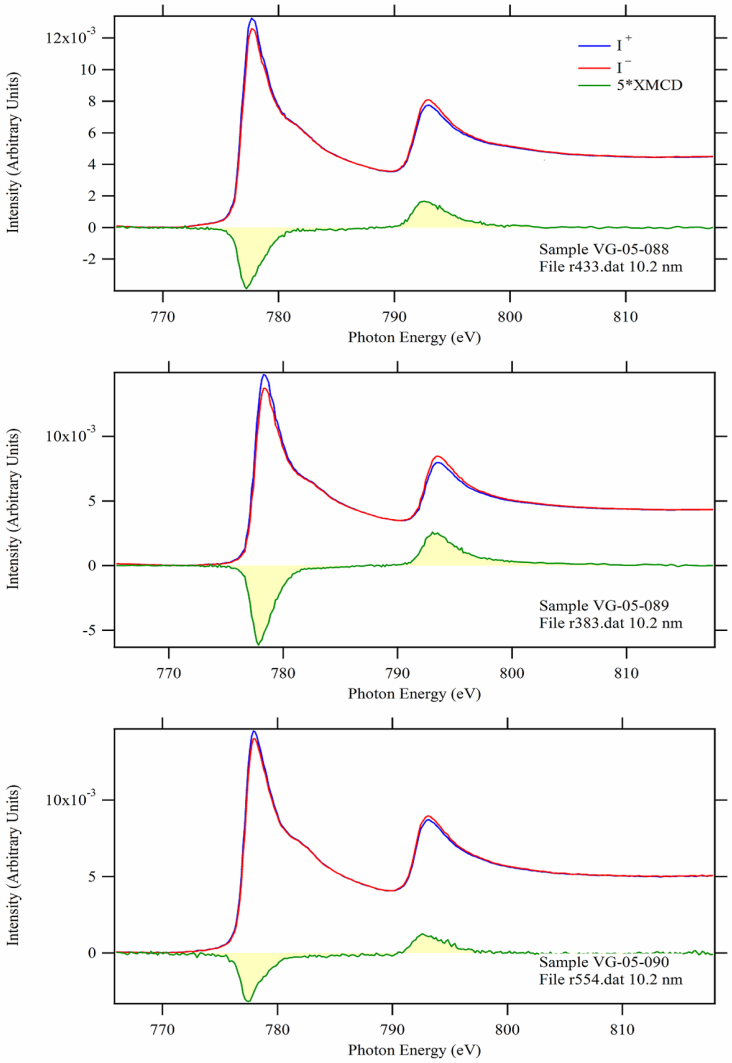

Figure B.2: *XMCD data for Co at 300 K (courtesy J. Claydon et al). Samples VG05-088+089+090 (t_{nom} = 10.2 nm).*

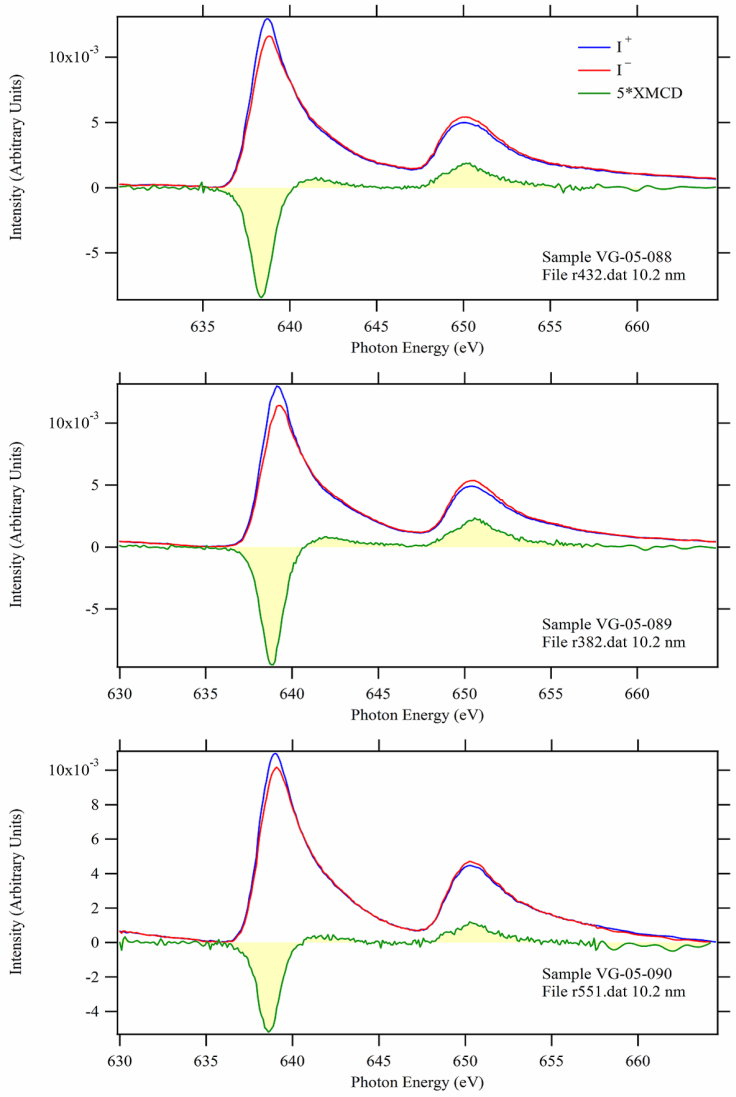

Figure B.3: *XMCD data for Mn at 300 K (courtesy J. Claydon et al). Samples VG05-088+089+090 (t_{nom} = 10.2 nm).*

Figure B.4 shows an overview of the measured values from samples VG05-088, VG05-089, and VG05-090.

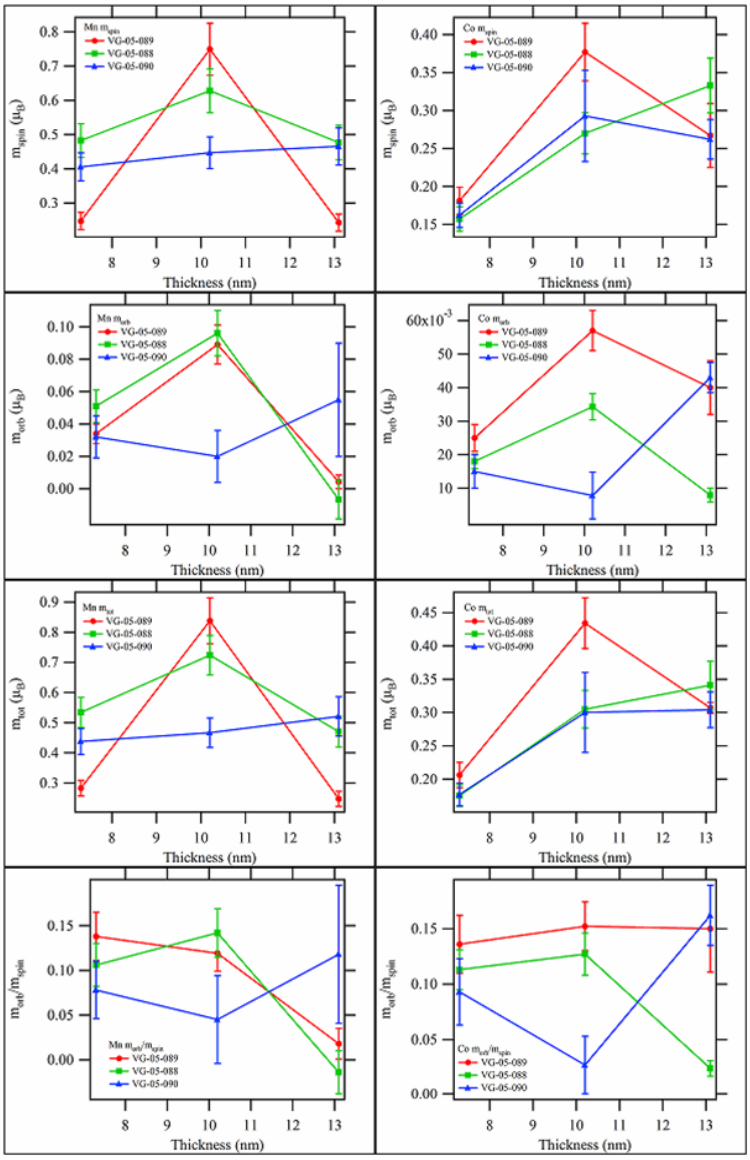

Figure B.4: *XMCD data for Mn at 300 K (courtesy J. Claydon et al). Samples VG05-088+089+090. All thicknesses are nominal.*

Tables B.1 and B.2 summarize the sample parameters and estimates of the stoichiometry.

B.4 Conclusions

In order to validate the calculations, a systematic study of the local spin and orbital moments on samples with different thickness and stoichiometry was done. The obtained

Sample name, source materials and nominal thicknesses	**Fabrication date**	**Substrate material**	**Temperature of effusion -cells and nominal and measured rates**	**Substrate temperature and stoichimetry estimated from rate ratios and ICP-OES results for calibration samples**	**Comments**	**Results of XMCD analyses Average magnetic moment in units of Bohr magnetrons μ_B**
VG-CoMnGa-04-077 Co, Mn, Ga t = 20 nm	8/12/04	Two GaAs WT#52 (commercial epi-ready) Special samples holder with NiAlCo magnets SAMPLES: A(smaller): outside B-field B (larger): in B-field (6.6 mT) In-bonding No buffer layer	T(Ga): 983 C T(Mn): 1150 C Nominal/meas. rates (nm/s): Co: 0.0100/ 0.0095* Mn: 0.0097/ 0.0100 Ga: 0.0207/ 0.0202 * Co source with feedback control Check/adjusting Co rate on FTM3: 0.0235 nm/s(Ga par.) Average total rate = 0.0637 nm/s (Ga parameters)	300 C Estimated stoichiometry: Co2.23 Mn 1.21 Ga 1.00	Both samples sent for XMCD at Daresbury on 081204: Sample A: grown outside B-field Sample B: grown in B-field (6.6 mT parallel to sample plane)	**Grown in field, (B) (without field, A)** **Co moments:** m_l = 0.068 +/- 0.011 (0.056 +/-0.003) m_s = 0.74 +/0.09 (0.69 +/- 0.09) **Mn moments:** m_l = -0.0063 +/- 0.0049 (-0.0182 +/- 0.0032 m_s = 0.43 +/-0.05 (0.59 +/- 0.07)
VG-CoMnGa-05-040 Co, Mn, Ga, Al t (nominal) = 2.9, 5.8, 8.7, 10.1 nm (6 + 6 + 6 + 4 min) + 10 Å Al	7/4/05	One GaAs piece NBI#9 (QW + Schottky on p-type substrate) Special sample-holder with shutter, substrate size: 8 x 17 mm2 Shutter moved about 4 mm in 3 steps In-bonded No buffer layer	T(Ga): 900 C T(Mn): 1036 C GROWN WITH 5 times LOWER rates than normal Nominal/meas. rates (nm/s): **HERE ALL RATES SHOULD BE MULTIPLIED BY 0.2:** Co: 0.0100/ 0.00994-958-992-983* Mn: 0.0070/ 0.0066 Ga: 0.0162/ 0.0160 * Co source with feedback control Mn+ Ga rates: 0.0298/286/292 nm/s (Ga par.) Average of total rates for 4 layers = (0.0453/443/455/438) nm/s Total average rate over 22 min: = 0.0448 nm/s (Ga parameters) Aim for 155/140/162 (sum = 457) (recipe after ICP-12) ON AVERAGE achieved: 156/132/160 X 0.2 (sum = 448x 0.2)	Co2MnGa thin film grown at 300 C Al-capped at –18 C after cooling for 3 hours) Low rate Estimated stoichiometry: C02.67 Mn 1.09 Ga 1.00	As-desorption at 450 C (60 min) + 500 C (2 min) = As-rich surface All 4 samples sent for XMCD at Daresbury on 080405. XMCD on April 11-14, 2005	**Absorption spectra recorded but not analysed due to oxidation effects**
VG-CoMnGa-05-041 Co, Mn, Ga, Fe, Al t (nominal) = 2.9, 5.8, 8.7, 14.1 nm + x nm Fe(*) + 1 nm Al (6 + 6 + 6 + 12 min) Actual thicknesses: 2, 4, 6, 10 nm (*) 2.1 mg Fe used in W-boat in LL : Fe to be re-calibrated	8/4/05	One GaAs piece NBI#9 (QW + Schottky on p-type substrate) Special sample-holder with shutter, substrate size: 8 x 17 mm2 Shutter moved about 4 mm in 3 steps In-bonded No buffer layer	T(Ga): 900 C T(Mn): 1036 C Nominal/meas. rates (nm/s): **HERE ALL RATES SHOULD BE MULTIPLIED BY 0.2:** Co: 0.0100/ 0.00* Mn: 0.0070/ 0.0072 Ga: 0.0162/ 0.0161 * Co source with feedback control Mn+ Ga rates: 0.0311/293/300/ 308/309 nm/s (Ga par.) Av. = 0.0304 nm/s Average of total rates for 4 layers = (0.0451/447/461/ 468/) nm/s Total average rate over 30 min: = 0.0459 nm/s (Ga parameters) Aim for 155/140/162 (sum = 457) (recipe after ICP-12) ON AVERAGE achieved: 155/143/161 X 0.2 (sum = 459x 0.2)	Co2MnGa thin film grown at 300 C Fe-capped at 100 C (after 20 minutes) Al-capped at 45 C after cooling for 25 min) Low rate Estimated stoichiometry: C02.67 Mn 1.17 Ga 1.00	New As-desorption procedure (à la Cavendish): 450 C (60 min) + 550 C (30 min) + 570 C (2 min) = Ga-rich surface All 4 samples sent for XMCD at Daresbury on 080405. XMCD on April 11-14, 2005	**Absorption spectra recorded but not analysed due to absorption in Fe layer**

Table B.1: *XMCD samples: Growth parameters and comments.*

Sample name, source materials and nominal thicknesses	Fabrication date	Substrate material	Temperature of effusion -cells and nominal and measured rates	Substrate temperature and stoichimetry estimated from rate ratios and ICP-OES results for calibration samples	Comments	Results of XMCD analyses Average magnetic moment in units of Bohr magnetrons μ_B
VG-CoMnGa-05-088 Co, Mn, Ga, Al t (nominal) = 7.3 nm 7.3 + 2.9 nm = 10.2 nm 7.3 + 2.9 + 2.9 nm = 13.1 nm Al-capping in LL: 15 Å (9.5 A / 10 secs)	7-12/10/05	WT#116 GaAs (100) (epi-ready, Si-doped, WV11549/Si) Special sample-holder with shutter, substrate size: 8 x 17 mm2 Shutter moved about 4 mm in 3 steps In-bonded No buffer layer	T(Ga): 908 C T(Mn): 1092 C Nominal/meas. rates (nm/s): **HERE ALL RATES SHOULD BE MULTIPLIED BY 0.2:** Co: 0.0100/ 0.00987* Mn: 0.0080/ 0.0080 Ga: 0.0188/ 0.0191 * Co source with feedback control with TF x 5 = 6.70 Mn+ Ga rates: (0.0376) nm/s (Ga par.) Co rate on FTM3: 0.0099 nm/s(Ga par.) Total rate: (0.0500-470) nm/s Average of total rate = 0.0482 nm/s (Ga parameters) Aim for 113/160/188 (sum = 461) (recipe after ICP-16) ON AVERAGE achieved: 99/160/191 X 0.2 (sum = 450 x 0.2)	250 C Al-capped at 20 C in load-lock chamber, LL) Low rate Estimated stoichiometry: Co 1.86 Mn 0.99 Ga 1.00	As desorption: 250 C/10 min 450 C/60 min 550 C/20 min 650 C/10 min	**Data for 10.2 nm sample:** **Co moments:** m_l = 0.034 +/- 0.004 m_s = 0.27 +/- 0.03 **Mn moments:** m_l = 0.096 +/- 0.014 m_s = 0.63 +/-0.06
VG-CoMnGa-05-089 Co, Mn, Ga, Al t (nominal) = 7.3 nm 7.3 + 2.9 nm = 10.2 nm 7.3 + 2.9 + 2.9 nm = 13.1 nm Al-capping in LL: 15 Å (9.5 A / 10 secs)	13/10/05	WT#116 GaAs (100) (epi-ready, Si-doped, WV11549/Si) Special sample-holder with shutter, substrate size: 8 x 17 mm2 Shutter moved about 4 mm in 3 steps In-bonded No buffer layer	T(Ga): 908 C T(Mn): 1092 C Nominal/meas. rates (nm/s): **HERE ALL RATES SHOULD BE MULTIPLIED BY 0.2:** Co: 0.0100/ 0.00987* Mn: 0.0080/ 0.0080 Ga: 0.0188/ 0.0196 * Co source with feedback control with TF x 5 = 6.30 Mn+ Ga rates: (0.0403-377) nm/s (Ga par.) Co rate on FTM3: 0.0113 nm/s(Ga par.) Total rate: (0.0518-488) nm/s Average of total rate = 0.0503 nm/s (Ga parameters) Aim for 113/160/188 (sum = 461) (recipe after ICP-16) ON AVERAGE achieved: 113/161/196 X 0.2 (sum = 470 x 0.2)	250 C Al-capped at 20 C in load-lock chamber, LL) Low rate Estimated stoichiometry: Co1.95 Mn0.98 Ga 1.00	As desorption: 250 C/10 min 450 C/60 min 550 C/20 min 650 C/10 min	**Data for 10.2 nm sample:** **Co moments:** m_l = 0.057 +/- 0.006 m_s = 0.38 +/- 0.04 **Mn moments:** m_l = 0.089 +/- 0.012 m_s = 0.75 +/-0.08
VG-CoMnGa-05-090 Co, Mn, Ga, Al t (nominal) = 7.3 nm 7.3 + 2.9 nm = 10.2 nm 7.3 + 2.9 + 2.9 nm = 13.1 nm Al-capping in LL: 17 Å (9.5 A / 10 secs)	14/10/05	WT#116 GaAs (100) (epi-ready, Si-doped, WV11549/Si) Special sample-holder with shutter, substrate size: 8 x 17 mm2 Shutter moved about 4 mm in 3 steps In-bonded No buffer layer	T(Ga): 908 C T(Mn): 1092 C Nominal/meas. rates (nm/s): **HERE ALL RATES SHOULD BE MULTIPLIED BY 0.2:** Co: 0.0100/ 0.00983* Mn: 0.0080/ 0.0080 Ga: 0.0188/ 0.0217-183 * Co source with feedback control with TF x 5 = 7.00 Mn+ Ga rates: (0.0373-368) x 0.2 nm/s (Ga par.) Co rate on FTM3: 0.0117 x 0.2 nm/s(Ga par.) Total rate: (0.0518-488) x 0.2 nm/s Average of total rate = 0.0487 x 0.2 nm/s (Ga parameters) Aim for 113/160/188 (sum = 461) (recipe after ICP-16) ON AVERAGE achieved: 117/160/200 X 0.2 (sum = 477 x 0.2)	250 C Al-capped at 20 C in load-lock chamber, LL) Low rate Estimated stoichiometry: Co1.97 Mn0.96 Ga 1.00	As desorption: 250 C/10 min 450 C/60 min 550 C/20 min 650 C/10 min	**Data for 10.2 nm sample:** **Co moments:** m_l = 0.0078 +/- 0.007 m_s = 0.29 +/- 0.06 **Mn moments:** m_l = 0.020 +/- 0.016 m_s = 0.45 +/-0.05

Table B.2: *XMCD samples Growth parameters and comments.*

results did not exhibit the expected systematic change.
All analyses of the XMCD data on the Co_2MnGa thin films show magnetic moments on the Mn atoms which are much smaller than expected. On average the Mn moments are 4-5 times smaller than expected in a well ordered Co_2MnGa crystal at low temperature: At 300 K the measured average value of m_{tot} for Mn falls between 0.25 μ_B and 0.85 μ_B, the theoretical value is 2.91 μ_B and measured bulk value is 3.01 μ_B, Webster *et al.* [5].

The measured Co moments values at 300 *K* lie between 0.1 μ_B and 0.45 μ_B and thereby on average fall below the expected theoretical value of 0.65μ_b, and the experimental bulk value 0.52 μ_B with a factor of 2. All in all the XMCD data indicate that at 300 K the grown Co_2MnGa thin films do not exhibit the expected magnetic properties of a Heusler alloy: the hypothesis that a large magnetic moment is transferred from Co to Mn is not supported by the XMCD analyses of our samples. At 300 K the average Co moment is indeed reduced from its bulk value but the expected corresponding increase of the average Mn moment is not found. No significant difference was observed between VG05-088, VG05-89, and VG05-090, even though the stoichiometries are quite different: VG05-088: $Co_{1.86}Mn_{0.99}Ga_1$, VG05-089: $Co_{1.95}Mn_{0.98}Ga_1$, and VG05-090: $Co_{1.97}Mn_{0.96}Ga_1$.

The reasons for these discrepancies are at present not fully understood. The behavior cannot be explained by the calculations only. Even though we theoretically found that Mn-defects on Co-sites anti-align itself with the applied field, one needs a very high Mn on Co-site defect-concentration of approximate 38 % to explain the missing Mn moment. One explanation could be that the Heusler alloy is not fully saturated. But as in our case where a magnetic field incident with 45 ° to the sample plane, is applied with a magnitude of 0.8 T, the thin film should indeed be saturated. As mentioned earlier the XMCD-technique is expected to probe approx. 5 nm, which corresponds to the thinnest part of VG05-088 - VG05-090 (t_{nom} = 7.3 nm), which in addition to the 1.5 nm Al-cap is more than the technique can probe. Therefore we expect the measured thickness dependency to be a result of the coupling with an eventually stronger magnetization beneath the probing depth. Structurally and magnetically characterizations have been performed on VG05-088 and VG05-089. The data are presented in section 3.3.4. Table B.3 summarizes the results by comparing the relation between the measured magnetic moment/magnetization with the theoretically expected value at 300 K.

Sample:	t_{real} [nm]	XMCD $\frac{m_{Mn}+2m_{Co}}{m_{bulk}}$	VSM $\frac{M_{Co_2MnGa}}{M_{bulk}}$
VG05-088:	5.3	0.24	0.13
VG05-088:	7.6	0.36	0.34
VG05-088:	9.7	0.31	0.45
VG05-089:	5.3	0.19	0.15
VG05-089:	7.6	0.46	0.61
VG05-089:	9.7	0.23	0.70

Table B.3: *Comparison of XMCD measurements of the local magnetic moments from Co and Mn, compared with VSM saturation magnetization measurement. The measurements are performed at* 300 *K.* $m_{bulk} = 3.71\mu_B$ *has been chosen to* 90 % *of the theoretically expected low temperature value.* M_{bulk} *is chosen to 711KA/m, Webster* et al. *[5]. Stoichiometries: VG05-088 is estimated to be* $Co_{1.86}Mn_{0.99}Ga_1$ *and VG05-089 is estimated to be* $Co_{1.95}Mn_{0.98}Ga_1$.

A fairly good agreement for both samples are observed for the thinnest films, while the the magnetization measurements are higher for the thickest films. This behavior can be explained if oxide has penetrated the 1.5 nm Al-cap and oxidized the top Co_2MnGa layer. But the XMCD measurements showed no evidence of oxidation. On the contrary the Mn L3 peaks were very clean in appearance. Another explanation could be an impurity layer caused by diffusion and chemical reactions, which does not include oxygen. We estimate this layer to be between 3 nm and 10 nm, due to the fact that $m_{Mn} + 2m_{Co}$ (XMCD) does not seem to increase from $t_{real} = 7.6$ nm to $t_{real} = 9.7$ nm, implying that the coupling with the non-diffused Heusler layer is constant. Furthermore we expect the layer to act strongly on Mn compared to Co, due to the relative larger decrease in Mn moment, compared to Co moment. This is in good agreement with Auger spectroscopy measurements (see section E), where measurements have shown that Mn tends to diffuse towards the surface, even though the structure is capped with approximately 2 nm Al. Furthermore As-bonding at the substrate interface is known to significantly change the local magnetic moments in e.g. Fe/GaAs structures [94, 95].

To conclude on the dynamics of the local magnetic moments more measurements are needed in particular on samples with other cap layers and complementing experimental techniques should be applied to the same samples that are used for the XMCD study, as it has been done with VG05-088 and VG05-089:

- the crystal structure should be checked by XRD
- the magnetic properties should be checked by magnetometry

Furthermore it would be interesting to compare the XMCD results with the type and density of defects, analyzed using NMR (e.g. looking for Mn- and Co-antisites).

Appendix C

Recipe for samples in series after VG-CoMnGa-05-072(July 05)

Recipe as of 270705 after ICP-16 round (July 15, 2005): Use nominal rates: Co/Mn/Ga = 0.0113/0.0160/0.0188 nm/s (all measured by FTM3 using Ga-parameters).

Co from e-beam source no. 1 with feed-back: 0.0100 nm/s on FTM1 with TF = 1.34 and Co-parameters, corresponding to 0.0113 nm/s on FTM3 with TF = 1.95 and Ga-parameters).

Mn from DCA-effusion cell no. 1: 0.0080 nm/s (on FTM3 with TF = 1.163 and Mn-parameters, corresponding to 0.0160 nm/s on FTM3 with TF = 1.95 and Ga-parameters).

Ga from VG-effusion cell no.2: 0.0188 nm/s with TF = 1.95 and Ga-parameters.

Total rate on FTM3 with TF = 1.95 and Ga-parameters: 0.0461 nm/s.

1. Mount samples on cleaned (glass bead blasted) stainless steel (SS) holder: For example two GaAs samples grown at HC with As-cap and one Si-sample. At least one of the GaAs samples should be mounted with In-bonding to promote better thermal contact. All three samples should be secured by clips. Document sample mounting on the data sheet is made for this purpose.

2. Introduce the sample holder into LL, pump LL down and wait until p(LL) is below 1 x 10-7 before introducing sample holder into growth chamber.

3. Introduce the sample holder into growth chamber, rotate sample holder slowly while looking through the view port to visual inspect for correct position of sample holder in growth chamber station. Position station in correct growth position = the level marked RHEED. When the Mn and Ga-sources are active the sample should be kept closer to the sample shutter = in a position 30 mm below the RHEED position (otherwise some material will be deposited on the sample holder, seen as ”shadows” on some of the samples, eg VG-CoMnGa-04-068). This LOW position is used whenever there is no deposition taking place.

4. Ramp up slowly the Mn and Ga effusion cell temperatures: Mn-cell (DCA-cell = effusion cell no. 1) to around 1150 C and Ga-cell (VG-cell = effusion cell no. 2) to

985 C (for the rates given above). The Mn cell temperature regulation function far better if the current limitation on the SORENSEN power supply is set to a level just above the minimum current needed to maintain the chosen temperature. With the present state of the Mn DCA effusion cell the 1150 C is maintained with V = 35.3 V and I = 10.2 A. (this is 20 months after the second repair of the DCA cell within one year and 6 months after the last Mn charge filling to about 1/3 of the full capacity of the conical PBN crucible with a Ta lid with 8 MM diameter hole)

5. Check for water flow to the chamber cooling canals and water flow to the two electron gun sources. Transfer LN2 to Ti sublimation pump cryopanel and to the two cryopanels inside the growth chamber. Start Ti sublimation pump with sublimation time = 2 minutes and off time = 10 minutes. These times are recommended for growth conditions the growth chamber pressure is typically 2-4 x 10-7 mb. Keep LN2 transfer system running at all times during growth in order to minimise outgassing.

   Note Dec. 2005:: after running for 3 months the typical pressure level during growth is 5 x 10-9 mbar (Dec. 2005). The Ti-sublimation pump should only be run once every 6 hours.

6. Start the Balzers quadropole mass spectrometer using the QUADSTAR 422 software. Use MEASURE programme and the CHANNELTRON detector (with V = 1280 V bias) and choose MID with "VERSUS TIME" and programme CoGaMnAs and SAVE CYCLE DATA with date as data file-name like "121204a.mdc". If more than one data file is used for the same sample use b,c, d etc Carry out desorption of the As-cap on the GaAs samples. Ramp up sample holder temperature to 250 C over 5 minutes and keep the temperature there for 10 minutes (water desorption) then run the following sequence (Dec. 2005 after consultation with Jill Claydon, Univ. of York): 450 C for 60 min, 550 C for 30 min and 570 for 2 min (increase upper limit on potentiometer to 3.0, and remember to decrease it again after growth). The mass spectrometer output record shows clearly the progress of the As desorption process. Ramp down to the growth temperature for the Co2MnGa, typically 200 or 250 C Wait at least one hour after the end of the As desorption process before growing the Co2MnGa layer.

   For GaAs substrates without As-cap: use 650 C for 30 minutes to remove oxygen.

   Check GaAs crystal surface quality by RHEED (20 keV, 30 microamp). Use RHEED operating instructions. Take pictures.

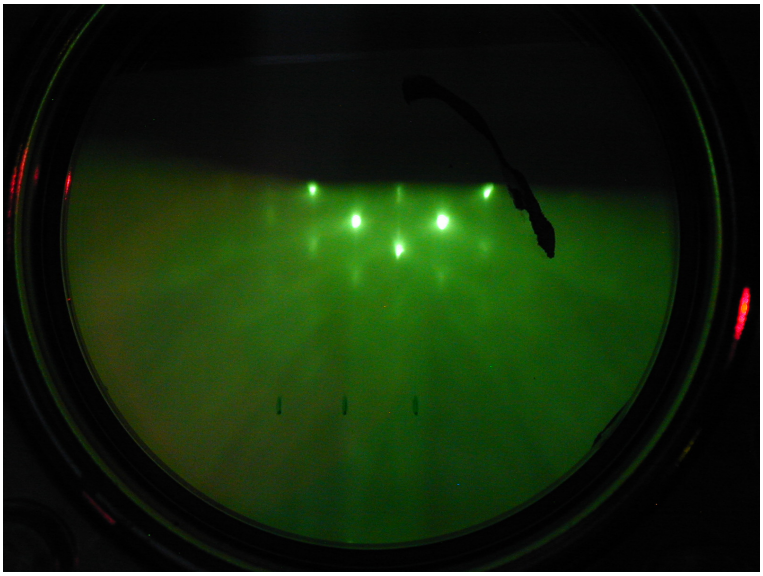

(a) VG05-074 on NBI#41 ($In_{0.28}Ga_{0.72}As$)

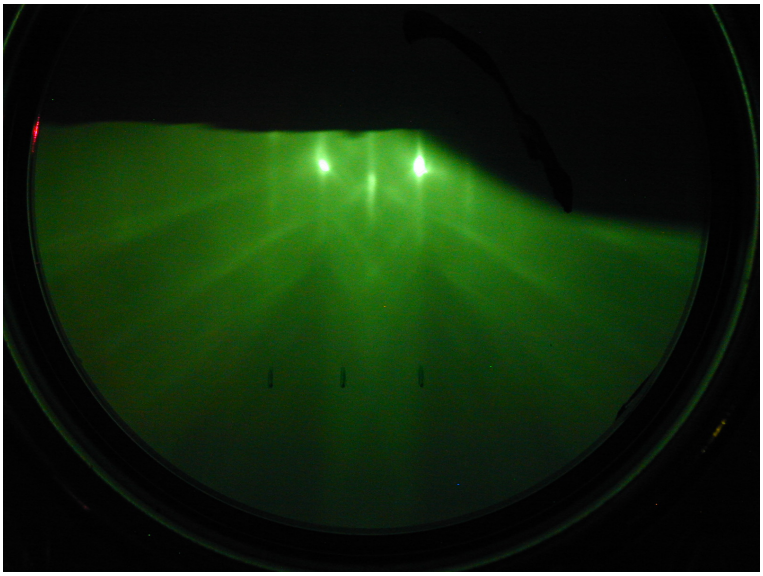

(b) VG05-075 on NBI#9 (spinLED structure)

Figure C.1: *RHEED(20kV) patterns after desorption.*

7. Check Mn and Ga rates with Film Thickness Monitor 3 = FTM3 and crystal 1 = left hand connector using the following material settings in the Intellemetrics ALLOY-programme: Mn3 with tooling factors: TF(Mn) = 1.163 and Ga3 with TF(Ga) = 1.95. Adjust cell temperatures by measuring changes in thickness over 3 to 6 minutes until rates are 0.0080 nm/s for Mn and 0.0188 nm/s for Ga. These rates should match a Co-rate of 0.0100 nm/s (on FTM1) (with TF = 1.34) in order to grow Co2MnGa.

The total rate on FTM3 has to be 0.0461 nm/s (Ga-parameters).

8. Start LabView programme to record the FTM3 (crystal 1) resonance frequency versus time. Use the following file-numbering system to name data file in the small window made for this purpose: `c:\users\cdd\vg-CoMnGa-04-xxxxA.txt` (it is important to write ".txt"). Start LabView programme by clicking once on the ARROW in the upper panel. If several data files are used for the same sample the other data files are named B,C,D, etc.

9. Start Co electron gun source (e-gun no. 1) using MANUAL control (and after checking water flow to the two e-guns). Adjust electron beam visually in the centre of the Co-filled crucible (keep clear of edges of the crucible) and adjust Co rate manually to around 0.005 nm/s (around 57 mA).

   If you want a CoGa-buffer layer: Prepare growth of CoGa buffer layer with the following rates: Co-rate = 0.005 nm/s as measured by FTM1 (crystal 1) with Co1 material file (TF(Co) = 1.340) and Ga-rate 0.0188 nm/s (measured on FTM3 as above). Start rotation of sample holder station with 6-7 RPM (important to have a high rotation rate because we grow fast). It is important NOT to start the sample rotation until the evaporation rates have been measured because the rotation interferes with the FTM-measurements (geometry or electrical noise ?). Grow CoGa buffer layer. The buffer layer is typically grown to a total thickness of 4 nm as measured by the FTM3 (crystal 1) set for Ga. It is only during the growth that the Co-shutter is opened. The Ga-shutter is also opened before the growth in order to check the Ga-rate. During growth the sample shutter is opened.

10. Anneal the CoGa buffer layer by heating sample holder to 250 °C or 300 °C for at least 10 minutes before starting growth of the Co2MnGa layer. Keep all 3 sources running and stable during this period, which should be used to manually increase the Co-rate to 0.0100 nm/s and check the rates for Mn and Ga again.

    Check surface quality of CoGa buffer layer by RHEED. 20 keV and 30 μA. Take pictures.

11. Load Ga-parameters into FTM3 and start programme CoMnGa into Intellemetrics programme ALLOY. Still with the Co source under MANUAL control start the programme RUN = F1. The programme will read the Co and Ga parameters into the FTM1 and FTM3 monitoring algorithms, respectively, and it will ramp up the Co e-gun source to a power level of around 65 mA which corresponds to a rate around 0.0100 nm/s as measured by FTM1 (crystal 1) and it will try to keep the Co rate stable around that rate. When the programme has reached the feed-back stage change from MANUAL to AUTO mode on the e-gun control (this is after "EL 0.010" and after "CE 0.010" when the display shows "TL 100.0 nm" and the programme has re-set both the Co (FTM1) and the Ga (FTM3) thickness indications to zero). Check Ga rate and Mn+Ga rates over 3 minutes before starting growth (using Ga parameters), the sum should be around 0.0400 nm/s (note: this sum is always higher than the nomial value = 0.0160 + 0.0188 = 0.0348 nm/s (Ga-parameters)). Check total rate on

FTM3 after starting deposition. In some cases it is better to use lower growth rates, say Z times lower. This may be achieved by multiplying all TF's with Z (typically 2 to 5).

12. Start sample rotation at 6-7 RPM, and grow Co2MnGa to a total thickness of 10 to 250 nm with the rates indicated above: Co 0.0100 nm/s, Mn: 0.0080 nm/s and Ga: 0.0188 nm/s. With these nominal rates it should take nominally 90 minutes to grow 250 nm. Every 30 minutes the growth is interrupted and the Ga and Mn+Ga rates are measured over 3 minutes. If needed the effusion cell temperatures are re-adjusted. Both the Mn and the Ga cells give rates that tend to decrease with time. After growth: Again record Ga rate and Mn+Ga rates over 3-6 minutes (using Ga parameters).

13. Ramp down Co e-gun source manually (slowly over around 2 minutes) and ramp down Mn and Ga cells slowly to 600 °C. Anneal samples by heating sample station to 350 °C for a short time, nominally 2 minutes. Cool sample to around 50 °C. Decrease current limit of sample heater power supply to 0.5. Stop LabView programme (press "green" button).

    Check surface quality of the grown thin film by RHEED. 20 keV, 30 μA. Take pictures.

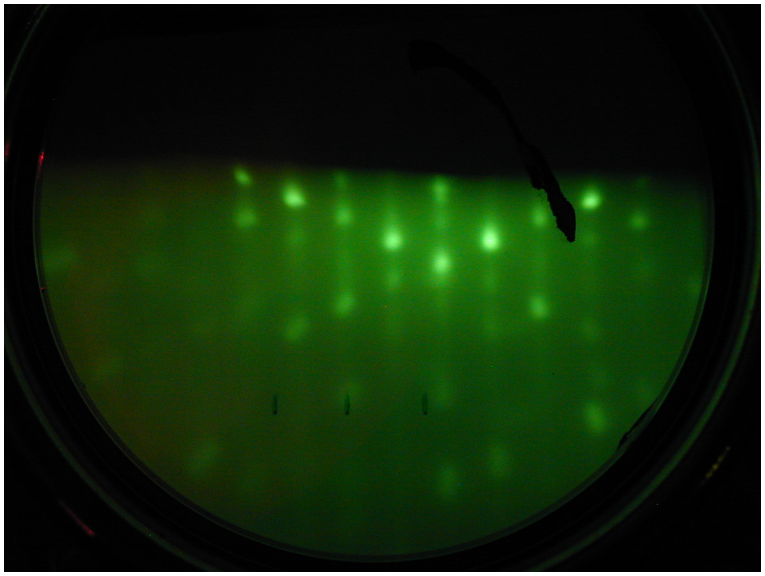

(a) VG05-074 on NBI#41 ($In_{0.28}Ga_{0.72}As$)

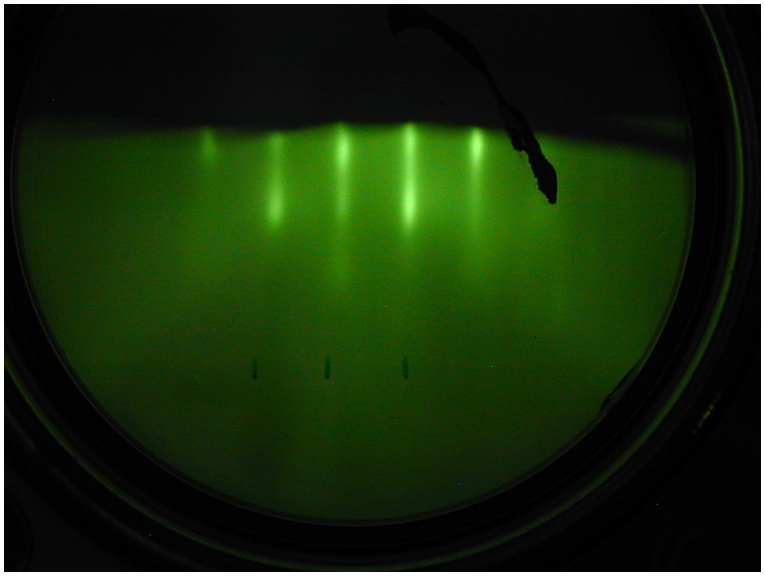

(b) VG05-075 on NBI#9 (spinLED structure)

Figure C.2: *RHEED(20kV) patterns after growth.*

14. Transfer sample holder to LL and then to atmosphere. Be careful to place the samples in separate small labeled boxes with Co2MnGa layer facing upwards and (when needed) mark backside of samples with red ink and use yellow Post-It tape for mounting.

Appendix D

Stoichiometry determination techniques

D.1 Stoichiometry determination by use of ICP-OES

ICP-OES: Inductively Coupled Plasma - Optical Emission Spectroscopy

D.2 Procedure:

1. The stoichiometry is determined for thin films of CoMnGa grown on Si substrates. The thin film material is dissolved in 1.8 ml of 35 % HNO3 acid. The weight of the dissolved material is determined to within 10^{-10} kg (0.1 microgramme). Note: the Si substrate is not etched by the acid.

2. The solution is injected and vaporized at a controlled rate into a low-pressure inductively driven Ar plasma.

3. The atomic spectral lines emitted from the plasma are resolved and detected and the concentration of atoms is determined to within 10^{-5} mol/g. An example: for a 9.4 x 9.0 mm^2 thin-film sample VG05-063 with nominal CoMnGa thickness of 79 nm the stoichiometry of the dissolved thin film material was found to be: 49.50 at. % Co 25.29 at. % Mn
25.21 at. % Ga
corresponding to the composition Co(1.96 +/- 0.02) Mn(1.00 +/- 0.01) Ga (1.00 +/- 0.01). The weight of the thin film material was 37.2 microgramme which gives a film thickness of 53 nm (assuming a mass density of 8.34g/cm^3)

4. The method is calibrated against bulk standards of Co, Ga, Mn and Co2MnGa. Pieces from a bulk sample of Co2MnGa delivered by Goodfellow Ltd. have been included in all ICP-analyses of CoMnGa thin films (4 to 6 thin films are typically analysed in every round).

Two examples of ICP analysis reports are shown here:

15th round (June 2005);
ICP-OES analyses of one bulk Heusler-alloy and six thin films

Goodfellow 17.01.05 N=2	*GNS*	*SD*	*%RSD*	*95%CONF*	*mol/100g*	*STOICH.*			
Co	47.96%	0.00%	0.01%	0.01%	0.8139	2.000	1.997	2.039	
Ga	28.41%	0.07%	0.23%	0.09%	0.4075	1.001	1.000	1.021	
Mn	21.93%	0.01%	0.06%	0.02%	0.3992	0.981	0.980	1.000	
#05-054 N=2	*GNS/ppm*	*SD*	*%RSD*	*95%CONF*	*mmol/kg*	*STOICH.*			*Mass(g)*
Co	0.477	0.000	0.04%	0.03%	0.00810	2.000	2.408	2.433	14.5
Ga	0.234	0.000	0.06%	0.02%	0.00336	0.831	1.000	1.010	7.1
Mn	0.183	0.001	0.40%	0.10%	0.00333	0.822	0.990	1.000	5.6
Total mass(g)									**27.2**
#05-058 N=2	*GNS/ppm*	*SD*	*%RSD*	*95%CONF*	*mmol/kg*	*STOICH.*			*Mass(g)*
Co	0.597	0.006	0.95%	0.79%	0.01012	2.000	2.215	2.106	17.3
Ga	0.319	0.003	0.98%	0.43%	0.00457	0.903	1.000	0.951	9.3
Mn	0.264	0.003	1.03%	0.38%	0.00481	0.950	1.052	1.000	7.7
Total mass(g)									**34.3**
#05-059 N=2	*GNS/ppm*	*SD*	*%RSD*	*95%CONF*	*mmol/kg*	*STOICH.*			*Mass(g)*
Co	0.606	0.000	0.03%	0.000	0.01029	2.000	1.932	2.120	18.1
Ga	0.371	0.001	0.21%	0.001	0.00532	1.035	1.000	1.097	11.1
Mn	0.267	0.000	0.18%	0.001	0.00485	0.944	0.911	1.000	8.0
Total mass(g)									**37.2**
#05-060 Si N=2	*GNS/ppm*	*SD*	*%RSD*	*95%CONF*	*mmol/kg*	*STOICH.*			*Mass(g)*
Co	0.423	0.000	0.09%	0.001	0.00718	2.000	2.079	2.142	12.9
Ga	0.241	0.000	0.13%	0.000	0.00345	0.962	1.000	1.030	7.3
Mn	0.184	0.000	0.09%	0.000	0.00335	0.934	0.971	1.000	5.6
Total mass(g)									**25.8**
#05-060 InAs N=2	*GNS/ppm*	*SD*	*%RSD*	*95%CONF*	*mmol/kg*	*STOICH.*			*Mass(g)*
Co	0.463	0.001	0.15%	0.001	0.00785	2.000	2.024	2.124	13.6
Ga	0.271	0.001	0.38%	0.001	0.00388	0.988	1.000	1.049	7.9
Mn	0.203	0.000	0.05%	0.000	0.00370	0.942	0.953	1.000	6.0
Total mass(g)									**27.5**
#05-061 N=2	*GNS/ppm*	*SD*	*%RSD*	*95%CONF*	*mmol/kg*	*STOICH.*			*Mass(g)*
Co	0.499	0.001	0.12%	0.001	0.00847	2.000	1.799	1.813	14.8
Ga	0.328	0.000	0.15%	0.001	0.00471	1.112	1.000	1.008	9.7
Mn	0.257	0.001	0.34%	0.001	0.00467	1.103	0.992	1.000	7.6
Total mass(g)									**32.2**

Table D.1: *ICP analysis report #15*

16th round (July 2005)
ICP-OES analyses of one bulk Heusler-alloy and six thin films

Goodfellow 17.01.05 N=2	*GNS*	*SD*	*%RSD*	*95%CONF*	*mol/100g*	*STOICH.*			
Co	49.30%	0.10%	0.20%	0.13%	0.8365	2.000	1.991	2.042	
Ga	29.29%	0.06%	0.21%	0.09%	0.4201	1.004	1.000	1.026	
Mn	22.51%	0.02%	0.08%	0.02%	0.4097	0.980	0.975	1.000	
#05-059R N=2	*GNS/ppm*	*SD*	*%RSD*	*95%CONF*	*mmol/kg*	*STOICH.*			*Mass(g)*
Co	0.599	0.003	0.46%	0.39%	0.01016	2.000	1.910	2.127	14.5
Ga	0.371	0.002	0.43%	0.22%	0.00532	1.047	1.000	1.113	7.1
Mn	0.262	0.002	0.64%	0.23%	0.00478	0.940	0.898	1.000	5.6
Total mass(g)									**27.2**
#05-062 N=2	*GNS/ppm*	*SD*	*%RSD*	*95%CONF*	*mmol/kg*	*STOICH.*			*Mass(g)*
Co	0.468	0.000	0.10%	0.06%	0.00794	2.000	2.041	2.037	17.3
Ga	0.271	0.000	0.12%	0.04%	0.00389	0.980	1.000	0.998	9.3
Mn	0.214	0.000	0.13%	0.04%	0.00390	0.982	1.002	1.000	7.7
Total mass(g)									**34.3**
#05-063 N=2	*GNS/ppm*	*SD*	*%RSD*	*95%CONF*	*mmol/kg*	*STOICH.*			*Mass(g)*
Co	0.556	0.001	0.14%	0.001	0.00944	2.000	1.963	1.958	18.1
Ga	0.335	0.001	0.34%	0.002	0.00481	1.019	1.000	0.997	11.1
Mn	0.265	0.000	0.17%	0.001	0.00482	1.022	1.003	1.000	8.0
Total mass(g)									**37.2**
#05-066 N=2	*GNS/ppm*	*SD*	*%RSD*	*95%CONF*	*mmol/kg*	*STOICH.*			*Mass(g)*
Co	0.442	0.003	0.62%	0.004	0.00750	2.000	1.678	2.051	12.9
Ga	0.312	0.002	0.78%	0.003	0.00447	1.192	1.000	1.222	7.3
Mn	0.201	0.002	1.21%	0.003	0.00366	0.975	0.818	1.000	5.6
Total mass(g)									**25.8**
#05-067 N=2	*GNS/ppm*	*SD*	*%RSD*	*95%CONF*	*mmol/kg*	*STOICH.*			*Mass(g)*
Co	0.387	0.000	0.09%	0.000	0.00657	2.000	1.839	1.998	13.6
Ga	0.249	0.000	0.20%	0.001	0.00357	1.087	1.000	1.086	7.9
Mn	0.181	0.000	0.08%	0.000	0.00329	1.001	0.921	1.000	6.0
Total mass(g)									**27.5**
#05-068 N=2	*GNS/ppm*	*SD*	*%RSD*	*95%CONF*	*mmol/kg*	*STOICH.*			*Mass(g)*
Co	0.492	0.001	0.22%	0.002	0.00834	2.000	2.065	2.172	14.8
Ga	0.282	0.000	0.05%	0.000	0.00404	0.969	1.000	1.052	9.7
Mn	0.211	0.000	0.03%	0.000	0.00384	0.921	0.951	1.000	7.6
Total mass(g)									**32.2**

Table D.2: *ICP analysis report #16*

D.3 Stoichiometry Analysis by Energy Dispersive Spectroscopy

EDS-data Comparison between data obtained by analysis of CoMnGa thin films grown on GaAs and on Si (two different substrates in same growth):

This analytical method is non-destructive and probes by X-ray fluorescence the material composition down to a depth of the penetration length of the beam of high energy electrons used to excite the electronic states of the atoms in the sample under study (typically 1 micrometer at 10 keV). For thin films the signals from the substrate material are therefore affecting the analysis. We have corrected for the effect of the GaAs and Si signals by simply subtracting the Si and As components and by substracting a part of the Ga signals that corresponds to the As signal (GaAs substrates have been checked, they give 50 %-50 % Ga-As). The following table includes analysis results on samples from four growth. The results show that to within 3-5 % the stoichiometry of CoMnGa thin films grown on Si and GaAs substrates are the same.

D.4 Comparison of stoichiometry analyses of CoMnGa thin films

13 thin film samples of 200 nm CoMnGa grown on Si at 200 C have been sent for stoichiometry analysis BOTH by EDS (Energy Dispersive Spectroscopy based on X-ray flourescence) at the IPL institute at DTU AND by ICP-OES (Inductively Coupled Plasma - Optical Emission Spectroscopy) at Ris National Laboratory, Dept. of Nuclear Chemistry. In addition 4

Sample name **date and nominal thickness**	**Result of EDS analysis (at. %)**	**CoMnGa-stoichiometry ratios (derived from EDS at. % with correction for substrates)**	**Relative difference between EDS stoichiometry on GaAs and Si substrates (relative to Si)**	**Comments**
VG-CoMnGa-04-005 April 7, 2004 255 nm	**On GaAs with In-bonding:** Co: 45.9 +/- 1.2 % Mn: 27.1 +/- 3.0 % Ga: 23.0 +/- 1.5 % As: 4.0 +/- 5 % **On Si with clips:** Si: 26.0 Co: 36.2 +/- 1.8 % Mn: 22.1 +/- 4.3 % Ga: 14.8 +/- 2.2 %	**On GaAs:** **Co/Ga = 2.43 +/-0.08** **Mn/Ga = 1.43 +/- 0.07** **On Si:** **Co/Ga = 2.45 +/- 0.10** **Mn/Ga = 1.50 +/- 0.10**	Co/Ga: - 0.8 % Mn/Ga: - 4.7 %	Includes 5 nm CoGa buffer layer
VG-CoMnGa-04-008 April 23, 2004 255 nm *)	**On GaAs with In-bonding:** Co: 47.0 +/- 1.2 %, Mn: 27.5 +/- 2.8 % Ga: 24.4 +/- 1.4. % As: 1.1 +/- 12.5 % **On Si with clips:** Si: 11.1 Co: 42.8 +/- 1.3 % Mn: 24.8 +/- 3.0 % Ga: 21.3 +/- 1.4 %	**On GaAs:** **Co/Ga = 2.02 +/- 0.05** **Mn/Ga = 1.18 +/- 0.05** **On Si:** **Co/Ga = 2.01 +/- 0.05** **Mn/Ga = 1.16 +/- 0.05**	Co/Ga: + 0.5 % Mn/Ga: + 1.7 %	Includes 5 nm CoGa buffer layer Sample sent to Toshiba for PCAR and MOKE, 270404 *) NOTE: Due to the use of Xtal#2 on FTM3 the sample shutter was open during source calibrations, this sample is probably much thicker than 255 nm (cf. Si and As signals in EDS
VG-CoMnGa-04-010 April 28, 2004 255 nm	**On GaAs with In-bonding:** Co: 43.7 +/- 1.2 %, Mn: 24.3 +/- 2.8 % Ga: 27.7 +/- 1.4. % As: 4.4 +/- 5 % **On Si with clips:** Co: 35.0 +/- 1.3 % Mn: 18.9 +/- 3.0 % Ga: 18.5 +/- 1.4 %	**On GaAs:** **Co/Ga = 1.87 +/- 0.05** **Mn/Ga = 1.04 +/- 0.05** **On Si:** **Co/Ga = 1.89 +/- 0.05** **Mn/Ga = 1.02 +/- 0.05**	Co/Ga: -1.1 % Mn/Ga: +2.0 %	Includes 5 nm CoGa buffer layer **For comparison:** **ICP-analysis:** **On Si with clips:** Co: 44.23 +/- 0.30 % Mn: 34.23 +/- 0.20% Ga: 21.60 +/- 0.12 % **Co/Ga = 2.048 +/- 0.025** **Mn/Ga = 1.585 +/- 0.018**
VG-CoMnGa-04-015 May 11-12, 2004 255 nm	**On GaAs with In-bonding:** Co: 45.3 +/- 2.2 %, Mn: 21.2 +/- 6.2 % Ga: 25.5 +/- 2.4. % As: 4.6 +/- 6.0 % **On Si with clips:** Si: 30.6 Co: 35.7 +/- 2.0 % Mn: 16.7 +/- 6.7 % Ga: 17.0 +/- 2.3 %	On GaAs: **Co/Ga = 2.16 +/- 0.13** **Mn/Ga = 1.01 +/- 0.10** **On Si:** **Co/Ga = 2.10 +/- 0.09** **Mn/Ga = 0.98 +/- 0.09**	Co/Ga: +2.9 % Mn/Ga: +3.1 %	Includes 5 nm CoGa buffer layer **For comparison:** **ICP-analysis:** **On Si with clips:** Co: 47.69 +/- 0.30 % Mn: 32.15 +/- 0.15 % Ga: 20.16 +/- 0.10 % **Co/Ga = 2.366 +/- 0.026** **Mn/Ga = 1.595 +/- 0.015**

Table D.3: *EDS results on samples from four growth. The results show that to within 3-5 % the stoichiometry of CoMnGa thin films grown on Si and GaAs substrates are the same.*

similar sets of EDS + ICP analyses have been made on pieces of bulk reference Co_2MnGa material delivered to DTU and to Toshiba Europe by Goodfellow. The results are shown in table D.4.

The conclusions from a comparison of the two analytical methods are:

1. The ICP-OES method gives reproducible results within a few percent. If the DTU-Goodfellow standard is used as reference the absolute stoichiometry for thin films (weighing of the order of 0.030 mg or more) may be determined to within +/- 2 % for the three elements.

2. The EDS method gives reproducible results to within +/- 10 results differ significantly and systematically both from the expected result for the Goddfellow standard and from the ICP results. Two different acceleration voltages have been used for the EDS-analyses 10 and 15 keV. For the two voltage settings 10 keV (15 keV) a comparison of the EDS to the ICP results and to the Goodfellow standard shows that:

   a on average the Mn/Ga ratio of Co2MnGa by EDS deviates by -36 % (+12 %) for thin films and -49 % (+31 %) for bulk and

   b on average the Co/Ga ratio of Co2MnGa by EDS deviates by -16 % (+22 %) for thin films and -20 % (+35 %) for bulk.

   (the numbers in parenthesis refer to 15 keV results)

The reasons for the failure of the EDS-method to determine the stoichiometry of Co2MnGa are at present unknown.

	RESULTS OF ICP-OES ANALYSES				RESULTS OF EDS ANALYSES					
	Co-icp	Mn-icp	Ga-icp		Co-eds	Mn-eds	Ga-eds		Co/Ga dev. (rel. to icp)	Mn/Ga dev. (rel. to icp)
SAMPLE NAME									**% deviation**	**% deviation**
THIRD ROUND REPEAT ICP (100904)										
VG-CoMnGa-04-040	1.523	0.925	1.000		eds analyses to be added later					
VG-CoMnGa-04-039	1.672	0.927	1.000		eds analyses to be added later					
VG-CoMnGa-04-026	2.194	0.873	1.000		1.820	0.510	1.000		-17.0	-41.6
SECOND ROUND ICP										
VG-CoMnGa-04-026	2.237	0.866	1.000		1.820	0.510	1.000		-18.6	-41.1
VG-CoMnGa-04-027	2.166	0.907	1.000		1.850	0.600	1.000		-14.6	-33.8
VG-CoMnGa-04-028	1.955	0.839	1.000		1.770	0.630	1.000		-9.5	-24.9
VG-CoMnGa-04-031	2.471	0.968	1.000		2.120	0.650	1.000		-14.2	-32.9
FIRST ROUND ICP										
VG-CoMnGa-04-010	2.048	1.585	1.000		1.890	1.020	1.000		-7.7	-35.6
VG-CoMnGa-04-015	2.366	1.595	1.000		2.100	0.980	1.000		-11.2	-38.6
VG-CoMnGa-04-025	3.160	1.450	1.000		2.190	0.860	1.000		-30.7	-40.7
BULK REFERENCES										
Goodfellow-DTU (1st ICP round) FIRST PIECE	2.098	1.065	1.000		1.680	0.540	1.000		-19.9	-49.3
Goodfellow-DTU (2nd ICP round) SECOND PIECE (opposite edge)	2.080	1.036	1.000							
Goodfellow-DTU (3rd REPEAT ICP round) FOURTH PIECE (middle)	2.048	1.080	1.000							
Goodfellow-DTU (3rd REPEAT ICP round) FIRST PIECE-repeated	2.050	1.041	1.000							
Goodfellow-DTU (3rd REPEAT ICP round) THIRD PIECE (edge)	2.059	1.034	1.000							
Goodfellow (Toshiba) (IPL-eds)	2.460	1.403	1.000		2.420	1.230	1.000		-1.6	-12.3
Goodfellow (Toshiba) (Cambridge-eds)	2.460	1.403	1.000		2.090	1.450	1.000		-15.0	3.3
NEW EDS METHOD (15 keV)										
(after Oct. 12, 2004)										
BULK REFERENCE:										
Goodfellow-DTU (eds 20/10/04)	2.050	1.041	1.000		2.760	1.360	1.000		34.6	30.6
THIN FILMS (still all on Si)										
VG-CoMnGa-04-050	1.979	0.972	1.000		2.490	1.050	1.000		25.8	8.0
VG-CoMnGa-04-052	1.639	1.004	1.000		2.050	1.120	1.000		25.1	11.6
VG-CoMnGa-04-054	1.514	0.970	1.000		2.006	1.206	1.000		32.5	24.3
7th round ICP, second round new EDS										
VG-CoMnGa-04-059	1.801	0.990	1.000		2.320	1.170	1.000		28.8	18.2
VG-CoMnGa-04-060	1.868	0.988	1.000		2.230	1.110	1.000		19.4	12.3
VG-CoMnGa-04-061	1.909	1.114	1.000		2.360	1.250	1.000		23.6	12.2

Table D.4: *Comparison of stoichiometry of analyses of CoMnGa thin films and bulk reference materials by ICP-OES (Risoe) and by EDS (IPL-DTU)(all thin film samples are about 200 nm thick and grown on Si at 200 C), all analyses normalized to Ga = 1.000*

Appendix E

Depth profiling using Auger-electron spectroscopy (AES)

Method:

AES performed during depth profiling with Ar-beam by John Larsen (Dept. of Physics, DTU, B312):

Sputtering parameters	
Voltage	2kV
Current	$1.8 \cdot 10^{-6} A$
Area	3×3mm^2

For an estimated relative sputter yield of 3 for Co_2MnGa the etching rate is approx. 3.5 ML/min. Sputter yield for other materials (table values):

Au: 4

Al: 2.5

Al_2O_3: 0.2

Co: 2

Sample name and substrate material	**Thin film materials and nominal thicknesses**	**Substrate tempera-ture during growth**	**Layer thickness or depth in sputter minutes (50 % levels)**	**Observed interdiffusion**	**Comments**
VG-04-006 on GaAs	5 nm CoGa + 5 nm Co + 3 nm Au	30 C	Au: 0-2 min Co: 2-13 min Ga: 10-… min As: 12-… min	None	Test samples to compare GaAs and Si No oxygen
VG-04-006 on Si	5 nm CoGa+ 5 nm Co + 3 nm Au	30 C	Au: 0-2 min Co: 2-12 min Ga: 8-12 min Si: 14-…min	None	Test samples to compare GaAs and Si No Oxygen
VG-04-001	5 nm Co2MnGa+ 4 nm Al + 5 nm Au	200 C	Au: 0-3 min O=: 3 – 10 min Al: 4-10 min Mn: 3 – 13 min Co: 10 – 18 min Ga: 12 -...min As: 13 - ...min	O into Al Mn into AlO	Mn diffuses to surface and oxidizes
VG-04-036	2 x (1 nm Al + O) + 5 nm Co2MnGa + 3 nm Al	-30 C	Al: 5-11 min and 15-22 min O: 5 – 7 min and 16-22 min Co: 10-18 min Mn: 7-18 min Ga: 11-17 min and 22-…min As: 22 - ...min	O into Al Mn weakly into upper AlO layer	Well-defined AlO barrier grown at - 30 C
VG-04-034	2 x (1 nm Al + O) + 5 nm Co2MnGa + 3 nm Al	200 C	Al: 7-23 min O:7-9 min and 11-27 min Co: 7 – 26 min Mn. 7-23 min Ga: 7-? and 24-… min As: 25 -… min	O into Al O into CoMnGa Mn into upper AlO layer	No clear AlO barrier CoMnGa film oxidized
VG-04-042	5 nm Co2MnGa + 3 nm Al	- 22 C	O: 0 – 5 min Al: 0 – 8 min Co:7 – 16 min Mn. 5 – 13 min Ga: 7 - ...min As: 13 - …min	Mn weakly into AlO layer	Mn diffuses to surface and oxidizes 3 nm Al cap at – 22 C is OK for protection of CoMnGa thin film

Table E.1: *Table of results*

The AES results are summarized in table E.1. Results for sample VG04-034 and VG04-036 and plotted in Figure E.1 and E.2 respectively:

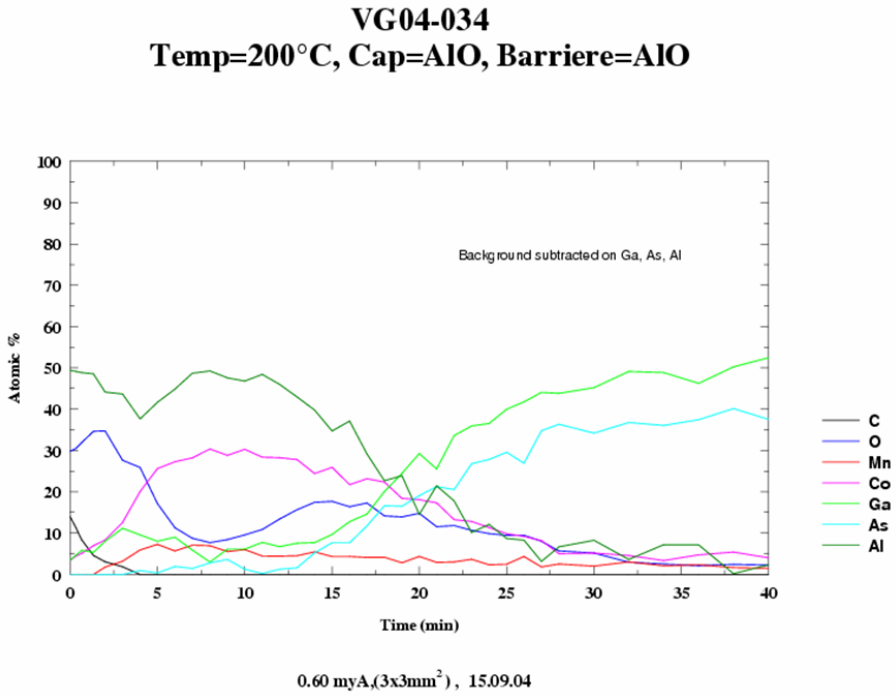

Figure E.1: *VG04-034: Auger results*

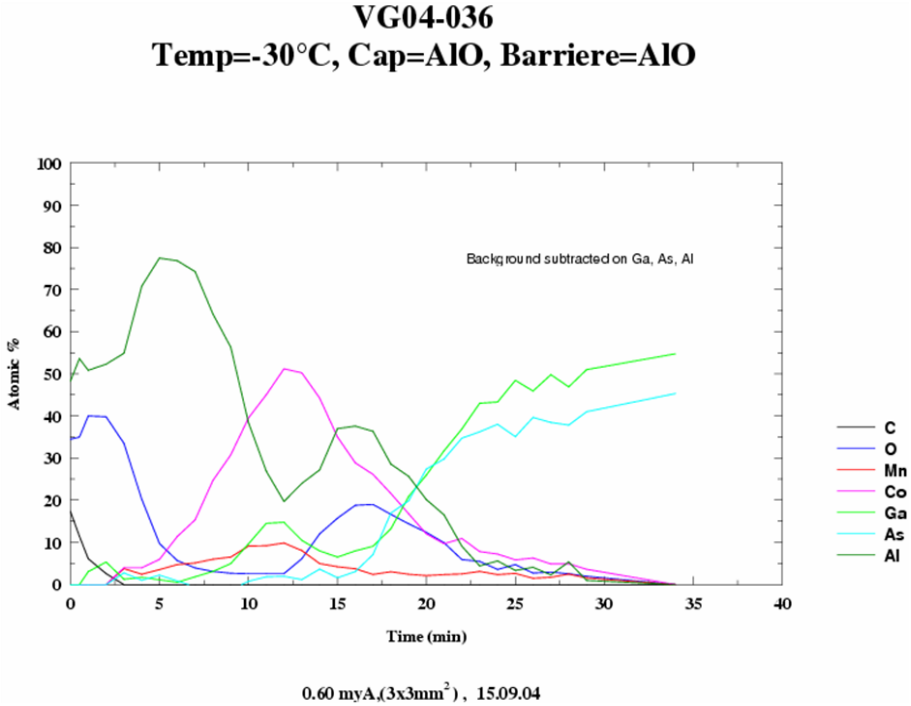

Figure E.2: *VG04-036: Auger results*

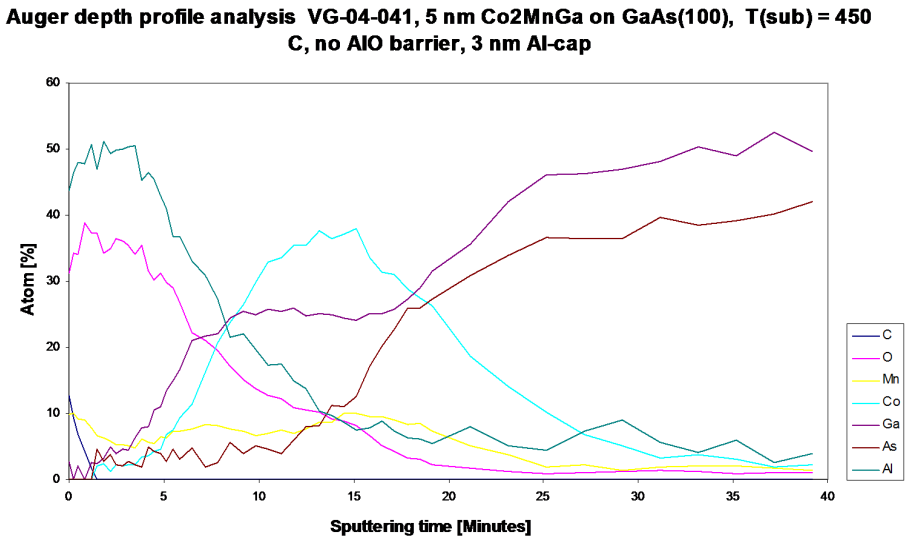

Figure E.3: *VG04-041: Auger results*

E.1 Conclusions

At growth temperatures of 450 °C, inter diffusion is observed of Mn towards both surface and substrate and Co towards the substrate.

Mn:

Mn tends to diffuse to the surface and oxidize. With Au-capping of 3 nm this does not happen at a substrate temperature of 30 °C (or lower) but it does happen at a substrate temperature of 200 °C even with Au-capping (at 200 °C Al-capping it is even worse, Mn diffuses into the Al-O). Mn does not diffuse into substrate.

Al:

Capping with 3 nm Al at low temperature protects the Co_2MnGa thin film

Co:

Co shows no appreciable diffusion to the surface.

As:

As does not diffuse into Co2MnGa at 200 °C or below.

Appendix F

Lithography recipes

This appendix shortly describes the lithography process, which has been used to fabricate the different types of samples.

F.1 UV lithography: Hall bars, TLM-samples, F/I/SC-devices

F.1.1 GaAs etch

1. Resist Microposit 1470, 6000rpm - 1100nm
2. Prebake 5 min. 90 °C
3. Exposure ca. 6-8 sec.
4. Develope Microposit 351, 45 sek
5. Post-bake 15 min 120 °C
6. Semiconductor etch: Wet-etch (chemicals) or Ion-etching. Etch-time depends on the semiconductor material and build-in heterostructures
7. Resist strip Acetone

Wet etch

NH3:H2O2:H2O, 8:3:400
Etch-rate:

GaAs: 40 nm/min

Ion etch (B-Chamber)

T=15 °C, P_{Ar}= $4.4 \cdot 10^{-4}$ mBar 20 mA, 500 V
Etch-rate:

GaAs: 58nm/min

F.1.2 Metal etch

1. Resist Microposit 1470, 6000rpm - 1100nm
2. Prebake 5 min. 90C
3. Exposure ca. 6-8 sec.
4. Post-bake 15 min 120C
5. Develope Microposit 351, 45 sek
6. Thin film etch: Ion-etch (B-chamber). Etching-time depends on material and film thickness.
7. Resist strip Acetone

Thin film etch

T=15 °C, P_{Ar}= $4.4 \cdot 10^{-4}$ mBar 20 mA, 500 V
Etch-rate:

Co_2MnGa: 40nm/min

Fe: 50 nm/min

Au: 40 nm/min

F.1.3 Au or SiO lift-off

1. Resist Microposit 1470, 6000 rpm - 1100 nm
2. Prebake 5 min. 90 °C
3. Exposure ca. 6-8 sec.
4. Soak 5 min. Chlorobenzene
5. Develope Microposit 351, 60 sec.
6. Ready for deposistion
7. Lift off with Acetone

F.2 SEM lithography recipes: F/N/N and F/S/F

A description of the device can be found in Appendix J

1. Rinse sample in hot acetone, methanol and 2-propanol
2. Sample ashed in 20 seconds
3. Deoxidize 5-10 minutes in 18 % HCl. Rinse in Millipore water.
4. Pre-bake 5 minutes at 185 °C
5. Spin 4 % PMMA at 6000 rpm in 60 seconds
6. Hard-bake resist at 185 °C for 5 minutes
7. Expose sample in SEM
8. Develop 60 seconds in MIBK:2-propanol (1:3)
9. Post-bake at 115 °C for 5-10 minutes 10. Sample ashed in 6seconds
10. Shallow-etching in either H3PO4:H2O2:H2O (1:1:38) 100 nm/min
11. Rinse 30 seconds in millipore water

Appendix G

Electrical measurements: Details

G.1 Transport measurements (Hall configuration)

The sample is mounted in a perpendicular field geometry, in either an 8T or 12T magnet. A constant current is used (typically 100 nA to 10 μA) to bias the device. Most measurements start with a base temperature measurement (1.5 to 2 K). Both Rxx and Rxy are measured from -8 T to 8 T or -12 T to +12 T.

The actual data is normally plotted just along the positive axis as there is usually an offset to the Hall at zero field which can be eliminated. This is due to mixing of resistance components. Rxx(positive B) = [Rxx(+B)+Rxx(-B)]/2 Rxy(positive B) = [Rxy(+B)-Rxy(-B)]/2

Any sets of contacts which have a large Hall voltage at zero field are generally ignored.

The gradients of the Hall effect are determined to get the Hall constants. The extraordinary Hall constant is determined in the range 0 to 0.1 T and the normal Hall constant in the range 6 to 8 T or 10 to 12 T depending on the sweep range.

Some devices were measured every 50 K up to 300 K.

G.2 Transmission Line Measurements (TLM)

A list of the TLM-results for a large number of devices are seen in 3.5.2.

Growth	Description	Meas. Date	R//channel (Ω)	R//contact (Ω)	R(Au/FM/Au) (Ω)	R(FM/GaAs) (Ωmm²)	IV-asymmetry @+/-50μA
04-072, HCØ273	20 nm CoMnGa + Au	050308	-	-	Small	10 +/- 5	-
05-018, NBI#7	35 nm CoMnGa + Au, TLM-1 300 K	050311	263	62	Small	5.5 +/-0.2	1.25
05-018, NBI#7	35 nm CoMnGa + Au, TLM-1 77 K	050311	283	64	Small	27 +/-1	-
05-026, NBI#7	3.5 nm buffer + 35 nm CoMnGa + Au. TLM-1	050315	-	-	1500	2.2 +/- 0.2	-
05-026, NBI#7	3.5 nm buffer + 35 nm CoMnGa + Au. TLM-2	050315	-	-	1800	1.9 +/-0.3	1.11
05-027, NBI#7	3.5 nm buffer + 35 nm CoMnGa + Au, TLM-1	050311	-	-	1k-10k	5 +/-2	-
05-027, NBI#7	3.5 nm buffer + 35 nm CoMnGa + Au, TLM-2	050311	155	52	1200 +/-300	6 +/-0.6	-
05-028, NBI#7	17 nm Co + Au, TLM-1	050310	95	87	100	4 +/-1	1.76
05-028, NBI#7	17 nm Co + Au, TLM-2	050310	30+/-20	108	20	3 +/-1	-
05-029, NBI#7	35 nm CoMnGa + Au	050315	160	48	40	4.3 +/-0.2	1.13
05-026A, NBI#7	35 nm CoMnGa + Au, Bias 30 s	050510	44	50	10	3.0 +/-0.3	1.16
05-026A, NBI#7	35 nm CoMnGa + Au, Bias 60 s	050510	300(usikker)	-	10-20	2.2 +/-0.2	0.92
05-027, NBI#7	Buffer + 35 nm CoMnGa + Au, Bias 30 s	050510	-	-	10k-160k	>10	1.2
05-027, NBI#7	Buffer + 35 nm CoMnGa + Au, Bias 60 s	050510	115	52	150-2k	13 +/-2	1.32
05-028A, NBI#7	17 nm Co + Au, Bias 30 s	050510	185	81	ca. 0 - 5k	10 +/-1	2.08
05-029, NBI#7	35 nm CoMnGa + Au. Substrate ion-etched. Bias 30 s	050510	50	65	85 +/-10	6 +/-1	1.08
05-029, NBI#7	35 nm CoMnGa + Au, Bias 60 s	050510	96	56	110 +/-20	3.2 +/-0.2	1.12
05-031, NBI#7	25 nm Al, TLM-1, dark areas on sample, most contacts > 100 MΩ	050624	-	-	> 150 k	> 10 M	-
05-031, NBI#7	25 nm Al, TLM-2, dark areas on sample, most contacts > 100 MΩ	050624	-	-	> 40 k	> 9 M	-
05-032, mesa-etched, NBI#7	35 nm CoMnGa, TLM-1, resistance inhomog.en, TLM-fit not possible.	050627	-	-	300-2000	1.6	1.00
05-032, mesa-etched, NBI#7	35 nm CoMnGa, TLM-2, resistance inhomogen. TLM-fit not possible. As-desorption problem?	050627	-	-	500-1400	12	1.4
05-033, mesa-etched, NBI#7	15 nm Co grown at 100°C. TLM-1, Substrate was not ion-cleaned, TLM-fit not possible	050627	-	-	80-130	0.10	1.02
05-033, mesa-etched, NBI#7	15 nm Co grown at 100°C. TLM-2, Substrate was not ion-cleaned	050627	50	15	20-80	0.06	1.02
05-037, mesa-etched, NBI#7	84 nm CoMnGa. TLM-1, TLM-fit not possible	050628	-	-	50-500	4.5	1.03
05-048, mesa-etched, NBI#7	10 nm Fe + 2 nm Au. TLM-A	050628	110	130	40-70	0.025	1.01
05-048, mesa-etched, NBI#7	10 nm Fe + 2 nm Au. TLM-B	050628	50	30	30-1000	0.017	1.01
05-048, mesa-etched, NBI#7	10 nm Fe + 2 nm Au. TLM-C	050628	65	40	2-25	0.03	1.01
05-048, mesa-etched, NBI#7	10 nm Fe + 2 nm Au. TLM-D	050628	45	30	10-240	0.022	1.01
05-048, NBI#9	10 nm Fe	051001	ca 7k ?	-	14k-270k	12-250	2.6
05-048, C2398	10 nmFe, Sample C1	051001	-	-	Small to 200	0.8-600	1.0
05-048, C2398	10 nmFe, Sample C2	051001	-	-	Small to 200	0.1-400	-
05-075, C2398	15 nm H + 2.4 nm Au	051001	-	-	Small	120-200	-
05-071, NBI#10	5.8 nm H + Au	051028	ca. 300 ?	-	Small	60	2.7
05-075, C2509	15 nm H + 2.4 nm Au, Sample A	051028	ca. 200 ?	-	Small	25	1.3
05-075, C2509	15 nm H + 2.4 nm Au, Sample B	051028	95	87	Small	22	1.4
05-101, NBI#9	#9/100/I/H/101/TLM, Sample AA, ej forskudt	051214	-	-	Small	70-900	-
05-101, NBI#9	#9/100/W/H/101/TLM, Sample AB, forskudt	051214	-	-	Small to 20k	10-80	-
05-101, NBI#9	#9/100/I/H/101/TLM, Sample AC, forskudt	051221	-	-	40 to 20k	4-120	-
05-101, NBI#77	#77/97/W/H/101/TLM, Sample AD	051222	-	-	Small	8-110	-
05-102, NBI#77	#77/97/W/I-LL/H/102/TLM, Sample AF	051223	-	-	Small	2-4	-
05-098, NBI#77	#77/-/-/I-LL/H/98/TLM, Ion etched mesa after	060117	ca. 50k	-	Small	1000	2.5 @ +/-10 μA

Table G.1: *List of the measured TLM-results.*

Appendix H

PCAR measurements: Details

Setup

The mechanical part of the setup was a commercial Attocube positioning system (see Figure H.1). It moves the ”sample-table” by controlling piezoelectric ”legs” which push or pull the ”sample-table” in the x,y, and z directions.

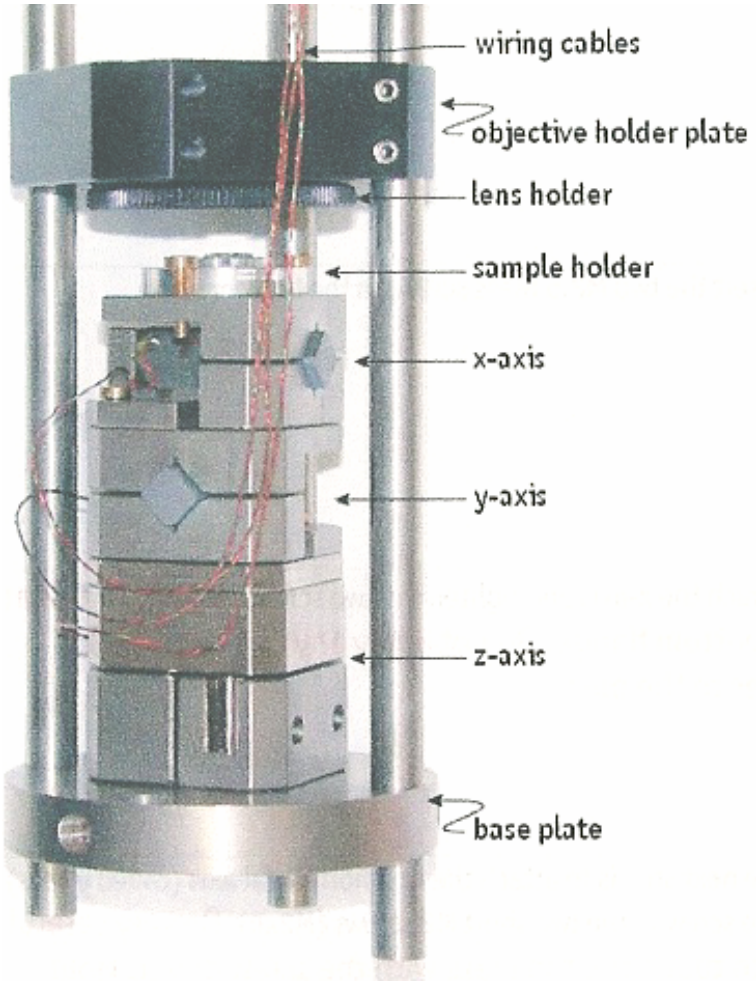

Figure H.1: *Specs: Step size 5nm, cryogenic movements*

The sample was mounted on the "sample table" and electrical contacts to the sample holder were established with thin cobber wires. The table was initially placed in the lowest possible position and the x and y-position were centered. The Nb needle was placed on the lens holder, see Figure H.1, (1 – 2mm) above the center of the sample. See appendix H.3 for the technical details we used for fabricating the Nb needles. The attocube positioning system was then mounted in a sealed container. The container was pumped down below 10^{-2}mbar and flushed with helium gas three times before it was filled up to an overpressure on 200mbar of helium gas. This procedure was done to ensure as little contamination in the container as possible. The positioning system will in the best case not work if some water gets into the piezoelectric mechanics before the whole system is cooled down. In the worse case the system will break down. The container is then mounted in either a helium transport dewar (T = 4.2 K) or in a Variable Temperature Insert (VTI) in an Oxford cryostat (T = 1.6 K). In the VTI a magnetic field up to 14 Tesla can be applied. The electrical setup for applying a bias and measuring the differential

conductance together with a description of a procedure to establish a ”good” contact can be seen in H.2. A ”good” contact has a diameter in the order or lower than the electron mean free path. This criteria is called the Sharvin limit [105] and ensures that we only measure the conductance of the contact interface [48]. Normally [45, 48] a ”good” contact has been initially identified as having a resistance between $1 - 100\Omega$.
Getting a ”good” contact was indeed quite tricky! The first conducting contact was often the best. By repeating crashing into the film surface the needle-tip was broaden and the measurements decreased in quality. The typical needle-tip radius was around 4μm. In [45, 48] the typical needle-tip radius was less than 100μm and between $1 - 10\mu$m respectively. Figure H.2 shows one of the best needles.

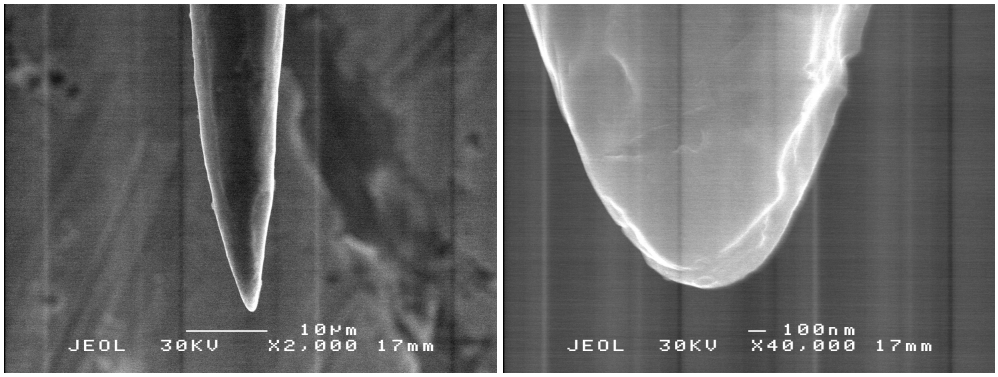

Figure H.2: *Needle8: a tip radius below* 100 *nm*

When a ”good” contact was established, the voltage bias was changed while measuring the differential conductance. The dc-voltage was swept from around -10 mV to 10 mV, while the ac-voltage amplitude was around 20 μV.

H.1 Electrical setup

The apparatus used for the measurements can be schematically seen in Figure H.3.

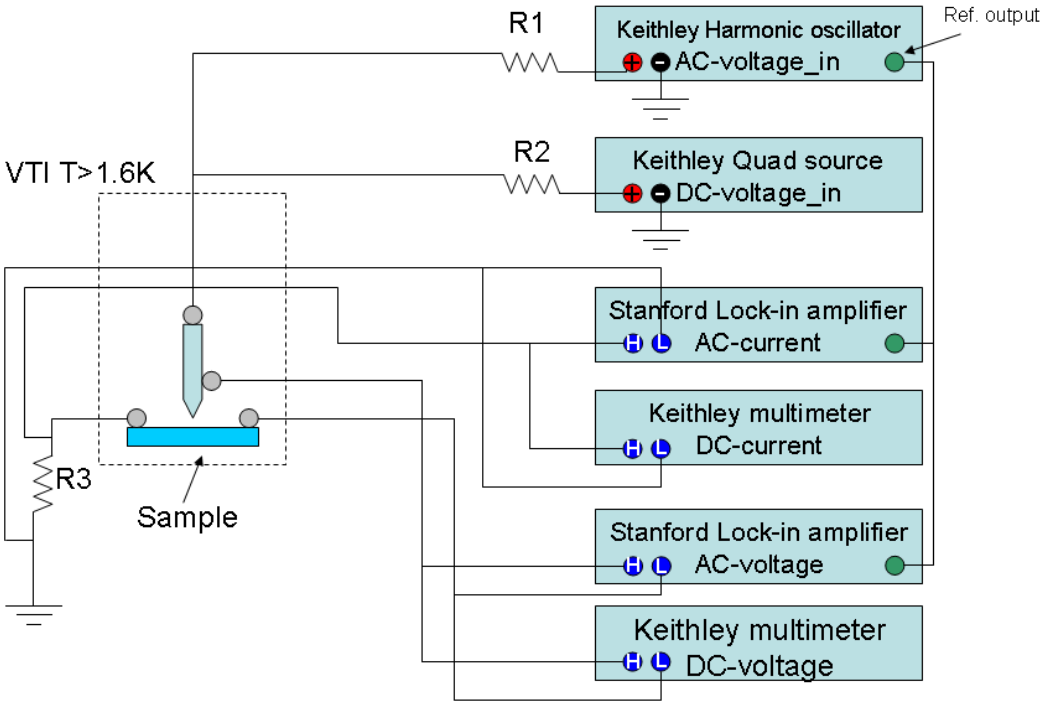

Figure H.3: *Sketch of the set-up*

The applied ac and dc voltage is made by putting a known larger ac or dc voltage through $R1$ and $R2$, where $R1$ and $R2$ are larger than the contact resistance, converting the voltages to constant currents. The voltage drop over the contact is measured directly, and the current through the contact is measured as a voltage drop over a known resistance $R3$. The typical dc-voltage between the needle and the sample was swept from around -10 mV to 10 mV, while the ac-voltage amplitude was around 20 μV.

H.2 Procedure to establish a ”good” contact

In order to establish a good point contact, the following procedure was used:
Raise the z-position, with low frequency and amplitude (ex. 700 Hz, 20 V) until the tone from the attocube change frequency (Put your ear to the cryostat). This means that the needle touches the sample. Keep notice of the instruments, is the contact conducting? This procedure seldom makes a conducting contact in the first attempt. This is probably due to oxide on both the thin film and the needle. Raise the amplitude (maximum is 70 V). Move a bit away and try to approach the sample again. Do this until a ”good” contact is established.

H.3 Needle fabrication

Several ways of sharpening a needle tip are described in the literature. In [45] mechanical polishing is used getting needle tips with a radius below 100 μm. [48] uses first a mechanical polishing and afterwards an electrochemical etching in a potassium-hydroxide solution. The process chosen in this work is an all chemical process. The process is described in [123, 124]. A very simple electrochemical etching device, see Figure H.4, was used.

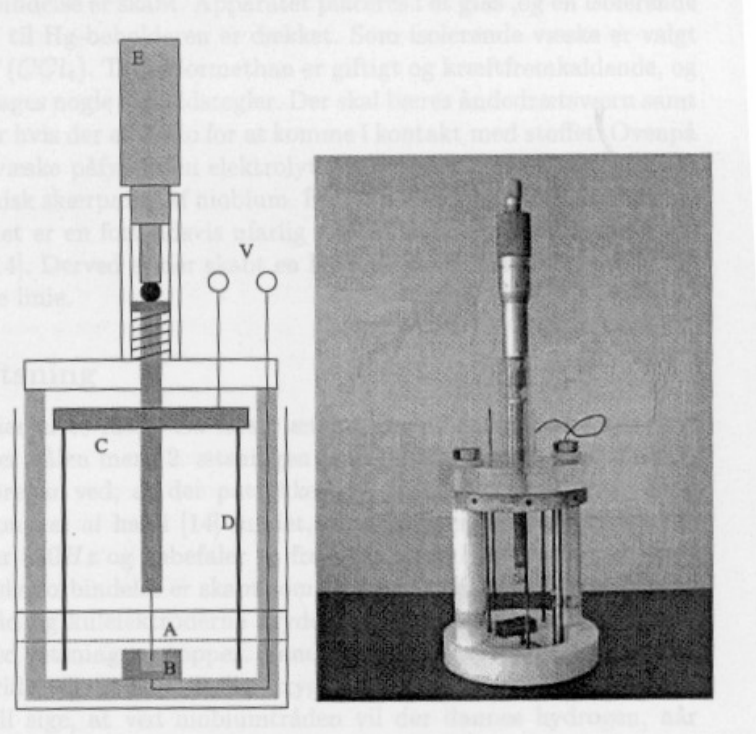

Figure H.4: *Picture and drawing of the electrochemical etching device*

Niobium was chosen as the needle material. With a high critical temperature T = 9.25 K and the property of being a hard material, Nb is ideal for this purpose. A piece (1-1.5 cm) of 99.9 % Nb wire with a diameter of 0.25 mm was placed between the end of the rod in the middle and the small cobber beaker at the bottom of the device. The beaker contains mercury to establish an electrical contact to the niobium wire. The wire must not touch the bottom of the beaker, see Figure H.4. The position of the wire piece can be controlled with the micrometer screw at the top of the device. A wire connects the mercury beaker in the bottom to the outside of the device through a teflon tube. At the top of the device a cobber plate electrically connects 6 carbon rods. The ends of the rods are in a level below the mercury dewar. The carbon rods are connected to the outside through a wire. The Nb wire piece and the carbon rods are the electrodes in the electrochemical process. In order to control the position of the etch an insulating liquid

is gently poured (be careful not to pour directly into the mercury beaker and push the mercury away) into the device until the liquid is in a level above the mercury beaker. As an insulating liquid, tetracloroomethane CCl_4 is used. Tetracloroomethane is toxic and can cause cancer, so please follow the by the law decided safety regulations. On top of the insulating liquid, an electrolyte is now even more gently (to cause as little mixing of the two liquids as possible) poured into the device. As an electrolyte a 2-molar natriumhydroxide $2 - M\ NaOH$ solution was chosen because it is a relatively non dangerous liquid. The two liquids are not reacting with each other and therefore separated in layers. The etching will act on the Nb wire at the interface between the two liquids. This is marked with a dashed line in Figure H.4. When the wire is etch through the lower piece will drop down into the mercury beaker and the electrochemical process will stop automatically. The process is divided into two parts. Part 1 is the rough etch cutting the wire into two potential needles. Part 2 is the refined process where the needle tip is sharpened.

Part 1 An ac-voltage is applied between the mercury beaker and the cobber plate. The chosen amplitude and frequency was 10 V – rms and 50 *Hz*. This etch takes 4-6 hours, which is quite slow.

Part 2 By use of the micrometer screw, the needle tip is situated in a way that it just only breaks the surface of the electrolyte. Now a 50 *Hz* sinusoidally voltage with amplitude 4.5 V – rms is applied trough the micrometer screw (E) and the cobber plate (C) with a duration of 1 *s*. If the needle is kept out of contact with oxygen, it is important that the needle potential ends in a negative period to reduce the amount of oxide in the needle. This procedure is made about 100 times.

We favorite short and sharp needle tips, they are more difficult to deform, when the needle hits the film surface. Figure H.5, H.6, and H.7 show three different needles. Needle 8 has undergone part 2 while 10*a*&*b* have not. A difference is clearly seen.

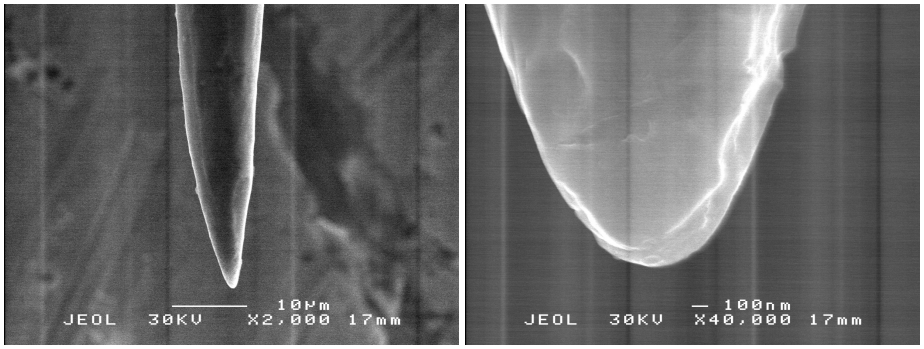

Figure H.5: Needle8: a tip radius below 100 *nm*

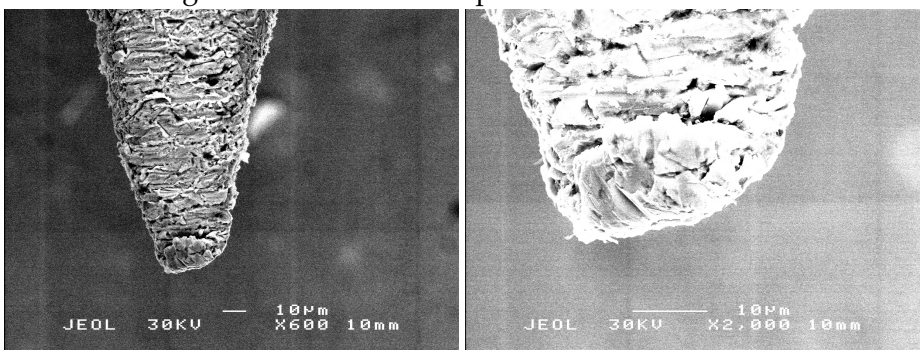

Figure H.6: Needle10a: a tip radius around 10 μm

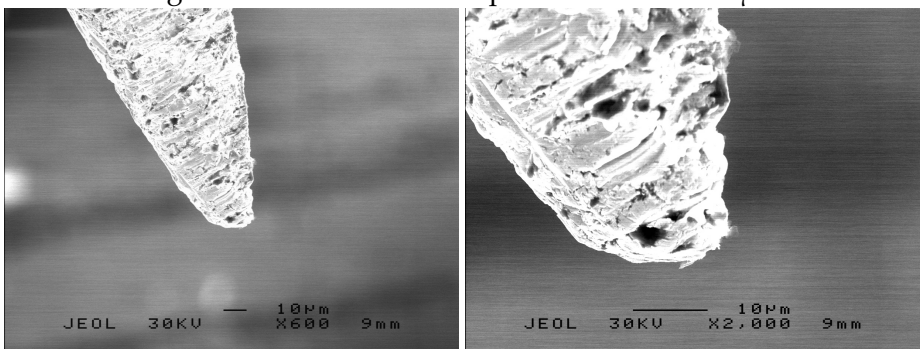

Figure H.7: *Needle10b: a tip radius below* 10 μm

H.4 PCAR improvements

In this section we will describe the efforts we believe are important in an improvement of the setup.

- The adding of ac and dc signals should be done using operation amplifiers.
- The establishment of a ”good” contact should be automated, with a feedback to the

positioning system in order to stop approaching the film as soon as the contact is made.

- Efforts should be done to avoid oxidation of the needles (and the films if possible). This could properly be done by keeping the needles in vacuum or in some sort of solvent such as propanol. The needles which have been used have varied a lot in quality. This procedure needs to be reproducible and produce good needles every time. We recommend that needles are etched at the Cavendish in order to have the needle etching process close to the setup.
- The needle holder and sample holder should be remade in a proper way. The existing hardware was ″homemade″ with the emphasis that it should work as quickly as possible. The design could be made in a much better way. The video camera could also be implemented to give the user the advantage of seing when the needle touches the film.
- The contacts are very sensitive to even small mechanical excitations. A damping system would increase the life time of a ″good″ junction.

H.4.1 PCAR conclusion

In conclusion a mechanical and electrical setup for PCAR-measurements have been established. Measurements have been made on the normal metals *Au* and *Cu* and show $P = 0$ %. Measurements on *Co* a ferromagnet known in literature show $P = 44$ % as expected. Finally measurements have been done on two different thin-films of Co_2MnGa showing $P = 55$ % and $P = 50$ %. Some problems with the measurements or the fitting procedure are still present. The fitted temperature seldom corresponds to the measured sample temperature. The reason is still unknown but could be associated with:

- The numerical fitting procedure. Recheck with literature. This has been done and we am quite confident that the problem should be found elsewhere.
- The thermal connection between the sample holder and the sample. The thermometer is mounted next to the chip carrier. Both are fixed with ″GE varnish″ to establish a good thermal contact. It would be surprising if the problem is to be found here.
- The electrical system
  - The adding of ac and dc. One of the instruments needs to be floating. If this is not the case the setup will not show the correct data.
  - The four point measurement. If the film is of low conductance, the placement of the probes on the film is very important. We know that the conductivity of the Heusler alloys (which show the highest fitting temperature) is low due to a carrier density of around 10^{20} cm^{-3} (normal metal: 10^{22})
  - The needle tip is too wide. Either from the beginning or due to plastic deformation during the establishment of a ″good″ contact.

More investigations need to be done to localize the problem.

Appendix I

Ferromagnet-Insulator-Superconductor (F/I/S): Details

The fabrication of the tunnel junctions have followed the method described by Tedrow and Meservey [38, 39, 40, 41]: a thin aluminium film is used as the superconducting electrode and the oxide tunnel barrier is a thin layer of AlxOy The F-I-S samples eg. Co_2MnGa/AlxOy/Al are grown in two configurations:

1. GaAs/Co_2MnGa/AlxOy/Al/Au and
2. GaAs/Al/Al_xO_y/Co_2MnGa/Au

where growth sequence 2) is the easiest and also the one used by Tedrow and Meservey.

The thickness of the superconducting thin film is chosen to be less than 10 nm in order to ensure that the thin film remains superconducting in a magnetic field of up to 3 Tesla applied parallel to the plane of the film.

Configuration 1) (2004)

This approach was chosen as the first approach. The recipe is described in the following:

Co2MnGa/Al_2O_3/Al/Au

1. Co2MnGa-sample (100 nm × 4.5 mm × 4.5 mm) in VG-chamber DTU
2. In Alcatel-chamber
   - **a** Rinse w. Ar-ions. DTU
   - **b** Deposition of Al + Oxidation DTU
3. Mesa: hall-bar DTU

4. SiO UV lithography lift-off DTU
5. Au contacts UV lithography, lift-off HC
6. Al (3-4 nm) + Au(15-20 nm) e-beam lithography, lift off HC
7. Scribe and bond HC/DTU

A calibration of the Al-oxidation process (3b) in the Alcatel chamber is shown in Figure I.1.

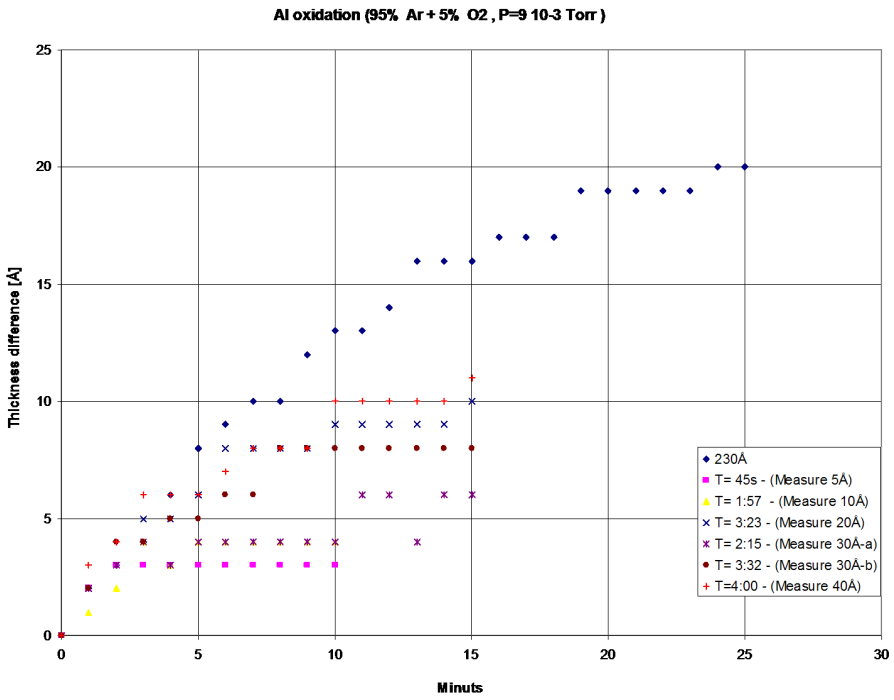

Figure I.1: *Test on Al oxidation by use of "sputtering" in 95 % Ar+5 % O_2. The conclusion is that this technique oxidizes approx. 4 Å Al pr. minute to a thickness of approx. 6 Å Al_xO_y pr. minute*

Data from two of the measured samples are shown in Figure I.2:

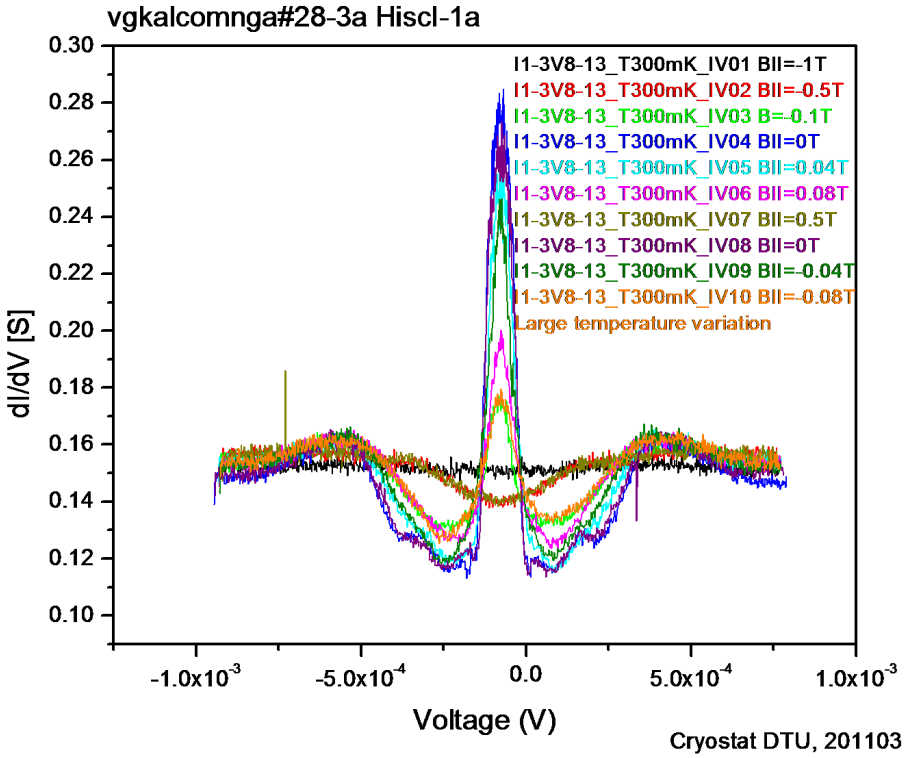

(a)

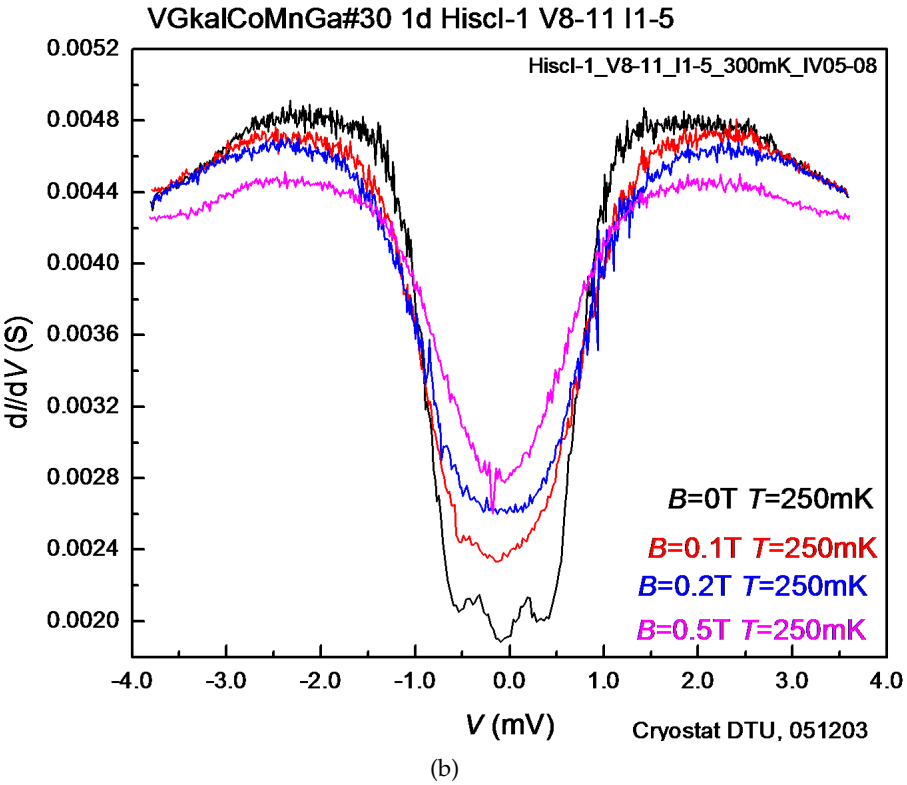

(b)

Figure I.2: *Measurements on Al/AlOx/Co_2MnGa at* T = 400mK.

Configuration 1) (2005)

In this approach the Al_xO_y oxide barrier was grown by slow oxidation at low oxygen partial pressure and low substrate temperature in order to achieve a dense epitaxial oxide barrier [125]. We chose an oxygen partial pressure of $1 - 3 \cdot 10^{-4}$ mbar and a substrate temperature around -40 °C. The oxidation time was 20-30 minutes. Al_xO_y was grown on top of Co_2MnGa by first growing a 1 nm thin Al layer (also at around -40 °C) and then the oxidation process was carried out. This sequence was repeated twice in order to minimize the density of pinholes in the barrier. During the oxidation process we observed a change of the mass of the deposited 1 nm Al-layer by about 40% indicating that it was oxidized up to around 50 % of the nominal Al_2O_3 composition. As an example we here show the growth parameters for the fabrication of sample VG-05-103, see table I.1, which was grown in the first of the configurations above.

Sample name VG- Sources and nominal thicknesses	Substrate material	Temperature of Ga and Mn cells T(Ga) (C) and T(mn) (C) and set and achieved growth rates (nominal) Comments on RHEED	As desorption paramameters	Comments and average growth rates
VG-CoMnGa-AlO-Al-05-103 Co, Mn, Ga, Al, Au t = 12 nm (25 min) Co2MnGa + 1 nm Al + oxidation + 1 nm Al + oxidation + 8.8 nm Al + 13.5 nm Au Au-capping in LL 135 Å 11 A/ 120 sec	Two GaAs pieces: -NBI#21 (delta-doped + As-capped) -NBI#10 (delta-doped + As-capped) No In bonding No buffer layer	T(Ga): 908 C T(Mn): 1094 C Bottom Co2MnGa-layer: Nominal/meas. rates (nm/s): **HERE ALL RATES SHOULD BE MULTIPLIED BY 0.2:** Co: 0.0100/ 0.000997* Mn: 0.0080/ 0.0084 Ga: 0.0188/ 0.0200 * Co source with feedback control with TF x 5 = 6.70 **After 16th ICP round:** **HERE ALL RATES SHOULD BE MULTIPLIED BY 0.2:** **with new rate notation:** **aim for 113/160/188 (sum = 461)** **ON AVERAGE achieved: 155/167/200** **X 0.2 (sum = 522 x 0.2)** **Flash annealing of bottom layer:** **350 C/2 min** **Cool down overnight to –43 C before deposition of insulator and Al top layer** **Fine streaky RHEED reflexes** Insulator-layer, AlxOy: Al: 0.01 nm/s **(feedback control):** **T(substrate) = -43.1 C** **1) First Al layer:** **1.nm over 100 secs** **(FTM2 with TF = 0.63)** **e-gun: 33 mA** **Still RHEED reflexes (weaker)** **2) Oxidation at** **p(O2) = 2.8 x 10-4 mb** **over 25 min** **Still RHEED reflexes** **3) Second Al layer:** **1.nm over 100 secs** **e-gun: 30 mA** **Weak RHEED spots** **T(sub) = -44.4 C** **4) Oxidation at** **p(O2) = 1.1 x 10-4 mb** **over 20 min** **Still weak RHEED spots !** Top superconductor layer (aim for Hc > 2.5 T): Al: 0.01 nm/s **(feedback control):** **T(substrate) = -45.2 C** **8.8 nm Al over 15 min** **RHEED: fine epitaxial Al layer !!**	**Desorption:** **250 C/ 10 min** **450 C/ 30 min** **550 C/ 60 min** **570 C/ 2 min**	**First of two Tedrow-Meservey FIS-samples** Bottom layer: **Co2MnGa grown at 250 C** **(slow growth) Mn+ Ga rates: (0.0388) x 0.2 nm/s (Ga par.)** **Co rate on FTM3: 0.0155 x 0.2 nm/s(Ga par.)** **Average of total rate = 0.0543 x 0.2 nm/s** (Ga parameters)

Table I.1: *VG-05-103: growth sequence 2). Grown on 30-11-2005 - 01-12-2005*

RHEED patterns between the different steps can be seen in Figure I.3

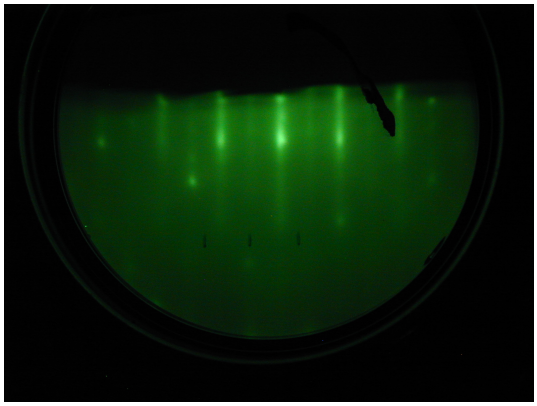

(a) After growth of bottom Co2MnGa-layer. Along ($0\overline{1}1$)-direction.

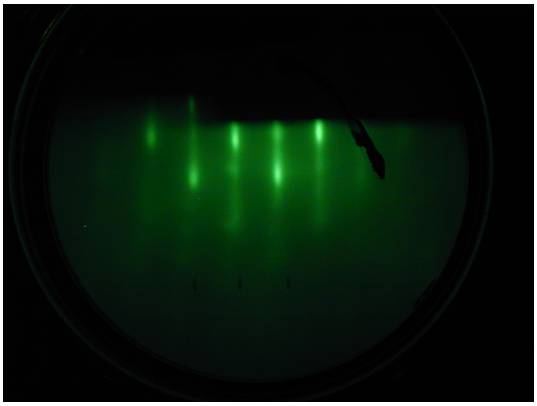

(b) After growth of bottom Co2MnGa-layer. Along (001)-direction.

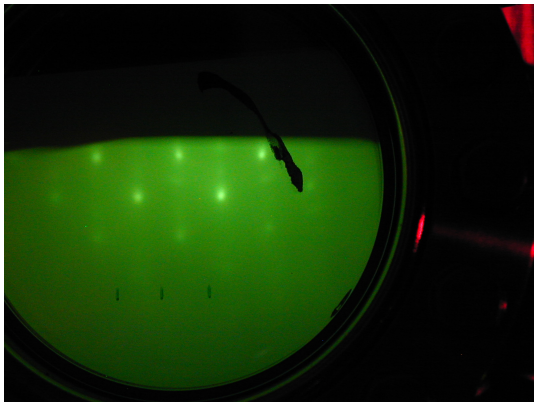

(c) After growth of 1nm Al. Along ($0\overline{1}1$)-direction.

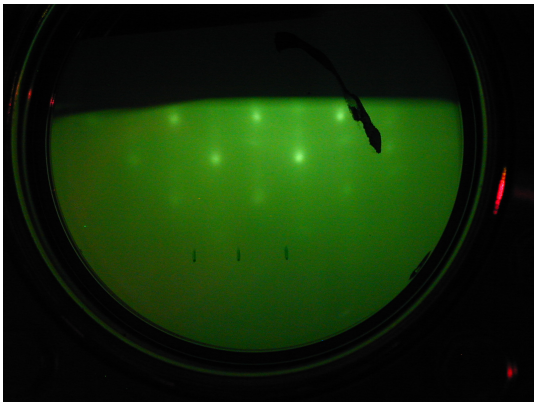

(d) After oxidation of Al. Along ($0\overline{1}1$)-direction.

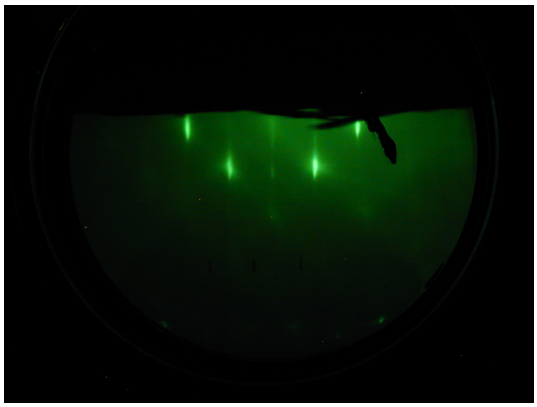

(e) After growth of top Al-layer. Along ($0\overline{1}1$)-direction.

Figure I.3: *VG05-103: RHEED(20 kV) patterns in between the different growth steps.*

Configuration 2) (2005)

By using same oxidation parameters as described in configuration 1 (2005), we have observed epitaxial growth of the Co_2MnGa-Al_xO_y-Al thin film structures grown on GaAs. RHEED patterns in between the different steps can be seen in Figure I.4

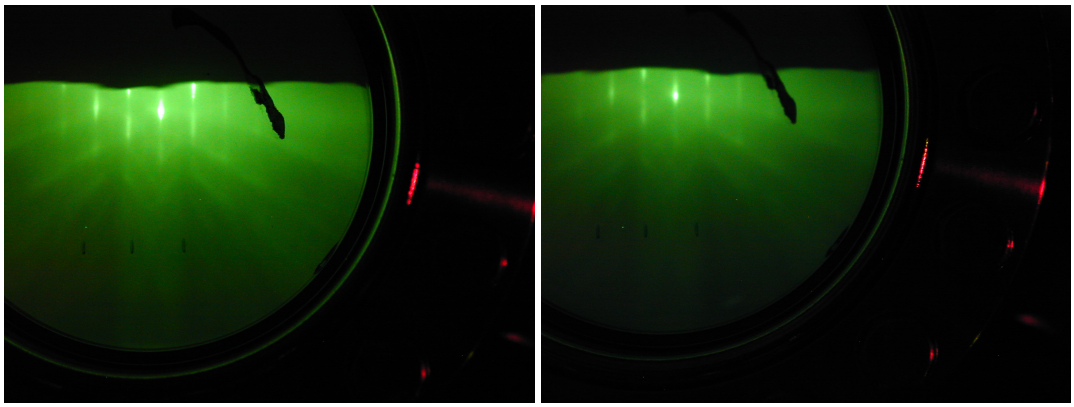

(a) After growth of bottom Al-layer. Along $(0\overline{1}1)$-direction.

(b) After oxidation Along $(0\overline{1}1)$-direction.

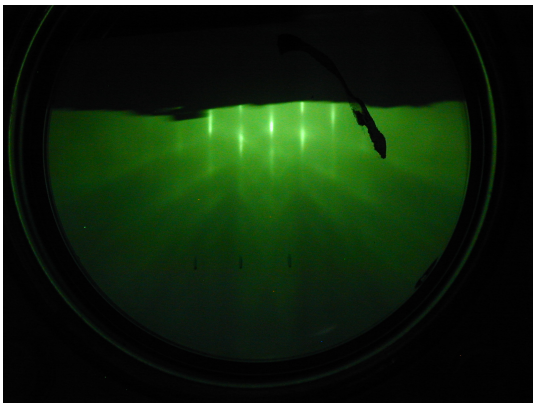

(c) After growth of top Co2MnGa-layer. Along $(0\overline{1}1)$-direction.

Figure I.4: *VG05-104: RHEED(20kV) patterns in between the different growth steps.*

Same mask set has been used for processing all the above described devices. A picture of a sample is seen in Figure I.5:

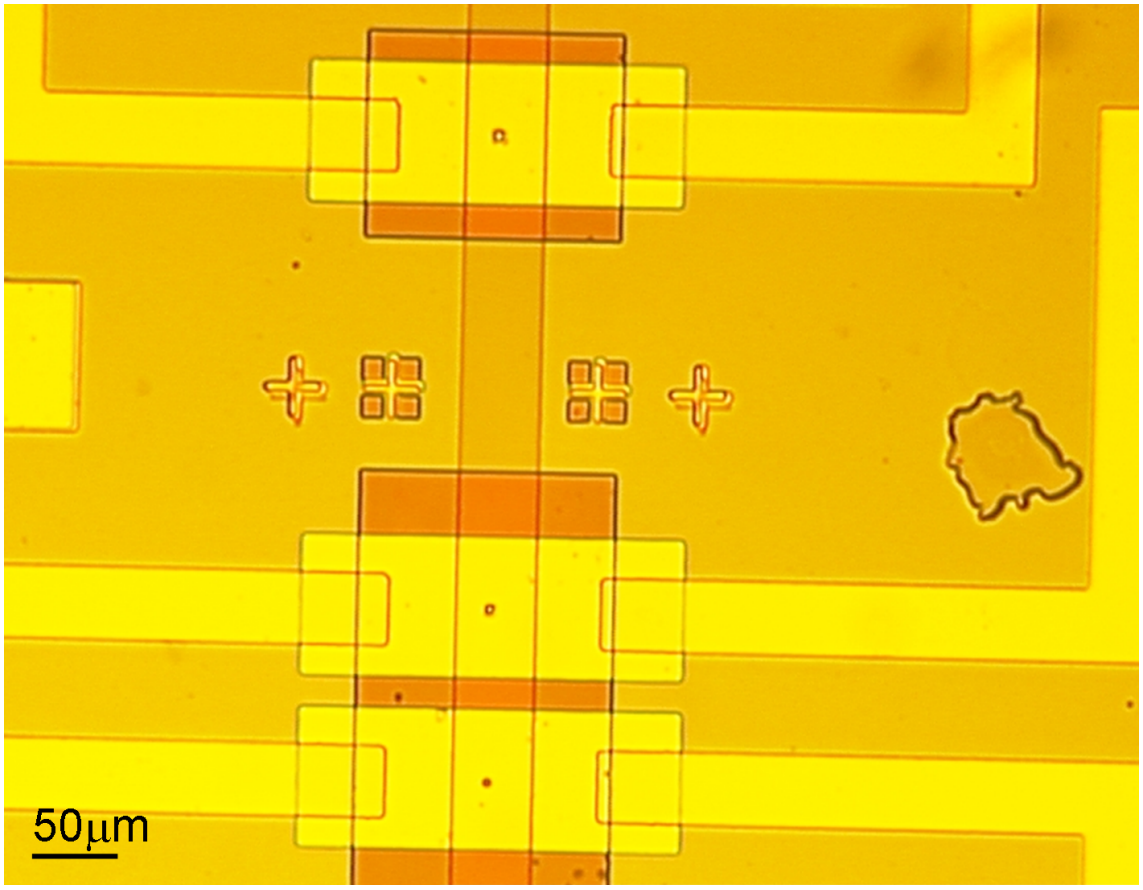

Figure I.5: *Microscope picture of a F/I/S sample.*

Appendix J

Description of preparation of F/S/F and F/N/F

SEM lithography were used to define sub-micron mesas between sub-micron ferromagnetic contacts. The samples was intended to characterize the spin-injection by non-local techniques as done by Jedema *et al.* [106]. A sketch of the idea and the different processing steps can be seen below:

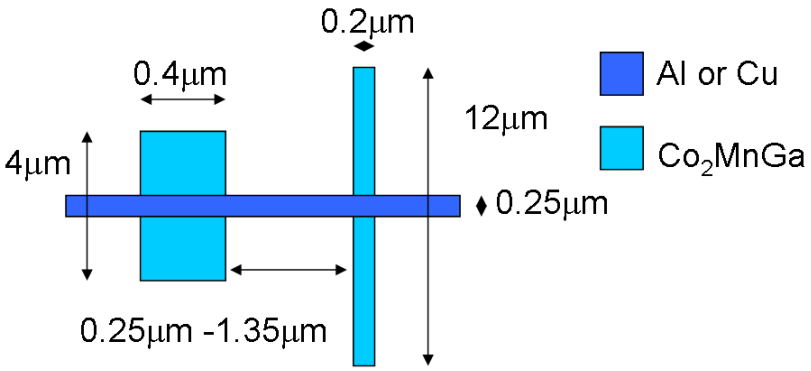

Figure J.1: *Sketch of the idea and the different processing steps.*

Step	Process	Equipment	Parameters	Necessities
1	Growth of HN-layer	VG-chamber:	GaAs-substrate+ 10-20nm Co2MnGa+ 10nm Al or Cu	
2	Etch H-Mesa	B-chamber	100nm etch	UV-lithography see step 2 sketch
3	Growth Contacts+Gates (lift-off)	Alcatel or chamber on HCØ	2x100nm Au	UV-lithography see step 3 sketch
4	Etch Ferromagnetic contacts	B-chamber	100nm etch	SEM-lithography see step 4 sketch
5	Rinse+ growth of N-mesa (lift-off)	VG	5nm rinse + 10nm Al or Cu mesa	Etch-rates in AlxOy and Al in B-camber + SEM-lithography see step 5 sketch
6	Growth of Au contact (lift-off)	Alcatel	5Å In+ 10nm Au	SEM-lithography see step 6a or 6b sketch

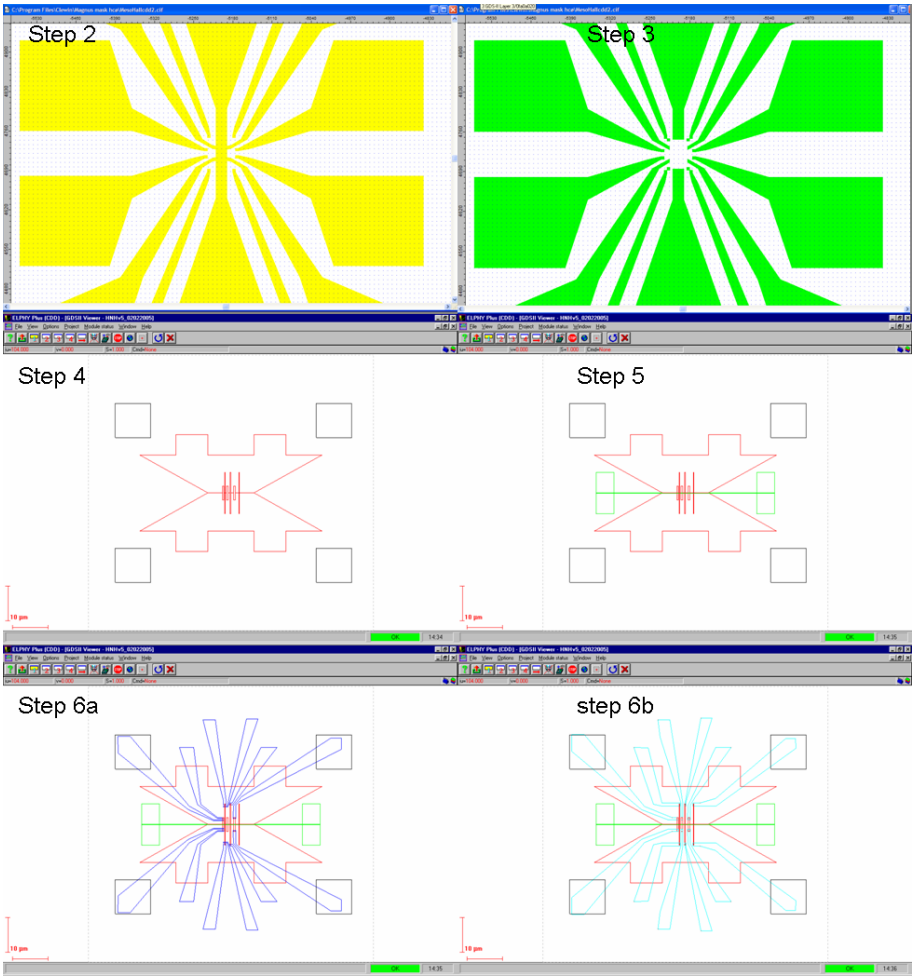

Figure J.2: *SEM information.*

After practising quite a bit on the SEM step 4, we succeeded in defining and developing the contacts shown in the sketch above (step 4). The used recipe can be seen in Appendix F.

A picture showing the developed resist is shown below.

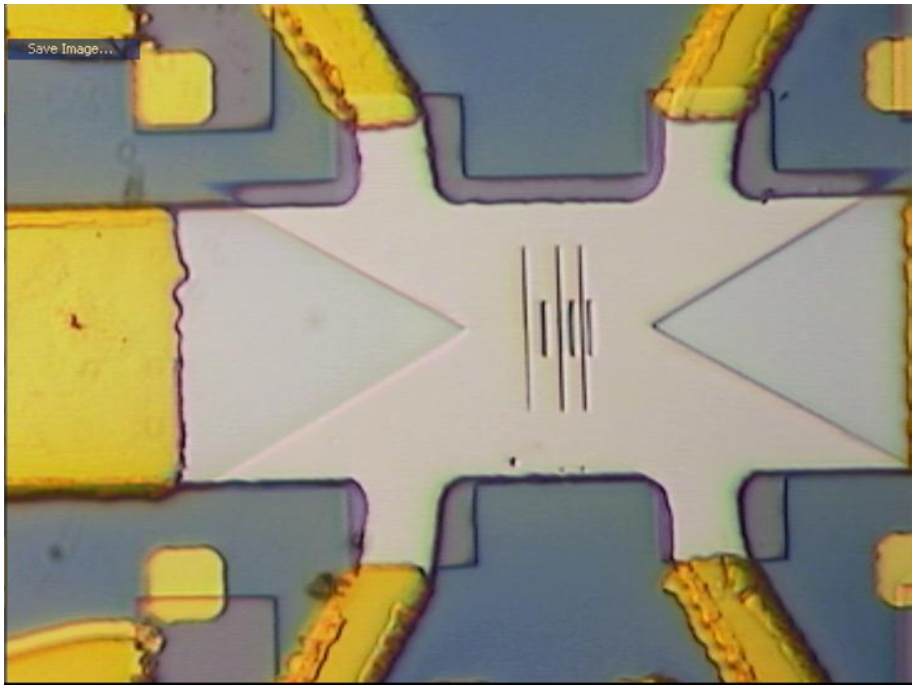

Figure J.3: *The SEM parameters were: Dose= 0.2; Resist sensitivity= 300=>; scan rate= 10.*

Everything up to this seemed to work alright, even though the alignment was quite difficult. But when we realized that our Ar beam we use for etching Co2MnGa, etches the PMMA-resist as well as the Heusler alloy, we were quite disappointed. The picture below shows the same spot after etch:

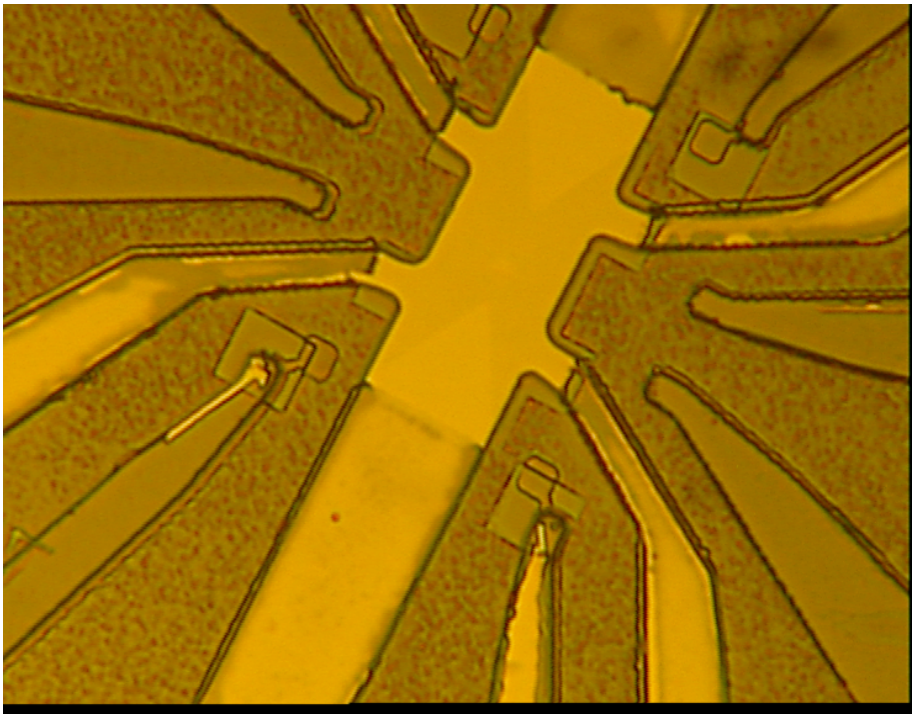

Figure J.4: *Sample after etch*

As seen on the picture above, the Heusler-alloy is not etched through, but the thin contacts defined in PMMA resist are completely gone. At this point we decided to stop the project. There were simply too many parameters to study even before the alignment hurdle was to be considered. Now a year later we guess that the reason for the poor effect of the PMMA-resist during etch, is due to heating. The sample was not cooled down during the Ar beam etch, which results in heating up the resist and makes it ”flow” away.

Appendix K

Semiconductor structures used for spinLEDs

K.1 C2294

The structure is grown on undoped GaAs [100]. Table K.1 shows the growth parameters.

Layer	Material	Thickness [nm]	Dopant	Density [cm^{-3}]	Comment
0	GaAs [100]	4E5			Substrate
1	GaAs	500	Be	1.00E18	Nominal doping level
2	GaAs	500			
3	InGaAs	5			20% In
4	GaAs	200			
5	GaAs	100	Si	1.00E18	
6	AlGaAs	15	Si	1.00E18	x=0.33 alloying Schottky barrier
7	AlGaAs	15	Si	3.33E18	x=0.33 alloying Schottky barrier
8	GaAs	1			Nominal GaAs interrupt before As cap
9	As				Cap

Table K.1: *Growth parameters for C2294.*

The structure has a AlGaAs schottky barrier and a GaAs/$In_{0.2}Ga_{0.8}As$ QW. Time resolved Photoluminescence spectroscopy showed a radiative recombination lifetime of electrons τ on 264 ps at $T = 5\ K$ (see Figure K.1). Very similar results obtained at low temperature have been reported by Haiping *et al.* [112]. Neither the temperature dependence or the magnetic field dependence of the radiative lifetimes have been measured, due to lack of time.

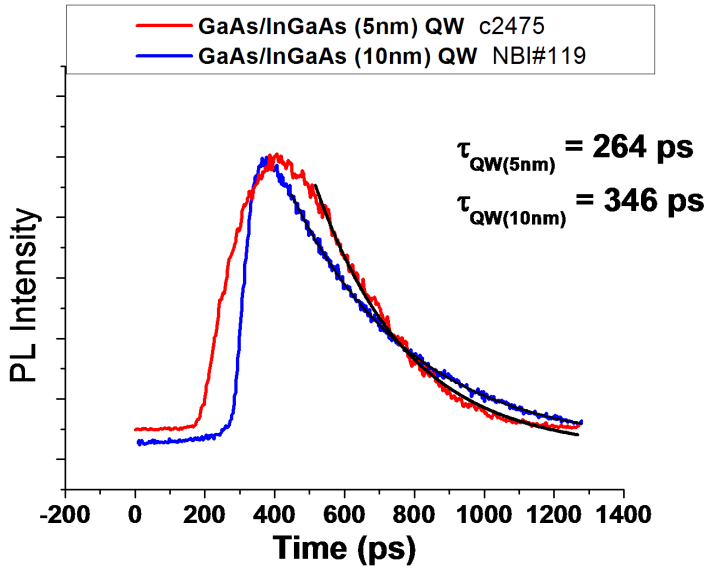

Figure K.1: *Time-resolved photoluminescence measurements at T=5K. The samples are reference samples, without barrier and doping in the cladding layers, as the only difference to the spinLED structures.*

Figure K.2 shows calculated conduction and valence band.

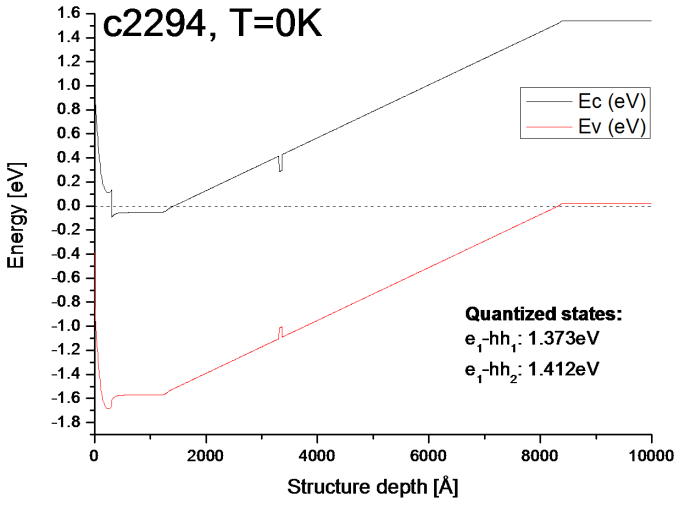

Figure K.2: *Band diagram calculations in case of C2294. The insert shows calculated recombination energies.*

The expected emission energy of the 5 *nm* GaAs/$In_{0.2}Ga_{0.8}As$ QW shown in the figure has been calculated by use of a 1d Poisson/Scrödinger solver. Further details can be found in M. Figure K.3 shows a spectra of the emitted light.

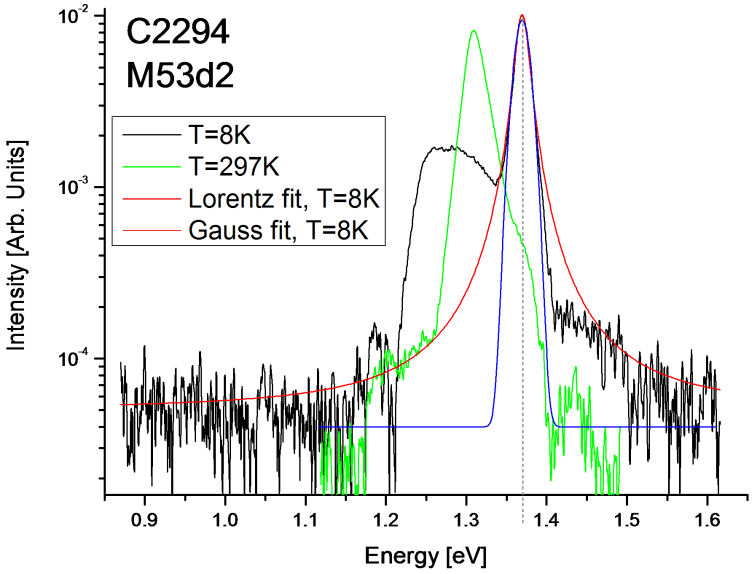

Figure K.3: *Energy spectra of light emitted from C2294. At T=4 K, the main peak is observed at E=1.370 eV*

The reason for the rather wide line of C2294 is not fully understood. The same is the case for the rather large shoulder observed around 1.3eV. Indium segregation could be the case even though the observed energy difference between the shoulder peak and the main peak seem a bit to large (approximate a factor of two). The observed behavior could also be explained by inhomogeneities in the QW thickness. Measurements on other pieces of the wafer show some deviation in the observed main peak position, and the magnitude of the shoulder peak, indicating that the wafer is not homogeneous.

K.2 C2398

C2398 is very similar to C2294 but has two QW with different thickness. This structure was designed in order to give information about the spin scattering events in the area between the two QWs. Table K.2 shows the growth parameters.

Layer	Material	Thickness [nm]	Dopant	Density [cm^{-3}]	Comment
0	GaAs [100]	Be	1.00E18	Nominal doping level	Substrate
1	GaAs	500	Be	1.00E18	Nominal doping level
2	GaAs	100			
3	InGaAs	10			20% In
4	GaAs	100			
5	InGaAs	5			20% In
6	GaAs	50			
7	GaAs	50	Si	1.00E18	
8	AlGaAs	15	Si	1.00E18	x=0.33 alloying Schottky barrier
9	AlGaAs	15	Si	5.00E18	x=0.33 alloying Schottky barrier
10	GaAs	1			Nominal GaAs interrupt before As cap
11	As				Cap

Table K.2: *Growth parameters for C2398.*

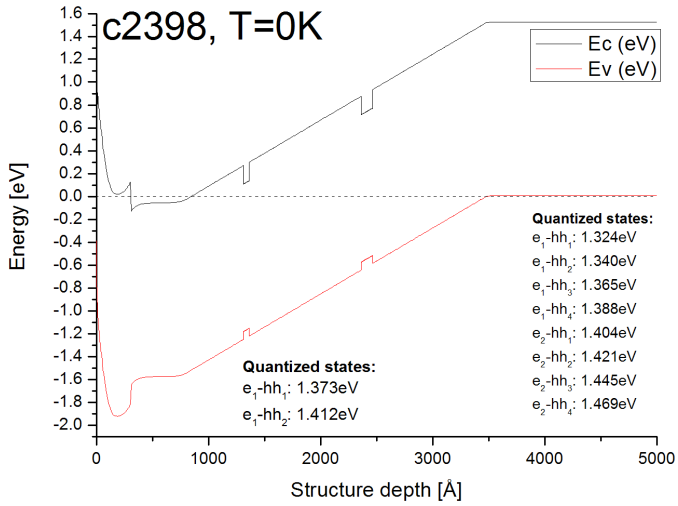

Figure K.4: *Band diagram calculations in case of C2398. The inserts show calculated recombination energies.*

Figure K.5 illustrates a spectra of the emitted light.

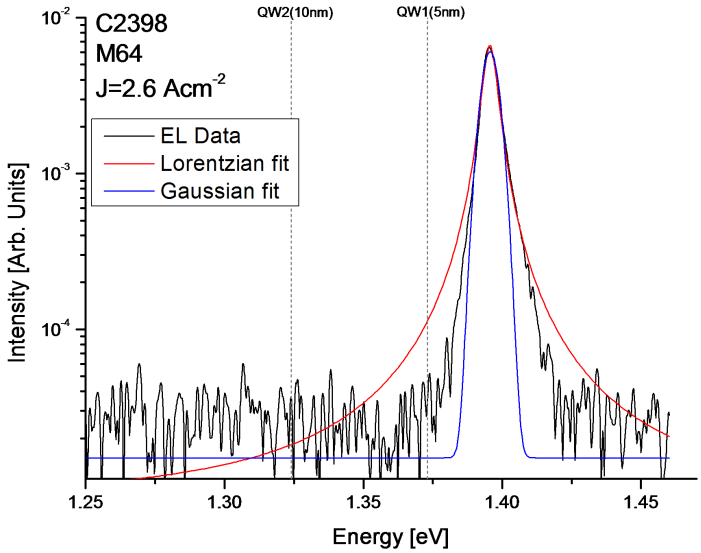

Figure K.5: *Energy spectra of light emitted from C2398. At T=4 K, the main peak is observed at E=1.396 eV*

Only one peak is observed in the energy spectra of C2398, even though there are two QWs in the structure. From comparison with the calculations we expect the emitted light to come from the 5 nm QW. We have no explanation for why we do not see emitted light other than at that bias all recombination happens in the 5 nm QW. We do expect to see emitted light from the 10 nm QW at higher biases. We realized this after the measurements were finished, and therefore it has not been done.

K.3 NBI#9

This hetero structure is like C2294 and C2398 based on a GaAs/InGaAs QW. Contrary to the Cavendish wafers this structure has a graded doped barrier. Table K.3 shows the growth parameters.

Layer	Material	Thickness [nm]	Dopant	Density [cm^{-3}]	Comment
0	GaAs [100]	4E5	Zn	1E19	Substrate
1	GaAs	1000	Be	1E18	Nominal doping level
2	GaAs	150			
3	InGaAs	10			17.8% In
4	GaAs	40			
5	GaAs	200	Si	1.00E17	
6	GaAs	15	Si	1.00E17-5.00E18	Schottky barrier graded doping
7	GaAs	15	Si	5.00E18	Schottky barrier
8	As				Cap

Table K.3: *Growth parameters for NBI#9.*

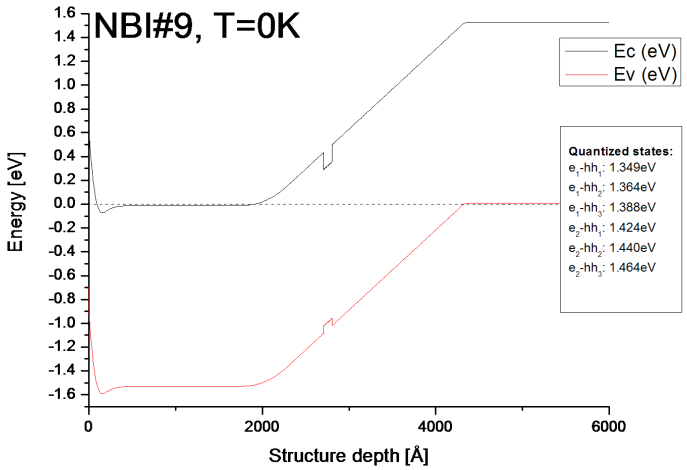

Figure K.6: *Band diagram calculations in case of NBI#9. The insert shows calculated recombination energies.*

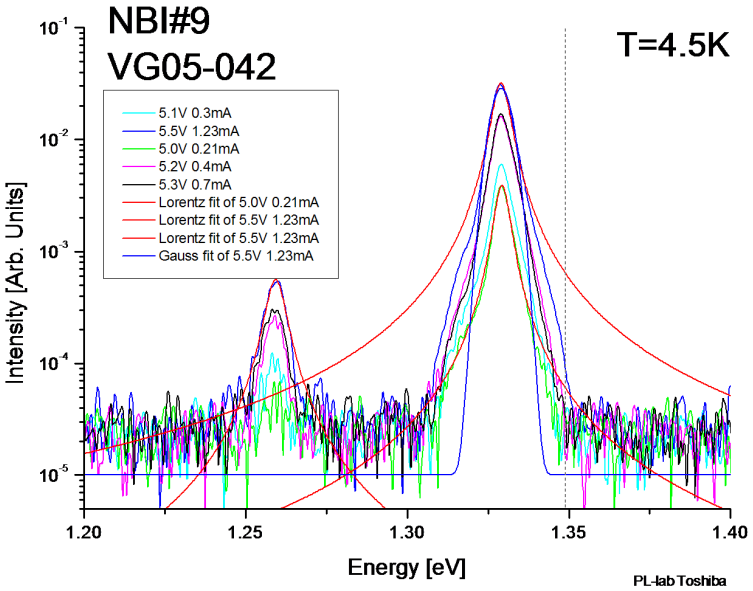

Figure K.7: *Energy spectra of light emitted from NBI#9. At T=4.5 K peaks are observed E=1.329 eV and E=1.259 eV.*

The small peak at E=1.259eV in NBI#9 seems to appear from the noise level at biases above 5.0V. We expect this to be due to a defect band with energies just below the InGaAs

bandgap. Similar behavior is reported by Haiping *et al.* [112, 116], with approximate the same energy difference. Haiping *et al.* explain the splitting by Indium segregation in the QW.

Appendix L

Optics: Details

L.1 Calibration procedure of the wave retarder component

The calibration of the wave retarder component was made as depicted in Figure L.1.

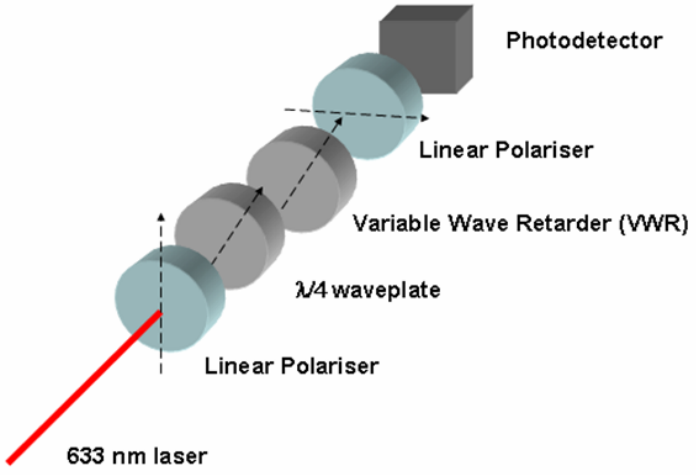

Figure L.1: *Wave retarder calibration setup.*

The calibration was done by tuning the wave retarder control unit until the corresponding intensity detected by the photodetector showed zero and maximum signal as showed in Figure L.2.

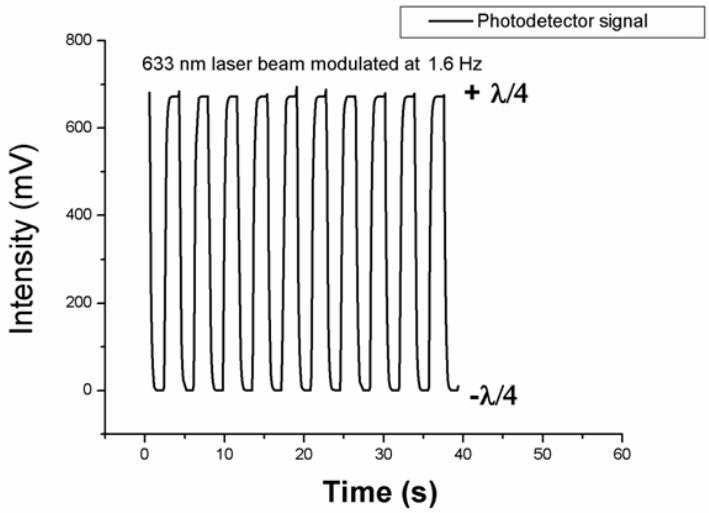

Figure L.2: *Calibrated wave retarder signal.*

L.2 Jones calculus: Measurement of intensity of right and left circular polarized light

Figure L.3 schematically shows the two methods used for detection of circular polarized light.

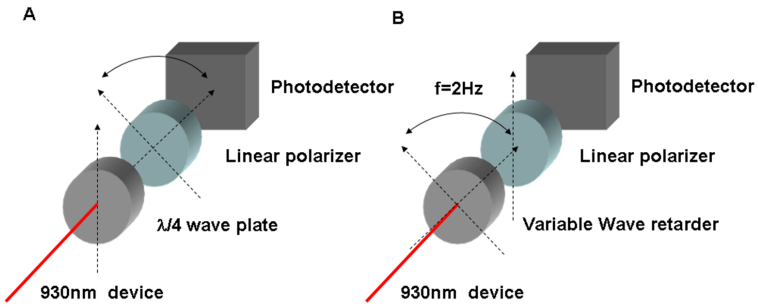

Figure L.3: *A) the "manual" setup, B) the "automatic" setup*

Jones calculus (by R. C. Jones in 1941.) is a mathematical technique for describing the amplitudes and phases of light (electric fields) propagating through different optical components. Each optical component can be described by a 2×2 Jones matrix. Table L.1 shows the Jones matrices for the components involved in the Hanle setup. The polarization states of light can likewise be described by Jones vector. Table L.2 shows the normalized Jones vectors of the polarization states involved in the setups see figure L.3

Optical component	Jones Matrix
Linear polarizer aligned 45° from the vertical axis	$\frac{1}{2}\begin{pmatrix} 1 & 1 \\ 1 & 1 \end{pmatrix}$
Linear polarizer aligned −45° from the vertical axis	$\frac{1}{2}\begin{pmatrix} 1 & -1 \\ -1 & 1 \end{pmatrix}$
Linear polarizer aligned vertical	$\begin{pmatrix} 0 & 0 \\ 0 & 1 \end{pmatrix}$
Quarter-wave plate, fast axis vertical	$e^{i\pi/4}\begin{pmatrix} 1 & 0 \\ 0 & -i \end{pmatrix}$
Quarter-wave plate, with axis rotated +45° from vertical axis	$e^{i\pi/4}\begin{pmatrix} \frac{1}{2}-i\frac{1}{2} & \frac{1}{2}+i\frac{1}{2} \\ \frac{1}{2}+i\frac{1}{2} & \frac{1}{2}-i\frac{1}{2} \end{pmatrix}$
Quarter-wave plate, with axis rotated −45° from vertical axis	$e^{i\pi/4}\begin{pmatrix} \frac{1}{2}+i\frac{1}{2} & \frac{1}{2}-i\frac{1}{2} \\ \frac{1}{2}-i\frac{1}{2} & \frac{1}{2}+i\frac{1}{2} \end{pmatrix}$

Table L.1: *Jones matrices for different optical components*

Polarization	Jones vector
Linear polarization with vertical polarization axis α. For $\alpha = 0$ the polarization axis is horizontal	$\begin{pmatrix} 0 \\ 1 \end{pmatrix}$
Linear polarization with polarization axis α. For $\alpha = 0$ the polarization axis is vertical	$\begin{pmatrix} \sin\alpha \\ \cos\alpha \end{pmatrix}$
Right circular polarized light	$\frac{1}{\sqrt{2}}\begin{pmatrix} 1 \\ -i \end{pmatrix}$
Left circular polarized light	$\frac{1}{\sqrt{2}}\begin{pmatrix} 1 \\ i \end{pmatrix}$

Table L.2: *Normalized Jones vectors for different polarization states*

The measured intensity is given as $|\overrightarrow{E}|^2$. The connection between in and out coming light and is given by:

$$\overrightarrow{E}_{out} = \bar{J} \cdot \overrightarrow{E}_{in} \tag{L.1}$$

Consider Figure L.3 (A) with incoming light circular polarized with both right and left helicity given by the pre-factors r and l:

$$\overrightarrow{E}_{in} = \frac{l}{\sqrt{2}}\begin{pmatrix} 1 \\ i \end{pmatrix} + \frac{r}{\sqrt{2}}\begin{pmatrix} 1 \\ -i \end{pmatrix} \tag{L.2}$$

$$|\overrightarrow{E}_{in}|^2 = l^2 + r^2 \tag{L.3}$$

The total intensity of the incoming light is given by equation L.3. After propagating through the quarter-wave plate with fast axis aligned vertical followed by a linear polarizer +45° to vertical axis, the A-vector is given as:

$$\overrightarrow{E}_{+45^\circ} = \frac{1}{2}\begin{pmatrix} 1 & 1 \\ 1 & 1 \end{pmatrix} e^{i\pi/4}\begin{pmatrix} 1 & 0 \\ 0 & -i \end{pmatrix}\overrightarrow{E}_{in} \tag{L.4}$$

$$\overrightarrow{E}_{+45^\circ} = \frac{l}{\sqrt{2}} e^{i\pi/4}\begin{pmatrix} 1 \\ 1 \end{pmatrix} \tag{L.5}$$

$$|\overrightarrow{E}_{out}|^2 = l^2 \tag{L.6}$$

which is linear light with same intensity as the original left circular polarized light, given by equation L.6.
If the linear polarizer is shifted to $-45°$, the E-vector of the light is given as:

$$\overrightarrow{E}_{-45°} = \frac{1}{2}\begin{pmatrix} 1 & -1 \\ -1 & 1 \end{pmatrix} e^{i\pi/4} \begin{pmatrix} 1 & 0 \\ 0 & -i \end{pmatrix} \overrightarrow{E}_{in} \tag{L.7}$$

$$\overrightarrow{E}_{-45°} = \frac{l}{\sqrt{2}} e^{i\pi/4} \begin{pmatrix} 1 \\ 1 \end{pmatrix} \tag{L.8}$$

$$|\overrightarrow{E}_{out}|^2 = r^2 \tag{L.9}$$

Ones again the polarization state is linear, but now with same intensity as the original right circular polarized light given by equation L.9.

Let us now consider figure L.3 B. We are only interested in intensity and polarization state of the light in the two outer positions of the wave retarder. In those positions the Jones matrices are given by those of a quarter-wave plate with fast axis rotated ±45° from the vertical axis. With incoming light given by $\overrightarrow{E}_{in}$, the Jones calculus takes following form:

$$\overrightarrow{E}_{+45°} = \begin{pmatrix} 0 & 0 \\ 0 & 1 \end{pmatrix} e^{i\pi/4} \begin{pmatrix} \frac{1}{2} - i\frac{1}{2} & \frac{1}{2} + i\frac{1}{2} \\ \frac{1}{2} + i\frac{1}{2} & \frac{1}{2} - i\frac{1}{2} \end{pmatrix} \overrightarrow{E}_{in} \tag{L.10}$$

$$\overrightarrow{E}_{+45°} = r \cdot e^{i\pi/4} \begin{pmatrix} 0 \\ 1+i \end{pmatrix}, |\overrightarrow{E}_{+45°}|^2 = r^2 \tag{L.11}$$

$$\overrightarrow{E}_{-45°} = \begin{pmatrix} 0 & 0 \\ 0 & 1 \end{pmatrix} e^{i\pi/4} \begin{pmatrix} \frac{1}{2} - i\frac{1}{2} & -\frac{1}{2} - i\frac{1}{2} \\ -\frac{1}{2} - i\frac{1}{2} & -\frac{1}{2} + i\frac{1}{2} \end{pmatrix} \overrightarrow{E}_{in} \tag{L.12}$$

$$\overrightarrow{E}_{-45°} = l \cdot e^{i\pi/4} \begin{pmatrix} 0 \\ 1+i \end{pmatrix}, |\overrightarrow{E}_{-45°}|^2 = l^2 \tag{L.13}$$

Again we measure linear polarized light with same intensity as the original intensity of right or left circular polarized light.

Appendix M

Band diagram calculations: Details

1D Poisson/Schrödinger is a band diagram calculator, written by Greg Snider[113]. The program uses the method of finite differences to find one-dimensional band diagrams of a semiconductor structure. The calculations were reproduced by a web-solution offered by the Ioffe institute [114]. I have mainly used the program default settings. Schottky boundary conditions have been applied at the surface. The Schottky barrier height is determined by the barrier of the semiconductor. In the following sections the used material parameters and input files are shown.

M.1 Material parameters

M.1.1 GaAs

Energy Gap = 1.519eV
Conduction band offset relative to gaas = 0.000 eV
Relative dielectric constant =13.100
Electron effective mass = 0.067
Cond. band degeneracy = 1.000
Heavy hole effective mass = 0.350
Light hole effective mass = 0.090
Donor level = 6.00E-03 eV
Default donor concentration = 0.00E+00 cm-3
Acceptor level = 30.00E-03 eV
Default acceptor concentration = 0.00E+00 cm-3
Deep donor level = 600.00E-03 eV
Default deep donor concentration = 0.00E+00 cm-3
Deep acceptor level = 700.00E-03 eV
Default deep acceptor concentration = 0.00E+00 cm-3
Default barrier height = 0.600 eV
Default electron mobility = 8.500E+03 cm2/V-s
Default hole mobility = 4.000E+02 cm2/V-s

Default electron recombination time = 1.000E-12 s
Default hole recombination time = 1.000E-12 s
Default absorption coefficient = 0.000E+0

M.1.2 $Al_{0.3}Ga_{0.7}As$

Energy Gap = 1.893 eV
Conduction band offset relative to gaas = 0.232 eV
Relative dielectric constant =12.200
Electron effective mass = 0.092
Cond. band degeneracy = 1.000
Heavy hole effective mass = 0.662
Light hole effective mass = 0.108
Donor level = 30.00E-03 eV
Default donor concentration = 0.00E+00 cm-3
Acceptor level = 40.00E-03 eV
Default acceptor concentration = 0.00E+00 cm-3
Deep donor level = 000.00E-03 eV
Default deep donor concentration = 0.00E+00 cm-3
Deep acceptor level = 000.00E-03 eV
Default deep acceptor concentration = 0.00E+00 cm-3
Default barrier height = 0.741 eV
Default electron mobility = 4.000E+03 cm2/V-s
Default hole mobility = 4.000E+02 cm2/V-s
Default electron recombination time = 1.000E-10 s
Default hole recombination time = 1.000E-10 s
Default absorption coefficient = 0.000E+00

M.1.3 $In_{0.2}Ga_{0.8}As$

Energy Gap = 1.289 eV
Conduction band offset relative to gaas = -.161 eV
Relative dielectric constant =13.384
Electron effective mass = 0.064
Cond. band degeneracy = 1.000
Heavy hole effective mass = 0.462
Light hole effective mass = 0.108
Donor level = 6.82E-03 eV
Default donor concentration = 0.00E+00 cm-3
Acceptor level = 10.00E-03 eV
Default acceptor concentration = 0.00E+00 cm-3
Deep donor level = 200.00E-03 eV

Default deep donor concentration = 0.00E+00 cm-3
Deep acceptor level = 200.00E-03 eV
Default deep acceptor concentration = 0.00E+00 cm-3
Default barrier height = 0.600 eV
Default electron mobility = 4.000E+03 cm2/V-s
Default hole mobility = 4.000E+02 cm2/V-s
Default electron recombination time = 1.000E-10 s
Default hole recombination time = 1.000E-10 s
Default absorption coefficient = 0.000E+00

M.1.4 $In_{0.178}Ga_{0.822}As$

Energy Gap = 1.315 eV
Conduction band offset relative to gaas = -.143 eV
Relative dielectric constant =13.353
Electron effective mass = 0.064
Cond. band degeneracy = 1.000
Heavy hole effective mass = 0.462
Light hole effective mass = 0.108
Donor level = 6.69E-03 eV
Default donor concentration = 0.00E+00 cm-3
Acceptor level = 10.00E-03 eV
Default acceptor concentration = 0.00E+00 cm-3
Deep donor level = 200.00E-03 eV
Default deep donor concentration = 0.00E+00 cm-3
Deep acceptor level = 200.00E-03 eV
Default deep acceptor concentration = 0.00E+00 cm-3
Default barrier height = 0.600 eV
Default electron mobility = 4.000E+03 cm2/V-s
Default hole mobility = 4.000E+02 cm2/V-s
Default electron recombination time = 1.000E-10 s
Default hole recombination time = 1.000E-10 s
Default absorption coefficient = 0.000E+00

M.2 Input files

M.2.1 c2294

c2294
surface schottky v1
GaAs t=10
AlGaAs t=150 x=.3 Nd=3.33e18

AlGaAs t=150 x=.3 Nd=1e18
GaAs t=1000 Nd=1e18
GaAs t=2000
InGaAs_GaAs t=50 x=.2 dy=1
GaAs t=5000
GaAs t=5000 Na=5e18
substrate
fullyionized
v1 0.0
schrodingerstart=3210
schrodingerstop=3460
temp=0K
dy=5

M.2.2 c2398

c2398 Scrodinger for QW1
surface schottky v1
GaAs t=10 AlGaAs t=150 x=.33 Nd=5e18
AlGaAs t=150 x=.33 Nd=1e18
GaAs t=500 Nd=1e18
GaAs t=500
InGaAs_GaAs t=50 x=.2 dy=1
GaAs t=1000
InGaAs_GaAs t=100 x=.2 dy=1
GaAs t=1000
GaAs t=5000 Na=1e18
substrate
fullyionized
v1 0.0
schrodingerstart=1300
schrodingerstop=1370
temp=0K
dy=5

M.2.3 NBI#9

NBI9
surface schottky v1
GaAs t=150 Nd=5e18
GaAs t=50 Nd=2.5e18
GaAs t=50 Nd=7.5e17
GaAs t=50 Nd=2.5e17

```
GaAs t=2000 Nd=1e17
GaAs t=400
InGaAs_GaAs t=100 x=.178 dy=1
GaAs t=1500
GaAs t=10000 Na=1e18
substrate
fullyionized
v1 0.0
schrodingerstart=2600
schrodingerstop=2900
temp=0K
dy=10
```

Appendix N

Hanle fitting model

The fitting procedure is based on Equation 1.17 shown as N.1 in this appendix, which is the steady-state solution to the Bloch-Thorrey Equation with $\mathbf{S_0}(0, S^*_{0y}, S^*_{0z})$ where $S^*_{0y} = S_0 cos\psi$ and $S^*_{0z} = S_0 sin\psi$.

$$S_z = S^*_{0y}\eta\frac{(B/\Delta B)^2 cos\varphi sin\varphi}{1+(B/\Delta B)^2} + S^*_{0z}\eta\frac{1+(B/\Delta B)^2 cos^2\varphi}{1+(B/\Delta B)^2} \tag{N.1}$$

$\Delta B = (\frac{g^*\cdot\mu_B}{\hbar}T_s)^{-1}$ is the Hanle curve half-width, corresponding to the condition $\Omega T_s = 1$, η describes the longitudinal spin relaxation prior to recombination or the spin detection efficiency in the semiconductor $\eta = \frac{T_s}{\tau}$, where T_s is the spin lifetime and τ is the radiative lifetime, φ is the Hanle angle, ψ is the magnetization tilting angle and B is the applied magnetic field. Figure N.1 illustrates the involved angles.

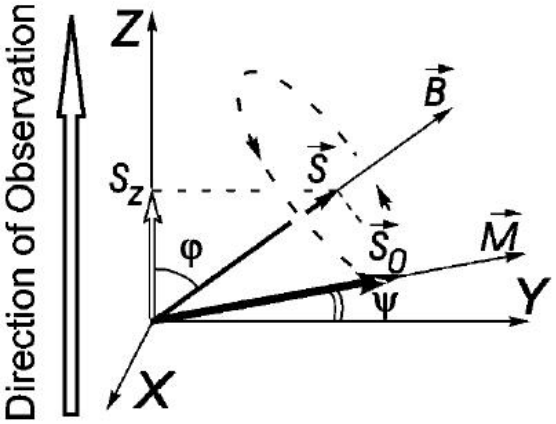

Figure N.1: *Tilting of the magnetization* **M** *of the thin ferromagnetic film under application of the oblique magnetic field* $\mathbf{B}(0, B_y, B_z)$ *in the oblique Hanle effect experimental configuration. Adadpted from [36]*

The main purpose of the fit is to find ΔB and thereby the spin lifetime T_s, by using

$g = -1.8$ for $In_{0.2}Ga_{0.8}Mn$. To do this we need to know the dependence of S^*_{0y} and S^*_{0z} on an applied field B. The first step is to calculate the tilting angle as a function of the applied field.

N.1 B-dependence of the tilting angle ψ

The magnitude of the tilt angle ψ is dependent on the saturation magnetization M and the external applied magnetic field $\mathbf{H_e xt} = \mathbf{B}/\mu_0$. The tilt angle is found by minimizing the total energy density of the film, approximated by the potential energy and the demagnetization energy

$$u = -\mu_0 \cdot (\mathbf{M} \cdot \mathbf{H_{ext}}) - \frac{\mu_0 \cdot (\mathbf{M} \cdot \mathbf{H_d})}{2}, \tag{N.2}$$

where $\mathbf{H_d} = -\mathbf{M_z}$ is the demagnetization field and $\mathbf{M_z}$ is the out-of-plane magnetization. By using the convention shown in figure 1.8, Equation N.2 is reduced to

$$u = -M \cdot B \sin\phi + \psi + \frac{\mu_0 \cdot M^2}{2} \cdot \sin^2(\psi). \tag{N.3}$$

The minimum is obtained by following relation:

$$\frac{B}{\mu_0 M} = \frac{\sin\psi \cos\psi}{\cos\phi \cos\psi - \sin\phi \sin\psi} \tag{N.4}$$

for $\phi = 60°$ and $\frac{B}{\mu_0 M} < 1$ the variation can be approximated linear as it can be seen in figure N.2.

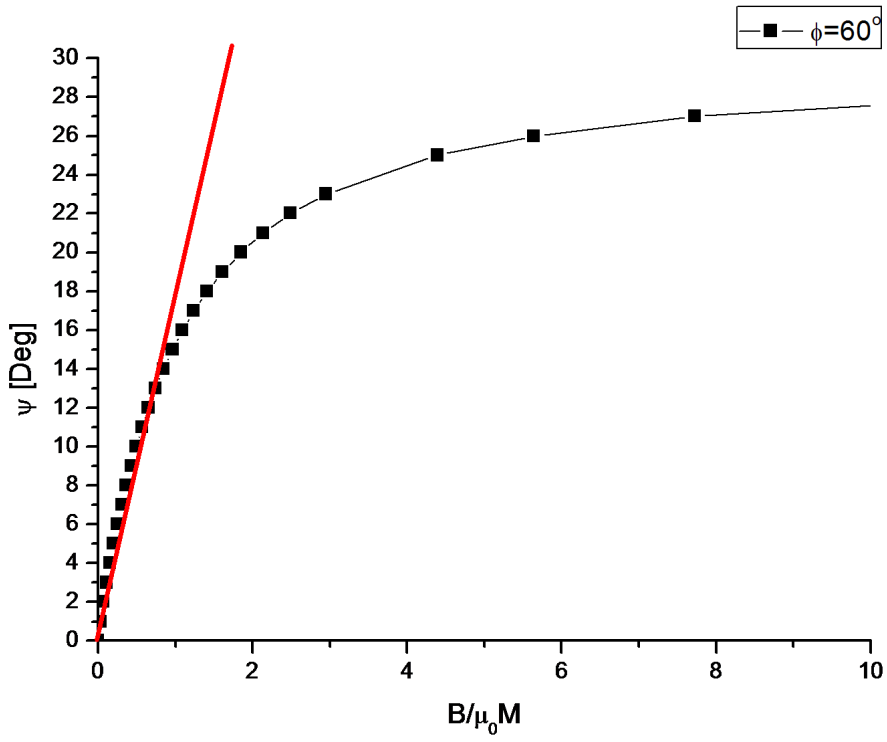

Figure N.2: *Tilting angle of the magnetization* **M** *of the thin ferromagnetic film under application of the oblique magnetic field* $\mathbf{B}(0, B\sin\phi, B\cos\phi)$.

The saturation magnetization of thin Co_2MnGa films is found from extraordinary hall effect in thin films with an applied magnetic field perpendicular to the film plane to $\mu_0 M_s \approx 1.7$T, which makes it reasonable to model the tilting axis ψ as linear dependent of B. Furthermore the tilting axis is small (less than approximately 10°). This allows us to use the magnitude of the in-plane coercive field B_c to model the switching of the magnetic spin S_0.

$$S_0(B) = \tanh(S_q * (B - B_c/\sin\phi)) \tag{N.5}$$

S_q is the squareness of the hysteresis curve, B is the magnetic field applied with an angle ϕ to the normal of the film plane.